



UNIVERSIDAD DE CHILE
FACULTAD DE CIENCIAS FÍSICAS Y MATEMÁTICAS
DEPARTAMENTO DE INGENIERÍA MECÁNICA

VARIATIONS ON THE DOUBLE-MULTIPLE STREAMTUBE MODEL FOR DARRIEUS STRAIGHT-BLADED VERTICAL-AXIS WIND TURBINES TO IMPROVE PREDICTIONS OF PERFORMANCE AND FLOW EXPANSION

TESIS PARA OPTAR AL GRADO DE
MAGÍSTER EN CIENCIAS DE LA INGENIERÍA, MENCIÓN MECÁNICA

MEMORIA PARA OPTAR AL TÍTULO DE
INGENIERO CIVIL MECÁNICO

RICHARD GEORG WENDLER ERNST

PROFESOR GUÍA:

WILLIAMS R. CALDERÓN MUÑOZ

MIEMBROS DE LA COMISIÓN:

RICHARD L. LEBOEUF

ALEJANDRO A. ORTÍZ BERNARDÍN

ÁLVARO A. VALENCIA MUSALEM

Este trabajo ha sido financiado parcialmente por
CONICYT-PCHA/Magíster Nacional/2013 - 221320449

SANTIAGO DE CHILE

2014

RESUMEN

El propósito del presente trabajo es formular una herramienta computacional de bajo costo que determine la potencia y la expansión de flujo de turbinas eólicas de eje vertical (VAWTs) tipo Darrieus. Esta herramienta puede ser útil para predecir el desempeño aerodinámico de VAWTs en ambientes urbanos o en granjas eólicas.

En este trabajo se realizan variaciones en el modelo doble-múltiple tubos de corriente (DMS) para turbinas Darrieus de álabes rectos (SB-VAWTs) con el fin de mejorar las predicciones de desempeño aerodinámico y expansión del flujo. Se presentan los antecedentes generales y el marco teórico del modelamiento de las Darrieus SB-VAWTs. El caso de referencia está compuesto por las mediciones de campo de una Darrieus SB-VAWT de 12 kW (6 m de diámetro) encontradas en la literatura y las simulaciones computacionales bidimensionales realizadas en el software ANSYS Fluent 13.0. Se plantea y verifica una representación matemática de las líneas de corriente para modelar el promedio temporal de la expansión de flujo alrededor de SB-VAWTs.

Se presenta una nueva formulación del modelo DMS basado en momentum con expansión de flujo. El desempeño aerodinámico y la expansión de flujo son calculados en MATLAB utilizando coeficientes aerodinámicos empíricos y los resultados de las simulaciones computacionales. Se propone una nueva formulación del modelo DMS basado en la conservación de energía mecánica. Ambas formulaciones estudiadas presentan problemas de convergencia para altas razones de velocidades de punta de álabes. Las predicciones de expansión de flujo se encuentran alejadas de las obtenidas en las simulaciones computacionales. Se cuantifica e interpreta el error de los modelos DMS basados en momentum y en energía al imponer la expansión obtenida por las simulaciones computacionales.

A partir de los datos de fuerza en el sentido del flujo y la expansión de los tubos de corriente, se propone una ecuación alternativa para el balance de momentum lineal considerando un modelo de múltiples tubos de corriente. Dicha relación permite la convergencia y una buena estimación de la expansión del flujo para todas las velocidades de rotación de turbina estudiadas. Se recomienda como trabajo futuro el mejoramiento del cálculo de las fuerzas aerodinámicas basadas en coeficientes aerodinámicos empíricos considerando los efectos dinámicos.

ABSTRACT

The purpose of this study is to formulate a low-cost computational tool to determine the power output and flow expansion of Darrieus vertical-axis wind turbines (VAWTs). This tool could be useful for the performance prediction of a Darrieus VAWT in an urban environment or wind farm.

Variations to the double-multiple streamtube (DMS) model for Darrieus straight-bladed VAWTs (SB-VAWTs) are developed in order to improve predictions of aerodynamic performance and flow expansion. The general background and the theoretical framework of the SB-VAWTs modeling are included. The field test measurements of a Darrieus SB-VAWT 12 kW (6 m diameter) and the two-dimensional computer simulations performed on the computational fluid dynamics (CFD) software ANSYS Fluent 13.0 are used as the reference case. The formulation and verification of a streamline mathematical representation to model the time-average flow expansion of SB-VAWTs are presented.

A new approach of the momentum-based DMS model with flow expansion is presented. Aerodynamic performance and flow expansion are calculated in MATLAB based on empirical aerodynamic coefficients and CFD simulation results. A novel energy-based DMS model is proposed. The momentum-based and energy-based DMS models show convergence issues for high tip-speed ratios. Predictions of flow expansion are not in good agreement with CFD simulation results. The error of the momentum-based and energy-based models are quantified and interpreted when the flow expansion from the CFD simulations is imposed.

Using the streamwise forces and flow expansion data from the CFD simulations, an alternative expression for the linear momentum balance based on a multiple streamtube model is presented. This relationship shows convergence and a good estimation of the flow expansion for all the studied tip-speed ratios. An improvement of the aerodynamic forces prediction based on empirical aerodynamic coefficients that considers dynamic effects is recommended for future work.

A mi familia
y a todas las personas que tratan de ver más allá de su nariz.

ACKNOWLEDGEMENTS

Agradezco a mi familia por todo el apoyo y cariño que me ha dado. A mis padres Marisa y Roberto por haber estado siempre a mi lado, traspasándome sus valores, preocupándose por mi educación y por supuesto, entregándome mucho cariño. A mis hermanos Michael y Erwin por ser mis amigos incondicionales y por todos los buenos momentos que hemos compartido. A mi Oma Alicia, Oma Trudi, Opa Billy, Opa Jorge, primos y tíos por su cariño y por hacer que me sienta orgulloso de pertenecer a esta familia. A mi tía Marta, Tante Renate y a la señora Betty por su cariño y preocupación. Vielen Dank an alle!

Quiero agradecer al profesor Williams Calderón por aceptar ser mi profesor guía y por las enseñanzas y motivación que me ha dado desde que lo conozco, y en especial durante el desarrollo de esta tesis. Al profesor Richard LeBoeuf por su interés en este trabajo y por la paciencia para corregir mi redacción en inglés. A los profesores Álvaro Valencia y Alejandro Ortíz por aceptar ser parte de mi comisión y por los valiosos conocimientos que me entregaron en sus cursos. Al profesor Mihir Sen por su ayuda en el desarrollo de este trabajo. A Celso Rangel por la buena disposición y facilitación de los archivos de su tesis de magíster, estudio que inspiró el presente trabajo. También quiero agradecer a todos los profesores, funcionarios y estudiantes de mi querido Departamento de Ingeniería Mecánica, que por espacio no alcanzo a nombrar aquí (4to y 5to piso del DIMEC y el taller Molina), y también a los profesores y funcionarios de Beauchef, con los que tuve la suerte de compartir mi estadía en la Universidad de Chile. A Cami, Gustavo, Juan Ignacio y Gretta. A mis compañeros de la oficina 402. Quiero agradecer a mis amigos de la Deutsche Schule Santiago y en especial al “banquito”, grupo en el que he encontrado grandes amigos de la vida. A los excelentes profesores que tuve el gusto de conocer en la DSS. A mis amigos mechones de la sección 3 por los años que compartimos en Beauchef. También a mis amigos mecánicos que me acompañaron durante tantos años en clases, proyectos y “actividades recreativas varias”, que espero sigamos teniendo en el futuro.

I want to thank the professors Hermann Fasel and Andreas Gross and their research group at the University of Arizona for receiving me so cordially at the their laboratory and for giving me such valuable experience and knowledge. A Nadia Álvarez, a los chilenos de Tucson, a Rodrigo, Alfonso, Ricardo y a toda la gente que conocí en la “U of A” por hacer que fuera una experiencia inolvidable. A CONICYT del Gobierno de Chile por la beca de magíster nacional y por la beca de estadías cortas de investigación para ingenieros.

Finalmente, quiero agradecer a todas las personas que he conocido a lo largo de mi vida y que han contribuido a forjar quien soy y que de una u otra forma han ayudado a que finalice esta etapa de mi vida. Especiales agradecimientos a la gente que conocí en las prácticas profesionales en Neumann, SNC-Lavalin y MPX por su simpatía, buena disposición y por introducirme al ejercicio profesional de la linda y desafiante carrera que es la ingeniería civil mecánica.

TABLE OF CONTENTS

1. INTRODUCTION.....	1
1.1. Motivation.....	1
1.2. Objectives	4
1.2.1. General objective	4
1.2.2. Specific objectives.....	4
2. GENERAL BACKGROUND	5
2.1. Energy	5
2.2. Renewable energies.....	6
2.2.1. Types of renewable energies	7
2.2.2. Worldwide available renewable energy resources.....	9
2.2.3. Levelized cost of energy	11
2.2.4. Current applications, small scale and future tendencies.....	11
2.3. Renewable energies in Chile	16
2.3.1. Electricity systems.....	16
2.3.2. Legislation	17
2.3.3. Renewable energy generation	19
2.4. Wind turbines	19
2.4.1. History	20
2.4.2. Basic theory.....	27
2.4.3. Comparison of technologies.....	29
2.5. The wind	36
2.5.1. General circulation.....	36
2.5.2. Steady wind boundary layer	38
2.5.3. Wind turbulence.....	39
2.5.4. Wind statistical distributions	39
2.5.5. Wind resource in Chile	41

2.6. Airfoil theory.....	41
2.6.1. Geometry.....	42
2.6.2. Kinematics.....	46
2.6.3. Aerodynamics	47
2.6.4. Unsteady aerodynamics.....	52
3. MODELING OF DARRIEUS SB-VAWTs.....	54
3.1. Coordinate system and geometry	54
3.2. Kinematics	59
3.3. Dynamics	69
3.4. One-dimensional momentum theory for an ideal wind turbine.....	74
3.5. Blade element momentum models	83
3.6. Single streamtube model.....	85
3.7. Multiple streamtube model	86
3.8. Double-multiple streamtube model	88
3.8.1. Basic model.....	88
3.8.2. Streamtube expansion.....	91
3.8.3. Dynamic stall.....	94
3.8.4. Modified Boing-Vertol dynamic stall model.....	95
3.8.5. Modified MIT dynamic stall model	97
3.8.6. Tower effects	101
3.8.7. Turbine struts losses.....	103
3.8.8. Blade tip losses.....	105
3.9. Vortex models.....	108
3.9.1. General considerations	108
3.9.2. Free-wake vortex model	108
3.10. Computational fluid dynamics	112
3.11. Dynamic effects.....	113
3.12. Control and optimization	114
3.12.1. Control	114
3.12.2. Performance improvement	116

3.12.3. Urban environment and wind farms	117
4. REFERENCE CASE.....	119
4.1. Uppsala University 12 kW SB-VAWT	119
4.1.1. General description	119
4.1.2. Turbine specifications	119
4.1.3. Experimental results.....	121
4.2. Two-dimensional CFD simulations	122
4.2.1. General description	122
4.2.2. Blade moment coefficient.....	125
4.2.3. Power coefficients.....	126
4.2.4. Force coefficients	128
4.2.5. Flow expansion around the turbine	131
4.3. Mathematical representation of the flow expansion	141
4.3.1. Time-averaged streamlines	141
4.3.2. Non-uniform spanwise streamtube expansion	144
4.3.3. Flow expansion and momentum theory	147
4.4. Three-dimensional corrections of the CFD simulations	152
5. VARIATIONS OF THE DMS MODEL	156
5.1. Modified DMS model – no flow expansion.....	156
5.1.1. Implementation	157
5.1.2. Dynamic stall model	159
5.1.3. Verification of the model.....	164
5.1.4. Comparison with the two-dimensional reference case.....	167
5.2. Modified DMS model – with flow expansion	173
5.2.1. Implementation	173
5.2.2. Results with empirical aerodynamic coefficients.....	178
5.2.3. Results with aerodynamic coefficients from CFD simulations.....	182
5.3. Discussion	185

6. ENERGY-BASED DMS MODEL.....	187
6.1. Formulation.....	187
6.2. Results with aerodynamic coefficients from CFD simulations	190
6.3. Discussion	192
7. FLOW EXPANSION CORRECTIONS.....	193
7.1. Corrections of the DMS models.....	193
7.2. Corrections based on regressions.....	196
7.3. Discussion	202
8. CONCLUSIONS AND FUTURE WORK.....	203
8.1. Conclusions.....	203
8.2. Future work.....	204
NOMENCLATURE	206
REFERENCES	212
APPENDIX A. AERODYNAMIC COEFFICIENTS.....	220
A1. Subsonic lift coefficients of the airfoil NACA 0012.....	220
A2. Subsonic drag coefficients of the airfoil NACA 0012	222
A3. Subsonic lift coefficients of the airfoil NACA 0015.....	224
A4. Subsonic drag coefficients of the airfoil NACA 0015	226
A5. Subsonic lift coefficients of the airfoil NACA 0018.....	228
A6. Subsonic drag coefficients of the airfoil NACA 0018	230
A7. Subsonic lift coefficients of the airfoil NACA 0021	232
A8. Subsonic drag coefficients of the airfoil NACA 0021	234
A9. Subsonic lift coefficients of the airfoil NACA 0025.....	236
A10. Subsonic drag coefficients of the airfoil NACA 0025	238
A11. Lift and drag coefficients of the airfoil NACA 0021	240
A12. Comparison of four NACA 00XX airfoils lift coefficients	241

APPENDIX B. THREE-DIMENSIONAL CORRECTIONS.....	242
B1. Function that imports aerodynamic coefficients.....	242
B2. Flow expansion data from the 2-D CFD simulations.....	242
B3. Function that interpolates the aerodynamic coefficients.....	243
B4. Three-dimensional correction (TDC) code.....	245

LIST OF FIGURES

2. GENERAL BACKGROUND

Figure 2.1. Global exergy of renewable energy sources.	10
Figure 2.2. Global cumulative installed wind and photovoltaic capacity.	13
Figure 2.3. ERNC cumulative installed capacity in Chile.	20
Figure 2.4. Classification of wind turbines.	22
Figure 2.5. Examples of wind turbines.....	25
Figure 2.6. Classification of VAWTs.....	25
Figure 2.7. Power coefficient curves vs. tip-speed ratio for some wind turbines.	30
Figure 2.8. Typical power performance curve of a Darrieus turbine.	32
Figure 2.9. Performance curve of Darrieus VAWTs for different solidities.....	33
Figure 2.10. General atmospheric circulation.....	37
Figure 2.11. Geostrophic and gradient winds.....	37
Figure 2.12. Typical vertical mean speed profile.....	38
Figure 2.13. Example of wind speed histogram in one year.	40
Figure 2.14. Wind resource in South America.....	42
Figure 2.15. Wing geometric definitions.	43
Figure 2.16. Airfoil nomenclature.	44
Figure 2.17. Geometry of four symmetric NACA 00XX airfoils.....	45
Figure 2.18. NACA 2412 airfoil geometry.	46
Figure 2.19. Rotation angles of a wing.	47
Figure 2.20. Aerodynamic forces acting on an airfoil.	48
Figure 2.21. Lift and drag definition.	48
Figure 2.22. Pressure coefficient distribution for a NACA 0012 airfoil.....	50
Figure 2.23. Lift dependency on the angle of attack for a non-symmetric airfoil.	51
Figure 2.24. Dynamic stall stages.....	53

3. MODELING OF DARRIEUS SB-VAWTs

Figure 3.1. General configuration of a SB-VAWT.....	55
Figure 3.2. Two-dimensional coordinate system definition for a SB-VAWT.	55
Figure 3.3. Partition of the flow field around the turbine.	56
Figure 3.4. Main geometrical parameters of a SB-VAWT.....	58
Figure 3.5. Geometrical parameters of a symmetrical blade.....	58
Figure 3.6. Three-bladed VAWT of two tiers.	59
Figure 3.7. Velocity vectors definitions for a SB-VAWT.....	60
Figure 3.8. Angle of attack definitions for a SB-VAWT.....	62
Figure 3.9. Alternative definition of the turbine kinematic parameters.....	63
Figure 3.10. Angle of attack calculation comparison for low tip-speed ratios.	64
Figure 3.11. Relative wind velocity vs. azimuthal angle.	65
Figure 3.12. Angle of attack vs. azimuthal angle.	65
Figure 3.13. Curvilinear flow effects on a rotating blade.....	66
Figure 3.14. Curvilinear flow influence on the angle of attack.....	68
Figure 3.15. Reynolds number vs. azimuthal angle.....	69
Figure 3.16. Definition of the turbine dynamic parameters.	70
Figure 3.17. Triangles of velocity and forces for different blade positions.	72
Figure 3.18. Blade tangential force coefficient vs. azimuthal angle.	73
Figure 3.19. Blade radial force coefficient vs. azimuthal angle.	73
Figure 3.20. Geometric relations of polar and Cartesian coordinates.....	74
Figure 3.21. Control volume for the one-dimensional momentum model.	75
Figure 3.22. Velocity and pressure variation along the flow direction.	78
Figure 3.23. Control volume for the turbine.....	79
Figure 3.24. Power and axial force coefficients vs. interference factor.....	81
Figure 3.25. Turbine flow states for various interference factors.	82
Figure 3.26. Turbulent-wake state of the turbine.	83
Figure 3.27. Flow around the turbine for the single streamtube model.	85
Figure 3.28. Flow around the turbine for the multiple streamtube model.....	87
Figure 3.29. Flow around the turbine for the double-multiple streamtube model.	89
Figure 3.30. Flow around the turbine for the double-multiple streamtube model.	90
Figure 3.31. Flow expansion of the DMS model.....	91

Figure 3.32. DMS model upstream expansion of a Darrieus CB-VAWT.....	94
Figure 3.33. Dye visualizations of some flow structures of a Darrieus SB-VAWT.	97
Figure 3.34. Diagram of the MIT dynamic stall model.	98
Figure 3.35. Tower wake-velocity deficit.....	102
Figure 3.36. Triangle of velocities for a strut segment.....	104
Figure 3.37. Upstream loss factor vs. blade height.....	106
Figure 3.38. Specific power vs. blade aspect ratio.	107
Figure 3.39. Vortex system for a single blade element.	109
Figure 3.40. Velocity induced by a vortex.	110
Figure 3.41. Typical power curves of a Darrieus VAWT with passive stall.....	116
Figure 3.42. Wind farm arrangement of counter-rotating Darrieus SB-VAWTs.	118
Figure 3.43. Incoming velocity profiles in urban environment or wind farms.	118

4. REFERENCE CASE

Figure 4.1. Uppsala University 12 kW SB-VAWT.....	120
Figure 4.2. Turbine power coefficient vs. tip-speed ratio of the 12 kW SB-VAWT.....	122
Figure 4.3. Computational domain and boundary conditions.....	123
Figure 4.4. Blade moment coefficients vs. azimuthal angle.....	126
Figure 4.5. Experimental and CFD simulations turbine power coefficients.	127
Figure 4.6. Blade streamwise force coefficients vs. azimuthal angle.....	128
Figure 4.7. Blade cross-stream force coefficients vs. azimuthal angle.....	129
Figure 4.8. Blade tangential force coefficients vs. azimuthal angle.....	130
Figure 4.9. Blade radial force coefficients vs. azimuthal angle.....	130
Figure 4.10. Mean power coefficients vs. tip-speed ratio.	131
Figure 4.11. Turbine streamwise force coefficients vs. azimuthal angle.	132
Figure 4.12. Turbine cross-stream force coefficients vs. azimuthal angle.	132
Figure 4.13. Streamline visualization of the CFD simulations.	134
Figure 4.14. Streamwise wake velocity profiles.	135
Figure 4.15. Streamline visualization of the CFD simulations.	136
Figure 4.16. Flow expansion manual measurements from the CFD simulations.	138
Figure 4.17. Streamtube lateral expansion.....	140

Figure 4.18. Mathematical modeling of the streamlines.....	142
Figure 4.19. Side-averaged non-uniform expansion ratio vs. tip-speed ratio.	145
Figure 4.20. Streamline visualization comparison.....	148
Figure 4.21. Streamwise force coefficients vs. interference factor.....	150
Figure 4.22. Predicted and measured streamtube widths.....	151
Figure 4.23. Turbine power coefficient with three-dimensional corrections.....	153
Figure 4.24. Three-dimensional corrections breakdown.....	154

5. VARIATIONS OF THE DMS MODEL

Figure 5.1. Diagram of the MDMSM-NFE with uniform streamtube width.....	157
Figure 5.2. Angle of attack vs. azimuthal angle.	160
Figure 5.3. Dynamic stall lift coefficients vs. angle of attack.....	162
Figure 5.4. Dynamic stall lift coefficients vs. azimuthal angle.....	162
Figure 5.5. Dynamic stall drag coefficients vs. angle of attack.....	163
Figure 5.6. Dynamic stall drag coefficients vs. azimuthal angle.	163
Figure 5.7. Modified MIT dynamic stall model modes vs. azimuthal angle.....	164
Figure 5.8. Reduced frequency vs. azimuthal angle.	164
Figure 5.9. Tangential force coefficient verification.....	165
Figure 5.10. Power coefficient verification.....	166
Figure 5.11. Turbine power coefficient comparison.....	168
Figure 5.12. Tangential force coefficient comparison.....	169
Figure 5.13. Instantaneous flow visualizations for blade under dynamic stall.	170
Figure 5.14. Instantaneous flow visualization of the rotating domain.....	171
Figure 5.15. Interference factor vs. azimuthal angle.	172
Figure 5.16. MDMSM-NFE flow expansion comparison.	173
Figure 5.17. Streamtube expansion.....	174
Figure 5.18. Triangle of velocities with streamtube expansion.....	175
Figure 5.19. Upstream and downstream intersection possibilities.....	177
Figure 5.20. Tangential force coefficient comparison.....	179
Figure 5.21. Power coefficient comparison.	180
Figure 5.22. MDMSM-WFE with empiric coefficients flow expansion comparison.....	180

Figure 5.23. Momentum balance convergence curves.	181
Figure 5.24. Tangential force coefficient comparison.	183
Figure 5.25. MDMSM-WFE with CFD coefficients flow expansion comparison.	184
Figure 5.26. Streamwise force coefficient comparison.	185
Figure 5.27. Upstream momentum balance convergence curves.	186
6. ENERGY-BASED DMS MODEL	
Figure 6.1. Diagram of energy-based DMS model.	188
Figure 6.2. Energy-based DMS model flow expansion comparison.	191
Figure 6.3. Energy balance convergence curves.	191
7. FLOW EXPANSION CORRECTIONS	
Figure 7.1. Momentum flow expansion corrections with CFD coefficients.	194
Figure 7.2. Energy flow expansion corrections with CFD coefficients.	195
Figure 7.3. Momentum flow expansion corrections with CFD coefficients.	196
Figure 7.4. Energy flow expansion corrections with CFD coefficients.	197
Figure 7.5. Streamwise force coefficient vs. interference factor.	198
Figure 7.6. DMSM-FEC flow expansion comparison.	200
Figure 7.7. Streamwise force coefficient vs. interference factor of the MSM-FEC.	201
Figure 7.8. MSM-FEC flow expansion comparison.	201

LIST OF TABLES

2. GENERAL BACKGROUND

Table 2.1. Global exergy of renewable energy sources.....	11
Table 2.2. Capital cost of some energy technologies.	12
Table 2.3. Levelized cost of energy of some energy technologies.....	12
Table 2.4. Consumption of primary energy sources in Chile.	17
Table 2.5. Electricity systems of Chile.	18
Table 2.6. Present state of ERNC projects in Chile.	20
Table 2.7. List of some of the largest HAWTs.....	27
Table 2.8. Airfoil thickness coefficients.....	45

3. MODELING OF DARRIEUS SB-VAWTs

Table 3.1. Geometric parameters of SB-VAWTs.....	57
--	----

4. REFERENCE CASE

Table 4.1. Nominal properties of the wind turbine.....	120
Table 4.2. Nominal properties of the generator.....	121
Table 4.3. Mesh information.	124
Table 4.4. CFD simulation parameters.....	124
Table 4.5. Solution parameters.....	125

5. VARIATIONS OF THE DMS MODEL

Table 5.1. Streamtube number convergence sensitivity for $TSR = 5$	182
--	-----

7. FLOW EXPANSION CORRECTIONS

Table 7.1. CFD simulation parameters.....	199
---	-----

1. INTRODUCTION

1.1. Motivation

With fossil fuel prices increasing every day and climate change becoming a major concern all over the world, the use and consumption of energy sources have become unavoidable issues for governments. Particularly, costs and sustainability of the conventional electrical power systems have raised the question of whether to continue with the present systems or to find better solutions. These are some of the reasons why, in recent decades, many new electric power sources, especially renewable sources, are being investigated and developed. Other important topics, such as efficient energy transmission and storage, are also being investigated.

During many decades the tendency was to build large, but few, conventional electric power plants (typically coal or gas thermoelectric plants and hydroelectric dams) to take advantage of economies of scale. That is, larger power plants have lower costs per unit of electrical energy produced than smaller ones. Where possible, they were also built near the consumption areas to avoid long transmission lines. Over time, the electrical grids grew and also were interconnected to each other; therefore, long transmission lines were required anyway. Some renewable power plants such as wind farms, thermal solar and photovoltaic power plants can also take advantage of economies of scale. Isolated areas require their own sources of electricity. Renewable energies such as hydro power from rivers, the wind and solar energy have been harnessed in those areas. When such resources are not available, fuel powered electric generators are commonly considered feasible solutions.

Some disadvantages of long transmission lines such as large power losses and visual impact of large transmission towers have boosted a new tendency: distributed electrical power generation. This can avoid the previously mentioned and other disadvantages such as pollution concentration, but it also brings great technical and economic challenges. Renewable energies such as solar power, wind energy and low enthalpy geothermal systems can be used in urban areas in the small scale without producing large impacts in homes and neighborhoods. Thus, electrical power generation can be installed in the places where it is consumed. However, for large urban areas, it can be difficult to satisfy the entire demand with only small scale on-site electrical power generation; therefore, some transmission lines or other alternative solutions will still be necessary in those cases. The present work was developed with small-scale wind energy in mind, but many

of its results can also be applied to the utility-scale.

Human civilizations have been harnessing wind energy for thousands of years. Sailing ships and windmills were among the most important early applications. By the end of the 19th century, Charles Brush constructed a 12 kW direct current electricity-generating wind turbine [1]. The airplane propeller design experience obtained during the early-mid 20th century helped achieve relevant improvements in wind turbine design such as the determination of the maximum performance defined by the Betz-Joukowsky limit for free-stream wind turbines. During an important part of the 20th century, the low prices of oil resulted in wind turbines not being economically feasible. However, the oil shocks of 1973 and 1978 forced society to re-think future energy sources of the future. This prompted more investigation of renewable sources for power generation.

After some successes and failures, continuous development and research, today the horizontal-axis wind turbine (HAWT) or propeller type wind turbine market is fully established and growing every year [2]. On the other hand, vertical-axis wind turbines (VAWTs), have been less studied and used. The most common electricity-generating types of VAWTs, the Savonius and Darrieus turbines, were invented during the early 20th century, but more research needs to be done to understand them better and achieve their technical and economic maturity [3]. The usual classification based on the turbine axis orientation can lead to confusion. For instance, a HAWT can be used as a VAWT if the rotational axis is vertical. However, this classification commonly refers to the typical use of each type of turbine; therefore, a HAWT installed as a VAWT should still be considered as a HAWT.

In general, due to the rotational axis orientation in relation to the wind direction, VAWT aerodynamics is more complex than HAWT aerodynamics. Usually, the blades of HAWTs move in a plane perpendicular to the wind direction. On the other hand, the blades of VAWTs can be upstream or downstream from other blades, which produce more complex aerodynamics. Many studies have been carried out to achieve a better understanding of VAWTs [4]. Some advantages of these types of machines in relation to HAWTs are: the ability to capture the wind from any direction due to its vertical-axis (omni-directionality); lower costs of supporting structure, installation and maintenance because the generator can be installed at ground level; and less negative influence on the surrounding environment such as noise [5] and local temperature changes [6]. However, a relatively lower performance of the Darrieus turbine and the considerably lower efficiency of the Savonius turbine, the difficulty to harness stronger winds at high altitudes, and an inadequate starting torque in the Darrieus turbine are some of their disadvantages relative to HAWTs [3].

Currently, Darrieus straight-bladed vertical-axis wind turbines (SB-VAWTs) are among the most studied VAWTs due to the relative simplicity of their design and their higher performance in comparison with the Savonius turbine [3]. Because of the complexity of the flow structure generated inside the rotor and wake [7], several analytical models have been developed and used to predict the performance of the SB-VAWTs [3]. Among the most common type of models, due to their simplicity and relatively high accuracy, are the blade element momentum (BEM) models, one of which is the double-multiple streamtube (DMS) model [4]. Other models and methods such as vortex models or computational fluid dynamics (CFD) simulations can produce more accurate turbine power output predictions; however, they usually require more computational resources [4].

Several modifications of the DMS model have been performed to improve its accuracy. Some of them include expansion of the streamtubes to take into account the conservation of mass [8], consideration of the dynamic stall in the calculation of the aerodynamic coefficients, finite aspect ratio of the blades [9] and drag forces of the struts [10]. Despite the work carried out by various authors, there are still some weak aspects in this model. For instance, failure of the model to converge at a high tip-speed ratio (*TSR*, non-dimensional parameter defined as the turbine radius times the rotational speed divided by the local free-stream wind velocity) or for high turbine solidity (σ , non-dimensional parameter defined as the number of blades times the chord length divided by the turbine radius) is a model limitation [7].

When a turbine is being designed or when its installation site is being evaluated, it can be helpful to have a tool that allows prediction of the aerodynamic performance of the turbine in an urban environment or wind farm. Quite complex unsteady and turbulent flows can be observed under those configurations. On the other hand, due to the wind variability in time and the range of possibilities of the turbine operation and control, many cases have to be taken into account in the design process.

The DMS model can be used to make fast and relatively accurate predictions of the turbine power output and the mean flow field around the turbine. The typical unsteady and turbulent components of the turbine wake are not intrinsically included in the DMS model but can be taken into account for some conditions such as the ones presented in the present work. Once the most relevant design cases are determined, the DMS model results can be used as an input for other more accurate, more complex models.

In summary, energy costs are increasing, environmental issues are a major concern, wind energy has experienced a large growth, Darrieus VAWT technology is still immature,

there is a growing need to take advantage of untapped renewable energy sources, models for fast performance assessment of Darrieus SB-VAWTs in urban areas or wind farms are not available. Therefore, the purpose of this work is to obtain a computational tool able to improve the predictions of power output and average flow field around Darrieus SB-VAWTs at low computational cost.

1.2. Objectives

1.2.1. General objective

The general objective of this work is to implement improvements to the double-multiple streamtube (DMS) model for Darrieus straight-bladed vertical-axis wind turbines (SB-VAWTs) to obtain more accurate predictions of the aerodynamic performance and average flow field around the turbine at low computational cost.

1.2.2. Specific objectives

The specific objectives of this work are the following:

- Implement the DMS model for Darrieus SB-VAWTs according to the literature.
- Determine the reasons why the DMS model does not converge in some cases.
- Propose and implement improvements to the DMS model to obtain more accurate predictions of the aerodynamic performance and average flow field around the turbine.
- Validate the model enhancements with cases from the literature.

All specific objectives except for the last one are achieved. See Chapter 8 for more details.

2. GENERAL BACKGROUND

The aim of this chapter is to establish the context and motivations of the present work. An introduction to renewable energies, the current worldwide use of wind energy, and some economic aspects of energy sources are presented here. A description of the wind energy in the Chilean electric sector is also addressed. A brief introduction to wind turbines and a comparison between technologies are also included. Finally, to put into context Chapter 3, which covers the modeling of Darrieus SB-VAWTs, some technical aspects of the wind resource and airfoil theory are discussed.

2.1. Energy

It is not odd to hear someone saying one of the following expressions: “my car ran out of gas,” or “there was an electrical grid blackout during the storm last night,” or “I am really tired, I am feeling out of energy.” Although the people use the concept of energy daily, it is an abstract notion and sometimes hard to define accurately. The concept of energy is within all these examples. In basic physics, energy is defined as the capability of a system to do work. Work is usually defined as the dot product of one force acting on a body and the resultant displacement. The concept of energy is more general than this and is used in a wide range of applications. For instance, some of the usual types of energy are: potential energy, kinetic energy, elastic energy, thermal energy, electrical energy, chemical energy and nuclear energy. It does not matter the nature of each energy type, all types must satisfy the law of conservation of energy that states: “energy can be neither created nor destroyed – it is always conserved” [11]. It is important to note that the energy is not always used to produce electric power. Some of the most common examples are direct uses of fuels such as transport or heating. For example, the energy of the wind changes from kinetic energy, to mechanical energy in the shaft of a turbine. Some portion of the available energy is also transferred to the environment as turbulence or heat, resulting in an inefficiency. The mechanical energy available on the turbine shaft is usually transformed by a generator into electrical energy or used to pump water or to grind grain.

Depending on its origin, the energy can be classified in two types: primary source and secondary source [12].

- **Primary source.** In this case the energy comes from a natural source. It is not

always necessary to perform a transformation process to use it. The primary sources can be classified in two.

- The **non-renewable sources** are limited in time. Some examples are: crude oil, natural gas, mineral coal, and nuclear fission.
- The **renewable sources** are sustainable in time. Some examples are: hydro energy, geothermal energy, biomass, solar and wind energy.
- **Secondary sources.** In this case the energy comes from a transformation process, which can be physical, chemical or biochemical, of primary sources. Some examples are: biogas, refined components of the crude oil such as gasoline, diesel fuel, kerosene and liquefied petroleum gas (LPG).

2.2. Renewable energies

Several kinds of renewable energies have been used throughout the history. Some examples are sailing ships and windmills, which use the energy of the wind. Watermills, which are powered by the energy of the water flowing down a river, wood for a fire or other types of biomass, are also common examples. However, with the invention of the steam engines and the subsequent invention of the internal combustion engines, renewable energy based technologies were set aside because of their higher costs (mainly because at that time, renewable energy technologies were not sufficiently advanced to establish a mass production, which could have had lower costs). At the end of the 20th century, when the high prices of fossil fuels and global warming became an issue, renewable energies regained an important position in the energy sector [2].

As stated earlier in this chapter, electrical conversion of the energy is not the only application of energy sources. However, considering that in most cases of renewable sources, it is complicated to store available energy; it is transformed into electrical power to be used immediately or chemically stored in batteries. Solar thermal and geothermal energy are exceptions to this rule: because of their nature, it is easier to store the available energy as thermal energy in heat accumulators. Hydro energy can also be stored in some cases, for example, with a dam located on a river [13].

It is important to note that the renewable sources are intermittent by nature. Therefore, in general, these sources are not able to regulate the power of an electrical grid by themselves [13]. The capacity factor, CF , of a power plant is defined as the ratio of its

actual energy output, AEO , over a period of time, to its maximum potential energy output, $MPEO$, operating at full nameplate capacity in that time, as shown in Eq. (2.1). In many renewable sources such as solar and wind energy, the capacity factor is around 30%, which is considered low in contrast with a 90% capacity factor of a conventional or geothermal thermoelectric plant [14].

$$CF = \frac{AEO}{MPEO} \quad (2.1)$$

2.2.1. Types of renewable energies

A list with a brief description of the different existing sources of renewable energies is presented in this section.

- **Hydro power.** Many different technologies have been developed to harness the energy available in the water. It is usually divided in two categories:
 - **Hydraulic power.** Is the power obtained from the superficial flows of water [15]. It is considered a renewable source because of the water cycle. The energy of the water running down a river or falling from a waterfall can be used to drive a turbine to obtain mechanical power on a shaft, which is usually used to drive an electric generator. There are two types of hydraulic power plants: run-of-the-river and conventional (or dams). The run-of-the-river power plants have small or no reservoir capacity and harness the kinetic energy of the water directly. The conventional power plants use a dam to accumulate water and utilize its potential energy. The latter usually have a large capacity for water accumulation, which can provide for local irrigation during dry seasons, but it can also change the local flora and fauna if not used properly.
 - **Sea and ocean power.** This kind of hydro power includes all the different phenomena that occur on the surface and below the surface of the seas and oceans such as: wave power, tidal power, marine currents, salinity and thermal gradients [16]. Many technologies have been developed to harness energy from these sources. However, the conventional hydraulic power plants are much more developed and have lower costs. Since almost 80% of the Earth's surface is covered by water, there is a huge potential for energy harnessing. Wave power generators extract kinetic energy from

waves, for example, moving floating devices up and down. Tides, marine currents, salinity and thermal gradients produce movements from the water below the surface of the seas. This kinetic energy can be harnessed by underwater turbines or other technologies.

- **Geothermal power.** The geothermal systems can extract thermal or electric power from the thermal energy that is within the Earth [17]. The geothermal systems are classified as high-enthalpy or low-enthalpy. The high-enthalpy systems are located close to places with high volcanic activity or a geological fault. Water and steam extracted from these systems can reach very high temperatures. Geothermal power plants use the steam, which was created from injected water or directly extracted from the geothermal system, to drive a conventional steam turbine to generate electric power. On the other hand the low-enthalpy systems can be located almost everywhere because they use the thermal gradient of the Earth's crust, which is, on average, between 25 and 30°C per 1 km of depth [18]. These types of systems also take advantage of the soil's thermal inertia to moderate performance throughout the year, and are usually used for acclimatization of buildings.
- **Solar power.** The most constant energy being received by the Earth is from the Sun [19]. The average radiation outside the atmosphere is 1,361 W/m². Solar energy is the most abundant energy on the planet: the surface of the planet, in one hour, receives the equivalent of all the energy consumed by all mankind in one year. This type of energy can be utilized for generating electrical power or for heating processes in domestic or industrial uses. It has the disadvantage that it is only available during the day. Therefore, it is useful to combine it with other energy sources or storage systems. There are two ways to generate electric power from solar energy: photovoltaic power (PV) and concentrating solar thermal power (CSP). The photovoltaic cells utilize the photoelectric effect to convert light into an electrical current. The concentrating solar thermal systems use high temperatures to vaporize water, or another equivalent working fluid, which drives a turbine as in a conventional power plant.
- **Wind power.** The movement of the air between the high and low pressure regions in the atmosphere, caused by the uneven heating of the Earth's surface by the Sun, is called wind. The air above a hot surface lowers its density, which causes it to rise, creating a low pressure zone. The air from the high pressure zones moves towards the low pressure areas. This is why the wind energy is considered an indirect type of solar energy [20]. The wind energy is harnessed by a moving

mechanism that is driven by the momentum transfer from the wind. Common examples are the sails of a ship, windmills and turbines. Wind turbines capture the kinetic energy from the wind, slowing it down, and provide mechanical power on a rotating shaft, which usually drives an electric generator.

- **Biomass.** The biomass is defined as all the organic renewable matter obtained from vegetal or animal sources [21]. It can be obtained from natural or artificial processes. That is the reason why there are many varieties of energy sources to produce biomass. These biological wastes are utilized directly as fuels, or to produce fuels. Some examples include animal droppings used to produce methane gas, and forest residues, such as bark, and other agricultural residues, such as corn or wheat residues, which are burned inside boilers to produce steam.

2.2.2. Worldwide available renewable energy resources

Due to the sparse distribution of measurement equipment installed on the Earth's surface, it is a hard task to estimate all the renewable energy resources available around the World. However, reasonable estimations can be made to try to quantify the available resources.

An estimation of the global renewable sources was made by Weston Hermann [22], in which the exergy approach was used. Exergy describes the quality of energy in addition to the quantity, providing deeper insight into work potential analyses which only utilize the first law of thermodynamics. In other words, exergy analysis provides a method to evaluate the maximum work extractable from a substance relative to a reference state [22]. A summary of the study's results are shown in Fig. 2.1. The publication states that the solar exergy available inside the Earth's atmosphere is of $86,000 TW$ ($1 TW = 10^{12} W$). This exergy is the force that produces many other renewable energy sources such as evaporation, biomass due to photosynthesis and winds. The exergy transferred to wind as kinetic energy and dissipated as friction is estimated to be $870 TW$. The friction within the surface boundary layer dissipates approximately one third of that exergy, while the remainder is dissipated through viscous friction in free stream atmospheric flow. Wind speeds in the atmosphere are heavily influenced by surface characteristics, but generally increase with altitude. Assuming a Weibull distribution with shape factor of 2 and a scale factor of 7.45, the average global wind speed 50 m above the ground is $6.60 m/s$ and has an exergy of $336 W/m^2$ perpendicular to the wind direction [22].

Figure 2.1 shows that the renewable sources such as wind and ocean energies are the

most abundant. One disadvantage of these sources is that they are distributed all around the globe, unlike the rivers for example, which have an overall much smaller potential, but higher energy density. Also, many times the populated areas are located near the rivers because of the water consumption. Therefore, no large electrical grids need to be constructed to distribute the energy. **F**

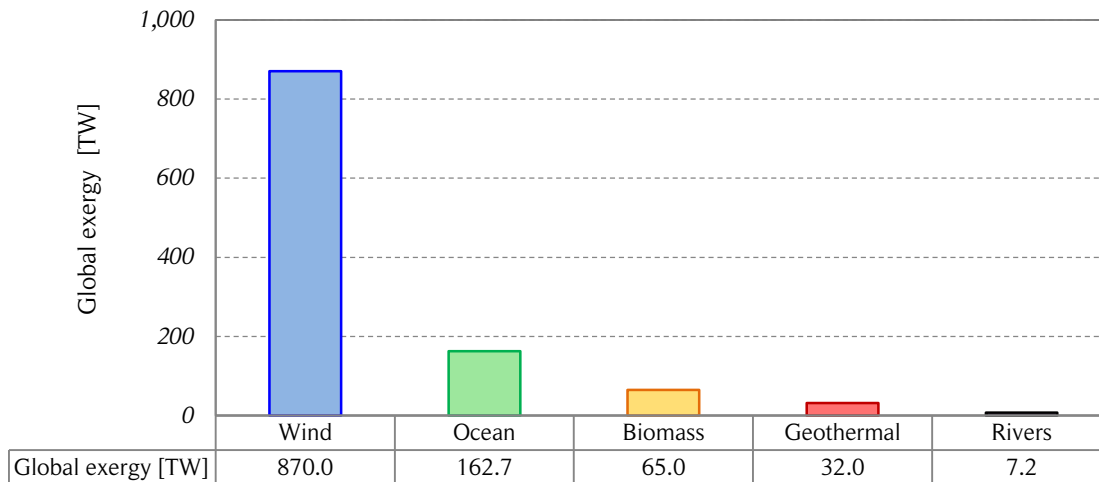


Figure 2.1. Global exergy of renewable energy sources.

The figure shows the global exergy of renewable energy sources in TW. The solar exergy of 86,000 TW is not shown for scale purposes and because some of the renewable energy sources are a consequence of the solar energy, therefore, some exergy would be considered twice. The wind exergy considers the whole atmosphere. Only the gravitational exergy of the World's major rivers is considered. The ocean exergy considers the ocean thermal gradient, the ocean surface waves and shallow ocean tides. Only land biomass is considered. Earth's atmosphere, ocean and crust are defined as the reference state. Source: own elaboration based on [22].

On the other hand, [22] also reports the estimated global occurrences of the following fossil fuels: coal, petroleum and natural gas. Their respective exergies are 270, 110 and 50 ZJ ($1 \text{ ZJ} = 10^{21} \text{ J}$). To establish a comparison of the magnitude of these finite resources with some of the renewable resources, the total exergies of the solar radiation on the Earth's surface and the wind in the atmosphere during one year were calculated. The global total primary energy consumption of 2012 according to [23] is 12,806 Mtoe (millions of tonnes of oil equivalent). If a conversion factor of $1 \text{ toe} = 41.87 \text{ GJ}$ is used, the resultant global energy consumption of the year 2012 is 0.54 ZJ. The results are presented in Table 2.1. The amount of available renewable energy during one year is much larger than the global energy consumption and also the total coal, petroleum and natural gas reserves all together.

Table 2.1. Global exergy of renewable energy sources.

Source	Available energy [ZJ]
Global energy consumption 2012	0.54
Global estimated coal reserves	270
Global estimated petroleum reserves	110
Global estimated natural gas reserves	50
Annual solar potential	2.7×10^6
Annual wind potential	2.7×10^4

The annual solar and wind potentials are calculated with the exergies in TW from [22], multiplied by 24 hours per day, 365 days per year and converted to the proper units for comparison. Source: own elaboration, based on [22, 23].

2.2.3. Levelized cost of energy

The levelized cost of energy (LCOE) is often utilized as a summary measure of the overall competitiveness of different generating technologies. It represents the cost of building and operating a generating plant over an assumed financial life and duty cycle. This cost is usually expressed in U.S. dollars (USD) per *kWh*. The key inputs to calculate the LCOE are cost of capital, fuel costs, fixed and variable operation and maintenance (O&M) costs, financing costs, and an assumed utilization rate for each plant type [24]. The importance of these factors varies among the technologies. For example, the renewable energies do not require fuels. This is the reason why LCOE is a reasonably good parameter for comparing different technologies, just as the net present value (NPV) in project finance. It is important to note that the LCOE is calculated under many assumptions, and can suffer considerable variations depending on local factors such as tax incentives, projected utilization rate of the plant and the existing resource mix [24]. The capital cost and the unsubsidized LCOE of some energy technologies according to [14] are presented in Tables 2.2 and 2.3, respectively. The LCOE presented in Table 2.3 does not include environmental factors and other externalities. Note that utility-scale wind energy is competitive with conventional technologies for both capital cost and LCOE. Small-scale wind energy has yet to decrease its capital cost to become more competitive.

2.2.4. Current applications, small scale and future tendencies

In the last two decades the market of renewable energy technologies (RETs) began to

Table 2.2. Capital cost of some energy technologies.

	Technology	Capital cost [USD/kW]	
		Minimum	Maximum
Alternative energy	Solar PV - Crystalline rooftop	3,000	3,500
	Solar PV - Crystalline utility scale	2,000	2,750
	Solar PV - Thin film utility scale	2,000	2,500
	Solar thermal - utility scale	5,600	7,300
	Fuel cell	3,800	7,000
	Biomass direct	3,000	4,000
	Geothermal	4,600	7,250
	Wind - utility scale	1,500	2,000
	Wind - small scale *	3,500	11,000
Conventional	Gas Peaking	800	1,000
	Integrated gasification combined cycle (IGCC)	3,750	5,250
	Nuclear	5,385	8,199
	Coal	3,000	8,400
	Gas Combined Cycle	1,006	1,318

*: Based on wind turbines between 0.16 and 4.7 kW. Source: [14, 25, 26].

Table 2.3. Levelized cost of energy of some energy technologies.

	Technology	Levelized cost [USD/MWh]	
		Minimum	Maximum
Alternative energy	Solar PV - Crystalline rooftop	149	204
	Solar PV - Crystalline utility scale	101	149
	Solar PV - Thin film utility scale	102	142
	Solar thermal	131	216
	Fuel cell	109	229
	Biomass direct	87	116
	Geothermal	89	142
	Wind - utility scale	48	95
	Energy efficiency	0	50
Conventional	Gas Peaking	200	231
	Integrated gasification combined cycle (IGCC)	88	116
	Nuclear	77	114
	Coal	62	141
	Gas Combined Cycle	61	89

Source: [14]

experience important growth, which has become stronger in the recent years. To illustrate this, the global cumulative installed capacity of wind energy and solar energy (only photovoltaics) for the last decade is presented in Fig. 2.2. Due to many reasons beyond the scope of this thesis, the costs of photovoltaic energy have dropped significantly and its efficiency has increased over the years [19]. This could cause the solar energy (i.e., photovoltaic and thermal) to become the most used RET. Nowadays, the installed capacity of wind energy is still larger than photovoltaic energy. However, it is important to note that the discussion should not be centered in which RET will become the most used technology. All efforts should be put into reaching a deeper understanding of the advantages and disadvantages of each RET, and how they can complement each other. If this job is done properly, a much cheaper and nature friendly electricity production could be achieved.

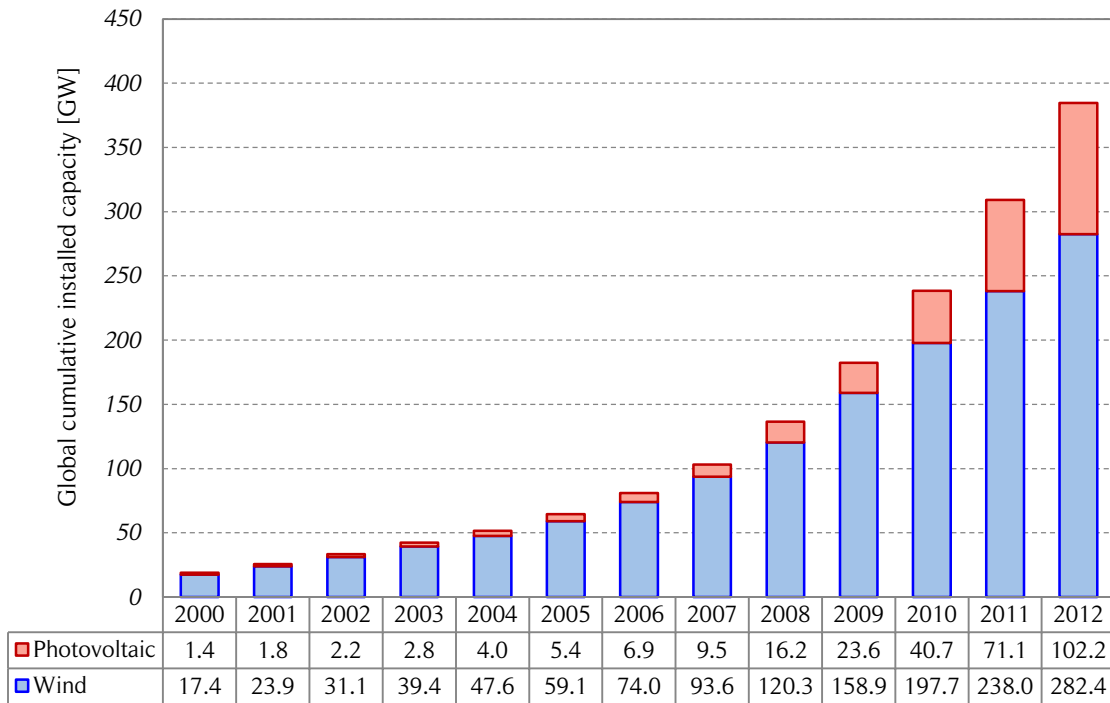


Figure 2.2. Global cumulative installed wind and photovoltaic capacity.

The figure shows the global cumulative wind and photovoltaic capacity between 2000 and 2012. Source: own elaboration based on [27, 28].

Despite the huge efforts that have been made all around the world to increase and promote the use of RETs, the present installed capacity of RETs is not enough to supply all the required energy. Many countries are setting ambitious goals to increase the use of

renewable energies. For instance, the members of the European Union (EU) through the Commission of the European Communities have set the “20-20-20” goal for the year 2020 [29]. This means reducing EU’s primary energy consumption by 20%, reducing greenhouse gas emissions by 20% and achieving 20% of renewable energy consumption by 2020. It is important to note that installed capacity is not the same as energy production. The capacity factor of many RETs is low. For example, as mentioned in Section 2.2, standard wind and solar power sources have a capacity factor of approximately 30%. On the other hand, many sources of renewable energies are of low density compared to conventional sources of energy. Therefore, a much greater installed capacity of RETs needs to be reached in order to satisfy the energy demand. If large wind or solar farms are constructed away from the consumption areas, the losses due to the long transmission lines or due to the storage mechanisms could become a major problem. In some cases, small communities are far away from the large populated areas and transmission lines could be unaffordable, therefore, a local generation of electrical energy is required.

Small-scale energy generation emerged from the previous considerations. In general, urban areas have high density population and power consumption. Although the satisfaction of the entire energy demand of urban areas is hardly achievable only with small-scale installed in-situ RETs, great amounts of energy due to the losses of long transmission lines could be spared if more distributed generation is used to complement the large conventional power plants. On the other hand, urban areas offer some advantages for small scale generation. Roofs of houses, tall buildings and street lightning, among other features, can be used to install photovoltaic panels or wind turbines. Other less obvious benefits such as wind concentration of buildings for wind turbines [30] are also available. Disadvantages such as noise, shadow flicker and glint must be taken into account to avoid a deterioration of the quality of life of nearby residents.

To improve the reliability, flexibility, and efficiency, modernized electrical grids, called smart grids, have been studied and implemented. Smart grids allow gathering information and managing in an optimal way the different components of a system such as the one in charge of the generation and storage of electricity [31]. This tool is crucial to manage the intermittency of renewable energies, especially in grids formed by numerous small scale elements.

Depending on the RET, different ranges for the small-scale can be defined. For instance, for small scale wind turbines, the diameter, the swept area or the height of the turbine could be a representative parameter of its size. However, usually the power is considered a better parameter to define the small scale category. According to Renewable UK [32],

micro wind turbines have rated power in the range 0 – 1.5 kW and small wind turbines have rated power in the range 1.5 – 50 kW. There are two common types of installation configurations for small scale wind turbines: mast mounted and roof mounted. The existing types of wind turbines and their advantages and disadvantages are discussed later in this chapter.

To illustrate the usage of non-utility scale wind energy, some statistics of micro and small-scale wind turbines are presented here. According to [33], by the end of 2010 there were 21,000 micro and small-scale wind turbines in the United Kingdom (UK). Over 90% of the small-scale turbines have rated power less than 10 kW, 6 kW being the most common size. By the same year, the total number of micro and small-scale turbines in the United States of America (USA) was 151,300 with a total installed capacity of 179 MW. According to [34], around 97% of the micro and small-scale wind turbines installed in the UK were horizontal-axis wind turbines (HAWTs) by the end of the year 2009.

Different strategies to support the use of small-scale RETs have been developed in many countries. Among the most used are the feed in tariff (FiT) and net metering.

- A **feed in tariff** (FiT) scheme provides a guaranteed premium price to the renewable electricity producer and puts an obligation on the grid operators to purchase the generated electricity output [35]. The price is typically guaranteed for a long period of time in order to encourage investment in renewable energy sources for electricity generation (RES-E). FiT schemes have been successful in European countries such as Germany, Denmark and Spain. The biggest advantage of FiT schemes is the long-term certainty of financial support. This lowers investment risks considerably, which is especially important for intermittent renewable resources such as wind energy.
- **Net metering** is an electricity policy which allows utility customers to offset some or all of their electricity use with self-produced electricity [35]. Net metering works by utilizing a meter that is able to measure and record energy flow in both directions. The meter spins forward when a customer is consuming power from the utility grid and spins backward when energy is being sent back to the grid. At the end of a given month, the customer is billed only for the net electricity used. Besides offsetting a home's energy consumption, if more energy is produced than consumed, depending on the legislative arrangements in place as well as the arrangements with the electric utility, producers can receive a payment for the positive balance. Net metering is gaining recognition as an effective RES-E promotion incentive and it is currently used in the USA and Australia. In Europe

only Denmark and Italy are using net metering. Time of use (TOU) metering employs a specialized reversible smart meter that is programmed to determine the time of electricity usage. This is especially useful for RES-E. Typically, the cost of energy is higher during the day; therefore, solar energy generation can leverage the daytime peak-price period.

2.3. Renewable energies in Chile

Currently, Chile is experiencing a remarkable process which incorporates a larger use of renewable energies in the electric sector and seeks to improve the energy consumption efficiency. The aim of this section is to establish the present situation, and also the opportunities and challenges the country is facing at the present time.

Chile is a long (4,300 *km*) and thin (180 *km*) country located on the Pacific coast of South America. According to the census of 2002 the country population was of 15.1 million and its capital, Santiago, had 5.8 million inhabitants. Due to its geography, Chile has many renewable energy resources such as hydro energy (rivers, lakes and sea), solar energy (especially in the Atacama Desert), wind energy (along the Pacific coast and in the Andes), geothermal energy (Pacific volcano belt or “ring of fire”), among others. On the other hand Chile has a lack of fossil fuels. The existing coal, natural gas and oil reserves are not enough for the present energy demand. Transport depends mainly on fossil fuels and building heating uses fossil fuels, wood or electricity. During many years, only conventional hydraulic (dams) and thermoelectric power plants were built and fuels had to be imported from other countries [36]. This situation persists, but it is slowly beginning to change because of the efforts that have been put into the development of renewable energies by the Chilean people and the authorities. The consumption of energy sources in Chile for the year 2012 are presented in Table 2.4. Note that renewable sources for the energy balance of the year 2012 were roughly one third of the total energy consumption.

2.3.1. Electricity systems

In 1982, Chile was a pioneer in the separation of the electricity generation, transmission and distribution functions. The three segments of the electricity sector are managed by private companies. The electricity generation segment is open (under certain conditions) and the prices are determined by a competitive market [38]. The European standard of 50 *Hz* nominal frequency is used. Each electricity systems is controlled by a *Centro de Despacho Económico de Carga* (CDEC, Center of Economic Load Dispatch).

Table 2.4. Consumption of primary energy sources in Chile.

	Primary energy source	Energy [Tcal]	Fraction
Fossil fuels	Crude oil	96,791	30.67%
	Coal	66,493	21.07%
	Natural gas	45,579	14.44%
Renewable sources	Wood and biomass	88,778	28.13%
	Hydroelectricity	17,336	5.49%
	Wind	351	0.11%
	Solar	185	0.06%
	Biogas	72	0.02%
	Total	315,585	100.0%

Energy balance of the year 2012. Source: [37]

Chile has four major interconnected electricity systems: *Sistema Interconectado del Norte Grande* (SING, Northern Interconnected System), *Sistema Interconectado Central* (SIC, Central Interconnected System), *Sistema Eléctrico de Aysén* (Electricity System of Aysén) and *Sistema Eléctrico de Magallanes* (Electric System of Magallanes). Some important characteristics of these four electricity systems are presented in Table 2.5. By the year 2012, the SING had 25.06% of the total installed capacity. Due to the mining activity in the North of the country, this system only supplied energy to 5.8% of the population. By the same year, the SIC had 74.11% of the total installed capacity and with an approximate expanse of 2,100 km, supplied energy to the 90% of the population, including Santiago, the capital of Chile [37].

2.3.2. Legislation

The legislation of renewable energies in Chile started in April 2008 with the publication of law 20.257 for the development of *Energías Renovables No Convencionales* (ERNC, Non-Conventional Renewable Energies). The following renewable energy resources are non-conventional renewable energies according to the ERNC law [38]:

- 1) Those whose primary source is biomass energy, being obtained from organic and biodegradable matter.

Table 2.5. Electricity systems of Chile.

System	SING	SIC	Aysén	Magallanes	Chile
Installed capacity [<i>MW</i>]	4,581	13,545	50	101	18,277
Oil derivatives	7.9%	14.8%	55.1%	14.0%	13.1%
Natural gas	46.4%	23.9%	0.0%	83.5%	30.0%
Coal	45.4%	10.9%	0.0%	0.0%	19.7%
Biomass	0.0%	2.9%	0.0%	0.0%	2.1%
Hydraulic run-of-the-river	0.3%	16.7%	41.0%	0.0%	12.4%
Hydraulic dam	0.0%	29.3%	0.0%	0.0%	21.4%
Wind	0.0%	1.5%	3.9%	2.5%	1.1%

Data updated to October 2012. SING stands for Sistema Interconectado del Norte Grande and SIC for Sistema Interconectado Central. Note that until 2012 solar power in Chile was used only in small-scale off-grid projects. Source: [39]

- 2) Those whose primary source is hydraulic energy and whose maximum installed capacity is 20 *MW*. A fraction of the installed capacity of the hydraulic power plants between 20 and 40 *MW* is considered an ERNC source with a coefficient varying linearly from 100% to 0%, respectively.
- 3) Those whose primary source is geothermal energy.
- 4) Those whose primary source is solar energy.
- 5) Those whose primary source is wind energy.
- 6) Those whose primary source is the energy of the sea (tides, waves and currents).
- 7) Other generators justified by the Comisión Nacional de Energía (CNE, National Energy Commission) under some criteria.

An extract from law 20.257 states [38]: “Each electricity company that withdraws electricity from electricity systems with an installed capacity greater than 200 *MW*, to trade it with distributors or final users, whether they are subject to price regulation or not, shall accredit before the Charge Division of the respective CDEC that an amount of energy equivalent to 10% of its withdrawals during each calendar year has been injected into any of those systems, by renewable, non-conventional means, owned or contracted, or through agreements for the transfer of the surplus.” As a transitory provision, all contracts signed after August 31st 2007 shall fulfill the following terms: between years

2010 and 2014 the obligation is 5%, between year 2015 and 2024 there is a progressive increase of 0.5% each year, reaching a 10% obligation at the end of that period.

In September 2013, the Chilean Senate passed law 20.698, known as the “law 20/25”, which establishes that by the year 2025, the energy obligation of the non-conventional renewable energy sources has to be 20% [40]. This law modifies the transitory provision of the law 20.257 for the contracts that were signed after July 1st 2013. These contracts shall fulfill an obligation 5% of ERNC by the year 2013 with increments of 1% per year from 2014 until 12% is reached in 2020. In 2021 the increments increase to 1.5% per year until 18% is accomplished in 2024. The 20% total has to be reached in 2025.

In March 2012, the Chilean Senate passed law 20.571, known as the “net metering law”, which establishes that the final users subject to pricing will be allowed to inject energy generated by ERNC sources to the distribution grid. The energy injections will have the same price as the purchased energy and each month will be discounted from the final user bill and if there is a surplus, it shall be saved for the bill of the following month. The maximum installed capacity of each final user cannot be greater than 100 kW. A regulation must establish the requirements for the connection and injection of energy of the final users [41]. Law 20.571 will not be applied until the required regulation is finished. This law should eventually increase the development of small scale generation in Chile.

2.3.3. Renewable energy generation

Non-conventional renewable energy power plants such as mini-hydro and biomass were installed in Chile long before law 20.257. However, that law resulted in a larger use of the RETs and also promoted the development of new RES-E in the country (see Fig. 2.3). The installed capacity of Fig. 2.3 considers only utility-scale projects. A quantification of small-scale generation in Chile published by official sources was not found. The present state of utility-scale ERNC projects in Chile is presented in Table 2.6. Note that wind energy has a huge potential for growth as evidenced by the approved *Resolución de Calificación Ambiental* (RCA, environmental qualification resolution).

2.4. Wind turbines

The aim of this section is to provide a brief introduction to wind turbines and to present a comparison between different technologies with their opportunities and challenges.

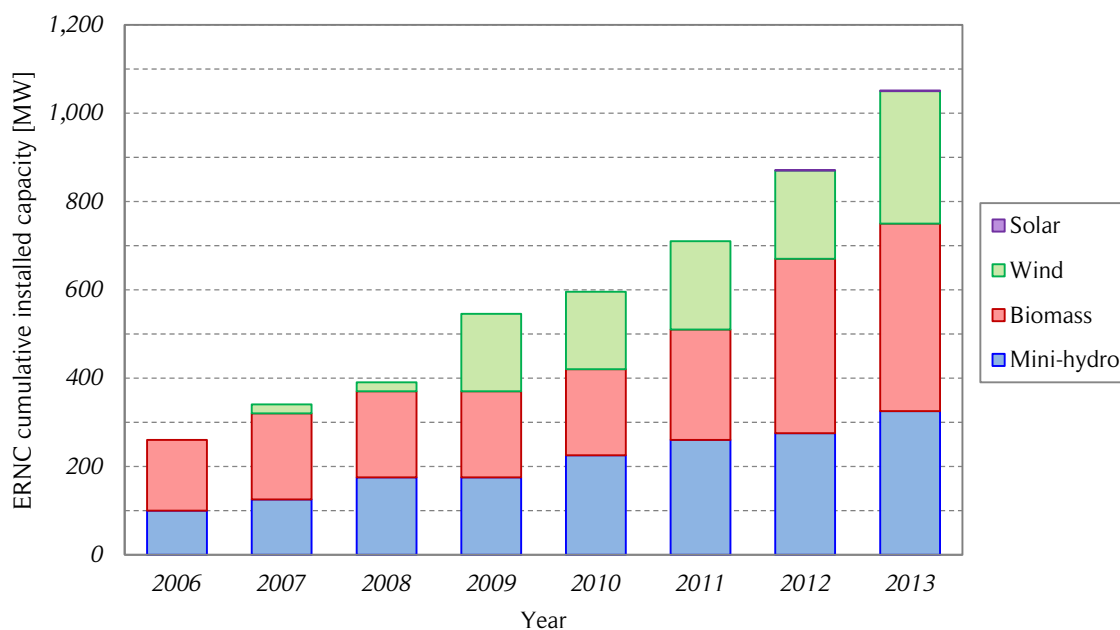


Figure 2.3. ERNC cumulative installed capacity in Chile.

The figure shows the ERNC cumulative installed capacity in Chile. Only utility scale projects are considered. Source: [42, 43].

Table 2.6. Present state of ERNC projects in Chile.

Source	Operation [MW]	Construction [MW]	Approved RCA [MW]	Qualifying [MW]
Biomass	444	32	84	87
Wind	335	457	4,340	1,761
Mini-hydro	332	68	283	213
Solar	7	128	5,337	4,781
Geothermal	0	0	120	0
Total country	1,118	685	10,164	6,842

Data updated to December 2013. ERNC stands for *Energías Renovables No Convencionales (Non-Conventional Renewable Energies)* and RCA for *Resolución de Calificación Ambiental (Environmental Qualification Resolution)*. Source: [43]

2.4.1. History

Windmills have been used for at least 3,000 years, mainly for grinding grain or pumping water. On the other hand, wind was an essential source of power for sailing ships for

even longer. In the 19th century the ship's sails were gradually changed to steam boilers and then to internal combustion engines. Currently, sailing ships are considered merely recreational. During the Middle Ages and for several years thereafter, mills were an integral part of the rural economy. At that time, the only available sources of power were animal traction, hydraulic power of rivers and the wind. In places where there were no available rivers for watermills, windmills were an attractive alternative and thus, spread across many countries around the world. Windmills were used for many years until simpler and cheaper alternatives such as steam engines, internal combustion engines, and electric motors (thanks to rural electrification) became available [1]. Today, most of the windmills are museum pieces or no longer exist. In some rural places, water pumps are still powered by windmills.

Electricity generation from wind started at the end of the 19th century with a 12 kW direct current electricity-generating turbine [1]. From then on, some private and governmental initiatives worked on making larger and better turbines for electricity generation. Several wind turbine developments were achieved during the 20th century thanks to the development of aerodynamics for airplanes. The efforts were mainly centered in lift driven horizontal-axis wind turbines (HAWTs) or propeller type wind turbines of two or three blades. In North America, the interest in wind turbines did not cease during the Second World War. With the reconstruction of Europe after the Second World War and the realization that the coal reserves were constantly decreasing, the development of wind turbines rose again in the 1950's in England, Denmark, Germany and France. However, due to the low prices of oil, wind energy for power generation could not reach an important position in the energy market until the oil price shocks happened in the 1970's [2]. The higher oil prices and the growing concern for the environmental impact of carbon emissions and pollutants were the impetus for the commercial development of wind turbines. As a result, all the work that had been done in North America and Europe during the previous decades could be used for commercial purposes [1].

Modern wind turbines are usually classified under two criteria: the rotation axis orientation; and the main driving force. This classification is presented in Fig. 2.4. The rotation axis of horizontal-axis wind turbines (HAWTs) is contained in a horizontal plane (parallel to the ground); therefore, there are two main rotations in a HAWT: the rotation of the blades; and the rotation of the entire turbine, commonly known as yaw, which allows the turbine to be aligned with the wind direction. The rotation axis of vertical-axis wind turbines (VAWTs) is aligned with the vertical direction, thus, perpendicular to the ground. Therefore, VAWTs do not need to be aligned with the wind direction; in other words, they are omni-directional. The main driving force for wind turbines can be lift or

drag. It is important to note that this classification refers to the main driving force and not the only acting force, because, in general, both forces are acting simultaneously on the turbine blades.

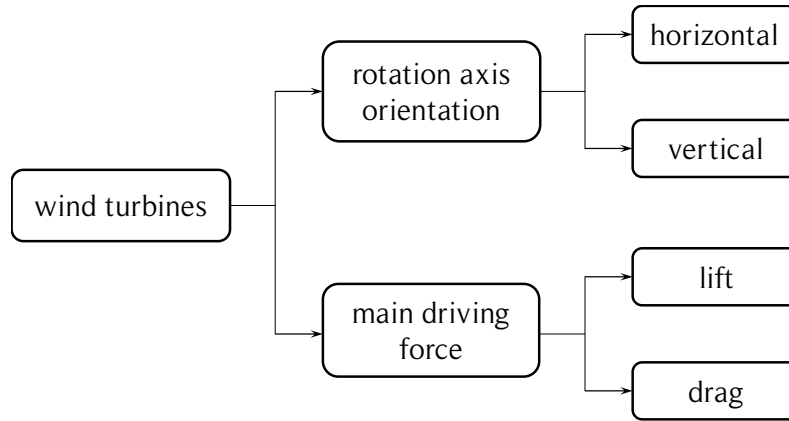


Figure 2.4. Classification of wind turbines.

The figure shows the two common classifications of wind turbines: rotation axis orientation and main driving force. Source: own elaboration.

The first VAWTs can be traced down to 1700 BC in Mesopotamia. These VAWTs were used as windmills. Today there still exist some ruins of those mills in Iran and Afghanistan (old Persia). The first designs were made of four or more vertical squared sails joint to a vertical axis. The symmetry of the design did not allow the windmill to rotate when wind was blowing; therefore, a structure was built to block the wind on one side. This feature solved the problem and allowed the rotation of the windmill, but this resulted in a windmill that would only operate when the wind was blowing from the proper direction; see Fig. 2.5 (a). Later in China, a different design of windmills with sails harnessed the wind energy from any direction [2]. The simplicity of these designs spread through the world and these types of windmills were used for many centuries. It was later discovered that lift-driven horizontal wind-mills, such as the Dutch mills, were more efficient because they can work at higher rotational speeds. This caused a decrease of the use of VAWTs.

During the 20th century interest in VAWTs reappeared. In 1927 the Finnish engineer Sigurd Savonius presented a drag driven turbine (known as Savonius rotor) and in 1931 the French aeronautical engineer Georges Darrieus patented a lift driven turbine (known as Darrieus rotor) [2]. Some examples of these and other wind turbines are presented in Fig. 2.5. A complete description of Darrieus VAWTs is available in [89]. In the late



Picture: Ghader Agheli.

(a) VAWT (drag): Nashtifan windmills (Iran), Safavid dynasty (1501 – 1736), number of blades: 6, blade height: 15 m, rotor diameter: 7 m.



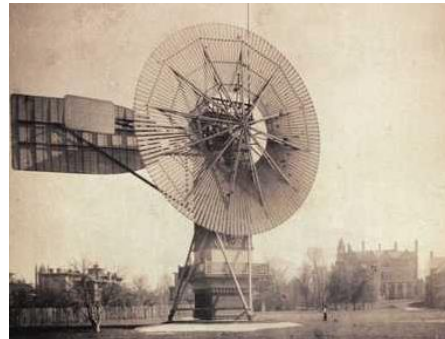
Picture: Jan de Goede.

(b) HAWT (lift): Ground sailer polder mill, Amsterdam – Sloterveer (Netherlands), year 1674, turbine diameter: 25.9 m.



Picture: Ironman Windmills Co.

(c) HAWT (lift): Water pumping windmill – Ironman Windmill Co. (USA), rotor diameter: 2.4 m, vane for wind tracking.



Picture: Western Reserve Historical Society.

(d) HAWT (lift): Built by Charles F. Brush (USA), year 1888, rotor diameter: 17 m, hub height: 18.3 m, rated power 12 kW DC.



Picture: Christian Wagner.

(e) HAWT (lift): Alstom ECO 80 (France), rotor diameter: 80.0 m, rated power: 1.67 MW, upwind rotor yaw and blade pitch control.



Picture: Gillaume Paumier.

(f) VAWT (lift): Lavalin Éole Research Turbine (Canada), rotor diameter: 64 m, rotor height: 96 m, rated power: 3.8 MW at 15 m/s.



Picture: Southwest Windpower.

(g) HAWT (lift): Skystream 3.7 – Xzeres (Southwest Windpower) (USA), rotor diameter: 3.66 m, downwind rotor with stall control, rated power: 2.4 kW at 13 m/s.



Picture: Windspire.

(h) VAWT (lift): Windspire v1.2 – Windspire (USA), rotor diameter: 1.2 m, rotor height: 6.1 m, rated power: 1.2 kW, output: 120 VAC.



Picture: Pcon Windkraft.

(i) VAWT (drag): S30-190-15 – Pcon Windkraft (Germany), rotor diameter: 1.9 m, rotor height: 1.5 m, rated power: 352 W (at 12 m/s).



Picture: Helix Wind.

(j) VAWT (drag): S322 – Helix Wind (USA), rotor diameter: 1.21 m, rotor height: 2.65 m, rated power: 2.0 kW, output: 110/240 VAC, 50/60 Hz.



Picture: HIS&E Co., Ltd.

(k) VAWT (lift and drag): KSV-300W HIS&E (China), rotor diameter: 1.24 m, rotor height: 1.46 m, rated power: 300 W, output: 12 VDC.



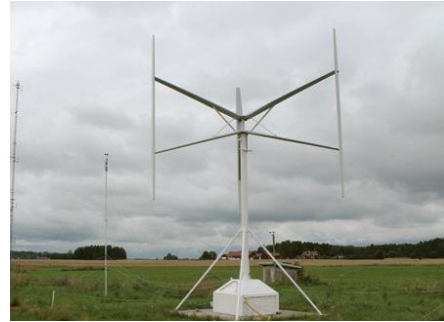
Picture: Urban Green Energy.

(l) VAWT (lift): eddyGT – UGE Inc. (USA), rotor diameter: 1.8 m, rotor height: 2.7 m, rated power: 1.0 kW (at 12 m/s), off-grid/grid-tie compatible.



Picture: Hannes Grobe.

(m) VAWT (lift): HMW Generator – Heidelberg Motors (Germany), rotor diameter: 10.0 m, rotor height: 5.6 m, rated power: 20.0 kW (at 14 m/s).



Picture: Uppsala University.

(n) VAWT (lift): Uppsala University SB-VAWT (Sweden), rotor diameter: 6.0 m, rotor height: 5.0 m, rated power: 12.0 kW (at 12 m/s).

Figure 2.5. Examples of wind turbines.

The figure shows some examples of wind turbine designs used in the past and present. A brief description is included in each case.

1960's, Peter South and Raj Rangi, from the National Research Council (NRC) of Canada, reintroduced the Darrieus concept. In the following decades, the utility-scale curved-blades Darrieus turbines were investigated by some research centers such as the Sandia National Laboratories of the USA. A classification of VAWTs is presented in Fig. 2.6. Many analytical and semi-analytical aerodynamic models have been formulated to predict the loads and performance of Darrieus turbines [4].

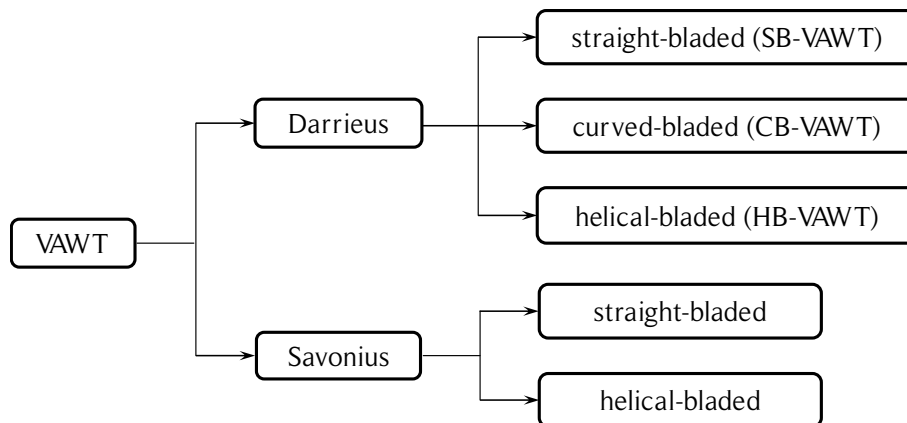


Figure 2.6. Classification of VAWTs.

The figure shows a typical classification for VAWTs. Source: own elaboration.

Some examples of the classification of VAWTs presented in Fig. 2.6 are showed in Fig. 2.5: *(h)*, *(m)* and *(n)* are Darrieus straight-bladed VAWTs (SB-VAWTs) also known as “H-rotor” because of their shape; *(f)* is a Darrieus curved-bladed VAWT (CB-VAWT) also known as “egg-beater” because of the shape of the blades in a parabolic or Troposkien shape; *(l)* is a Darrieus helical-bladed VAWT (HB-VAWT) also known as Gorlov rotor; *(i)* is a straight-bladed Savonius; *(j)* is a helical-bladed Savonius; *(k)* is a straight-bladed Savonius / Darrieus CB-VAWT. It must be noted that some VAWTs such as the Madaras rotor (Magnus effect) are not included in this classification. In some cases HAWTs are installed with a vertical axis, and on the other hand, sometimes VAWTs are installed with a horizontal axis; therefore, a clear specification of the installation of a turbine is required to avoid misunderstandings.

For different reasons that are not completely clear and are outside the scope of this work (some disadvantages of the Darrieus turbines are discussed later on in this chapter), utility scale Darrieus CB-VAWTs did not reach enough maturity to gain a relevant place in the wind turbine market. The only significant commercial exploitation of VAWT technology was by FloWind Inc., which had 500 installed turbines in California with a total rated capacity of 100 MW. Their designs were apparently not competitive with HAWT technology and FloWind went bankrupt in 1997 [55]. During the late 1990s and the following years a new interest appeared for small scale VAWTs. This is especially due to the urban friendly characteristics of VAWTs that are discussed later in this chapter.

HAWTs have been used for many years along mankind’s history. Some of the most common old designs of HAWTs are the Dutch mills and the North American windmills for pumping water, which are shown in Tab. 2.8. The modern HAWTs were highly benefited from the propeller design theory developed through the 20th century. In North America and Europe, during the 1950s, there already existed turbine prototypes in the power range between 100 and 1,250 kW [2]. During the 1970s, there was a re-emergence of wind energy, but this re-emergence started with a tremendous crash. In the USA, Germany, Sweden and some other countries, the government supported the development of large wind turbines designed by the aerospace industry. Nearly all of them failed after some hundreds of hours of operation due to technical problems. At that time, the current state of the art was not enough to build such large and expensive wind turbines.

In contrast to this, small Danish manufacturers of agricultural machines (Vestas, Bonus, Nordtank, Windworld, among others) were very successful with turbine rotor diameters between 12 and 15 m produced in series and equipped with asynchronous generators. With rated power between 30 and 75 kW, these turbines were technically and

economically feasible because a feed-in tariff was granted by the Danish government. Currently, many companies around the world have succeeded in the design, construction and operation of onshore and offshore HAWTs, with rotor diameters typically ranging from 60 to 120 m. To illustrate the state of development of this technology some of the largest HAWTs are presented in Table 2.7.

Table 2.7. List of some of the largest HAWTs.

Manufacturer	Model	Rated power [MW]	Rotor diameter [m]	Site type
Vestas	V164 8MW	8.0	160	offshore
Enercon	E126 7.5MW	7.5	127	onshore
Samsung	S7.0 171 7MW	7.0	170	offshore
Senvion (REpower)	6M series	6.0	126	onshore / offshore
Siemens	SWT-6.0 150	6.0	150	offshore
Alstom	Haliade	6.0	146	offshore
Gamesa	G5MW	5.0	128	offshore

Source: [56]

2.4.2. Basic theory

The wind passing through a turbine transfers a part of its momentum to the blades, producing the rotation of the turbine shaft. From another point of view, the wind transfers a certain quantity of its kinetic energy to the turbine, which is transformed into mechanical energy in the turbine shaft. The kinetic energy of the wind is quantified in the same way as for a particle or a body: a mass of air, m , that moves with a speed U_∞ has kinetic energy, K , as shown in Eq. (2.2).

$$K = \frac{1}{2} m U_\infty^2 \quad (2.2)$$

Power is defined as the work done in a certain period of time. Since the kinetic energy has the same units as work, the available power, \dot{W}_A , of a mass of air can be calculated as the change of kinetic energy in a period of time, Δt , as shown in Eq. (2.3), where \dot{m} is the mass flow rate.

$$\dot{W}_A = \frac{\Delta K}{\Delta t} = \frac{1}{2} \dot{m} U_\infty^2 \quad (2.3)$$

The mass flow rate, \dot{m} , of a fluid of density ρ and velocity U_∞ that is crossing a control surface A is calculated as the product of those values, as shown in Eq. (2.4). Note that in this case it is assumed that the velocity U_∞ is uniform over the area A .

$$\dot{m} = \rho A U_\infty \quad (2.4)$$

If Eqs. (2.3) and (2.4) are combined, Eq. (2.5) is obtained. Therefore, the available power, \dot{W}_A , is proportional to the fluid density, to the area of the control surface, which usually is the transversal section area of the turbine, and to the cube of its velocity. Note that the log law (see section 2.5) establishes that the free-stream velocity is a function of the vertical coordinate, $U_\infty(z)$, and therefore \dot{W}_A must be calculated integrating the value of $U_\infty(z)$ over the area A .

$$\dot{W}_A = \frac{1}{2} \rho A U_\infty^3 \quad (2.5)$$

The mechanical power output of the turbine shaft, \dot{W}_T , is calculated as the product of the mean torque on the shaft, τ , and its angular speed, ω , as shown in Eq. (2.6).

$$\dot{W}_T = \omega \tau \quad (2.6)$$

The turbine efficiency, η_T , is defined as the ratio between the available power output in the turbine shaft, \dot{W}_T , and the available power in the wind, \dot{W}_A . However, in the wind turbine discipline, this is known as the mean power coefficient, c_p , or just power coefficient, which is shown in Eq. (2.7). Note that the notation for the subscript of the power coefficient is a lowercase letter and a capital letter for the pressure coefficient.

$$c_p = \frac{\dot{W}_T}{\dot{W}_A} = \frac{\omega \tau}{\frac{1}{2} \rho A U_\infty^3} \quad (2.7)$$

For mechanical engineers it is well known that the Carnot cycle establishes a maximum theoretical efficiency of thermal machines, which is determined by the temperatures of the hot and cold reservoirs. The same concept is applicable to wind turbines. This maximum theoretical efficiency is known as the Betz limit and has a value of $c_p = 16/27 \approx 59,26\%$. According to [57], this theoretical limit should be called Betz-Joukowski limit because of the independent contribution to its determination by Albert Betz and Nikolái Zhukovski (Joukowski). The derivation of the Betz-Joukowski limit is discussed later in this work.

It should be noted that under some scenarios, the power coefficient is not a fair measurement of the turbine efficiency. Because of the flow expansion (decelerating wind), only a fraction of the available wind energy in the upstream area, A , really reaches the turbine. Nevertheless, the power coefficient with the effective available wind energy is usually not calculated because the effective area of the available energy varies with the operational conditions and typically is not known. Additionally, the flow around a turbine in a wind farm is also determined by other turbines. Therefore, since the area of the fluid far upstream that passes through the turbine is unknown, the swept turbine area is used in Eq. (2.7).

Another important dimensionless parameter to describe the efficiency of wind turbines is the tip-speed ratio, TSR , which is defined in Eq. (2.8), where R is the turbine radius. It is important to note that for most HAWTs and some VAWTs the rotational velocity of each part of the blade depends on its radius; therefore, at a blade radius, r , a local TSR can be defined (although it is no longer at the blade tip). The latter is not necessary for Darrieus SB-VAWTs because the blade radius is constant. For Darrieus CB-VAWTs the TSR is usually defined at the equator (maximum turbine radius). Note that the TSR is defined using the reference free-stream velocity and not the local wind

$$TSR = \frac{\omega R}{U_{\infty}} \quad (2.8)$$

The solidity of a turbine, σ , is a dimensionless parameter that relates the number of blades, N , the blade chord, c , and the turbine radius, R . One intuitive definition of the solidity for a unitary height Darrieus SB-VAWT is obtained from the ratio between the surface covered by the blades and the lateral surface of the circular cylinder described by the blade trajectory, $\sigma = (NcH)/(2\pi RH)$, where H is the blade length or span. For HAWTs the solidity is obtained from the ratio between the surface covered by the blades and a circular disk of radius R described by the blades trajectory, $\sigma = (NcR)/(\pi R^2)$. Note that in both cases a constant chord, c , is used. If only the dimensional quantities are considered, Eq. (2.9) is obtained.

$$\sigma = \frac{Nc}{R} \quad (2.9)$$

2.4.3. Comparison of technologies

Old HAWTs such as the Dutch windmills, which are lift-driven devices, have maximum power coefficients close to $c_p = 0.25$. Drag driven rotors such as the Persian mills have

maximum power coefficients close to $c_p = 0.16$, therefore, their efficiency is significantly lower than the lift-driven rotors. Modern HAWTs with well-designed blades, reach power coefficients near to $c_p = 0.50$, which is fairly close to the Betz-Joukowski theoretical limit. It must be noted that the theoretical limit considers a set of assumptions that omit from the model real phenomena such as wake turbulence. This could explain why the maximum theoretical limit is not reached by real turbines [2]. The power coefficient curves as a function of the TSR for some wind turbines is presented in Fig. 2.7. It should be noted that the plotted curves are only referential. Depending on the turbine parameters such as the turbine diameter, the number of blades, the blade chord, and on wind characteristics and turbine operation, significantly different curves can be obtained.

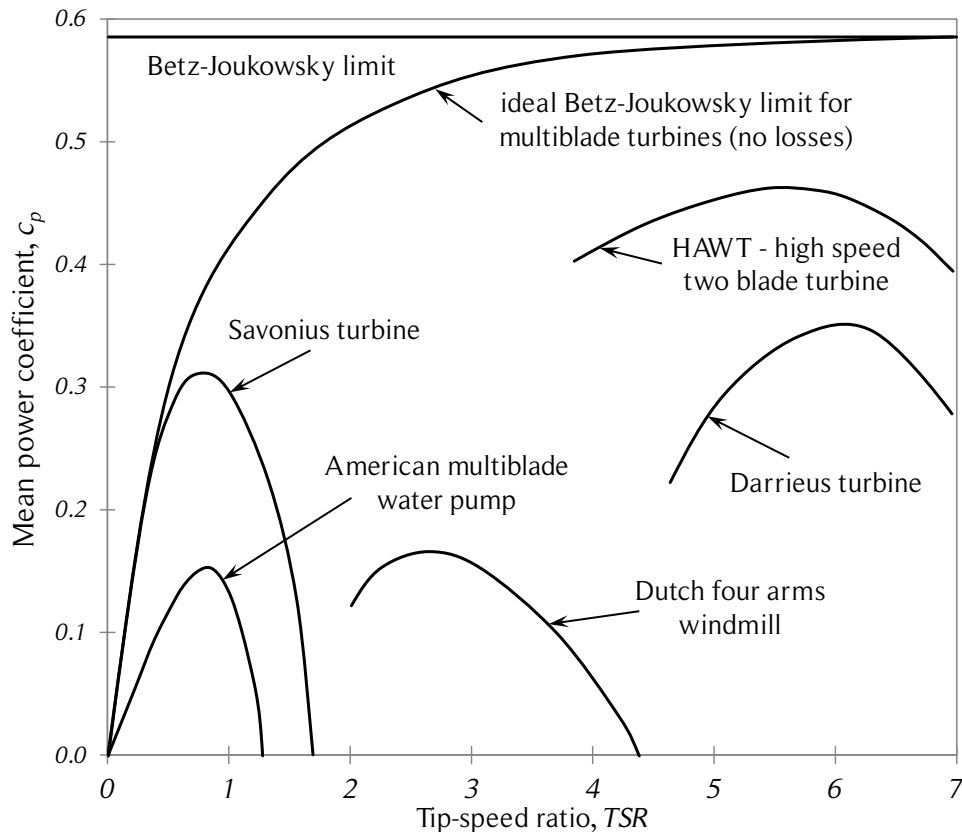


Figure 2.7. Power coefficient curves vs. tip-speed ratio for some wind turbines.

The figure shows the power coefficient curves as a function of the tip-speed ratio for some wind turbines. The Savonius and American multiblade curves were switched in some publications, which discouraged the Study of the Savonius turbine. Source: redrawn based on [58].

The reason for the difference in the maximum power coefficient of lift-driven and drag-driven devices is the magnitude of the aerodynamic forces for a given reference area.

Since the aerodynamic forces depend on the square of the relative velocity, the drag-driven devices experience smaller aerodynamic forces because they work at low TSR [2]. Lift-driven devices typically work at higher tip-speed ratios, reaching a maximum efficiency in a TSR range of 6 – 9. The Savonius turbine, which has a low lift to drag ratio, and, therefore, is not a purely drag-driven device, can achieve power coefficients near $c_p = 0.3$. Despite its relatively high maximum power coefficient, the Savonius rotor power coefficient usually is near $c_p = 0.2$. Therefore, it is not used for high-power applications [59]. For a two-bucket Savonius turbine with bucket overlapping, the maximum tip-speed ratio is $TSR = 1.57$ [4]. For turbines that are merely drag-driven devices, the highest TSR is usually less than 1. This is because the rotor half being pushed (motor side) is moving in the same direction as the wind, therefore cannot move faster than the wind. The other side of the rotor is experiencing a higher relative wind speed because it is moving against the wind. However, despite the low efficiency of drag-driven devices (or low lift-to-drag-driven devices), they are used anyway because of their simplicity and better self-starting torque characteristic, which allows harnessing the wind energy even at low speeds [2, 60]. Hybrid systems composed of Savonius and Darrieus turbines can combine the positive characteristics and diminish the disadvantages [61, 62].

When comparing different lift-driven devices such as HAWTs and VAWTs many characteristics have to be taken into account. Usually, the power coefficient is the first turbine characteristic to be compared. Since, for HAWTs, the wind passes through a disk, the maximum theoretical power coefficient is the Betz-Joukowsky limit $c_p = 16/27$, usually rounded to 59%. Despite this consideration, and according to [55], well-designed HAWTs should reach a maximum power coefficient of $c_p = 50\%$. In VAWTs, the wind passes through the rotor two times. Therefore, a vertical cylinder model is a better approach than a disk model. This cylinder usually is modeled as two disks in tandem (double streamtubes), which gives a slightly higher value for the maximum power coefficient $c_p = 16/25$ or 64% [55, 63]. Darrieus SB-VAWTs without struts could have a power coefficient of $c_p = 44\%$. Including aerodynamic losses of struts, c_p reduces to 40%. Darrieus CB-VAWTs have a c_p of 40% as well.

If the aerodynamics of both types of turbines is observed in more detail, other effects appear. In general, due to the vertical boundary layer and wind turbulence, the blades of HAWTs only experience small variations in the relative wind velocity magnitude and direction in one rotation. This allows the blades to operate at an optimum lift to drag ratio. On the other hand, Darrieus VAWTs blades present an intrinsic variation of the relative wind magnitude and angle of attack during one revolution, a topic that is discussed later in this work. This means that dynamic effects and especially dynamic stall

are relevant phenomena in the aerodynamics of Darrieus VAWTs. Generally, no pitching control for the blades is used this way for the sake of the turbine simplicity. As a result, a low lift to drag ratio is obtained [55], which explains the aforementioned lower performance of VAWTs. A typical performance curve as a function of the tip-speed ratio of a Darrieus turbine is presented in Fig. 2.8. The predominant physical phenomenon at each rotational speed range is also presented. The dynamic stall effects prevail at small tip-speed ratios, whereas secondary effects such as aerodynamic losses due to the blade struts are particularly significant for high tip-speed ratios [4].

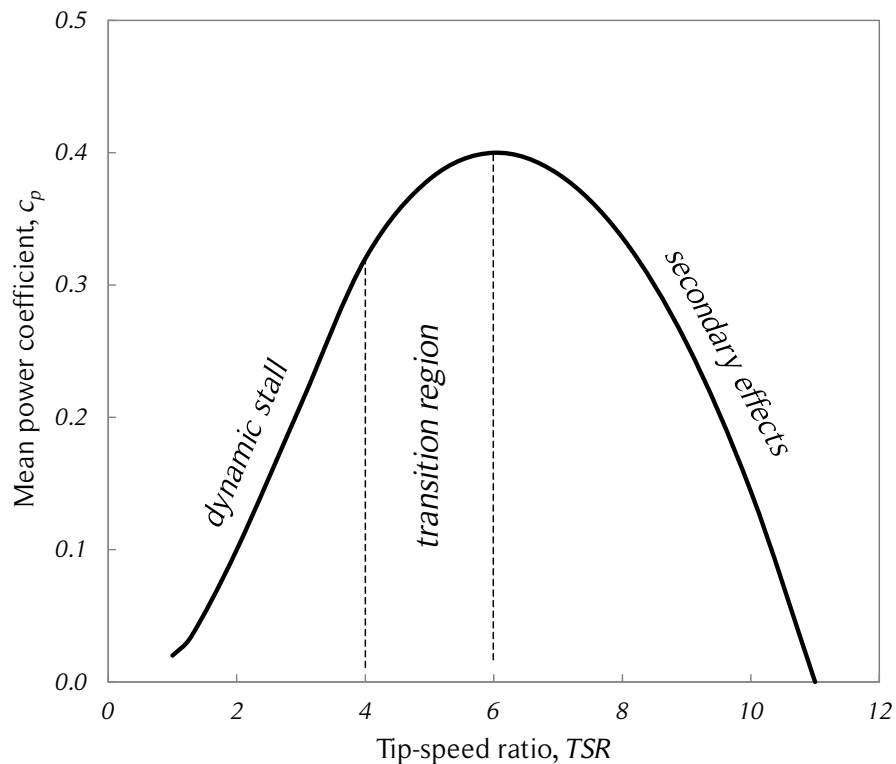


Figure 2.8. Typical power performance curve of a Darrieus turbine.

The figure shows a typical curve of the power performance as a function of the tip-speed ratio of a Darrieus turbine. The predominant physical phenomenon at each rotational speed range is also presented. Source: redrawn based on [4].

Other related relevant characteristic is the optimum TSR of both technologies. Because of the variation in one revolution of the angle of attack and magnitude of the relative speed, Darrieus VAWT design usually considers symmetric airfoils [4]. For high TSR , the angle of attack becomes smaller and therefore the lift as well. Hence, optimum rotational speed of Darrieus VAWTs is a moderate value, usually close to $TSR = 4 - 6$. The performance

curves of Darrieus VAWTs of different solidities are shown in Fig. 2.9. Up to a point, higher solidities have higher performance but a narrower optimal operational range.

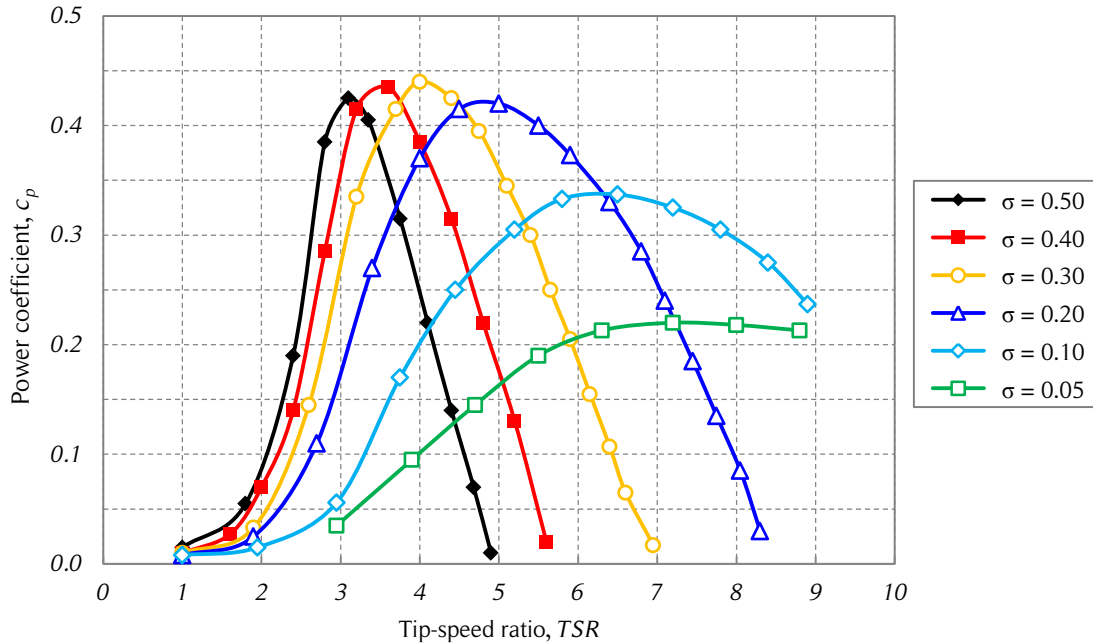


Figure 2.9. Performance curve of Darrieus VAWTs for different solidities.

The figure shows the power coefficient of Darrieus VAWTs of different solidities as a function of the tip-speed ratio. Source: redrawn from [55].

Optimum rotational speed of large HAWTs is close to $TSR = 9$ [55]. If a HAWT and a Darrieus VAWT have the same rated capacity, the drive train torque will be considerably larger for the VAWT because for the same power, the rotational speed will be smaller. In addition to this, if no pitch control for the blades is implemented, the mechanical shaft brake for protection in case of strong winds will have to be larger as well.

The pitch control also has to be taken into account when analyzing the turbine performance with dirty blades. According to [55], if no pitch control is used; dirty blades can cause a loss of nearly 33% of the rated power in Darrieus VAWTs. Turbines with pitch control can find the optimal blade pitch angle that minimizes the losses caused by the poorer aerodynamic performance of the dirty blades. The effect on the power coefficient of a Darrieus turbine depending on the blade surface roughness and on the blade attachments were investigated in [64, 65], respectively. The active and passive variable blade pitch of Darrieus SB-VAWTs have been researched by some authors (see [7, 66] for more details). The main advantages of turbines with variable pitch blades are

the possibility of achieving a better overall power performance and lower turbine self-starting torques. The main disadvantage is that the turbine ends up being a more complex machine, which usually means higher capital and maintenance costs, and a lower availability.

Darrieus wind turbines have high self-starting torques [4]. For the utility scale this is not a major concern because auxiliary starting devices can be used. However, this can be a relevant drawback for small-scale turbines because auxiliary systems increase the complexity of the system, which also increases the capital and maintenance costs. Another ingenious alternative for this problem of Darrieus SB-VAWTs is presented in [67]. The design considers two blades cut in half along the chord line. Each half can rotate with respect to the leading edge. For low winds, the blades are open to increase the drag forces, thus, the turbine acts like a Savonius rotor. For higher wind speeds, the blades are closed again and the turbine operates as a standard Darrieus SB-VAWT. The main disadvantage of this design is the higher complexity of the blades to achieve the proper transformation without compromising the structural strength and aerodynamic performance of the blades. Another alternative to improve the self-starting torque of Darrieus SB-VAWTs is to consider a turbine with more than one vertical tier. The offset angle of the other tiers has to be chosen so that the turbine has a lower self-starting torque as a turbine with the same diameter and height but no vertical tiers. This idea is discussed in detail in [68].

Darrieus VAWTs can present several advantages with respect to HAWTs in the structural characteristics and costs. The main reason for this is the omni-directionality of VAWTs. That is, they do not need a mechanism to follow the wind direction, and they will operate with wind coming from any direction. This results in less moving parts to control the turbine and the possibility of installing the generator at ground level. Both characteristics imply lower capital and maintenance costs. The generator at ground level also may present some disadvantages. The comparatively high torques present in VAWTs can require a stronger transmission shaft from the turbine to the generator, increasing the capital costs. Turbines that are installed near the ground can harness less wind energy. However, if the turbine is installed on a tower and the generator is no longer at ground level, what at the beginning seemed like an advantage may no longer be one [55].

Onshore and offshore wind farms of HAWTs may present some disadvantages due to the impact in the flora and fauna. Mortality of flying animals is one common disadvantage of HAWT wind farms. However, if this is considered in the wind farm design, this consequence can be avoided or at least diminished [44]. Other consequences, such as local small-scale or even large-scale climate changes due to the vertical mixing of air due

to the HAWTs rotation, are more difficult to avoid [6]. The aerodynamic and mechanical noise generated by the comparatively faster rotation of HAWTs, the shadow flickering and glint due to the blade rotation can have a negative impact on communities surrounding HAWT wind farms [44].

Both Darrieus and Savonius VAWTs, especially at small scale, are considered urban friendly. The comparatively slower rotation of Darrieus VAWTs improves safety, noise and vibration, which makes them a better option when considering installing a wind turbine in an urban environment. Some solutions to avoid visual pollution of small-scale wind turbines are presented in [69]. For example, some aspects of aerodynamic noise production of wind turbines are discussed in [70, 71]. The results of [71] show that depending on the position of the receiver, the turbine solidity, and the *TSR*, noise level can reach 65 *dB*, but for the majority of the cases the noise level is between 40 and 50 *dB*. According to [72], the noise level of small-scale wind turbines in urban environments should not be above 45 *dB*. Therefore, Darrieus VAWTs have a potential use in urban environments due to the low noise levels produced under operation.

Omni-directionality and the potential for better performance of Darrieus VAWTs in skewed flows caused by surrounding buildings such as rooftops are also characteristics that benefit VAWTs in urban environments. According to [30], a skewed flow of 25° can present an increase of about 30% in the power coefficient of a Darrieus SB-VAWT. Other examples of small scale wind turbines in urban environments are discussed in [73-75]. The performance improvement in skewed flows can also be exploited with airborne Darrieus VAWTs. Altaeros Energy, an initiative at the Massachusetts Institute of Technology (MIT) to introduce a commercial airborne wind turbine in Alaska [76], has been working since 2010 with an airborne HAWT. The technology developed by Altaeros Energy could be modified to produce airborne VAWTs. A technical list of many small scale wind turbines is presented in [77].

The future of very large scale wind turbines has not been clarified yet. For example, a 20 *MW* HAWT can have fatigue problems due to the blade self-weight. VAWTs do not have the same problem with the blades but have other fatigue problems due to the cyclic loading of the blades and struts during one rotation [55]. More details of offshore wind energy technologies are available in [78, 79]. On the other hand, according to [80-82], Darrieus SB-VAWT wind farms can harness more energy per area than best practice HAWT wind farms (see [83, 84] for more details about HAWT wind farms). According to [82], modern HAWT wind farms produce 2 – 3 *W/m*². Compact VAWT wind farms using counter-rotating turbines can achieve power densities an order of magnitude greater (around 30 *W/m*²).

2.5. The wind

The purpose of this section is to provide a brief introduction to the wind resource. The concepts addressed here are used in the following chapters of the present work. A more complete description of the wind resource is available in [1, 44].

2.5.1. General circulation

Global winds are produced by pressure differences caused by the uneven heating of the Earth's surface. The radiation absorbed at the equator is greater than at the poles. On the other hand, half of the surface has incident radiation (day) from the Sun while the other half radiates heat from the Earth (night). This configuration is changing constantly due to the Earth's rotation on its axis. The orbit of the Earth around the Sun also influences the global winds but in a larger time scale [44].

In general, winds in the atmosphere primarily respond to horizontal pressure gradients. The pressure gradients, inertia of the air, rotation of the Earth and the friction between the atmosphere and the Earth's surface affect atmospheric winds. The influence of each of these forces on atmospheric winds differs depending on the scale of motion. A diagram of the general atmospheric circulation is shown in Fig. 2.10. It should be noted that the figure is a simplification of the real phenomenon because the circulation shown in the diagram does not take into account the effect that the land masses have on the atmospheric winds.

The geostrophic wind is the resultant wind of a force analysis that considers only the pressure and Coriolis forces taking place between two regions with uneven pressures. It tends to be parallel to isobars (lines with the same pressure). This is shown in Fig. 2.11. Usually, the high and low pressure regions cause the isobars to be curved. If this happens, the respective centrifugal force also has to be taken into account, producing the gradient wind, shown in Fig. 2.11.

Smaller scale atmospheric circulation patterns can be divided into secondary and tertiary circulations. Secondary circulations include: hurricanes, monsoon circulation and extra-tropical cyclones. Tertiary circulations include: land and sea breezes, valley and mountain winds, foehn winds (dry, high-temperature winds on the downwind side of mountain ranges), thunderstorms and tornadoes. Depending on the local conditions, the latter type of circulation can cause large variations of the wind direction and intensity in short periods of time.

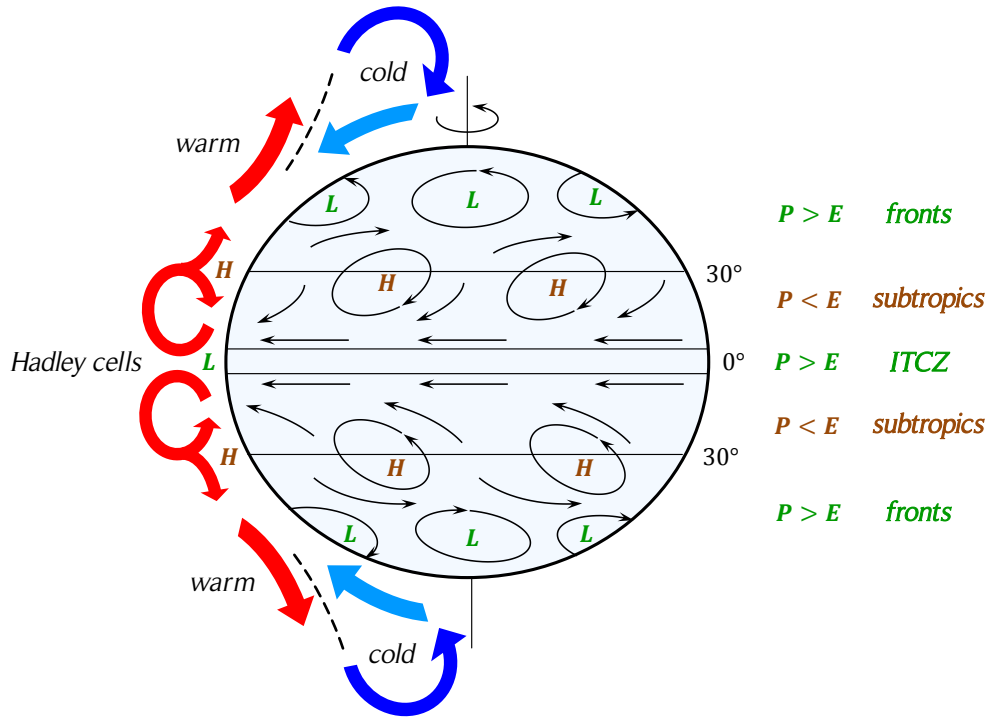


Figure 2.10. General atmospheric circulation.

The figure shows the general atmospheric circulation, the high (H) and low (L) pressure regions and the wind directions (black arrows). The Hadley cells are created when the air decreases its density because of its increment in temperature. The Hadley cells are present in the intertropical convergence zone (ITCZ). The polar jet streams are represented by the red and blue arrows near the poles. A balance of precipitation (P) and evaporation (E) as a function of the latitude is also presented. Source: based on [45].

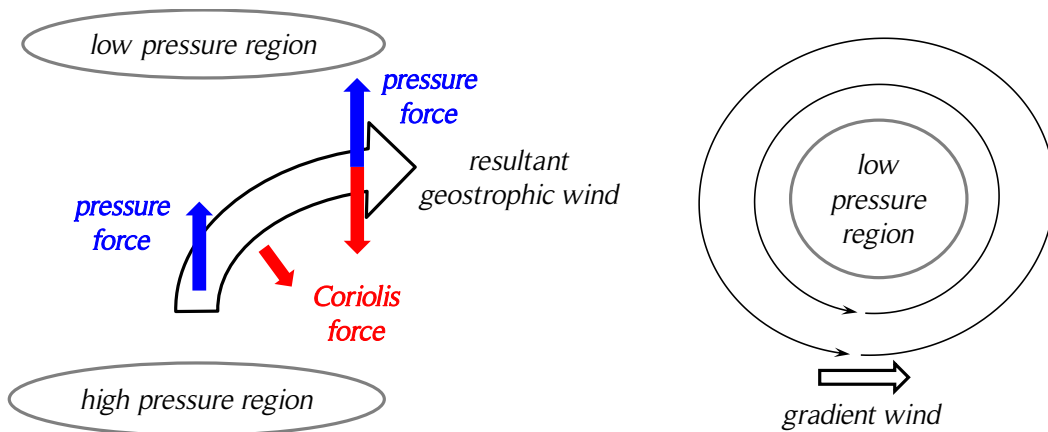


Figure 2.11. Geostrophic and gradient winds.

The figure shows the geostrophic wind (left) caused by the pressure and the Coriolis forces, and the gradient wind (right) caused by the pressure, Coriolis and centrifugal forces. Source: based on [44].

2.5.2. Steady wind boundary layer

In general, the wind velocity vector field depends on time and space. If there is no variation of the wind direction and magnitude with time, known as steady wind, only a speed variation with height due to the wind shear will exist. Two mathematical models or “laws” are usually used to model the vertical profile of wind speed over homogenous and flat terrains. The first approach, known as the log law (from logarithm), has its origins in boundary layer flow in fluid mechanics. The second approach is known as the power law and is based on empirical research. For real wind, both approaches are subject to the uncertainty caused by the variable and complex nature of turbulent flows. A typical vertical mean speed profile is shown in Fig. 2.12.

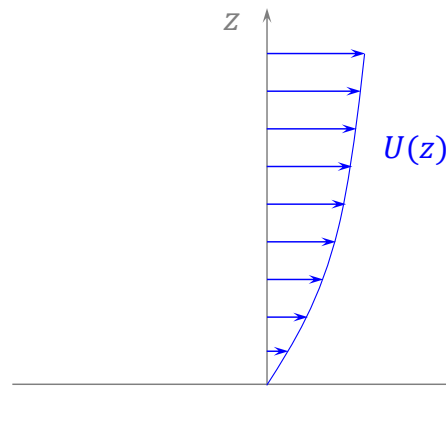


Figure 2.12. Typical vertical mean speed profile.

The figure shows a typical vertical mean wind velocity profile which can be modeled by the power law. Source: own elaboration.

One way to deduce the log law is using the momentum equation near the Earth’s surface. The details of its deduction are available in [44]. The power law profile represents a simple model for the vertical wind speed profile. Its basic form is shown in Eq. (2.10), where z_r is the reference height and α is the power law exponent. Under certain conditions, the power law exponent, α , is equal to $1/7$. In practice, the exponent varies with parameters such as elevation, time of day, nature of the terrain, and wind speed. Some empirical correlations presented in [44] have been developed by various authors to take into account the aforementioned parameters.

$$U(z) = U(z_r) \left(\frac{z}{z_r} \right)^\alpha \quad (2.10)$$

2.5.3. Wind turbulence

The dissipation of the kinetic energy of the wind into thermal energy by the creation and destruction of progressively smaller eddies is called turbulence. Turbulent winds may have relatively constant mean speed over a time period (an hour for instance) but the instantaneous speed can be quite variable. The wind turbulence is characterized by the following statistical properties: turbulence intensity, wind speed probability density function, autocorrelation, integral time scale/length scale, and power spectral density function [44]. In general, wind will have non-zero speed components in the longitudinal, lateral and vertical directions. Usually, the prevailing wind direction is designated $u(x, y, z, t)$. Each component is considered as the sum of two terms: a short-term mean wind speed, \bar{u} , and fluctuating wind speed with zero mean, u' , as shown in Eq. (2.11).

$$u = \bar{u} + u' \quad (2.11)$$

The turbulence intensity, TI , is a basic measure of wind turbulence. It is calculated from Eq. (2.12), where σ_u is the standard deviation of the wind speed and \bar{u} is the time-average wind speed. For a Weibull wind distribution, σ_u is calculated using Eq. (2.17), where \bar{U} is the mean wind speed and k the shape factor. The length of the sampling time period is usually no longer than one hour and in wind engineering, the convention usually establishes a 10 minute time period. The turbulence intensity is frequently in the range of 0.1 and 0.4. Some studies about the influence of turbulence on the performance of Darrieus VAWTs have been carried out (see Section 3.12).

$$TI = \frac{\sigma_u}{\bar{u}} \quad (2.12)$$

2.5.4. Wind statistical distributions

Given a geographical location and height, wind direction and magnitude can have important variations with time. However, over long periods of time, such as one year, the wind magnitude usually follows a certain pattern [44]. To illustrate this, a typical sample histogram of wind speed in one year is shown in Fig. 2.13. Statistical analysis of wind data have been developed to represent the time dependency, as shown in Eq. (2.13), where $F(U)$ is the cumulative distribution function and represents the time fraction or probability that the wind speed is smaller or equal to a given speed U , and $f(U)$ is the derivative of the cumulative distribution function $F(U)$ and is known as the probability density function.

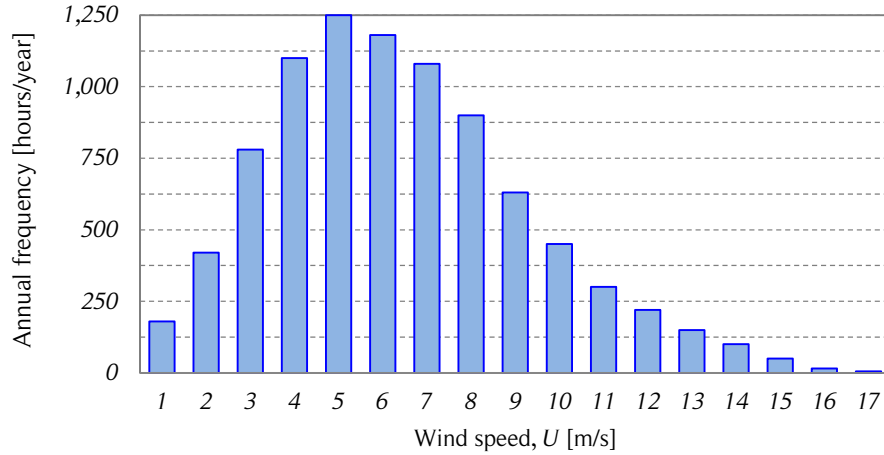


Figure 2.13. Example of wind speed histogram in one year.

The figure shows an example of a wind speed histogram in a time period of one year. The wind speed was measured every hour. Source: [44].

$$F(U) = \int_0^U f(u) du \quad (2.13)$$

Two commonly used probability distributions are the Rayleigh and Weibull distributions. The Rayleigh distribution is the simplest velocity probability distribution because it only requires one parameter: the mean wind speed \bar{U} , as shown in Eq. (2.14).

$$f(U) = \frac{\pi}{2} \left(\frac{U}{\bar{U}^2} \right) \exp \left[-\frac{\pi}{4} \left(\frac{U}{\bar{U}} \right)^2 \right] \quad (2.14)$$

The Weibull probability density function requires two parameters: a shape factor, k , and a scale factor, s , as shown in Eq. (2.15). Both parameters are functions of the mean wind speed, \bar{U} , and the wind speed standard deviation, σ_u . These two parameters allow the Weibull distribution to represent a wider variety of wind regimes in a better way than the Rayleigh distribution. These two parameters can be obtained from Eqs. (2.16) and (2.17), where Γ is the mathematical gamma function. This information is useful to characterize the wind resource in the installation site of a turbine or wind farm. Hence, the uncertainty of the annual power output can be diminished. The Weibull parameters of the location site of the reference case for this study are presented in Section 4.1.3.

$$f(U) = \frac{k}{s} \left(\frac{U}{s} \right)^{k-1} \exp \left[-\left(\frac{U}{s} \right)^k \right] \quad (2.15)$$

$$\bar{U} = s \Gamma \left(1 + \frac{1}{k}\right) \quad (2.16)$$

$$\sigma_u^2 = \bar{U}^2 \left[\frac{\Gamma \left(1 + \frac{2}{k}\right)}{\Gamma^2 \left(1 + \frac{1}{k}\right)} - 1 \right] \quad (2.17)$$

2.5.5. Wind resource in Chile

The long coast of the Pacific Ocean on the west side of Chile may give one the impression that the country possesses a very good wind resource. But, Chile is not as privileged in wind resources as other countries. To illustrate this, the wind classes at 80 m in Central and South America are shown in Fig. 2.14. Note that only a few points are shown, therefore, there can be places with better and worse wind resources than the ones shown in the figure. Some of the points with the best wind resources in the country are located in places with rugged geography or far away from the populated areas. These disadvantages have to be taken into account when feasibility studies of the wind resources are being carried out. See [46, 47] for more details. On the other hand, due to the depth of the seabed of the Pacific Ocean and the seismic activity, offshore plants are less viable than in other places around the world. Despite these considerations, there are still several feasible locations for power plants and utility-scale wind power is growing in the Chilean electricity sector, as shown in Fig. 2.3.

Small-scale wind turbines are usually installed at lower heights than the utility-scale wind turbines and can benefit from the buildings in urban areas. Therefore, each location for small-scale wind energy has to be studied carefully to obtain good estimations of the available wind resource. This is crucial in the determination of the potential annual energy output and thus, in the economic evaluation of a small-scale wind energy project.

2.6. Airfoil theory

Aerodynamics of lift-driven devices, such as the Darrieus SB-VAWTs, is explained by airfoil theory. The aim of this section is to address the basic concepts needed to understand the following chapter, which covers the modeling of Darrieus SB-VAWTs. More details about airfoil theory are available in [49].

During the 20th century the field of aerodynamic experienced large advances. One of the first important steps was the use of wind tunnels to study the aerodynamics of bodies.

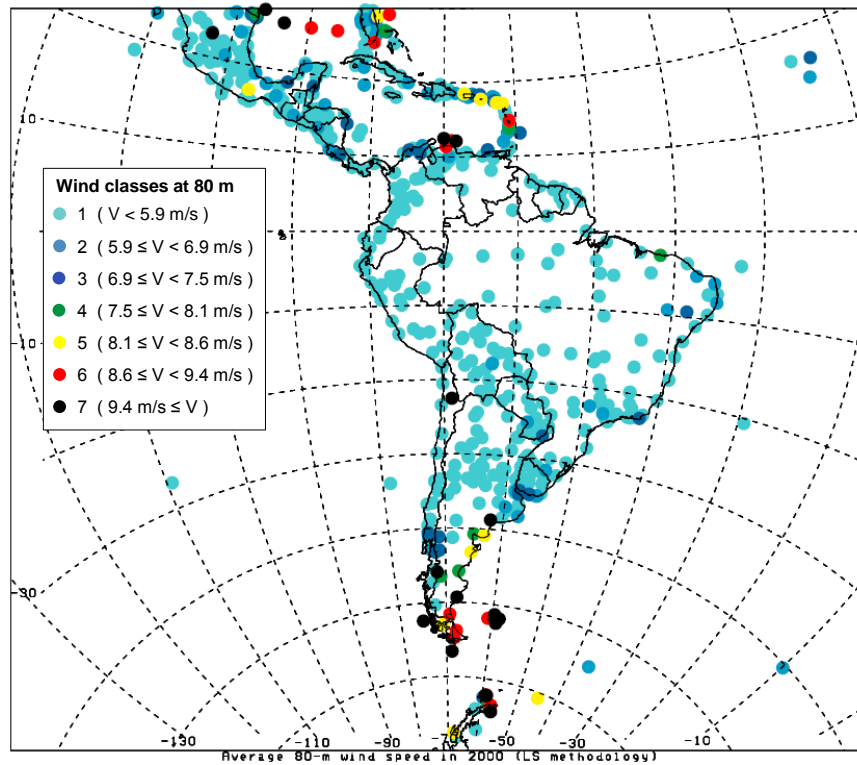


Figure 2.14. Wind resource in South America.

The figure shows the mean wind speed at 80 m for the year 2000 of some locations in Central and South America (Least Squares methodology). Source: [48].

The brothers Wilbur and Orville Wright used a wind tunnel to study several airfoil geometries before they accomplished the first powered manned flight in a heavier-than-air machine in the year 1903. In the period 1912 – 1918, another important step was accomplished by Ludwig Prandtl and his colleagues at Göttingen, Germany, when they showed that the aerodynamic modeling of wings could be separated in two parts: first, the study of the section of the wing, or airfoil, as an infinite length wing; and second, the modification of the properties of that airfoil to take into account the finite length of the wing [49]. This approach is still used today. The general definitions of a wing are presented in Fig. 2.15, in which the wing extends along the z -axis and any wing section parallel to the xy -plane is called an airfoil profile or airfoil shape.

2.6.1. Geometry

The design of the first airfoils and the respective wind tunnel experiments was mostly trial and error. Later, more systematic procedures were developed. In the early 1930s,

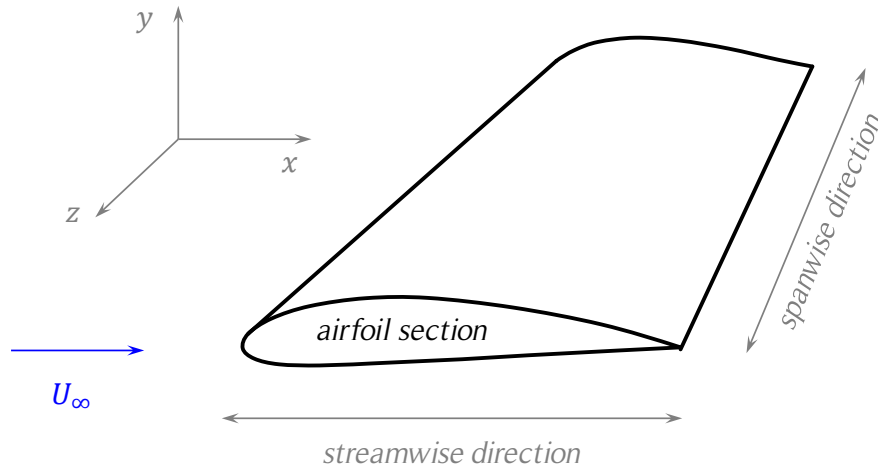


Figure 2.15. Wing geometric definitions.

The figure shows some general geometric definitions of a wing and one airfoil section. Source: redrawn from [49].

the National Advisory Committee for Aeronautics (NACA) of the USA, the precursor of the National Aeronautics and Space Administration (NASA) of the same country, concentrated on a series of systematic experiments of airfoils. Many of these NACA airfoils, whose nomenclature is a well-known standard, are in common use today [49]. Currently, large aircraft companies design their own airfoils according to their needs using old design standards and new advanced design tools such as computer simulations.

The airfoil nomenclature is shown in Fig. 2.16, which is defined under the following considerations: wind is flowing from left to right and the airfoil is positioned in such manner that an upper and lower surface can be defined. Considering the flow direction, the leading and trailing edges can be defined. The linear distance measured from the leading edge to the trailing edge is called chord. The shape of the airfoil at the leading edge is usually circular, with an approximate radius of 2% of the chord. The mean camber line is the set of the points that are located at half of the distance between the upper and lower surfaces. The airfoil thickness is the largest distance between the upper and lower surfaces. For different airfoils, the maximum thickness can be located at different positions y on the chord line. The camber is the largest distance between the mean camber line (midway between the upper and lower surfaces) and the chord line.

The shape of NACA airfoils are generated by specifying the shape of the mean camber line and then specifying a symmetrical thickness around the mean camber line to obtain the upper and lower surfaces [49]. Many years ago the NACA defined a logical numbering system to identified different airfoil shapes. The first family of NACA airfoils

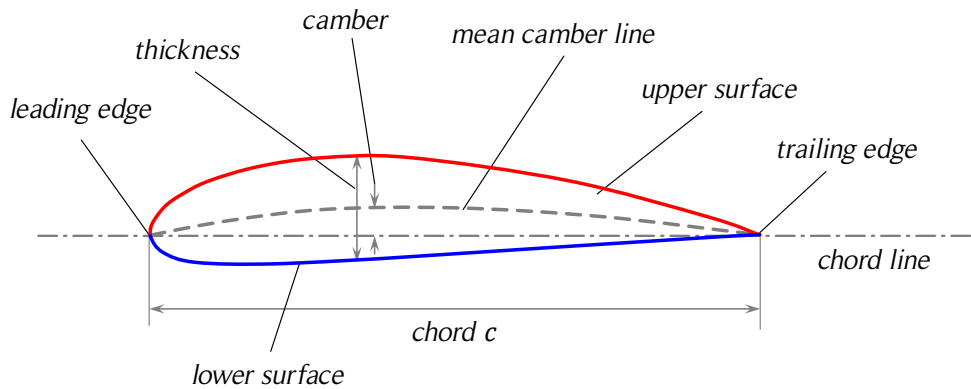


Figure 2.16. Airfoil nomenclature.

The figure shows a non-symmetric airfoil and the nomenclature for its parts.

Source: redrawn from [49].

was developed in the 1930s and was the “four-digit series”. Later, other families of airfoils like the “five-digit series” and the “six-digit series” were developed. The NACA 2412 airfoil is a commonly used non-symmetric airfoil of the 4-digit series. In this nomenclature, the first digit is the maximum camber in hundredths of chord: $m = 2\% c$; the second digit is the location of maximum camber along the chord from the leading edge in tenths of chord, $p = 40\% c$; and the last two digits define the maximum thickness in hundredths of chord, $t = 12\% c$. When an airfoil has no camber, the mean camber line is coincident with the chord line, producing a symmetric airfoil, usually denoted NACA 00XX. For example, the NACA 0012 is a symmetric airfoil with a 12% thickness. This nomenclature and profile equations are available in [50].

For a NACA symmetric airfoil of the 4-digit series, the coordinates of the upper (x_U, y_U) and lower (x_L, y_L) surfaces are determined by Eqs. (2.18) – (2.21), where all coordinates are expressed as a fraction of the chord, c , thus, $0 \leq x \leq 1$ (see Fig. 2.17). To obtain the dimensional coordinates of the airfoil, both x and y coordinates have to be scaled by the respective chord c . For an airfoil of chord c , the non-dimensional thickness, t , is required to calculate the airfoil thickness along the chord, y_t , as it is shown in Eq. (2.21). For example, the non-dimensional thickness of a NACA 0012 airfoil is $t = 0.12$. Note that Eq. (2.21) gives a non-zero thickness at the trailing edge. If a smooth trailing edge at $x = c$ is required, the coefficients have to be modified. If the last coefficient of Table 2.8 is modified to $A_4 = 0.1036$, a zero thickness at the trailing edge is obtained, causing only a small change in the overall shape of the airfoil.

$$x = x_U = x_L \quad (2.18)$$

$$y_U = y_c + y_t \quad (2.19)$$

$$y_L = y_c - y_t \quad (2.20)$$

$$y_t = \frac{t}{0.2} [A_{0.5} \sqrt{x} - A_1 x - A_2 x^2 + A_3 x^3 - A_4 x^4] \quad (2.21)$$

Table 2.8. Airfoil thickness coefficients.

Coefficient	$A_{0.5}$	A_1	A_2	A_3	A_4
Value	0.2969	0.1260	0.3516	0.2843	0.1015

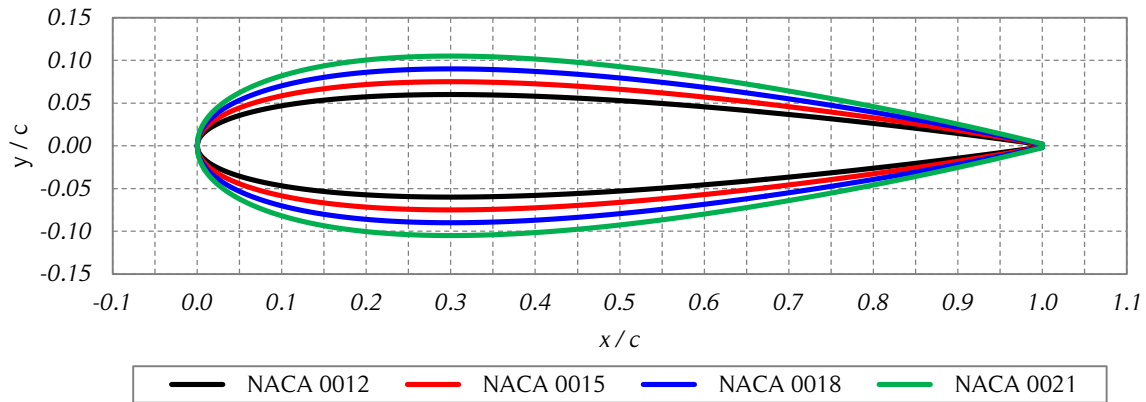


Figure 2.17. Geometry of four symmetric NACA 00XX airfoils.

The figure shows four common symmetric airfoils: NACA 0012, NACA 0015, NACA 0018 and NACA 0021. Source: own elaboration.

Since the thickness of the airfoil should be applied perpendicular to the mean camber line, the determination of the upper and lower surfaces for the non-symmetric airfoils of the NACA 4-digit series is a bit more complicated. The expressions for these corrections are presented in Eqs. (2.22) – (2.28). The NACA 2412 airfoil geometry is presented in Fig 2.18 as an example, where $m = 0.02$, $p = 0.4$ and $t = 0.12$.

$$x_U = x - y_t \sin \theta \quad (2.22)$$

$$x_L = x + y_t \sin \theta \quad (2.23)$$

$$y_U = y_c + y_t \cos \theta \quad (2.24)$$

$$y_L = y_c - y_t \cos \theta \quad (2.25)$$

$$y_c = \begin{cases} \frac{m}{p^2}(2px - x^2), & 0 \leq x \leq p \\ \frac{m}{(1-p)^2}[(1-2p) + 2px - x^2], & p < x \leq 1 \end{cases} \quad (2.26)$$

$$\theta = \arctan\left(\frac{dy_c}{dx}\right) \quad (2.27)$$

$$\frac{dy_c}{dx} = \begin{cases} \frac{2m}{p^2}(p-x), & 0 \leq x \leq p \\ \frac{2m}{(1-p)^2}(p-x), & p < x \leq 1 \end{cases} \quad (2.28)$$

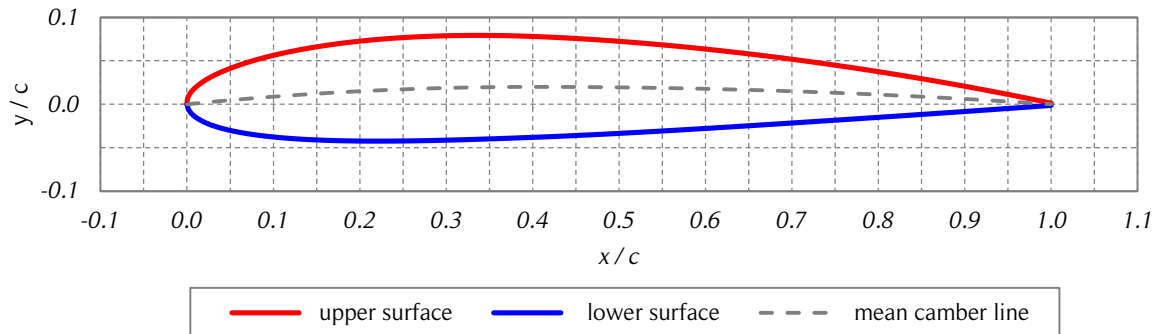


Figure 2.18. NACA 2412 airfoil geometry.

The figure shows the NACA 2412 non-symmetric airfoil. Source: own elaboration.

2.6.2. Kinematics

The position of a rigid body can be defined by the location of a point belonging to the body (for instance its geometric center or its center of mass) and the body's orientation. The movement of the body can be divided in two individual movements: the movement of the selected point, and the rotation of the body. The resultant movement of the body can be determined by the superposition of both movements. In aerodynamics, two different approaches are usually used: a moving body inside a still fluid, or a still body inside a moving fluid. The latter coincides with the typical configuration of experiments

(fixed body in a wind tunnel) and also is the most common approach in theoretical aerodynamics. In the latter case only the rotation of the body is of interest for the fluid dynamics. The three rotational angles (pitch, roll and yaw) used to describe the orientation are presented in Fig. 2.19. Since airfoils are defined as two-dimensional elements, only the pitch angle is of interest for the aerodynamic analysis of airfoils.

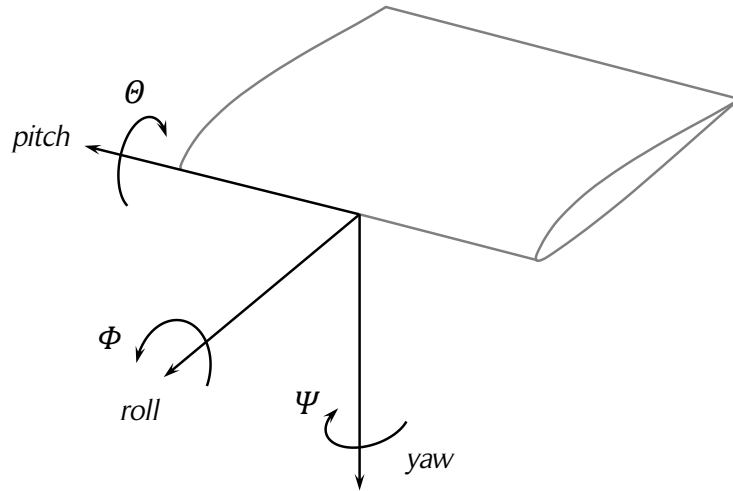


Figure 2.19. Rotation angles of a wing.

The figure shows the definition of the three rotation angles used to describe the rotation of a wing: pitch, roll and yaw. Source: own elaboration based on [49].

2.6.3. Aerodynamics

If gravity, electrical and magnetic forces are neglected, there are only two ways of transmitting forces from a fluid to a submerged body [49]:

- a) Pressure distribution over the body surface $P(s)$.
- b) Shear stress distribution over the body surface $\tau(s)$.

The pressure, $P(s)$, acts normal to the body surface and the shear stress, $\tau(s)$, acts tangential to the surface. Both distributions have units of force per unit area. The net effect of the pressure and shear stress acting on the entire surface produces a resultant force, F , and a moment, M , on the body, as shown in Fig. 2.20. The relative wind, U_∞ , is defined as the flow velocity far ahead from the body and is called the freestream velocity. The angle of attack, α , is defined as the angle between the chord, c , and U_∞ . The aerodynamic moment depends on the point about which moments are calculated. By

convention, moments which tend to increase α (pitch up or just pitch) are positive, and moments which tend to decrease α (pitch down or plunge) are negative (see Fig. 2.19). The resultant aerodynamic force, F , can be expressed by the sum of two perpendicular components: lift, F_L , and drag, F_D , as shown in Fig. 2.21. The lift and drag are perpendicular and parallel to the freestream velocity, respectively.

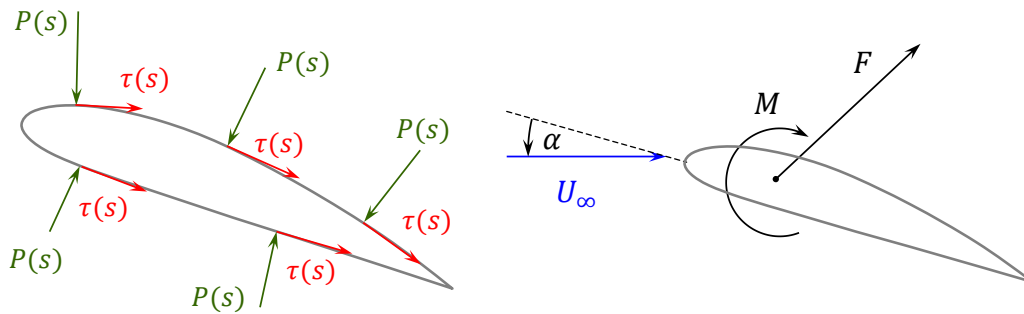


Figure 2.20. Aerodynamic forces acting on an airfoil.

The figure shows the pressure and shear stress distributions on the body surface (left) and the resultant force and moment (right). Source: redrawn from [49].

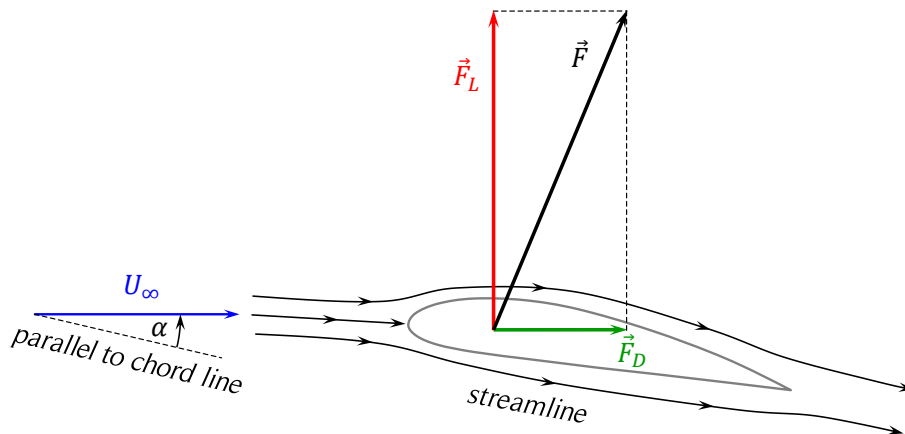


Figure 2.21. Lift and drag definition.

The figure shows the resultant aerodynamic force acting on an airfoil and its two perpendicular components: lift and drag. Source: redrawn from [49].

The integration of the pressure and shear stress distributions determines the resultant aerodynamic force and moment acting on the airfoil. The position and magnitude of the moment depends on the reference point. The magnitude and direction of the resultant force is independent of the reference point. The center of pressure of an airfoil is defined

as the geometrical point along the chord where the distributed load effectively acts on the body. If the center of pressure is used as the reference point for the calculation of the moments, the resultant moment must be zero. The center of pressure depends on the load distribution on the body surfaces. Hence, in general, its position will change with the variation of the angle of attack [49].

The aerodynamic center is the point on a body about which the aerodynamically generated moment does not depend on the angle of attack [49]. At first glance it may seem that this point does not exist, but its existence has been proved experimentally. On the other hand, within the respective assumptions, the thin airfoil theory shows that, not only does the aerodynamic center exist but that it is located at the quarter-chord point on the airfoil. For most conventional airfoils, the aerodynamic center is close, but not necessarily at, the quarter-chord point. In general, the positions along the chord of the aerodynamic center and the center of pressure will not be the same, thus, the resultant moment about the aerodynamic center will not necessarily be zero.

The aerodynamic force and moment can be expressed using dimensionless coefficients. Usually, for a dimensionless analysis, a dimensional quantity called freestream dynamic pressure, q_∞ , is defined, as shown in Eq. (2.29), where ρ is the density of the fluid and U_∞ is the freestream velocity.

$$q_\infty = \frac{1}{2} \rho U_\infty^2 \quad (2.29)$$

The lift, drag and moment coefficients are defined in Eqs. (2.30) – (2.32), where A is a reference area and l is a reference length. Usually, the reference area is defined as the product of the airfoil chord, c , and the wing span, s , therefore, $A = cs$.

$$c_L = \frac{F_L}{q_\infty A} \quad (2.30)$$

$$c_D = \frac{F_D}{q_\infty A} \quad (2.31)$$

$$c_M = \frac{M}{q_\infty A l} \quad (2.32)$$

For infinite wings, the coefficients may be defined per unit wing span ($s = 1 \text{ m}$). Hence, for two-dimensional airfoils, Eqs. (2.3) and (2.31) can be expressed as Eqs. (2.33) and (2.34), respectively.

$$F_L = \frac{1}{2} \rho c U_\infty^2 c_L \quad (2.33)$$

$$F_D = \frac{1}{2} \rho c U_\infty^2 c_D \quad (2.34)$$

Two additional dimensionless quantities, the pressure coefficient, c_p , and the skin friction coefficient, c_f , are defined in Eqs. (2.35) and (2.36), respectively, where the local pressure and shear stress are denoted P and τ , respectively, and P_∞ is the undisturbed local pressure far away from the body. To illustrate the pressure distribution over an airfoil, the pressure coefficient distribution for a NACA 0012 airfoil at an angle of attack $\alpha = 9^\circ$ is shown in Fig. 2.22. Note that the vertical axis orientation is reversed.

$$c_p = \frac{P - P_\infty}{q_\infty} \quad (2.35)$$

$$c_f = \frac{\tau}{q_\infty} \quad (2.36)$$

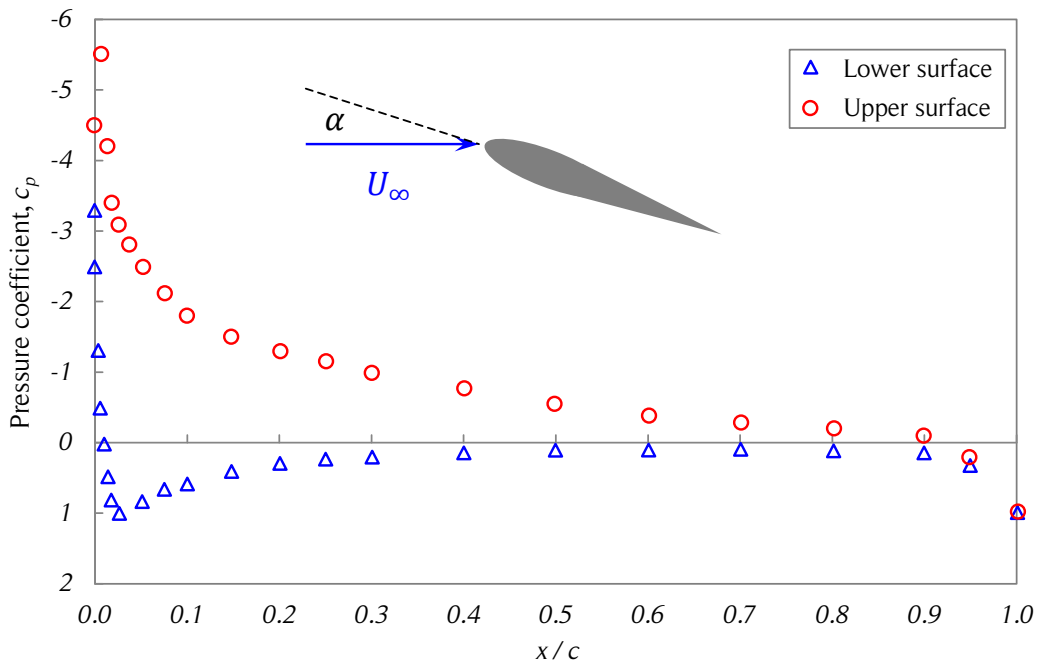


Figure 2.22. Pressure coefficient distribution for a NACA 0012 airfoil.

The figure shows the pressure coefficient distribution of a NACA 0012 airfoil at an angle of attack of 9° . Note that the vertical axis orientation is reversed. Source: redrawn from [49].

The typical variation of lift with the angle of attack for a non-symmetrical airfoil is shown in Fig. 2.23. For low angles of attack, the relation between the lift coefficient and the angle of attack is linear. The lift slope is called a_0 . For high angles of attack, a flow separation on the upper surface of the airfoil occurs. This creates a relative large wake of “dead air” behind the airfoil. The viscous forces produce part of the flow on the upper surface of the airfoil to go in the opposite direction of the freestream, which produces a decrease in lift and an increase in drag. This phenomenon is called stall. Thus, an airfoil operating under these conditions is called a stalled airfoil. The maximum lift coefficient reached before the stall condition is denoted $c_{L,max}$. For subsonic flows, the lift and drag coefficients are functions only of the Reynolds number and the angle of attack (and not the Mach number).

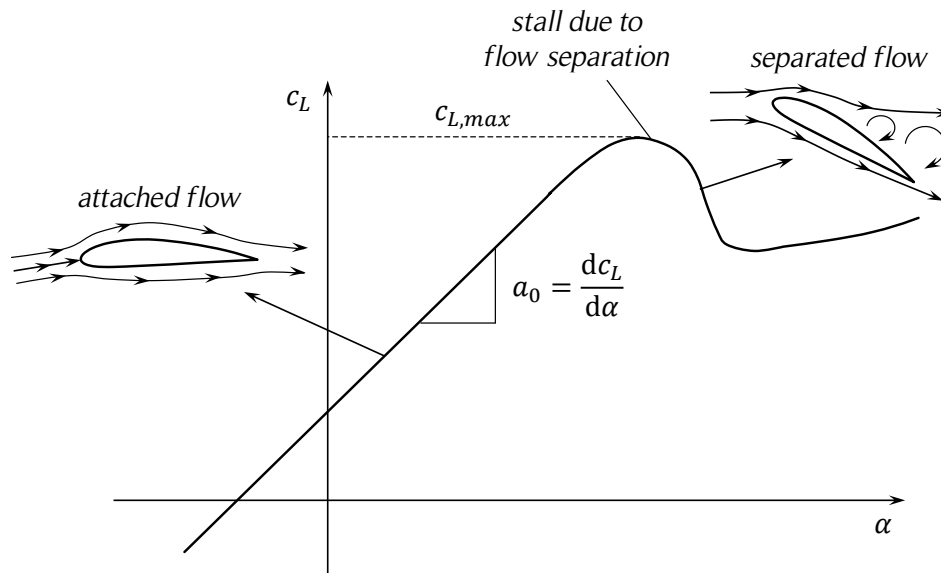


Figure 2.23. Lift dependency on the angle of attack for a non-symmetric airfoil.

The figure shows the lift dependency on the angle of attack for a non-symmetric airfoil. For low angles of attack the flow is attached, and for high values of the angle of attack the flow becomes separated. Source: redrawn from [49].

Because of the almost symmetric variation of the angle of attack for Darrieus SB-VAWTs with the azimuthal position of the blades, a phenomenon that is discussed later in this work, the designers of SB-VAWTs usually select symmetric airfoils for the turbine blades. Among the most commonly used airfoils are the NACA 0012, NACA 0015, NACA 0018 and NACA 0021. The lift and drag coefficients as a function of the angle of attack and the Reynolds number for these four NACA airfoils and also for the NACA 0025 airfoil are presented in Appendix A.

2.6.4. Unsteady aerodynamics

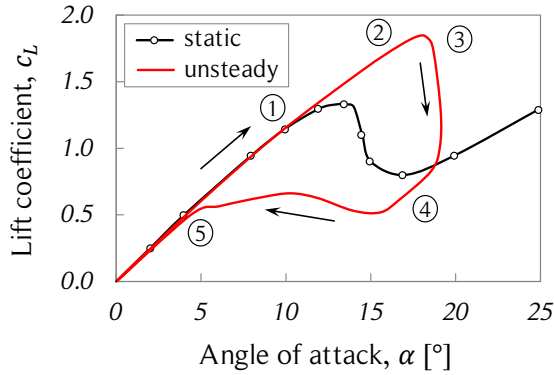
When the relative wind is changing magnitude and/or direction, or when the airfoil is pitching or plunging, the static aerodynamic coefficients mentioned in the previous sections are no longer valid at the instantaneous angle of attack. Depending on the operating characteristics, unsteady aerodynamics of airfoils usually is classified using two different criteria: circulatory and non-circulatory unsteady effects; and attached or separated flows [7]. The elasticity of blades brings additional unsteady effects that are taken into account by aeroelastic models. See [51] for more details.

The unsteady circulatory effects are the change of circulation about the airfoil due to the influence of vorticity in the wake and due to the motion of the airfoil. For attached flows, the vorticity in the wake can be taken into account by semi-empirical models such as the Beddoes-Leishman model [7]. However, due to the wake complexity of SB-VAWTs the implementation of such models is rather difficult and in many cases these effects are neglected. The non-circulatory aerodynamic loads are generally known as “added mass” forces. These forces arise from the acceleration of the air around the moving airfoil. It is assumed that this phenomenon occurs due to the compression and expansion waves formed at each side of the airfoil. These waves depend on the movement direction of the airfoil. This approach takes into account the compressibility of air, which is important for helicopter applications, but should not be significant for wind turbines [7].

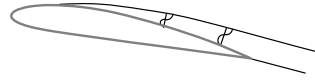
In unsteady aerodynamics, attached flows do not stall. Unsteady flows can switch from attached flows to separated flows. This transition is known as dynamic stall and is a relevant phenomenon because the lift, drag and moment coefficients can experience important variations (see Fig. 2.24).

For a pitching airfoil under dynamic conditions, stall occurs at higher angles of attack than under static conditions. Dynamic stall is characterized by the shedding and passage over the upper lifting surface of a vortex. The movement of the vortex produces a rearward motion of the center of pressure and a corresponding negative peak in the pitching moment about the quarter chord. After the vortex passes the trailing edge, the flow becomes fully separated and a significant drop of lift occurs. For an airfoil plunging from a high angle of attack, the reattachment of the flow usually occurs at an angle of attack below the static stall angle [7]. More details of the dynamic stall process are available at [52-54]. Several semi-empirical dynamic stall models have been developed to take into account this complex phenomenon in aerodynamic analysis of oscillating airfoils. These semi-empirical models usually take into account both circulatory and non-

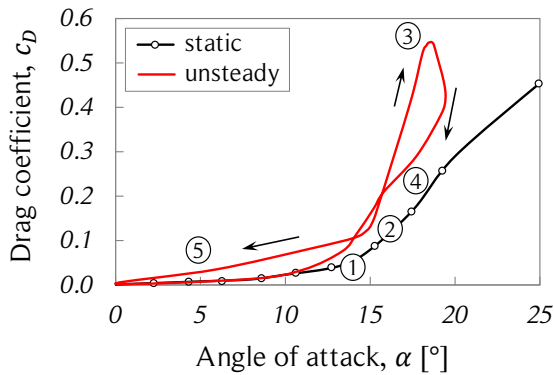
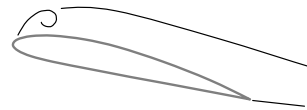
circulatory effects. The adaptations of two of these models for SB-VAWTs are presented later in this work.



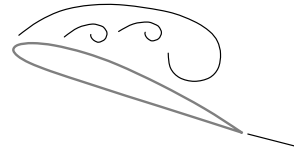
Stage 1. Airfoil exceeds static stall angle. Flow reversal takes place in upper surface boundary layer.



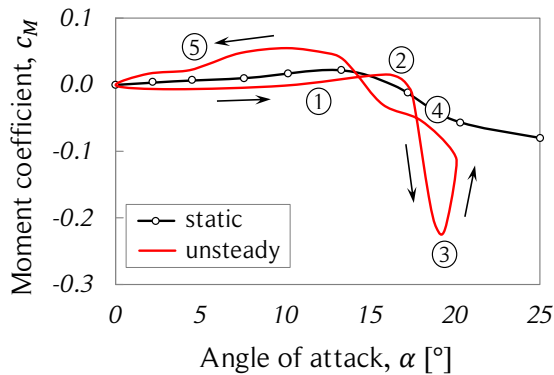
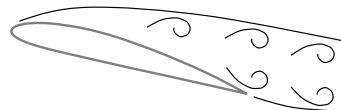
Stage 2. Flow separation at the leading edge, followed by the formation of a vortex. Moment stall.



Stage 2-3. Vortex convects over chord, inducing extra lift and rearward movement of the center of pressure.



Stage 3-4. Lift stall. After vortex reaches trailing edge the flow over the upper surface becomes fully separated.



Stage 5. When the angle of attack becomes low enough, the flow reattaches to the airfoil, front to back.

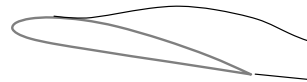


Figure 2.24. Dynamic stall stages.

The figure shows the typical curves of lift, drag, and moment coefficient as a function of the angle of attack and the five stages of dynamic stall for an oscillating airfoil. Source: redrawn from [7].

3. MODELING OF DARRIEUS SB-VAWTs

The aerodynamics of Darrieus SB-VAWTs is quite complex. Dynamic stall due to the periodic large variations of the angle of attack beyond the static stall angle during one rotation, vortex shedding, and blade interference because of the downstream flow perturbations produced in the upstream side are some of the characteristic phenomena of SB-VAWT aerodynamics. Several models for this type of turbine have been developed to obtain accurate predictions of the power output and the loads acting on the turbine blades. The aim of this chapter is to submit a summary of the models as a theoretical framework for the present work and the state of the art. It should be noted that the models for Darrieus SB-VAWTs presented here can be easily extended for other types of Darrieus turbines such as the CB-VAWT and the HB-VAWT.

3.1. Coordinate system and geometry

The coordinate system and geometric parameters chosen for this work are explained in detail in this section. Many coordinate system conventions have been used in the Darrieus SB-VAWTs literature according to different criteria. The coordinate system and nomenclature of this work introduce only few changes from the ones used in [4]. These changes were made to facilitate the notation.

The most commonly used coordinate system for SB-VAWTs is defined as follows. The rotation axis of the turbine matches the z -axis of the cylindrical coordinates, thus, the ground is parallel to the xy -plane. Because of the omni-directionality of the SB-VAWTs, no generality is lost if the wind is chosen to blow in the positive direction of the x -axis. In like manner, the direction of rotation of the turbine is chosen to match the increasing sense of the azimuthal angle. An isometric and elevation view of the coordinate system and the turbine are shown in Fig. 3.1. The blades of a SB-VAWT trajectory describe the lateral surface of a circular cylinder, which is represented with segmented lines. The power law of the vertical wind velocity profile, or boundary layer, is also shown.

If a plane parallel to the xy -plane is considered at a height z_p , a two-dimensional analysis of the turbine can be performed. In that case, the velocity profile is uniform because all points in that horizontal plane are at the same height. Thus, the cylindrical coordinate system is reduced to a polar coordinate system. A three-bladed turbine is shown in Fig 3.2. The two unit vectors, \hat{r} and $\hat{\theta}$, of the polar system are also shown.

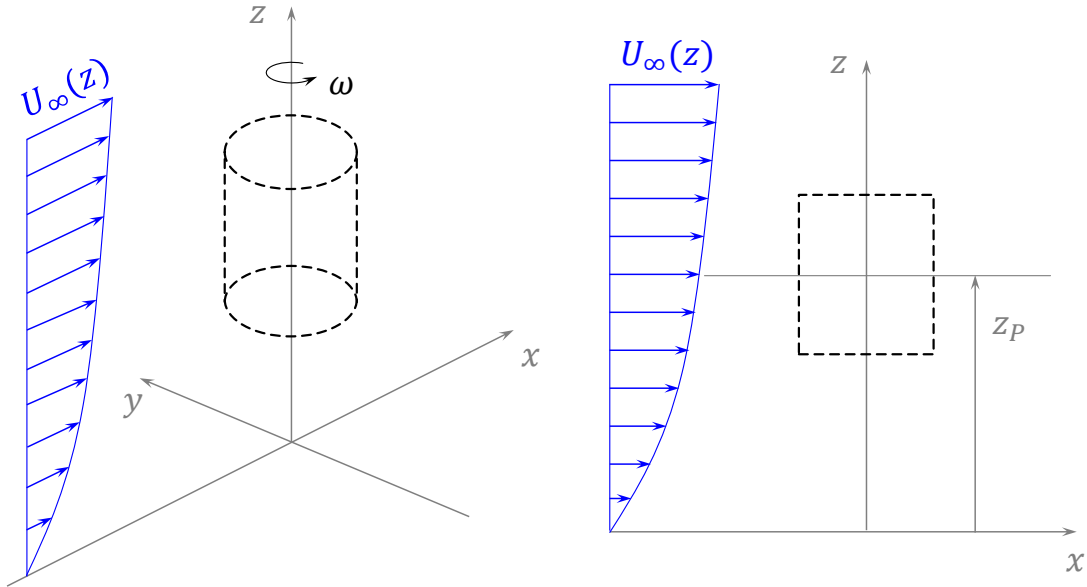


Figure 3.1. General configuration of a SB-VAWT.

The figure shows an isometric view (left) and an elevation view (right) of a SB-VAWT. Source: own elaboration.

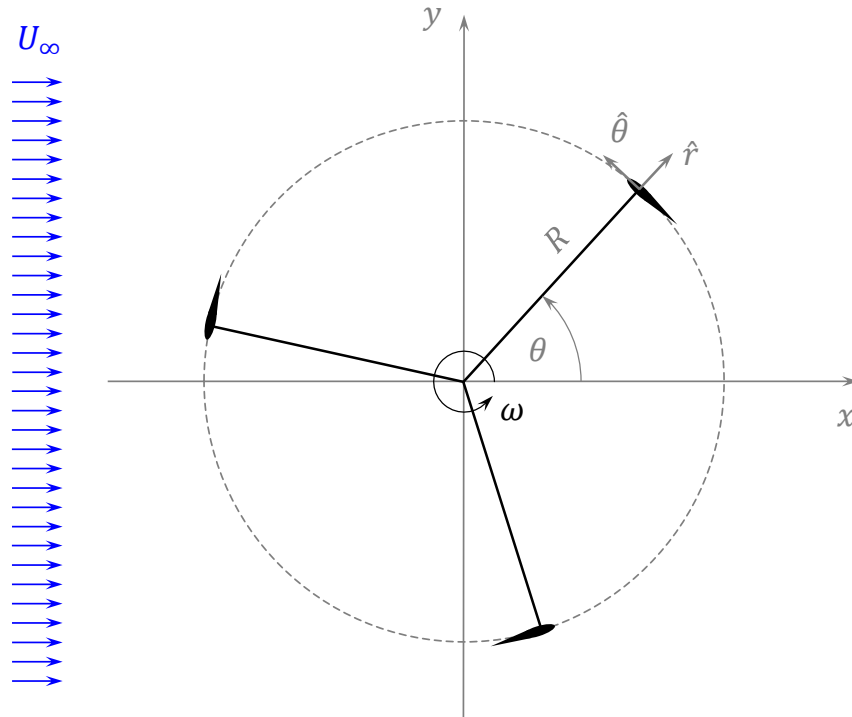


Figure 3.2. Two-dimensional coordinate system definition for a SB-VAWT.

The figure shows the two-dimensional coordinate system definition for a SB-VAWT in a plan view. A three-bladed turbine is shown to illustrate the polar system. Source: own elaboration.

If the turbine has more than one blade, then one blade has to be chosen to match the polar coordinates and the position of the other blades can be expressed as a function of the chosen one with the respective angular offset.

The physics of the SB-VAWTs is quite complicated. One way to help describe the flow field around the turbine is to classify it into four quadrants defined by two divisions: upwind and downwind halves; and considering the wind direction, left and right hand halves. Figure 3.3 shows the four main divisions of the flow field around the turbine. The nature of this type of turbine produces no symmetry in the x -axis nor in the y -axis. However, since the wind is blowing in the x -axis direction, the asymmetry in the y -axis is more pronounced than in the x -axis. This phenomenon is discussed later in this chapter. One disadvantage of the chosen coordinate system is that when the kinematic or dynamic variables such as the angle of attack are plotted as a function of the azimuthal angle, it is easier to read the data if the upwind and downwind halves are easily identified. This drawback is taken into account plotting the $[-90^\circ, 270^\circ]$ range instead of the $[0^\circ, 360^\circ]$ range of the azimuthal angle. Therefore, the ranges $[-90^\circ, 90^\circ]$ and $[90^\circ, 270^\circ]$ correspond to the downstream and upstream sides, respectively.

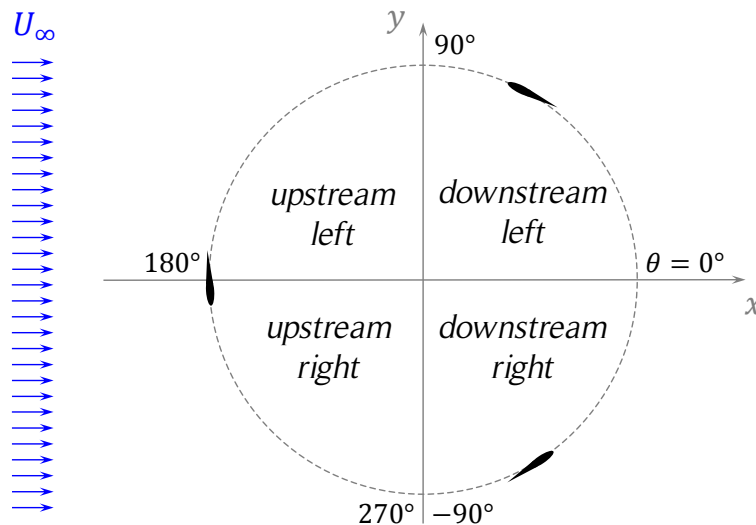


Figure 3.3. Partition of the flow field around the turbine.

The figure shows a partition of the flow field around a three-bladed turbine which helps to describe the behavior of Darrieus SB-VAWTs. Source: own elaboration.

The design of Darrieus SB-VAWTs considers numerous geometric parameters. A list of the main parameters and their description is shown in Table 3.1. Some parameters are shown in Figs. 3.4 and 3.5.

Table 3.1. Geometric parameters of SB-VAWTs.

Symbol	Parameter	Description
D	Turbine diameter	Diameter of the circumference described by the center of pressure of the blades.
R	Turbine radius	Half of the turbine diameter.
H	Turbine height	Total height of the blades. If the turbine has only one vertical tier, the turbine height is equal to the blade length of the blades. If the turbine has many tiers, the turbine height is equal to the sum of the height of all the tiers.
A	Turbine reference area	Cross-sectional area of the turbine. Is calculated as the product between the turbine diameter and height.
H_0	Ground clearance	Vertical distance between the ground and the bottom of the blades.
N	Number of blades	Number of blades of the turbine, usually 2, 3 or 4.
AG	Airfoil geometry	Geometry of the blades. Usually a symmetric airfoil is used, for instance, one of the NACA 4 digit series.
c	Blade chord	Distance between the leading edge and trailing edge of the blades.
σ	Turbine solidity	Non-dimensional parameter that establishes how much of the turbine is covered by blades. Is calculated as $\sigma = Nc/R$.
α_0	Blade fixation angle	Fixation angle of the blades, which is measured from the tangent of the path described by the center of pressure of the blades. Usually set to zero for symmetrical airfoils. For moving blades is considered as the reference angle. The angle is defined as positive if the leading edge moves away from the turbine center.
D_T	Tower diameter	Diameter of the turbine central tower or turbine shaft.
T	Number of vertical tiers	Number of vertical tiers of the turbine.
h	Tier height	Length of the blades of the respective tier. The sum of all tier lengths is equal to the turbine height.
λ	Tier offset angle	Offset angle between tiers. It can be set to zero, which is equivalent to a one tier turbine, or can be set to a non-zero value. Non-zero offset angles can improve the self-starting of the turbine.

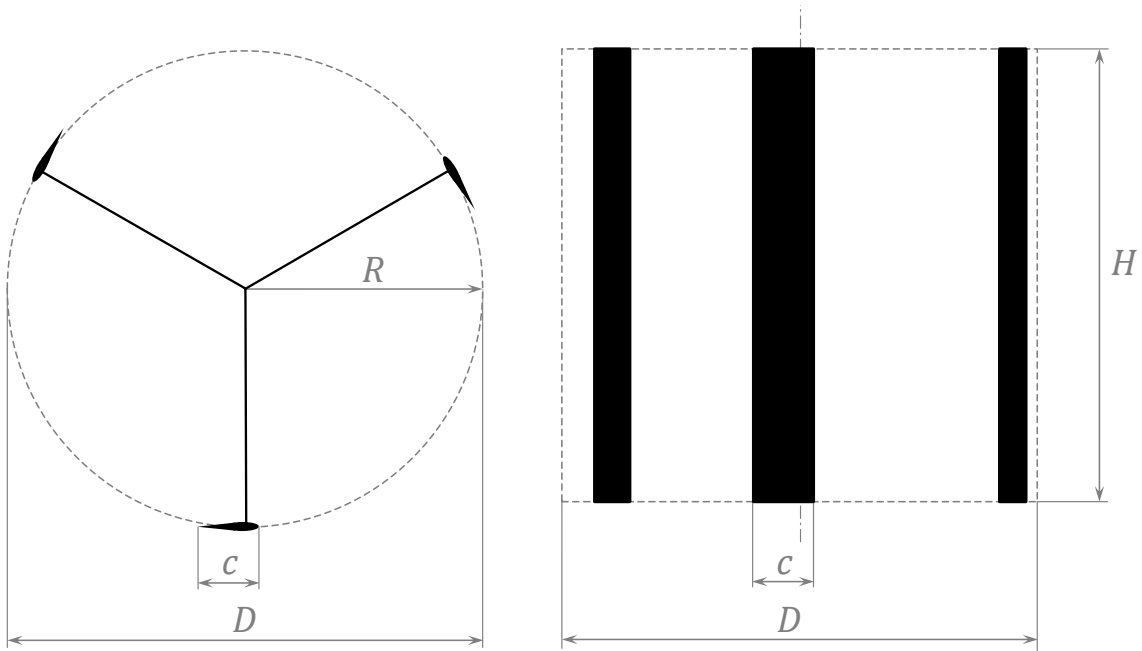


Figure 3.4. Main geometrical parameters of a SB-VAWT.

The figure shows the main geometrical parameters of a three-bladed turbine in plan view (left) and elevation view (right). Source: own elaboration.

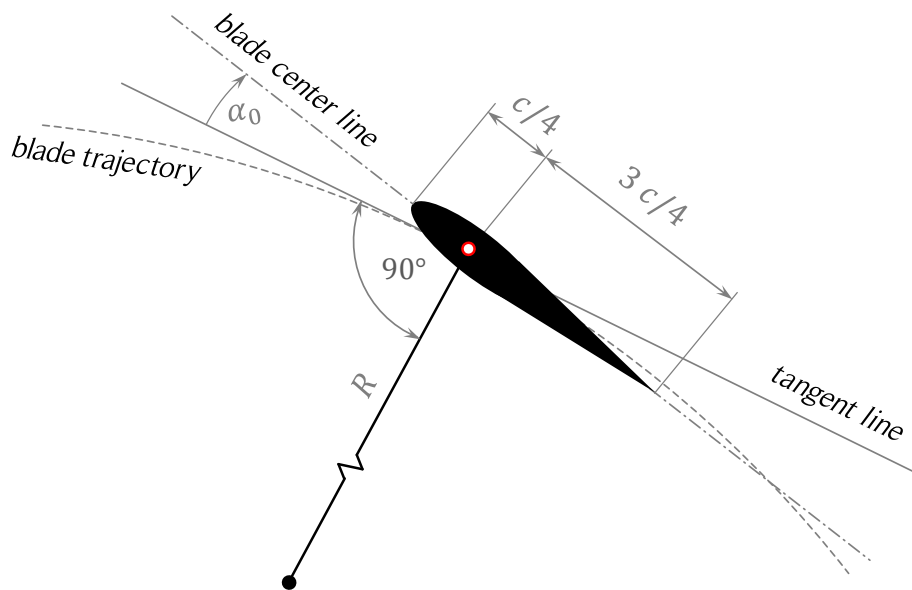


Figure 3.5. Geometrical parameters of a symmetrical blade.

The figure shows the geometrical parameters of a symmetric blade. The aerodynamic center is located at the quarter-chord point for symmetric thin airfoils. A non-zero blade fixation angle is shown. The blade fixation angle of SB-VAWTs with symmetric airfoils is commonly zero. Source: own elaboration.

A SB-VAWT can have more than one tier to improve its self-starting. The idea behind this design is to acquire the good self-starting characteristic of the HB-VAWTs without using more elaborated and more expensive helical blades. The offset angle between tiers should be calculated depending on the number of blades and the number of tiers of the turbine. One possible criterion is to set the offset angle of each tier to obtain equally spaced blades. For example, an offset angle for a two-bladed turbine of two tiers could be 90° . To illustrate this idea, a three-bladed turbine of two tiers with an offset angle of 60° is shown in Fig. 3.6. However, depending on the solidity of the turbine and the desired self-starting characteristic, another number of tiers, blades and offset angle might result in a better design. This topic is beyond the scope of this work and will not be treated in more detail here (see [68] for more details).

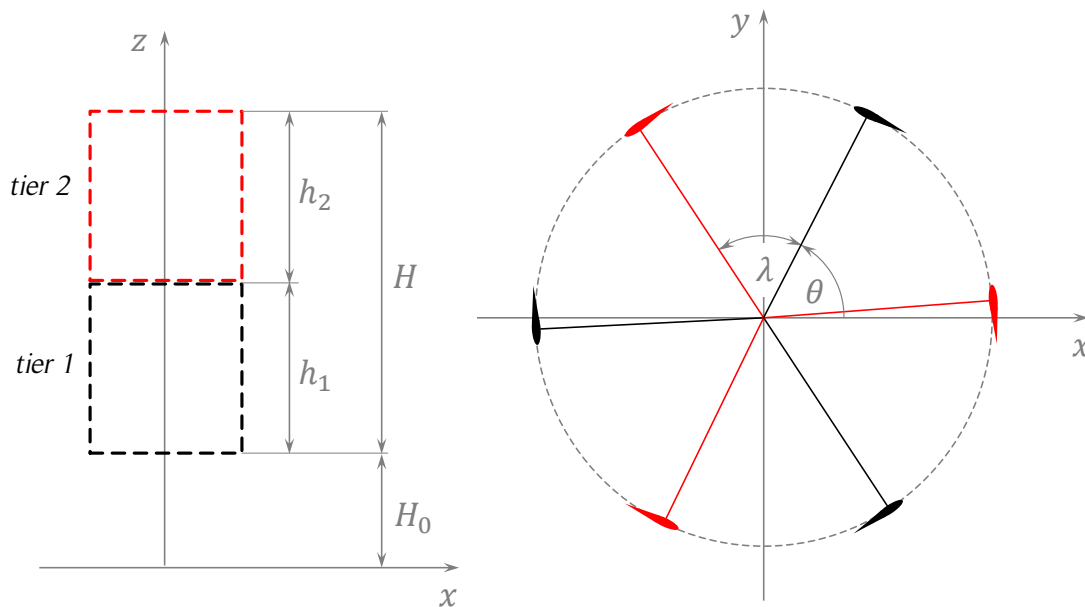


Figure 3.6. Three-bladed VAWT of two tiers.

The figure shows a three-straight-bladed VAWT of two tiers with an offset angle of 60° . Source: own elaboration.

3.2. Kinematics

As a first approach to describe the turbine kinematics and dynamics, a free-stream flow around the turbine is considered in Sections 3.2 and 3.3. The following sections include the flow perturbation that produces some modifications to the results presented in Sections 3.2 and 3.3. The resultant relative air velocity flowing around a rotating blade is the vector summation of the rotational velocity of the blade and the local wind velocity. The velocity of still air relative to a rotating blade is called V , the local wind velocity U ,

and the relative velocity W . The velocity vectors definitions for one blade are presented in Eqs. (3.1) – (3.3), where ω is the rotational speed of the turbine and R is the turbine radius, as shown in Fig. 3.7. The kinematics of the other blades is calculated in the same way but applying the respective azimuthal offset angle. The first blade is denoted B_1 , the second B_2 and so on. For an equispaced three-bladed Darrieus SB-VAWT, the offset between blades is 120° .

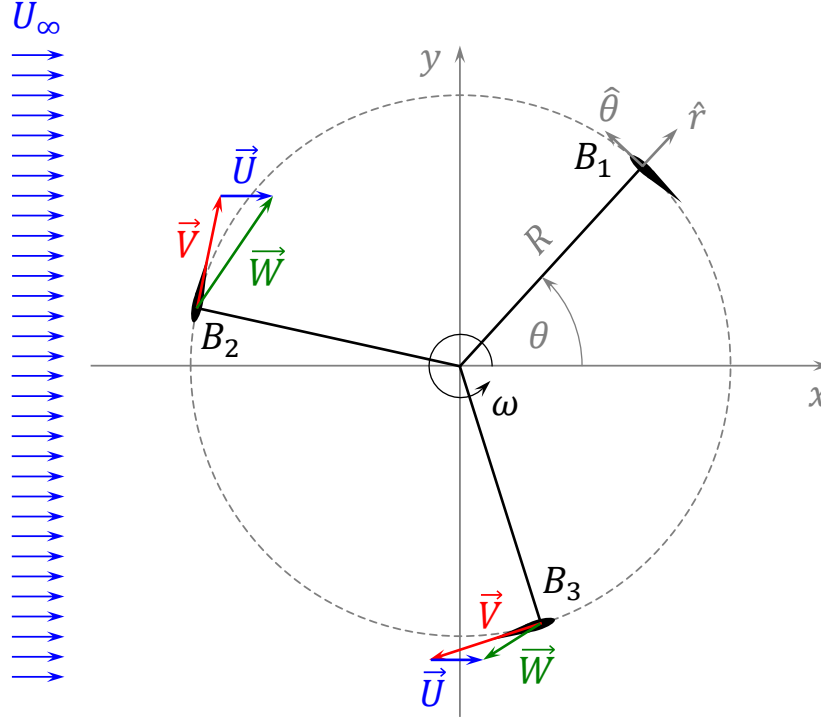


Figure 3.7. Velocity vectors definitions for a SB-VAWT.

The figure shows the coordinate system and the velocity vectors definitions for a Darrieus SB-VAWT. Source: own elaboration.

$$\vec{U} = U\hat{i} \quad (3.1)$$

$$\vec{V} = -\omega R\hat{\theta} \quad (3.2)$$

$$\vec{W} = \vec{U} + \vec{V} \quad (3.3)$$

Since in this section flow without interference is assumed, the local wind velocity does not vary with the azimuthal position, hence, $U = U_\infty$. A more general analysis should consider that the local wind velocity varies with the azimuthal position and can have non-zero components in all three dimensions, as shown in Eq. (3.4).

$$\vec{U} = U_x(x, y, z)\hat{i} + U_y(x, y, z)\hat{j} + U_z(x, y, z)\hat{k} \quad (3.4)$$

The turbine rotational speed, ω , is usually considered constant, but in general can be time dependent, $\omega = \omega(t)$. For one revolution, it is easier to express the rotational speed as a function of the azimuthal position of one blade, $\omega = \omega(\theta)$. For a constant rotational speed (or time-averaged), the tip-speed ratio is defined according to Eq. (3.5). Note that the *TSR* definition is with the free-stream velocity, U_∞ , and not with the disturbed velocity, U . The vertical velocity profile (or boundary layer) causes a vertical variation of the *TSR* (variation of U_∞). Commonly, the *TSR* at the equator of the turbine is chosen to describe the behavior of the entire turbine. If the horizontal free-stream velocity profile is not uniform, an average free-stream velocity can be calculated to determine the *TSR* at the respective height.

$$TSR = \frac{\omega R}{U_\infty} \quad (3.5)$$

Another relevant variable of the turbine kinematics is the angle of attack, α , which sometimes is also represented by the initials AoA. It is defined as the angle between the relative wind velocity, W , and the blade chord line. The angle of attack is calculated as the summation of the blade angle of attack, α_B , and the blade fixation angle, α_0 , as shown in Eq. (3.6). The blade angle of attack is measured from the relative velocity vector to the blade trajectory tangent line, as shown in Fig. 3.8. Usually, symmetric airfoils have $\alpha_0 = 0^\circ$, thus $\alpha = \alpha_B$. Oscillating blades have a time dependent blade fixation angle, $\alpha_0 = \alpha_0(t)$. Passive and active pitch control of blades can improve the power performance of Darrieus SB-VAWTs, but it requires a more complex design, which is discussed later in this chapter.

$$\alpha = \alpha_0 + \alpha_B \quad (3.6)$$

Based on Figs. 3.7 and 3.8, a vector analysis can be performed to obtain an expression of the relative velocity, W , and the blade angle of attack, α_B , as a function of the previously defined variables. The expressions are presented in Eqs. (3.7) and (3.8), respectively.

$$W = \|\vec{U} + \vec{V}\| \quad (3.7)$$

$$\alpha_B = \frac{\vec{W} \cdot \hat{r}}{\|\vec{W} \cdot \hat{r}\|} \arccos\left(\frac{-\vec{W} \cdot \hat{\theta}}{\|\vec{W}\|}\right) \quad (3.8)$$

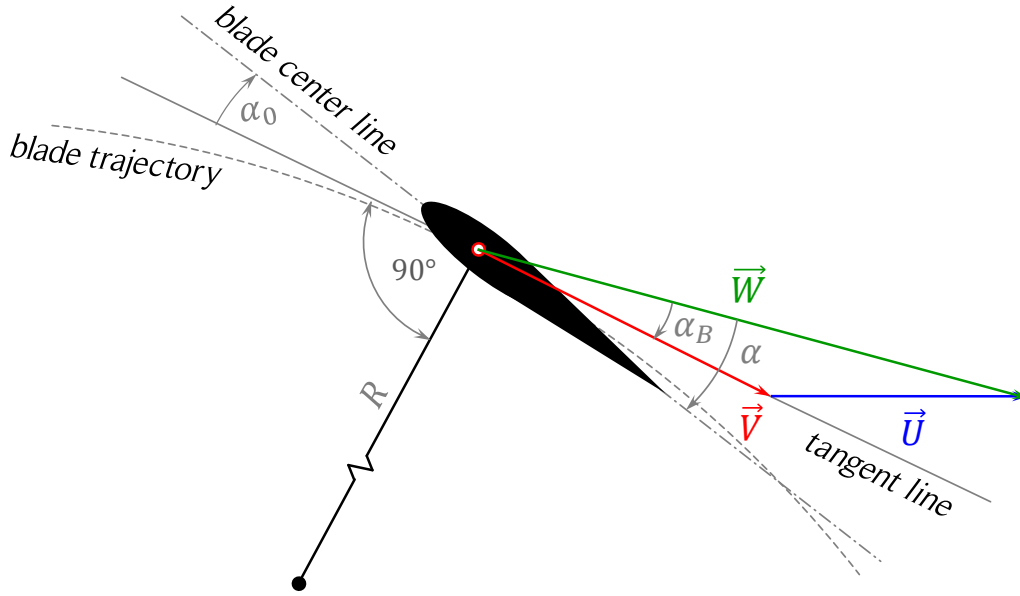


Figure 3.8. Angle of attack definitions for a SB-VAWT.

The figure shows the angle of attack definitions for a Darrieus SB-VAWT. Source: own elaboration.

The first term of the expression in Eq. (3.8) determines the sign of the angle of attack. To match the typical airfoil theory notation, the blade angle of attack is defined as positive if the dot product between the relative velocity and the radial unitary vector is positive. When $TSR = 1$ and $\theta = 270^\circ$, the blade rotational velocity has the same magnitude but opposite sign of the local wind velocity; therefore, the relative velocity is zero. In that case the expression for the blade angle of attack is undetermined. However, when the relative wind is $W = 0$, the aerodynamic forces will also be zero; hence, there is no need to calculate the blade angle of attack. An alternative and simpler way to calculate the relative velocity and the blade angle of attack is presented in Fig. 3.9 and Eqs. (3.9) and (3.10).

$$W = [(V + U \sin \theta)^2 + (U \cos \theta)^2]^{1/2} \quad (3.9)$$

$$\alpha_B = \arctan\left(\frac{U \cos \theta}{V + U \sin \theta}\right) \quad (3.10)$$

The previous note about the case $TSR = 1$ is still valid for these expressions. When $V + U \sin \theta = 0$, Eq. (3.9) is also undetermined. For $TSR < 1$ the flow can be reversed at $\theta = 270^\circ$, thus, the blade angle of attack $\alpha_B = 180^\circ$ can be reached. The expression of Eq. (3.10), which is commonly the expression for the calculation of the angle of attack

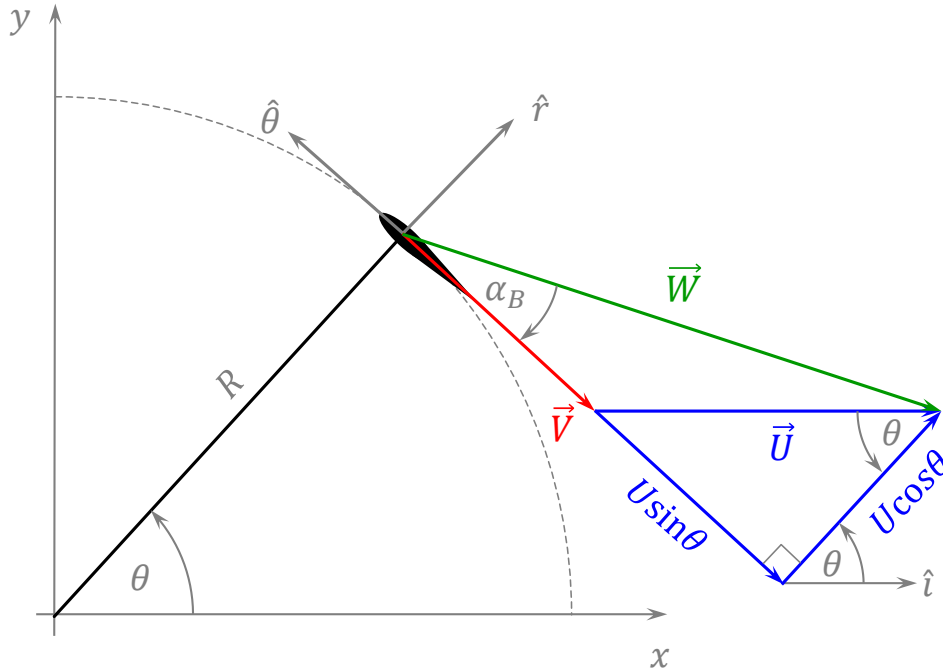


Figure 3.9. Alternative definition of the turbine kinematic parameters.

The figure shows an alternative definition of the turbine kinematic parameters of a SB-VAWT for a zero blade fixation angle. Source: own elaboration.

(see [4]), is not able to capture this phenomenon directly, because the range of the arctan function is $[-90^\circ, 90^\circ]$. To avoid domain divisions of Eq. (3.10), a different expression based on Eq. (3.8) is presented in Eq. (3.11).

$$\alpha_B = \text{sign}(\cos \theta) \arccos\left(\frac{V + U \sin \theta}{W}\right) \quad (3.11)$$

A comparison of the behavior of Eqs. (3.10) and (3.11) for $U = 10 \text{ m/s}$, $R = 3 \text{ m}$, $TSR = 0.25$ and $TSR = 0.75$ is presented in Fig. 3.10. It can be seen that both expressions produce the same shape, but Eq. (3.10) has an offset due to the range of the arctan function. Note that the angle at which the offset of $\pm 180^\circ$ depends on the angle at which the limits of the range $[-90^\circ, 90^\circ]$ are reached; therefore, depends on the TSR , which is an inconvenience for using Eq. (3.10). Usually, Darrieus SB-VAWTs operate at tip-speed ratios larger than $TSR = 1$ or even $TSR = 2$; thus, this might be not considered a relevant problem. However, the angle of attack is important to determine the dynamics of the turbine during its start-up (low TSR). Additionally, due to possible large variations of the wind magnitude and direction in time, the mathematical expression of the blade angle of attack of Eq. (3.11) should be used instead of Eq. (3.10).

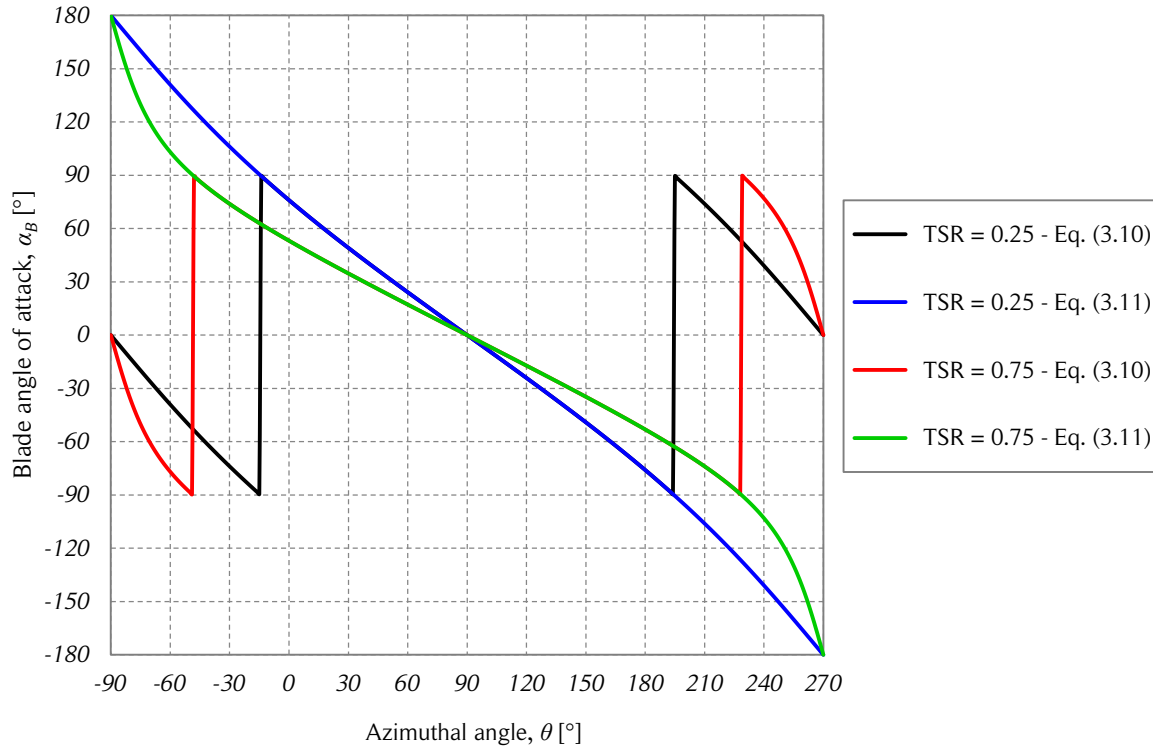


Figure 3.10. Angle of attack calculation comparison for low tip-speed ratios.

The figure shows the comparison of the calculation of the blade angle of attack as a function of the azimuthal angle of a Darrieus SB-VAWT blade for two low tip-speed ratios using two different expressions (freestream flow case). Source: own elaboration.

To illustrate the behavior of the relative wind velocity and the angle of attack of a Darrieus SB-VAWT, Eqs. (3.9) and (3.11) for $U_\infty = 10 \text{ m/s}$ and $R = 3 \text{ m}$ are plotted in Figs. 3.11 and 3.12, respectively. Note that under the assumption $U = U_\infty$, the tangential velocity of the blade can be expressed only as a function of the tip-speed ratio and the free stream velocity: $V = \omega R = TSR U_\infty$.

For a rotating blade of a Darrieus SB-VAWT, the velocity triangles vary along the chord due to the change of magnitude of the radius used to calculate the rotational speed at each location of the airfoil. To illustrate this phenomenon, the velocity triangles at the leading and trailing edges of a blade are presented in Fig 3.13. According to [85], a rotating symmetric airfoil behaves like a cambered airfoil in a rectilinear flow with a non-zero virtual angle of incidence. The virtual camber causes an upward shift of the lift curve and introduces an aerodynamic moment. The virtual incidence causes the lift curve to shift to the left. Combining these two effects, the angle of attack for zero lift should no longer be $\alpha = 0^\circ$ for the symmetric airfoil. This phenomenon depends on the blade chord

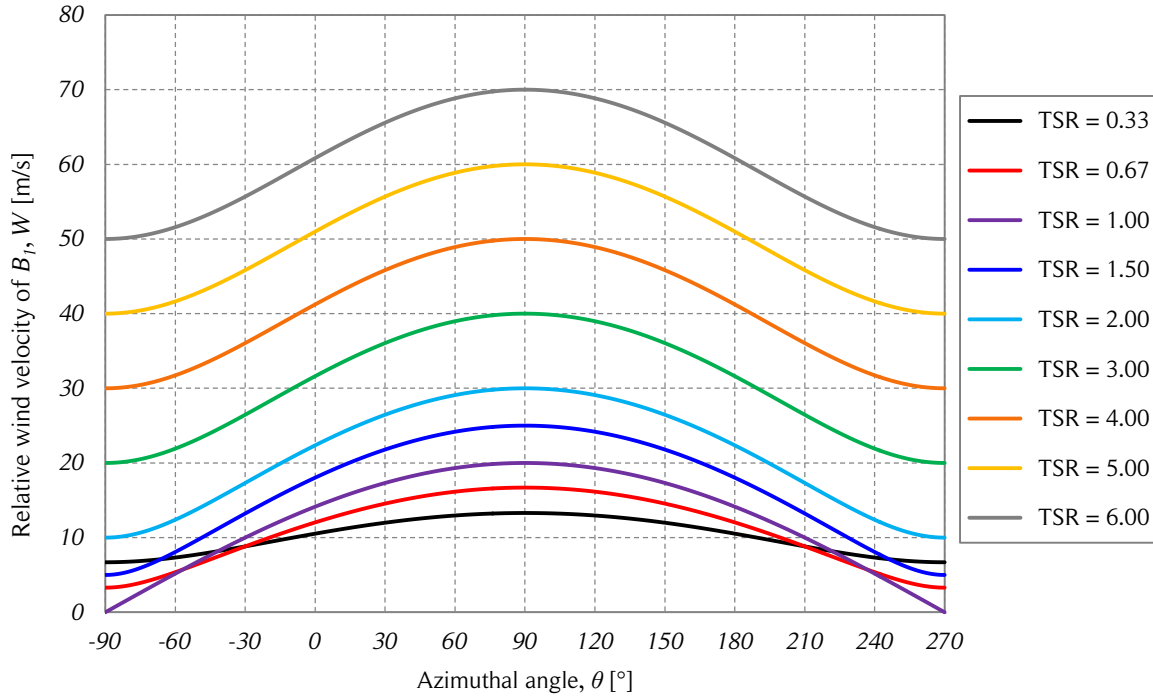


Figure 3.11. Relative wind velocity vs. azimuthal angle.

The figure shows the relative wind velocity of the blade B_1 as a function of the azimuthal angle for the case of freestream flow. Source: own elaboration.

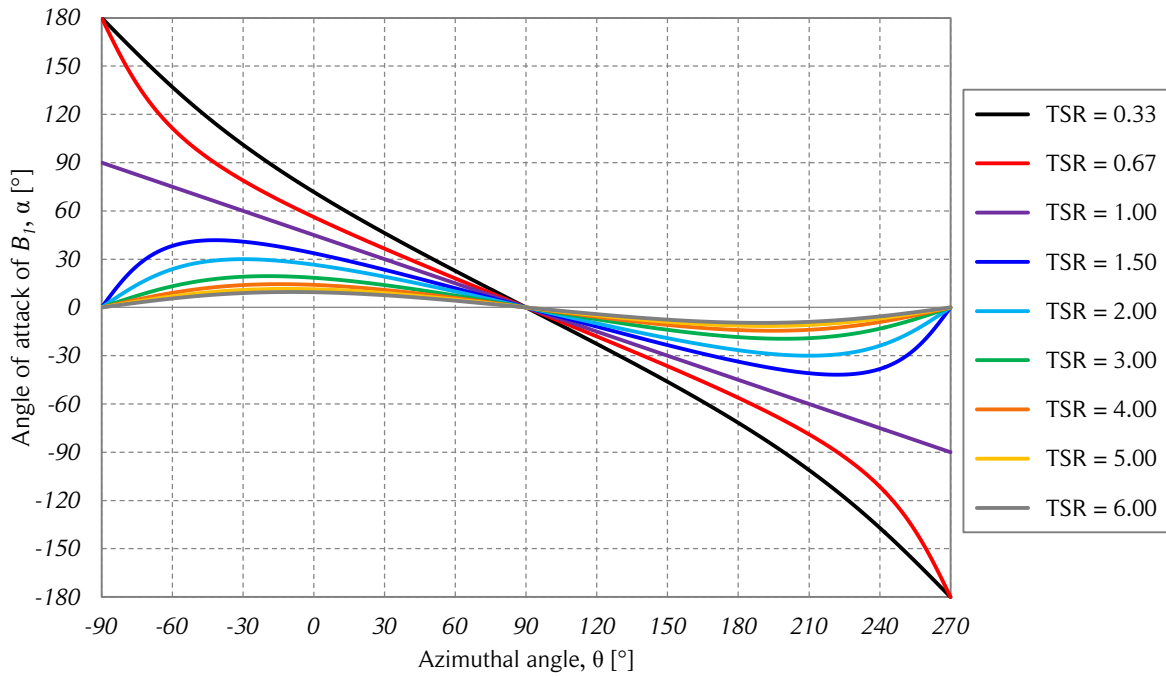


Figure 3.12. Angle of attack vs. azimuthal angle.

The figure shows the angle of attack of the blade B_1 as a function of the azimuthal angle for the case of freestream flow. Source: own elaboration.

to turbine radius ratio, c/R . If this ratio becomes larger, the influence of the curvilinear flow increases as well. One way to quantify the effect of this phenomenon is presented below. Two auxiliary variables are defined to simplify the calculations: β , the angular position from the point of interest located on the chord and measured from the azimuthal position of the quarter-chord position of the blade θ , and x_c , the distance between the quarter-chord and the point of interest, which is located on the chord line. Therefore, the relations presented in Eqs. (3.12) – (3.14) are valid. Note that β is negative when $x_c < 0$.

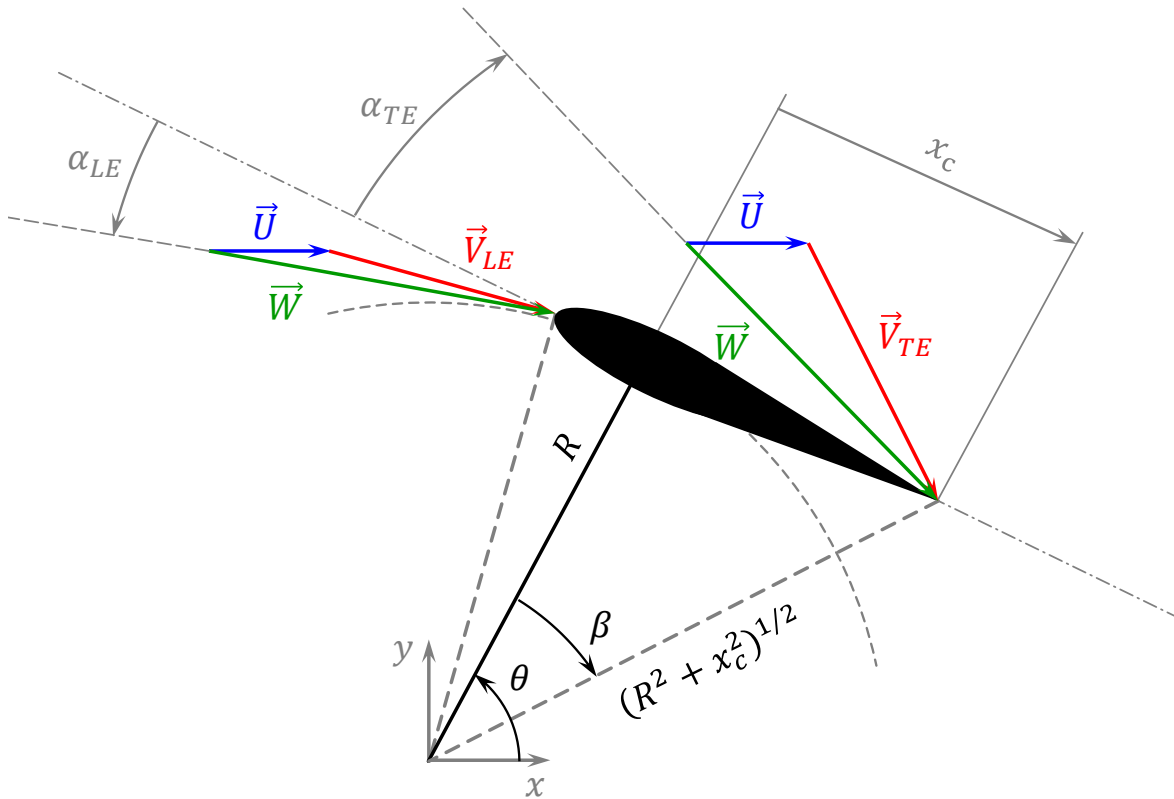


Figure 3.13. Curvilinear flow effects on a rotating blade.

The figure shows the curvilinear flow phenomenon present on a rotating blade of a Darrieus SB-VAWT. The triangles of velocities at the leading edge (LE) and trailing edge (TE) are shown. A large blade chord and a small turbine radius are shown to exaggerate the effect of the curvilinear flow. Source: own elaboration.

$$-\frac{1}{4}c \leq x_c \leq \frac{3}{4}c \quad (3.12)$$

$$\beta = \arctan\left(\frac{x_c}{R}\right) \quad (3.13)$$

$$V = \omega(R^2 + x_c^2)^{1/2} \quad (3.14)$$

Since the relative velocity, W , and blade angle of attack, α_B , are not linear functions of the turbine geometric and operational parameters, the expressions of Eqs. (3.15) and (3.16) have to be calculated for each TSR for a given turbine radius and blade chord.

$$W(\theta, x_c) = \left\{ [\omega(R^2 + x_c^2)^{1/2} + U \sin(\theta - \beta)]^2 + [U \cos(\theta - \beta)]^2 \right\}^{1/2} \quad (3.15)$$

$$\alpha_B(\theta, x_c) = \text{sign}[\cos(\theta - \beta)] \arccos\left(\frac{\omega(R^2 + x_c^2)^{1/2} + U \sin(\theta - \beta)}{W(\theta, x_c)}\right) \quad (3.16)$$

Substituting Eq. (3.13) in Eqs. (3.15) and (3.16) and calculating the average over the blade chord of the relative wind velocity and blade angle of attack yields Eqs. (3.17) and (3.18).

$$\bar{W}(\theta) = \frac{1}{c} \int_{-c/4}^{3c/4} W(\theta, x_c) dx_c \quad (3.17)$$

$$\bar{\alpha}_B(\theta) = \frac{1}{c} \int_{-c/4}^{3c/4} \alpha_B(\theta, x_c) dx_c \quad (3.18)$$

Since empirical aerodynamic coefficients are measured under rectilinear flow, average results from the curvilinear flow of Eqs. (3.17) and (3.18) should not be utilized directly to obtain the tabulated aerodynamic coefficients if no experiments support them. In fact, according to [7], for VAWT blades in attached flows, the angle of attack should be calculated at the 3/4-chord instead of the quarter-chord position to use the aerodynamic coefficients of the empirical data. At the 3/4-chord position $x_c = c/2$ and $\beta = \arctan[c/(2R)]$.

Typically, small-scale Darrieus SB-VAWTs have 2 or 3 blades and a rotor solidity, σ , below 0.25. To illustrate the effect of the flow curvature on the calculation of the angle of attack, a comparison between Eqs. (3.11), (3.16) and (3.18) is presented in Fig. 3.14. Note that Eq. (3.16) is used with the values at the 3/4-chord position: $x_c = c/2$ and $\beta = \arctan[c/(2R)]$. The geometric parameters were chosen as follows: $N = 3$, $c = 0.25$ and $R = 3$ m; thus, $\sigma = 0.25$ and $c/R = 0.833$. A free-stream velocity of $U_\infty = 10$ m/s and a $TSR = 4$ were used. The three curves are quite similar, but Eqs. (3.16) and (3.18) present a small shift to the right from Eq. (3.11). This phenomenon

is repeated for other values of the TSR . It can be concluded that for low blade chord to turbine radius ratio, c/R , the curvilinear flow does not have a large impact in the calculation of the angle of attack.

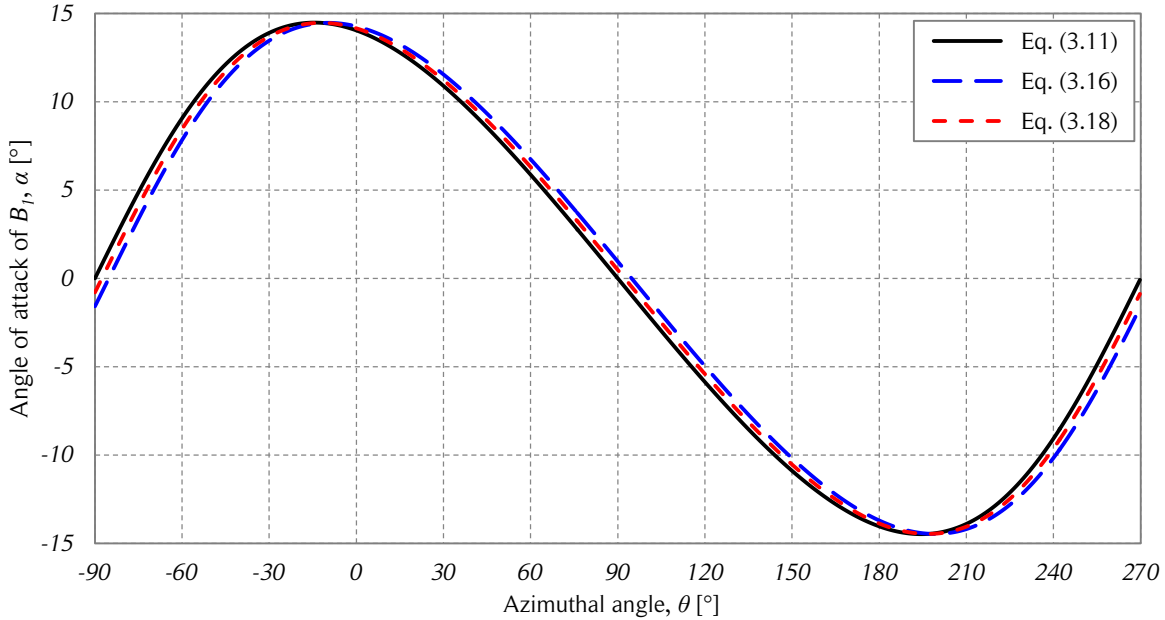


Figure 3.14. Curvilinear flow influence on the angle of attack.

The figure shows the angle of attack as a function of the azimuthal angle at $TSR = 4$ calculated by three different expressions for the case of freestream flow. The first one, Eq. (3.11), does not take into account the curvilinear flow. The other two expressions, Eq. (3.16) and (3.18), take into account the curvilinear flow, which causes a small shift to the right. Source: own elaboration.

Usually, the Reynolds number is defined in two different ways for Darrieus SB-VAWTs. The first one is called turbine or rotor Reynolds number Re_T and is calculated using the freestream velocity, U_∞ , and the turbine diameter, D , as shown in Eq. (3.19), where ρ is the air density, μ is the dynamic viscosity and ν is the kinematic viscosity. This definition is the same as the one used for a solid circular cylinder. The TSR gives additional information that relates the rotational velocity, ωR , of the turbine with the free-stream velocity, U_∞ . In general, the turbine Reynolds definition does not give much information about the physical phenomena present in the operation of Darrieus SB-VAWTs. Though, in the cases of high TSR , this definition might be useful because the turbine resembles a rotating solid circular cylinder.

$$Re_T = \frac{\rho D U_\infty}{\mu} = \frac{D U_\infty}{\nu} \quad (3.19)$$

The second definition is called blade Reynolds number, or just Reynolds number, Re , and is calculated using the instantaneous relative velocity, W , and the blade chord, c , as shown in Eq. (3.20). This definition represents the phenomena occurring near the blade and is the one used to calculate the aerodynamic coefficients. To illustrate the Reynolds number behavior of a Darrieus SB-VAWT, the Reynolds number is plotted as a function of the azimuthal angle for different TSR in Fig. 3.15 with $R = 3\text{ m}$, $c = 0.25$, $U_\infty = 10\text{ m/s}$, $\nu = 1.46 \times 10^{-5}\text{ m}^2/\text{s}$.

$$Re = \frac{\rho c W}{\mu} = \frac{c W}{\nu} \quad (3.20)$$

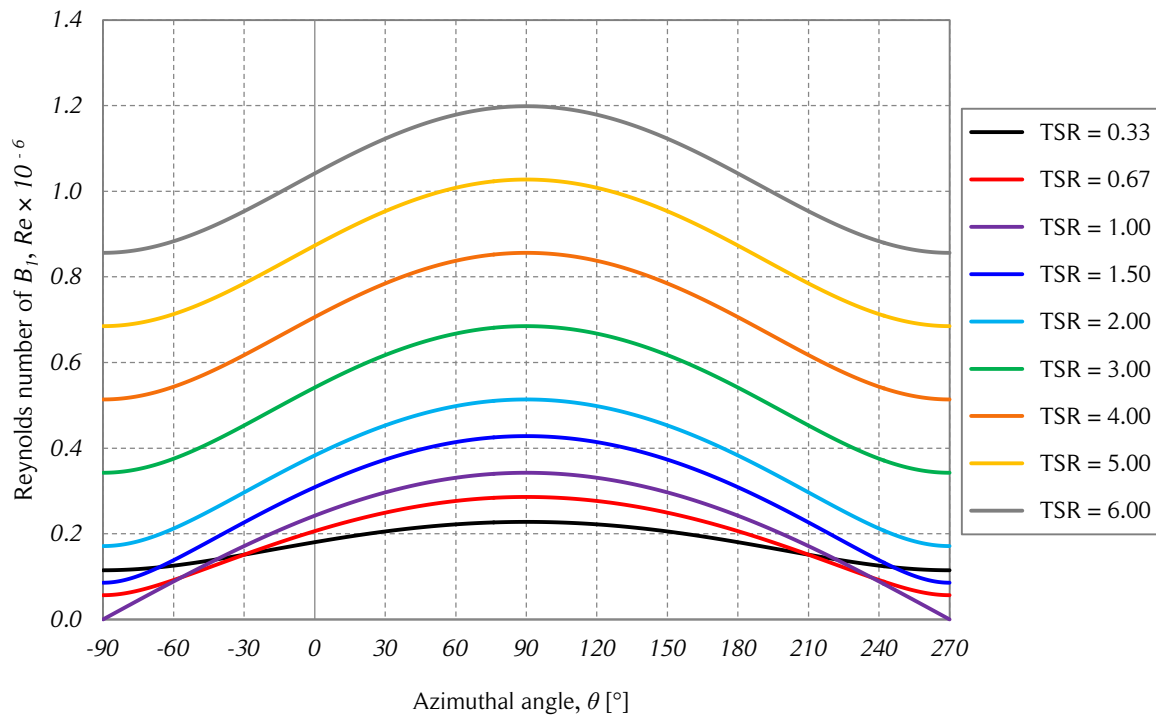


Figure 3.15. Reynolds number vs. azimuthal angle.

The figure shows the Reynolds number of the blade B_1 as a function of the azimuthal angle for the case of freestream flow. Source: own elaboration.

3.3. Dynamics

According to airfoil theory, for a subsonic flow, once the Reynolds number and the angle of attack are determined, the aerodynamic forces acting on the blade can be calculated from empirical aerodynamic data. The aerodynamic center of thin symmetric airfoils is located at the quarter chord. Hence, the lift and drag forces are assumed to act at that

position, as shown in Fig. 3.16. Note that there is no blade fixation angle; therefore, the angle of attack is assumed to be equal to the blade angle of attack. The drag is parallel to the relative wind velocity and the lift is perpendicular. The forces are calculated in two dimensions, which means, that the reference area is determined by the chord and a unitary length of the blade, as shown in Eqs. (3.21) and (3.22). Two possible decompositions of the resulting aerodynamic force are presented in Eq. (3.23).

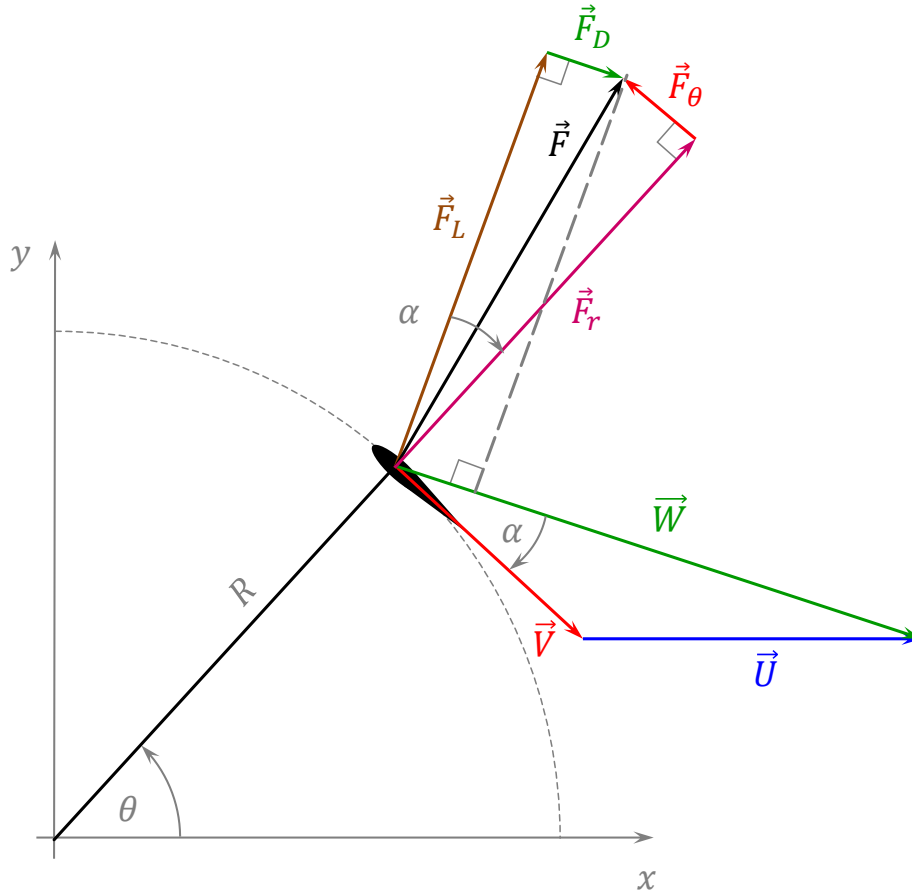


Figure 3.16. Definition of the turbine dynamic parameters.

The figure shows the definition of the turbine dynamic parameters of a Darrieus SB-VAWT for a zero blade fixation angle. Source: own elaboration.

$$F_L = \frac{1}{2} \rho c W^2 c_L(\alpha, Re) \quad (3.21)$$

$$F_D = \frac{1}{2} \rho c W^2 c_D(\alpha, Re) \quad (3.22)$$

$$\vec{F} = \vec{F}_L + \vec{F}_D = \vec{F}_\theta + \vec{F}_r \quad (3.23)$$

The vector form of the lift and drag can be expressed as shown in Eq. (3.24) and (3.25).

$$\vec{F}_L = \frac{1}{2} \rho c h c_L(\alpha, Re) \|\vec{W}\| (\hat{k} \times \vec{W}) \quad (3.24)$$

$$\vec{F}_D = \frac{1}{2} \rho c h c_D(\alpha, Re) \|\vec{W}\| \vec{W} \quad (3.25)$$

The angle of attack enables calculation of the tangential, \vec{F}_θ , and radial, \vec{F}_r , components of the resulting aerodynamic force, \vec{F} , as shown in Eq. (3.26) and (3.27). The behavior of the velocity triangles and aerodynamic forces at different azimuthal positions are presented in Fig. 3.17. Note that the radial force is larger than the tangential force. This is the typical behavior of the aerodynamic force of SB-VAWTs.

$$\vec{F}_\theta = (\vec{F} \cdot \hat{\theta}) \hat{\theta} = (F_L \sin \alpha - F_D \cos \alpha) \hat{\theta} \quad (3.26)$$

$$\vec{F}_r = (\vec{F} \cdot \hat{r}) \hat{r} = (F_L \cos \alpha + F_D \sin \alpha) \hat{r} \quad (3.27)$$

In like manner, the tangential and radial coefficients are defined from the lift and drag coefficients, as shown in Eqs. (3.28) and (3.29).

$$c_\theta = c_L \sin \alpha - c_D \cos \alpha \quad (3.28)$$

$$c_r = c_L \cos \alpha + c_D \sin \alpha \quad (3.29)$$

Two useful dimensionless parameters commonly used to compare Darrieus SB-VAWTs is the tangential and radial force coefficients, f_θ and f_r , respectively. These parameters are defined in Eqs. (3.30) and (3.31). The behavior of these two parameters for the free-stream flow case is presented in Figs. 3.18 and 3.19 using the same local air conditions and turbine geometric parameters as the ones previously used in this chapter. When flow interference is considered, the symmetry about $\theta = 90^\circ$ of Figs. 3.18 and 3.19 is lost. This is addressed in Chapter 4.

$$f_\theta = \frac{F_\theta}{\frac{1}{2} \rho D U_\infty^2} = c_\theta \frac{c}{D} \left(\frac{W}{U_\infty} \right)^2 \quad (3.30)$$

$$f_r = \frac{F_r}{\frac{1}{2} \rho D U_\infty^2} = c_r \frac{c}{D} \left(\frac{W}{U_\infty} \right)^2 \quad (3.31)$$

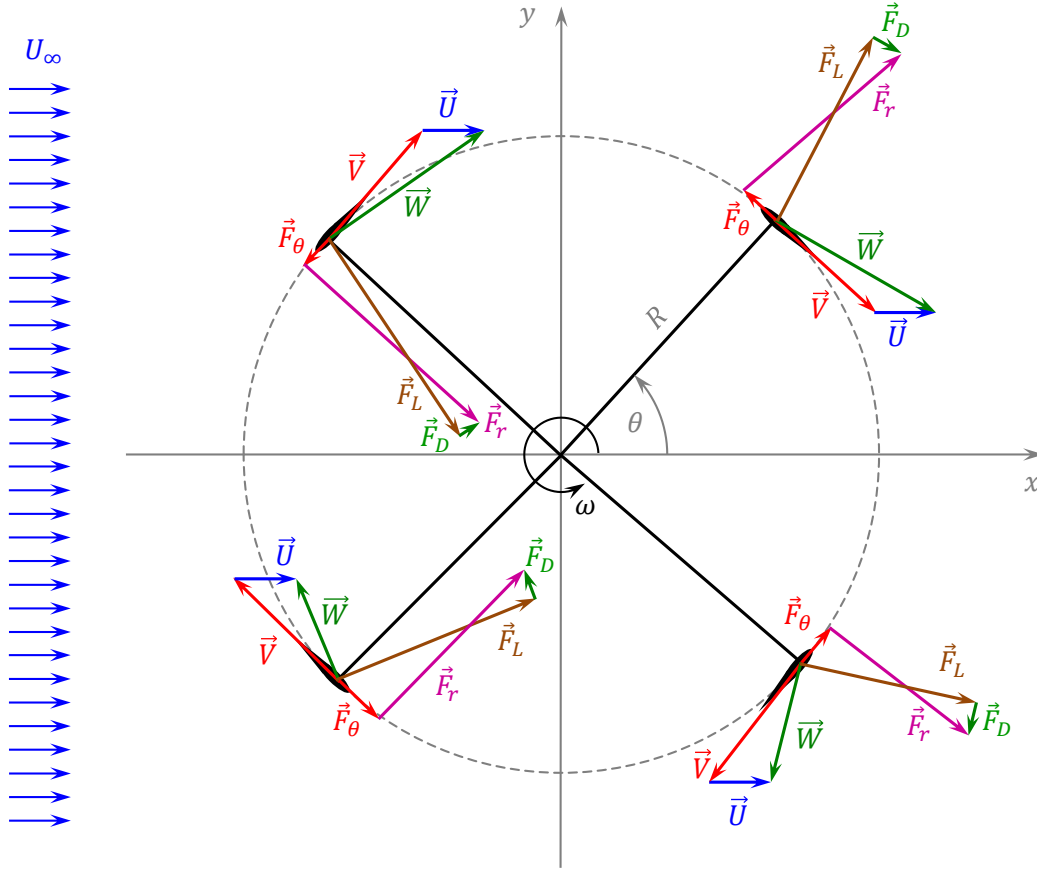


Figure 3.17. Triangles of velocity and forces for different blade positions.

The figure shows the triangles of velocity and the aerodynamic forces acting on the blades of a SB-VAWT for different azimuthal positions for the case of freestream flow. Source: own elaboration.

When coefficients aligned in fixed directions are required, another two other parameters are typically used in the modeling of Darrieus SB-VAWTs: the x and y components of the aerodynamical force, which are calculated according to Eqs. (3.32) and (3.33) and Fig.3.20. The inverse transformation is shown in Eqs. (3.34) and (3.35). The force coefficient in the x direction is called streamwise force coefficient and the one in the y direction is called cross-stream force coefficient.

$$f_x = f_r \cos \theta - f_\theta \sin \theta \quad (3.32)$$

$$f_y = f_r \sin \theta + f_\theta \cos \theta \quad (3.33)$$

$$f_\theta = f_y \cos \theta - f_x \sin \theta \quad (3.34)$$

$$f_r = f_x \cos \theta + f_y \sin \theta \quad (3.35)$$

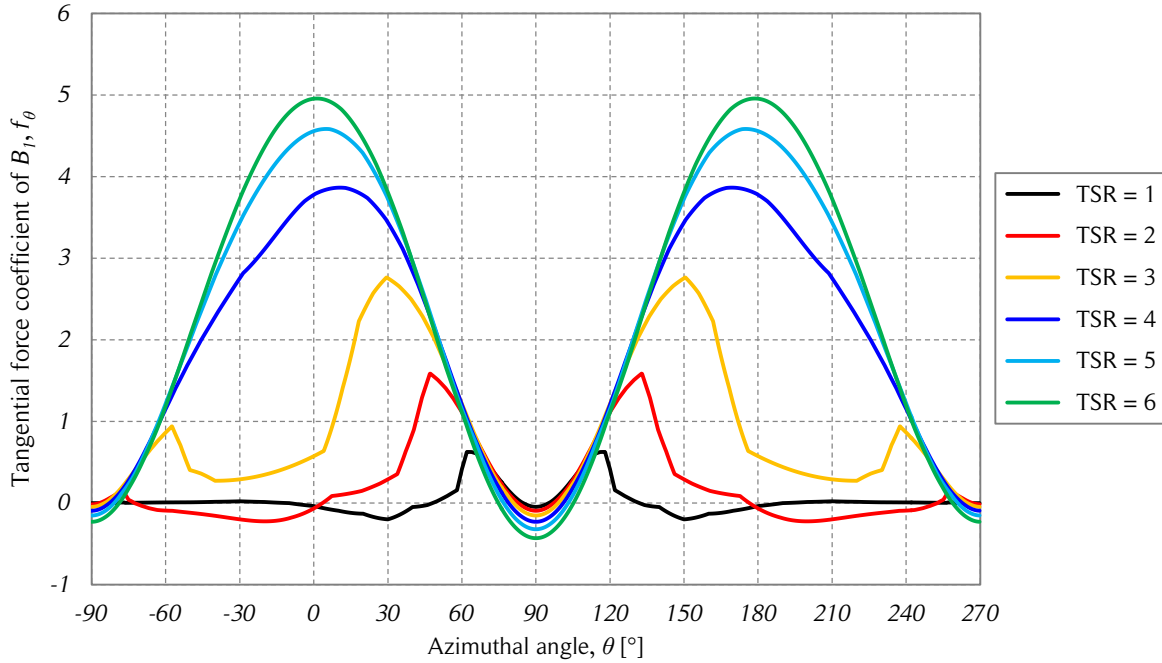


Figure 3.18. Blade tangential force coefficient vs. azimuthal angle.

The figure shows the tangential force coefficient of the blade B_1 as a function of the azimuthal angle for the freestream flow case. Source: own elaboration.

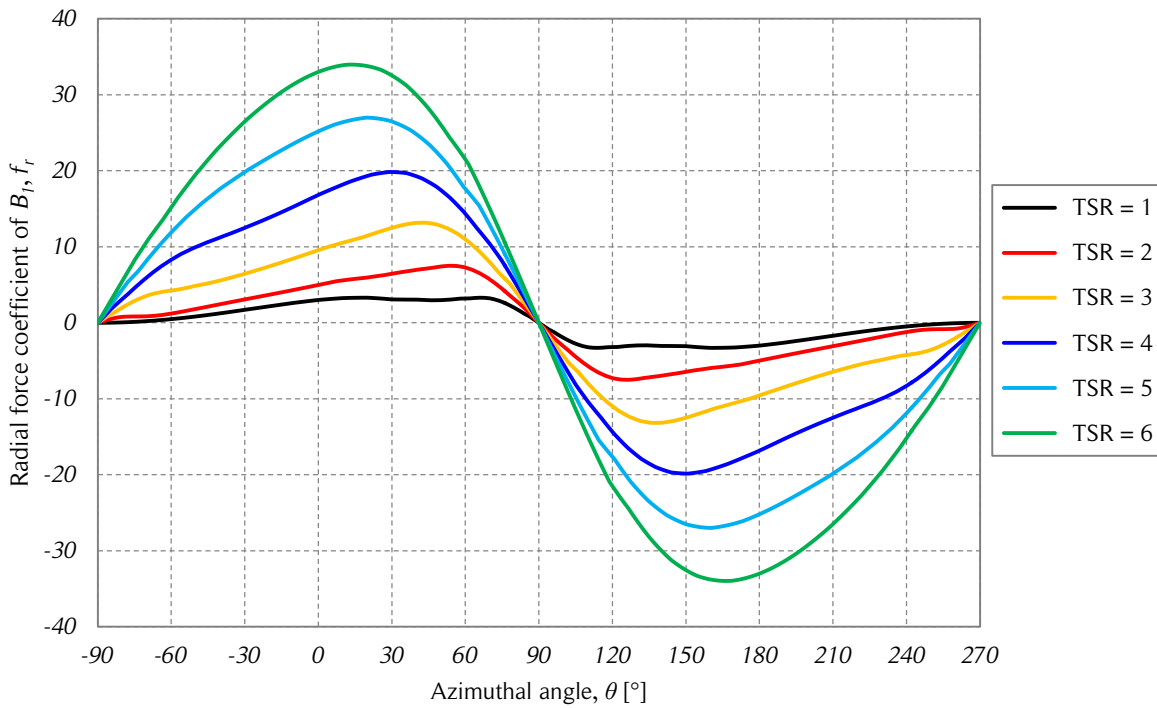


Figure 3.19. Blade radial force coefficient vs. azimuthal angle.

The figure shows the radial force coefficient of the blade B_1 as a function of the azimuthal angle for the freestream flow case. Source: own elaboration.

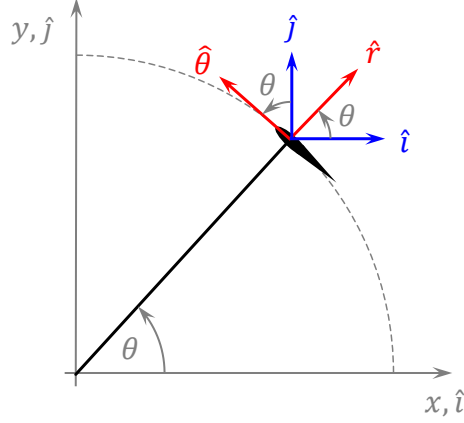


Figure 3.20. Geometric relations of polar and Cartesian coordinates.

The figure shows the polar and Cartesian coordinates geometric relations which are useful to transform the streamwise and cross-stream forces into tangential and radial forces. Source: own elaboration.

The torque produced by a blade on the turbine shaft, $\vec{\tau}_B$, can be calculated from the tangential force, \vec{F}_θ , and the moment acting on the blade, \vec{M} , as shown in Eq. (3.36). The moment is often neglected when its magnitude is considerably smaller than the product of the tangential force and the turbine radius.

$$\vec{\tau}_B = \vec{R} \times \vec{F}_\theta + \vec{M} \quad (3.36)$$

The instantaneous power contribution of each blade to the turbine shaft is calculated by the dot product of the rotational speed of the turbine and the torque, as shown in Eq. (3.37). The instantaneous turbine power is calculated by the sum of all motor torques generated by the N blades and the aerodynamic losses produced by the blade struts and other elements, as shown in Eq. (3.38).

$$\dot{W}_B = \vec{\omega} \cdot \vec{\tau}_B = \omega(RF_\theta + M) \quad (3.37)$$

$$\dot{W} = \sum_{i=1}^N \dot{W}_{B_i} - \sum \text{losses} \quad (3.38)$$

3.4. One-dimensional momentum theory for an ideal wind turbine

The purpose of a wind turbine is to produce mechanical power on a shaft. The wind blowing around a turbine passes a portion of its momentum to the blades, which

produces torque on the turbine shaft. This torque and the rotational speed provide mechanical power to the shaft.

The one-dimensional momentum theory is based on the conservation of linear momentum. This theory was developed over 100 years ago to predict the performance of ship propellers [44]. The analysis considers a control volume coincident with a streamtube; thus, there is flow only through two cross-sections of the streamtube: the inlet and the outlet. A schematic control volume is presented in Fig. 3.21. Note that the three-bladed HAWT shown in the figure is only referential because this model does not refer to the turbine type (except that the turbine must resemble a flat disc, called an actuator disc).

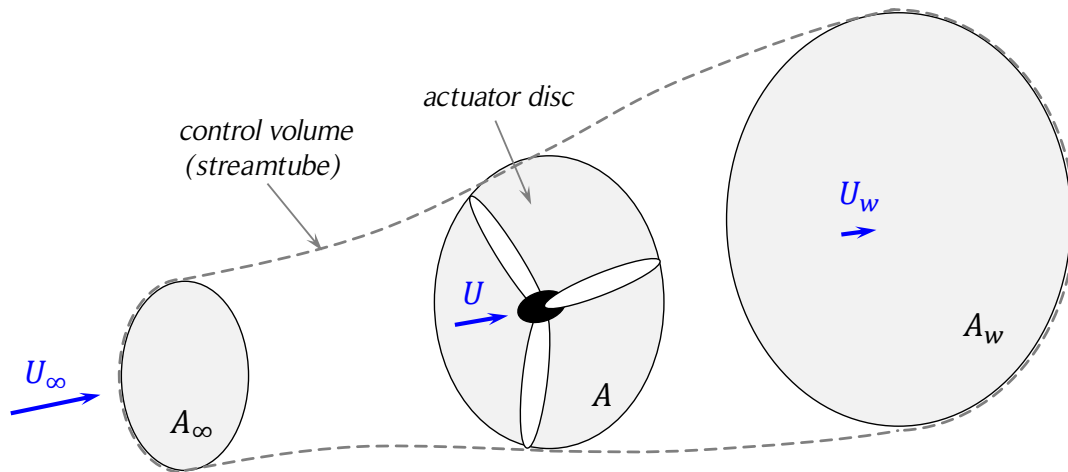


Figure 3.21. Control volume for the one-dimensional momentum model.

The figure shows the control volume for the one-dimensional momentum model for an ideal wind turbine. Note that the assumptions do not specify a turbine type. The three-bladed HAWT is only for reference. Source: own elaboration.

The turbine acts as a drag device slowing the wind from free stream speed, U_∞ , to a speed at the rotor plane, U , and finally to a wake speed, U_w ; thus, there is a spanwise expansion of the flow. The analysis considers the following assumptions:

- homogeneous, incompressible, steady state fluid flow;
- no frictional drag;
- a turbine with infinite blades;
- uniform pressure discontinuity at the actuator disc;
- uniform velocity at each cross-section of the streamtube;

- no flow through the lateral walls of the streamtube;
- a non-rotating wake;
- the static pressure far upstream and far downstream of the rotor is equal to the undisturbed ambient static pressure;
- the net force of the pressure distribution acting on the surfaces of the control volume is zero;
- the body forces acting on the control volume are negligible.

This concept was first developed by William Rankine (1865), William Froude (1878) and Robert Froude (1889) [5] and is the basis for modeling propellers, fans, and also HAWTs. This model was later modified for VAWTs. The model is explained with details in [44, 86] and is presented here with some notation modifications.

Before presenting the model details, the following must be noted. If the flow velocities are sufficiently slow in comparison with the speed of sound in the fluid, the flow can be considered incompressible. The speed of sound in a fluid is calculated as shown in Eq. (3.39) [49], where V_s is the speed of sound; γ is the adiabatic index, usually assumed as 1.4 because the air is composed mainly of diatomic molecules of nitrogen, N_2 , and oxygen, O_2 ; R is the molar gas constant; T is the absolute temperature; and M is the molar mass. In air under standard conditions, the speed of sound has an approximate value of 340 m/s . The Mach number, Ma , is defined in Eq. (3.40), where V_s is the speed of sound in the fluid and V_f is the actual speed of the fluid. If the Mach number is below 0.3 (the fluid velocity is slower than the 30% of the speed of sound in that fluid), the flow can be considered incompressible. In air under standard conditions, $Ma < 0.3$ means that the fluid velocity must be lower than 102 m/s or 367 km/h . Usually, this condition is satisfied for wind turbines; therefore, constant air density can be assumed.

$$V_s = \left(\frac{\gamma RT}{M} \right)^{1/2} \quad (3.39)$$

$$Ma = \frac{V_f}{V_s} \quad (3.40)$$

The mass flow rate, \dot{m} , passing through a control surface, A , can be calculated from Eq. (3.41), where U is the average speed of the flow in the control surface. The conservation of mass is represented by Eq. (3.42).

$$\dot{m} = \rho AU \quad (3.41)$$

$$\dot{m} = \rho A_{\infty} U_{\infty} = \rho A U = \rho A_w U_w \quad (3.42)$$

The wind decelerates in the streamwise direction, producing its expansion, which is shown in Eqs. (3.43) and (3.44).

$$U_{\infty} > U > U_w \quad (3.43)$$

$$A_{\infty} < A < A_w \quad (3.44)$$

While the wind slows down in the streamwise direction on the upstream side, the pressure rises. At the rotor there is a discontinuous pressure drop, ΔP , and on the downstream side the pressure continues to rise until the local ambient pressure is reached (see Fig. 3.22). The pressure difference before and after the rotor produces a thrust, F_x , in the direction of the wind, as shown in Fig. 3.23 and Eq. (3.45), where, for HAWTs, $A = \pi R^2$ is the actuator disc area, and R is the turbine radius.

$$F_x = A \Delta P \quad (3.45)$$

If the flow is stationary, incompressible, frictionless and no external forces act on the fluid upstream or downstream of the turbine, then Bernoulli's equation is valid from far upstream to just in front of the actuator disc and from just behind of the actuator disc to far downstream in the wake, as shown in Eqs. (3.46) and (3.47), respectively. The pressure just upstream of the rotor is called P_u and just downstream is called P_d ; thus, both terms are related to each other as shown in Eq. (3.48). Combining Eqs. (3.46) – (3.48) yields Eq. (3.49).

$$P_{\infty} + \frac{1}{2} \rho U_{\infty}^2 = P_u + \frac{1}{2} \rho U^2 \quad (3.46)$$

$$P_d + \frac{1}{2} \rho U^2 = P_{\infty} + \frac{1}{2} \rho U_w^2 \quad (3.47)$$

$$P_u = P_d + \Delta P \quad (3.48)$$

$$\Delta P = \frac{1}{2} \rho (U_{\infty}^2 - U_w^2) \quad (3.49)$$

The axial momentum equation in integral form is obtained from applying the Reynolds Transport Theorem to the linear momentum of a non-accelerating control volume. This is

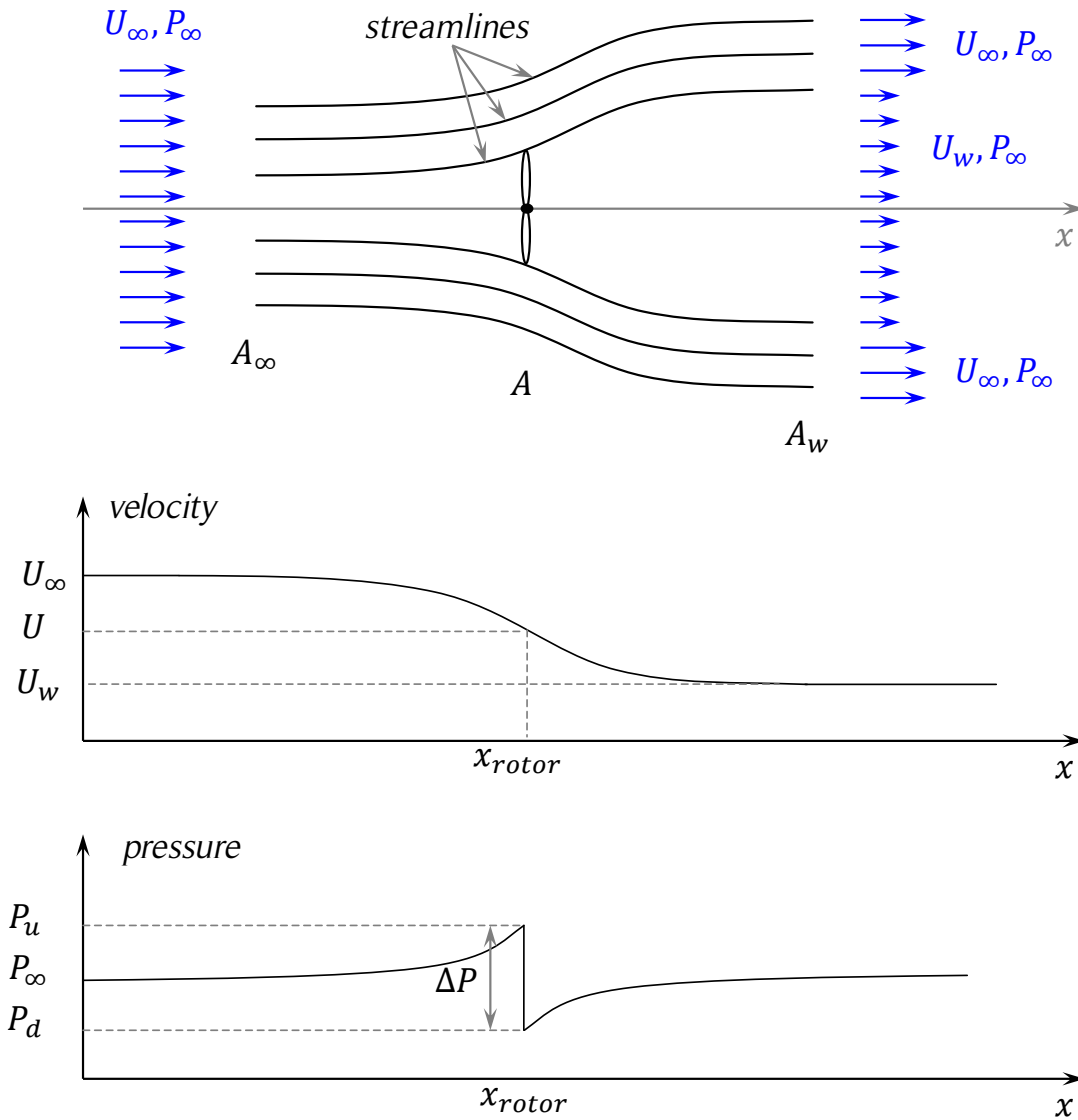


Figure 3.22. Velocity and pressure variation along the flow direction.

The figure shows the up- and downstream flow around the turbine, and the velocity and pressure variation along the flow direction. Source: own elaboration based on [86].

shown in Eq. (3.50), where t is time, ρ is the fluid density, \vec{V} is the velocity vector field of the flow, dV is the volume differential and $d\vec{A}$ is the surface differential. The triple integral over the control volume (CV) represents the forces produced by the changes of velocity with time. The double integral represents on the control surfaces (CS) represent the forces caused by the balance of fluid entering and exiting the surfaces of the control volume. The right side of Eq. (3.50) is equal to the sum of the surface and body forces

acting on the control volume. Note that the turbine is not considered part of the control volume and that the vector $d\vec{A}$ points outwards from the control volume.

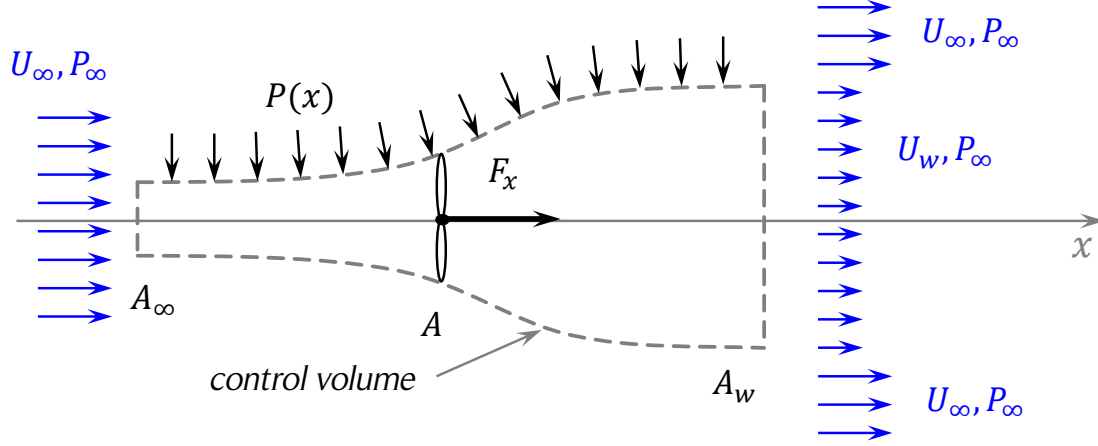


Figure 3.23. Control volume for the turbine.

The figure shows a control volume in the shape of a bottle. The lateral wall coincides with the flow streamlines. Therefore, there is no mass flow through the lateral wall. Source: own elaboration based on [86].

$$\vec{F} = \frac{\partial}{\partial t} \iiint_{CV} \rho \vec{V} dV + \iint_{CS} \vec{V} \rho \vec{V} \cdot d\vec{A} \quad (3.50)$$

$$\vec{V}(x, y, z, t) = u(x, y, z, t)\hat{i} + v(x, y, z, t)\hat{j} + w(x, y, z, t)\hat{k} \quad (3.51)$$

Applying the assumptions of the model to Eq. (3.50) yields Eq. (3.52), where $-F_x$ is the net force acting on the control volume. The force acting on the control volume is assigned a negative sign to obtain a positive thrust force on the turbine in the streamwise direction (due to the action-reaction law, both forces have the same magnitude but opposite direction), as shown in Eq. (3.53), where the mass conservation of Eq. (3.42) was used. Note that the pressure forces acting on the control volume are assumed to produce a zero net force on the volume, which is a strong assumption because the pressure distribution on the lateral face of the control volume (bottle shape) is unknown. Due to symmetry, the radial components of the pressure distribution are cancelled. However, the streamwise components are not cancelled.

$$-F_x = -U_\infty(\rho U_\infty A_\infty) + U_w(\rho U_w A_w) \quad (3.52)$$

$$F_x = \dot{m}(U_\infty - U_w) \quad (3.53)$$

If Eq. (3.45) and (3.53) are combined, an expression for the speed at the actuator disc can be obtained, as shown in Eqs. (3.54) and (3.55). Hence, the interference velocity, U , is the average of the free-stream and the wake velocities.

$$\frac{1}{2}\rho A(U_\infty^2 - U_w^2) = \rho AU(U_\infty - U_w) \quad (3.54)$$

$$U = \frac{1}{2}(U_\infty + U_w) \quad (3.55)$$

The integral energy equation for constant height on the control volume of Fig. 3.23 permits the calculation of the turbine power output, \dot{W}_T , which is shown in Eq. (3.56). This is possible due to the assumption of a frictionless flow (no losses). Rearranging terms and replacing the known value of the flow mass rate in Eq. (3.56) yields Eq. (3.57).

$$\dot{m} \left(\frac{P_\infty}{\rho} + \frac{1}{2} U_\infty^2 \right) = \dot{m} \left(\frac{P_\infty}{\rho} + \frac{1}{2} U_w^2 \right) + \dot{W}_T \quad (3.56)$$

$$\dot{W}_T = \frac{1}{2} \rho AU (U_\infty^2 - U_w^2) \quad (3.57)$$

The axial induction factor, a , also called interference factor, is defined according to Eq. (3.58). Equation (3.59) is obtained from Eqs. (3.55) and (3.58).

$$U = (1 - a)U_\infty \quad (3.58)$$

$$U_w = (1 - 2a)U_\infty \quad (3.59)$$

The available power on the turbine shaft, \dot{W}_T , is calculated from Eq. (3.60). The power coefficient, c_p , can be calculated from Eqs. (3.60) and (3.61), as shown in Eq. (3.62).

$$\dot{W}_T = \frac{1}{2} \rho A (1 - a) U_\infty^3 [1 - (1 - 4a + 4a^2)] = 2a(1 - a)^2 \rho AU_\infty^3 \quad (3.60)$$

$$\dot{W}_A = \frac{1}{2} \dot{m} U_\infty^2 = \frac{1}{2} \rho AU_\infty^3 \quad (3.61)$$

$$c_p = \frac{\dot{W}_T}{\dot{W}_A} = 4a(1 - a)^2 \quad (3.62)$$

Differentiating c_p with respect to the induction factor a yields Eq. (3.63).

$$\frac{dc_p}{da} = 12a^2 - 16a + 4 = 4(3a - 1)(a - 1) \quad (3.63)$$

The derivative of c_p is equal to zero for $a = 1/3$ and $a = 1$ are local maximum or minimum values of the power coefficient. Since $c_p(a) = 4a(1 - a)^2 \geq 0$ for $a \in [0,1]$, and $c_p(a = 1) = 0$ and $c_p(a = 1/3) = 16/27$, the maximum power coefficient $c_p = 16/27 \approx 59.26\%$ is reached for $a = 1/3$ (see Fig. 3.25). This maximum theoretical power coefficient is usually known as the Betz limit, but, as discussed in Section 2.4.2, it should be called Betz-Joukowski limit.

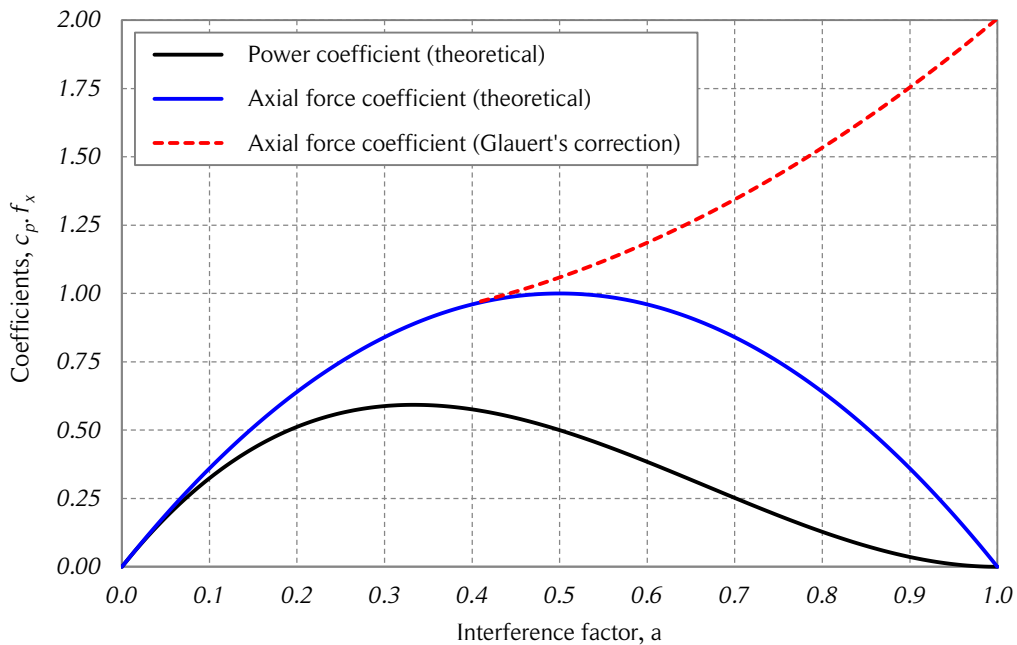


Figure 3.24. Power and axial force coefficients vs. interference factor.

The figure shows the power coefficient and axial force coefficient as a function of the interference factor for the one-dimensional momentum theory and Glauert's correction. Source: own elaboration based on [87].

Experimental results have shown that the assumptions of an ideal wind turbine, which lead to Eq. (3.55), are only valid for an axial induction factor $a < 0.4$. For higher values of a the flow around the turbine becomes more complicated, as shown in Fig. 3.24. When $a < 0$ the rotor acts as a propeller or fan, accelerating the flow. On the other hand, Eq. (3.59) indicates that for $a > 0.5$ the wake velocity would be negative. Experiments show that for a relevant range of values of the interference this is not the case. Empirical correlations have been developed for axial induction factors greater than 0.4.

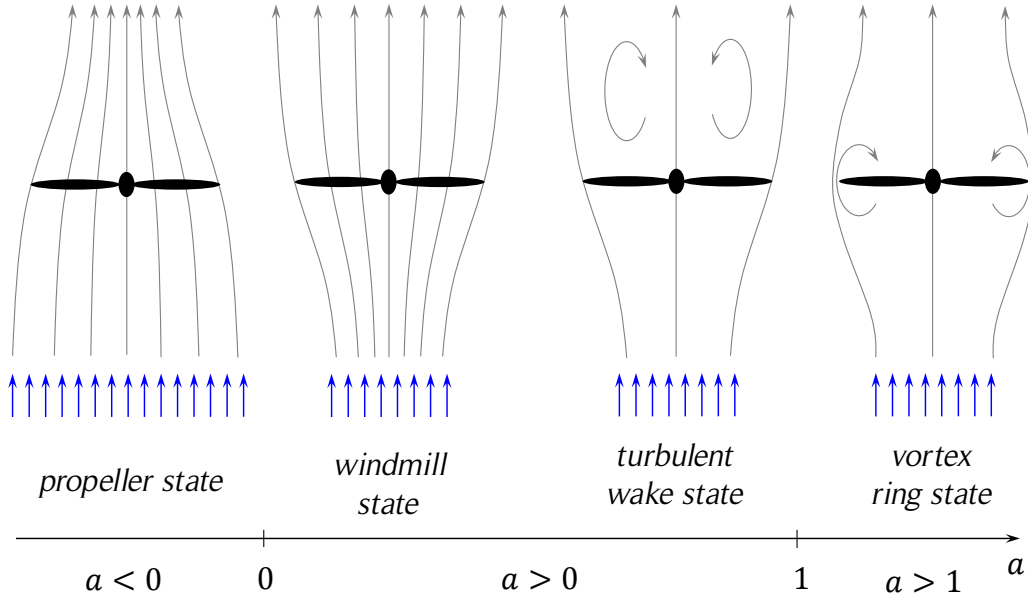


Figure 3.25. Turbine flow states for various interference factors.

The figure shows the flow states around the turbine for four different interference factor ranges. For higher values of the interference factor the vortex ring state changes to a propeller brake (not shown). Source: own elaboration based on [86].

The axial force coefficient or axial thrust coefficient, f_x , is defined as the axial force, F_x , acting on the turbine divided by the maximum available force in the flow, which is shown in Eqs. (3.64) and (3.65).

$$F_x = \rho AU(U_\infty - U_w) = 2a(1 - a)\rho AU_\infty^2 \quad (3.64)$$

$$f_x = \frac{F_x}{\frac{1}{2}\rho AU_\infty^2} = 4a(1 - a) \quad (3.65)$$

Hermann Glauert suggested an empirical correlation to overcome the problem of the momentum theory when $a > 0.4$. This is shown mathematically in Eq. (3.66) and graphically in Fig. 3.24 [87].

$$f_x = \begin{cases} 4a(1 - a), & a \leq 0.4 \\ 0.86 + 1.56(a - 0.143)^2, & a > 0.4 \end{cases} \quad (3.66)$$

The reason for the breakdown of the one-dimensional momentum model for values of $a > 0.4$ is that the free shear layer at the edge of the wake becomes unstable when the

velocity difference between U_∞ and U_w becomes too large. The wake vortices transport momentum from the outer flow into the wake. This situation is known as the turbulent-wake state and is shown in Fig. 3.26.

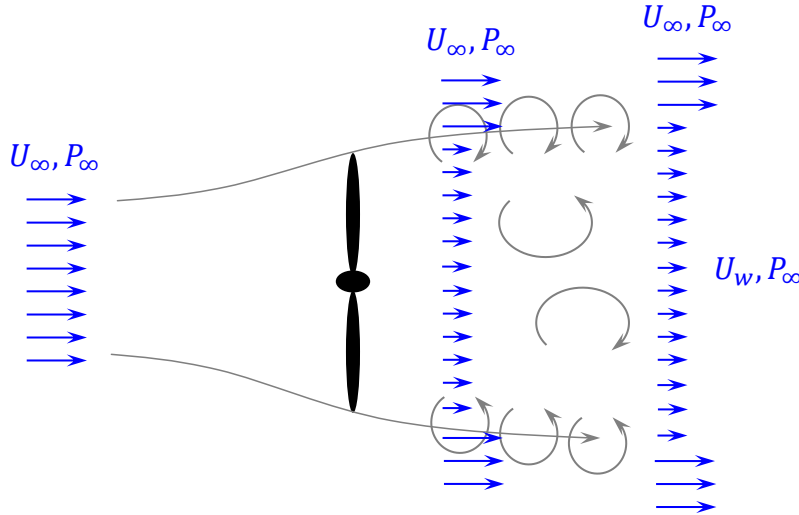


Figure 3.26. Turbulent-wake state of the turbine.

The figure shows the turbulent-wake state of the turbine which is produced by high values of the interference factor. Source: own elaboration based on [86].

Note that under the assumptions of the one-dimensional momentum model, the wind velocity in the wake, U_w , remains constant and does not recover to the freestream velocity, U_∞ . Under real conditions, according to [80], the wake velocity returns to 95% of the freestream velocity within six rotor diameters downstream from the turbine for Darrieus SB-VAWTs installed in counter-rotating pairs. According to the same reference, the typical recovery distance for HAWTs is at least twice as large. The recovery is explained by the momentum and energy exchange inside the atmospheric boundary layer (ABL). According to [84], the ABL has a characteristic height of 1 km. The driving force of the ABL is the geostrophic wind. Inside the ABL, there is a balance between pressure forces, Reynolds stresses, and Coriolis forces induced by the Earth's rotation. Therefore, for each case, the local topography and all the aforementioned phenomena determine how fast the recovery of the velocity deficit in the turbine wake will occur.

3.5. Blade element momentum models

The aim of blade element momentum (BEM) models is to find the interference factor which equates, in the streamwise direction, the average aerodynamic forces acting on the

turbine blades with the change of momentum of the entire flow passing through the rotor. Depending on the turbine type and geometry, the streamwise aerodynamic forces acting on the turbine blades have to be calculated in different ways. Besides the turbine geometric parameters and the rotational speed, usually, the only other inputs for calculating the aerodynamic forces are the angle of attack, α , and the magnitude of the relative velocity of the wind, W , at each blade position. With that information, the Reynolds number can be calculated; and therefore, the aerodynamic coefficients can be obtained from the empirical tabulated data.

The average streamwise aerodynamic force acting on the turbine blades, \bar{F}_x , is presented in Eq. (3.67). The change of momentum due to the wind deceleration is presented in Eq. (3.68), where the same notation of the previous sections of this chapter is used. For VAWTs the difficulty lies in finding W , which is a function of the induced wind velocity, U , which in turn depends on the azimuthal position of the blade. Since the aerodynamic coefficients are not available as an analytical function, usually an iterative process to obtain the induced velocity (or the induction factor) is used.

$$\bar{F}_x = \frac{1}{2\pi} \int_0^{2\pi} F_x(\theta) d\theta \quad (3.67)$$

$$F_x = \dot{m}(U_\infty - U_w) = \rho AU(U_\infty - U_w) \quad (3.68)$$

Different BEM models have been developed over the years for both Darrieus CB-VAWT and SB-VAWT [3]. The simplest approach was developed by Templin (1974) and it is known as the single streamtube model, which as its name says, only considers one streamtube for the momentum balance. Wilson and Lissaman (1974), and later Strickland (1975), introduced a multiple streamtube model, which considers many adjacent streamtubes in the cross-stream direction of the flow. This permits a better discretization of the flow field and, therefore, better estimations of the aerodynamic forces and turbine performance. In 1981, Paraschivoiu [88] introduced a modification of the multiple streamtube model which considers a division of the rotor in two halves: upstream and downstream. Therefore, there are two streamtubes in tandem in the streamwise direction and multiple streamtubes in the cross-stream direction, which explains the name: double-multiple streamtube (DMS) model. The main advantage of BEM models is that they are quite simple and require few computational resources. The main disadvantage is that they become invalid for high tip-speed ratios, TSR , and high turbine solidity, σ . The single streamtube and multiple streamtube models are discussed briefly in Sections 3.6 and 3.7, respectively. On the other hand, the DMS model is discussed in detail in Section 3.8.

3.6. Single streamtube model

In 1974, Templin developed the first single streamtube model to calculate the aerodynamic performance of a Darrieus CB-VAWT [4]. His model was inspired by the actuator disc theory. Thus, the purpose of the model was to find the induced velocity in the rotor, or equivalently, the respective interference factor. As was mentioned in the previous sections of this chapter, the thrust acting on the rotor in the flow direction is equal to the flow change of momentum, as shown in Eq. (3.69), where the same notation of the previous sections of this chapter is used (see Fig. 3.27). As a first approach, the induced velocity, U , is considered constant for the entire rotor; and thus, there is no flow expansion through the turbine.

$$F_x = \rho AU(U_\infty - U_w) \quad (3.69)$$

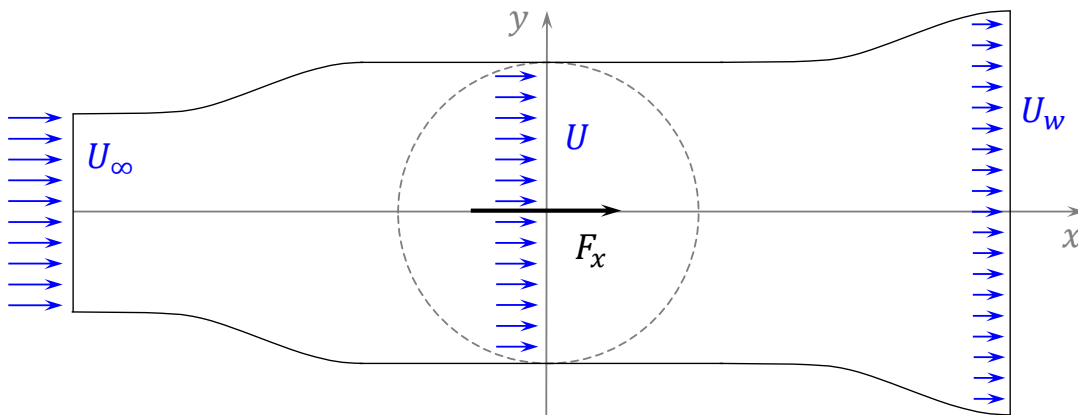


Figure 3.27. Flow around the turbine for the single streamtube model.

The figure shows the flow around the turbine for the single streamtube model. There is no flow expansion through the rotor. Note that the streamwise force is acting on the turbine. Source: own elaboration.

From the blade element theory (see Fig. 3.16), the average streamwise force acting on the blades of a unit height turbine is obtained from Eq. (3.70), where the radial and tangential coefficients of the aerodynamic forces are obtained from Eqs. (3.71) and (3.72), respectively. It is assumed that the blade fixation angle is zero, $\alpha_0 = 0$; therefore, $\alpha = \alpha_B$.

$$\bar{F}_x = \frac{1}{2\pi} \frac{1}{2} \rho c \int_0^{2\pi} (c_r \cos \theta - c_\theta \sin \theta) W^2 d\theta \quad (3.70)$$

$$c_\theta = c_L \sin \alpha - c_D \cos \alpha \quad (3.71)$$

$$c_r = c_L \cos \alpha + c_D \sin \alpha \quad (3.72)$$

Equating Eqs. (3.69) and (3.70) gives Eq. (3.73), which usually is expressed in terms of the interference factor, a , as shown in Eq. (3.74). Note that for a unit height turbine, the turbine cross-sectional area, A , becomes the turbine diameter, D , and the mean force of one blade has to be multiplied by the number of blades, N , to obtain the total force in the streamwise direction acting on the turbine.

$$\rho AU(U_\infty - U_w) = \frac{1}{4\pi} \rho c \int_0^{2\pi} (c_r \cos \theta - c_\theta \sin \theta) W^2 d\theta \quad (3.73)$$

$$a(1 - a) = \frac{Nc}{8\pi D U_\infty^2} \int_0^{2\pi} (c_r \cos \theta - c_\theta \sin \theta) W^2 d\theta \quad (3.74)$$

The expression for an iterative process to obtain the interference factor is presented in Eq. (3.75). The initial guess of the interference factor is typically $a = 0$. A convergence criteria, cc , as shown in Eq. (3.76), can be used to stop the iterative process. A typical value of the convergence criteria for the interference factor is $cc = 10^{-4}$.

$$a_{i+1} = \frac{1}{1 - a_i} \frac{Nc}{8\pi D U_\infty^2} \int_0^{2\pi} (c_r \cos \theta - c_\theta \sin \theta) W^2 d\theta \quad (3.75)$$

$$|a_{i+1} - a_i| \leq cc \quad (3.76)$$

As has already been mentioned, the BEM models are not valid for high TSR or high turbine solidities. Thus, in some cases no solution will be obtained from the iterative process. In those cases, it can be helpful to plot the curves of the blade element theory and the momentum balance as functions of the interference factor to find the maximum interference factor at which the model can find a solution.

3.7. Multiple streamtube model

In 1975, Strickland presented a modification of the single streamtube model that considered multiple streamtubes in the cross-stream direction passing through the turbine

[4], as it is shown in Fig. 3.28. The procedure is exactly the same as the one used in the single streamtube model but it has to be repeated for each of the streamtubes.

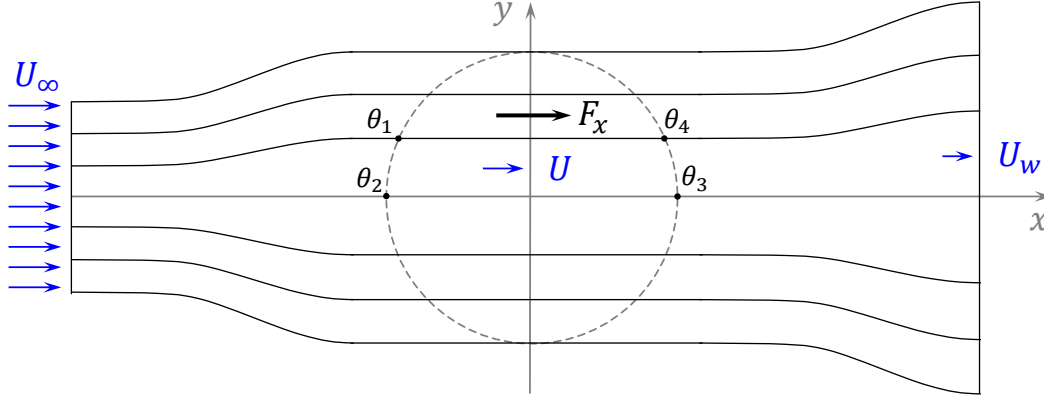


Figure 3.28. Flow around the turbine for the multiple streamtube model.

The figure shows the flow around the turbine for the multiple streamtube model using six streamtubes. In general, the induced and wake velocity at each streamtube will be different. There is no flow expansion through the rotor. The wind velocities and streamwise force are presented in different streamtubes, for clarity. Source: own elaboration based on [87].

In the multiple streamtube model each of the streamtube lateral limits (streamlines) intersects the blade trajectory twice. Since no flow expansion near the turbine is considered, the intersections of the streamlines and the blade trajectory occurs at the same y coordinate. These angular limits are denoted as θ_1 and θ_2 and define a circumference arc denoted $\Delta\theta = \theta_2 - \theta_1$. Note that $\theta_4 - \theta_3 = \Delta\theta$. This has to be taken into account when calculating the momentum balance and the mean aerodynamic streamwise forces acting on the blades at each streamtube. The modified expressions of the model of a unit height turbine for one streamtube with angular limits θ_1 and θ_2 are presented in Eqs. (3.77) and (3.78). These are analogous to Eqs. (3.68) and (3.70). The width of the streamtube can be calculated from the turbine radius, R , and the angular limits θ_1 and θ_2 . It must be noted that for the multiple streamtube case, the average aerodynamic streamwise force acting on the blades at each streamtube has to be weighted by the fraction of angular trajectory contained in the streamtube, $(2\Delta\theta)/(2\pi)$.

$$F_x = \rho R |\sin \theta_2 - \sin \theta_1| U (U_\infty - U_w) \quad (3.77)$$

$$\bar{F}_x = \frac{1}{2} \rho c \frac{N \Delta\theta}{\pi} \frac{1}{2} \left(\frac{1}{\Delta\theta} \int_{\theta_1}^{\theta_2} f(\theta) d\theta + \frac{1}{\Delta\theta} \int_{\theta_3}^{\theta_4} f(\theta) d\theta \right) \quad (3.78)$$

$$f(\theta) = (c_r \cos \theta - c_\theta \sin \theta)W^2 \quad (3.79)$$

Equating Eqs. (3.77) and (3.78) and rearranging terms yields Eq. (3.80) for each streamtube. The expression for the interference factor, a , is presented in Eq. (3.81). In like manner as the previous case, the iterative process can be performed using the expression of the interference factor for each streamtube. Convergence failure of the multiple streamtube model was discussed in [87].

$$R(\sin \theta_2 - \sin \theta_1)U(U_\infty - U_w) = \frac{Nc}{4\pi} \left(\int_{\theta_1}^{\theta_2} f(\theta)d\theta + \int_{\theta_3}^{\theta_4} f(\theta)d\theta \right) \quad (3.80)$$

$$a(1 - a) = \frac{Nc}{8\pi U_\infty^2 R |\sin \theta_2 - \sin \theta_1|} \left(\int_{\theta_1}^{\theta_2} f(\theta)d\theta + \int_{\theta_3}^{\theta_4} f(\theta)d\theta \right) \quad (3.81)$$

3.8. Double-multiple streamtube model

3.8.1. Basic model

In 1981, Paraschivoiu [88] presented a modification of the multiple streamtube model, known as the double-multiple streamtube (DMS) model that considered two streamtubes in tandem in the streamwise direction and multiple adjacent and parallel streamtubes in the cross-stream direction [4]. Therefore, five different velocities instead of three are defined along the streamwise direction for each streamtube (see Fig. 3.29): the freestream velocity, U_∞ , the upstream induced velocity, U_u , the equilibrium velocity, U_e , the downstream induced velocity, U_d , and the wake velocity, U_w . For each of the multiple streamtubes in the spanwise direction, two interference factors are defined: one for the upstream half, u_u , and one for the downstream half, u_d , which definitions are shown in Eqs. (3.82) and (3.83), respectively. Note that the interference factor, u , can be expressed in terms of a . The nomenclature of the DMS model for the interference factor, u , is kept in the present work.

$$u_u = \frac{U_u}{U_\infty} = 1 - a_u \quad (3.82)$$

$$u_d = \frac{U_d}{U_e} = 1 - a_d \quad (3.83)$$

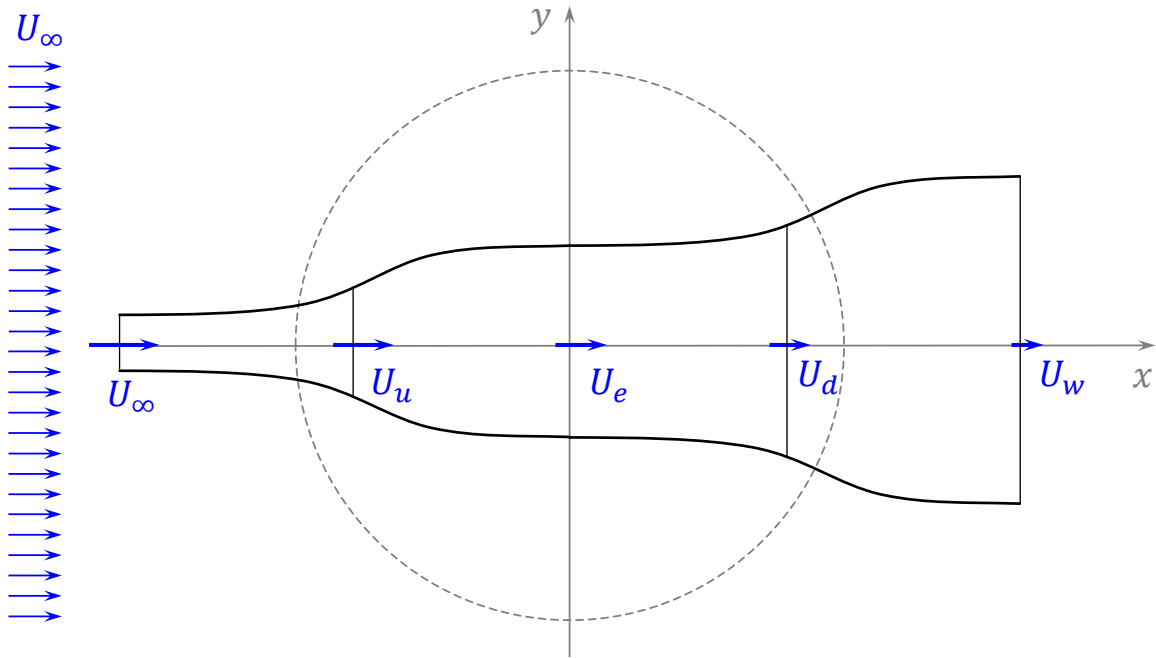


Figure 3.29. Flow around the turbine for the double-multiple streamtube model.

The figure shows two streamtubes in tandem in the streamwise direction of the double-multiple streamtube model (DMS). Source: own elaboration based on [4].

As a first approach, it is assumed that the wind velocity changes its magnitude in the streamwise direction but there is no velocity in the cross-stream direction and also no streamtube expansion (see Fig. 3.30). Paraschivoiu's DMS model (called *CARDAA* computer code) considers an equispaced angular division for the streamtube definition. This means having wider streamtubes near the center of the turbine and narrower streamtubes at both left and right turbine sides, which is shown in Fig. 3.30. To clarify the notation, two streamtubes in tandem are called one turbine streamtube. After these considerations, the expressions of the upstream and downstream interference factors can be obtained. Following the procedure of the multiple streamtube model, the upstream and downstream expressions of the balance of momentum are presented in Eqs. (3.84) and (3.85), respectively. According to the blade element theory, the expressions for the upstream and downstream sides are the same as the one for the multiple streamtube model with the respective angular limits, as shown in Eq. (3.86) and (3.87). Note that in the DMS model each tube only intersects the blade trajectory once. Therefore the weighting used in the multiple streamtube model changes.

$$F_{x,u} = \rho R |\sin \theta_2 - \sin \theta_1| U_u (U_\infty - U_e) \quad (3.84)$$

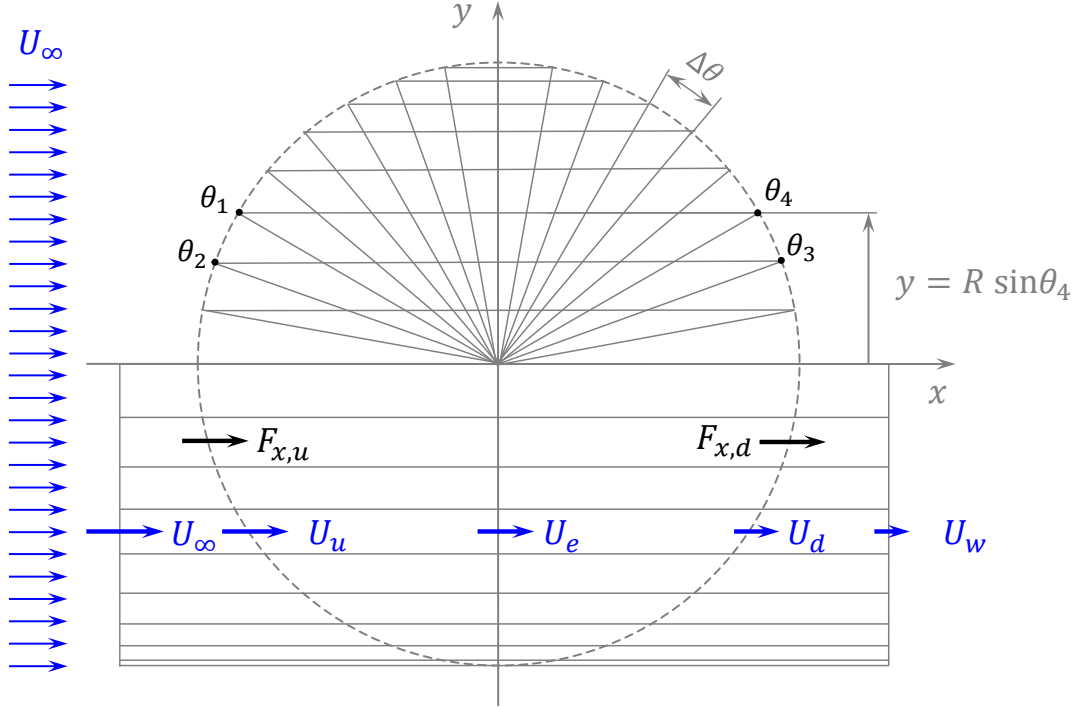


Figure 3.30. Flow around the turbine for the double-multiple streamtube model.

The figure shows the flow around the turbine for the double-multiple streamtube model with 18 turbine streamtubes (36 in total). The model considers a change of the magnitude of the streamwise wind velocities but no expansion of the streamtubes. Source: own elaboration based on [4].

$$F_{x,d} = \rho R |\sin \theta_4 - \sin \theta_3| U_d (U_e - U_w) \quad (3.85)$$

$$\bar{F}_{x,u} = \frac{1}{2} \rho c \frac{N \Delta \theta}{2\pi} \frac{1}{\Delta \theta} \int_{\theta_1}^{\theta_2} (c_r \cos \theta - c_\theta \sin \theta) W^2 d\theta \quad (3.86)$$

$$\bar{F}_{x,d} = \frac{1}{2} \rho c \frac{N \Delta \theta}{2\pi} \frac{1}{\Delta \theta} \int_{\theta_3}^{\theta_4} (c_r \cos \theta - c_\theta \sin \theta) W^2 d\theta \quad (3.87)$$

The interference factors for the upstream and downstream sides are calculated according to Eqs. (3.88) and (3.89), respectively.

$$u_u(1 - u_u) = \frac{Nc}{8\pi U_\infty^2 R |\sin \theta_2 - \sin \theta_1|} \int_{\theta_1}^{\theta_2} (c_r \cos \theta - c_\theta \sin \theta) W^2 d\theta \quad (3.88)$$

$$u_d(1 - u_d) = \frac{Nc}{8\pi U_e^2 R |\sin \theta_4 - \sin \theta_3|} \int_{\theta_3}^{\theta_4} (c_r \cos \theta - c_\theta \sin \theta) W^2 d\theta \quad (3.89)$$

In 1983, Paraschivoiu and Delclaux performed improvements on the DMS model [90]. The new model considered the angular dependency of the interference factors shown in Eqs. (3.88) and (3.89) (DMSV model or *CARDAAV* computer code). The “V” stands for the variation of the interference factor with the azimuthal angle, θ .

3.8.2. Streamtube expansion

The simplest approach of the DMS model presented in the previous section does not take into account the expansion of the flow. If the streamtubes of Fig. 3.30 are observed carefully, it can be noted that the continuity equation is not satisfied. In other words, there is no conservation of mass. In 1985, Paraschivoiu et al. presented a modified DMS model that considered flow expansion and conservation of mass (called *CARDAAX* computer code) [8]. For each streamtube, five cross flow control surfaces are defined (see Fig. 3.31): at ∞ , u , e , d , and w .

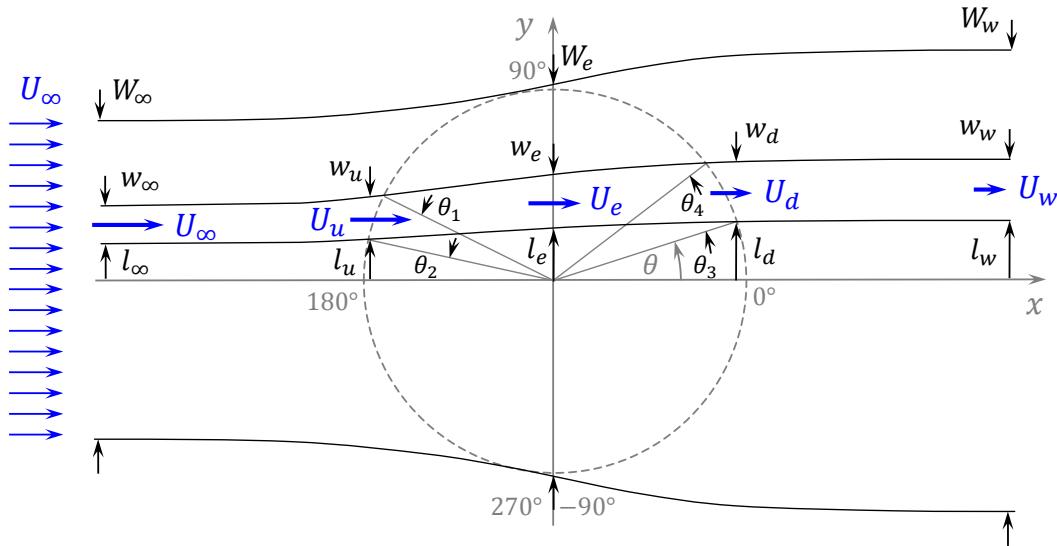


Figure 3.31. Flow expansion of the DMS model.

The figure shows the flow expansion around a Darrieus SB-VAWT for the DMSV model (*CARDAAX* computer code). Source: own elaboration based on [8].

For a two-dimensional model, a unit height is considered and thus the only parameters of importance to determine the expansion of the flow are the widths of the streamtube at

the five positions of interest. The conservation of mass along one turbine streamtube is presented in Eq. (3.90), where the air density does not appear in the expressions because it is considered constant. The equations and figures of [8] are changed to coincide with the notation of this work. Despite the flow expansion, all wind velocities are considered parallel to the freestream velocity. The deceleration of the wind in the streamwise direction of each turbine streamtube is presented in Eq. (3.91).

$$U_{\infty}w_{\infty} = U_uw_u = U_e w_e = U_d w_d = U_w w_w \quad (3.90)$$

$$U_{\infty} \geq U_u \geq U_e \geq U_d \geq U_w \quad (3.91)$$

A priori, the streamtube widths are unknown, which implies more calculations in the iterative process than in the basic approach with no expansion. The streamtube cross sections are calculated using an incremental approach. An undistorted central line coinciding with the x -axis is assumed. The streamtubes on the left and right sides are constructed progressively, starting from the center line, until the entire turbine is covered. This is shown in Fig. 3.31. The upstream spanwise coordinate of a streamtube, l_u , can be expressed in terms of the azimuthal angle, θ , and the turbine radius, R , as shown in Eq. (3.92) and its derivative, which is presented in Eq. (3.93).

$$l_u = R \sin \theta \quad (3.92)$$

$$dl_u = R \cos \theta d\theta \quad (3.93)$$

The continuity equation in an upstream tube using the differential approach of Eq. (3.93) and the expressions of the upstream interference factor of Eqs. (3.94) and (3.95) are presented in Eq. (3.96). Integrating Eq. (3.94) between θ and π yields Eqs. (3.97) – (3.99). Therefore, the total freestream width, W_{∞} , and the equilibrium width, W_e , of the flow passing through the turbine can be determined according to Eqs. (3.100) and (3.101), respectively.

$$U_u = u_u U_{\infty} \quad (3.94)$$

$$U_e = (2u_u - 1)U_{\infty} \quad (3.95)$$

$$dl_{\infty} = R u_u \cos \theta d\theta = (2u_u - 1)dl_e \quad (3.96)$$

$$l_{\infty} = - \int_{\theta}^{\pi} R u_u \cos \theta d\theta \quad (3.97)$$

$$l = - \int_{\theta}^{\pi} R \cos \theta \, d\theta \quad (3.98)$$

$$l_e = - \int_{\theta}^{\pi} \frac{R u_u \cos \theta}{(2u_u - 1)} \, d\theta \quad (3.99)$$

$$W_{\infty} = - \int_{\pi/2}^{3\pi/2} R u_u \cos \theta \, d\theta \quad (3.100)$$

$$W_e = - \int_{\pi/2}^{3\pi/2} \frac{R u_u \cos \theta}{(2u_u - 1)} \, d\theta \quad (3.101)$$

In the downwind half, the azimuthal angles which define the limits of the streamtube cannot be independently chosen as they are for the upstream side because they are defined by the respective width at the equilibrium position ($x = 0$) and the downstream expansion. If the angular limit, θ_3 , of one streamtube on the left side ($y > 0$) is known, the following limit, θ_4 , can be calculated from θ_3 and the streamtube width at the equilibrium position, w_e , as shown in Eqs. (3.102) and (3.103). This must be done carefully because some upstream tubes may not cross the blade trajectory on the downwind side.

$$w_d = \frac{w_e}{u_d} = R |\sin \theta_4 - \sin \theta_3| \quad (3.102)$$

$$\theta_4 = \arcsin \left(\frac{w_e}{R u_d} + \sin \theta_3 \right) \quad (3.103)$$

This extension of the DMS model uses the same expressions for the upstream and downstream interference factors used in the basic model. The expressions showed in Eqs. (3.88) and (3.89) have to be used with the respective upstream and downstream angular limits, which allows the use of an iterative process for the calculation of the interference factors and angular limits.

The calculation using the DMS model of the flow expansion of a 17 m Darrieus CB-VAWT of the Sandia Laboratories operating at 50.6 rpm is presented in Fig. 3.32 [8]. The streamtube expansion results in lower aerodynamic loads on the downstream side of the rotor in comparison with the calculations performed with the *CARDAAV* code.

According to [8], the streamtube expansion has little impact on the calculation of the turbine power coefficient. Therefore, the authors of the article suggest that it is more important to focus on the aerodynamic design of the turbine blades than on the flow expansion to obtain better estimations of the turbine power coefficient.

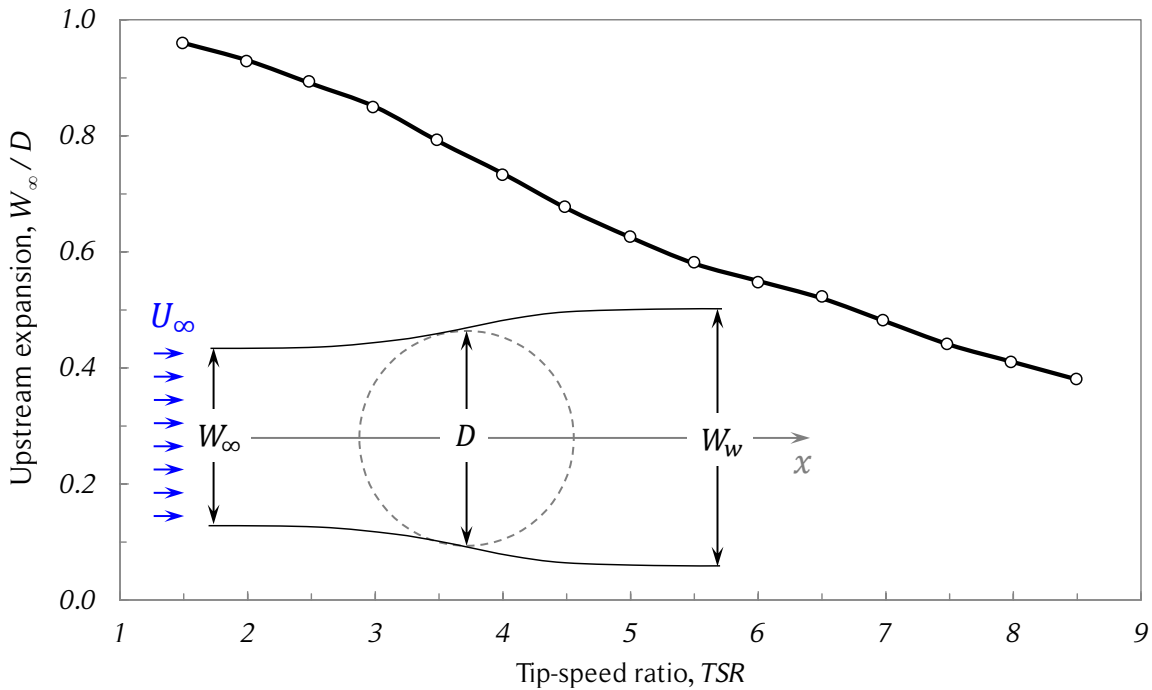


Figure 3.32. DMS model upstream expansion of a Darrieus CB-VAWT.

The figure shows the upstream flow expansion of a 17 m Darrieus CB-VAWT operating at 50.6 rpm obtained with the double-multiple streamtube model. Source: redrawn from [8].

3.8.3. Dynamic stall

Dynamic stall is a complex unsteady flow phenomenon found in the aerodynamics of all types of Darrieus turbines (SB-VAWTs, CB-VAWTs and HB-VATWs). Depending on the operational parameters, large and quick changes of the angle of attack can be observed in one turbine rotation. If the angle of attack becomes larger than the static stall angle, significant changes in the aerodynamic coefficients can result (see Fig. 2.24). Within a certain range of the characteristic parameters of the dynamic stall phenomenon, such as the angle of attack, the speed and amplitude of the angle of attack variations, the blade chord and the relative wind velocity, the lift forces acting on the airfoil under dynamic stall can be much larger than the ones under static stall. In extreme cases, the lift

coefficient can be increased by a factor of two or three for a period of time and then drop below the static stall values [7]. The moment and drag coefficients can also experience large variations in comparison with the static stall condition. Various empirical models have been developed to take into account this phenomenon. Most of them were developed for helicopters. The cyclic pitch of helicopter blades can be described by Eq. (3.104), where A_α and ω_α are the amplitude and angular frequency of the angle of attack variation, respectively. To take advantage of the dynamic stall effect, the angle of attack has to change from less than to greater than the static stall angle. For instance, if the static stall angle of attack is 10° , the following parameters of Eq. (3.104) would satisfy this condition: $\alpha_0 = 10^\circ$ and $A_\alpha = 8^\circ$.

$$\alpha(t) = \alpha_0 + A_\alpha \sin(\omega_\alpha t) \quad (3.104)$$

Darrieus turbines experience similar cyclic pitch variations of its blades, but typically, the angular pitch frequency, ω_α , is lower and the amplitude of the angle of attack variations, A_α , are larger. Therefore, some dynamic stall models have been modified for Darrieus turbines. Among these models are: the Boing-Vertol model (also known as Gormont's model), its adaptations performed by Strickland, later by Paraschivoiu et al., and later by Berg; and the Massachusetts Institute of Technology (MIT) dynamic stall model and its later modification by Noll and Ham [4]. Two dynamic stall models for Darrieus SB-VAWTs are presented here: the Boing-Vertol model with the modifications of Strickland, Paraschivoiu et al.[9]; and the MIT model with Pawsey's modifications [7].

3.8.4. Modified Boing-Vertol dynamic stall model

The Boing-Vertol dynamic stall model modified by Strickland and Paraschivoiu et al. [4] assumes that the slope of the lift versus angle of attack curve and the angle of attack for zero lift remains unchanged. The dynamic effects only modify the stall angle of attack. A modified angle in radians, α_m , is used for entering the two-dimensional aerodynamic coefficients data. The expression for the modified angle of attack is presented in Eq. (3.105), where α_e is the effective angle of attack, γ and K_1 are empirical constants, c is the blade chord, W is the relative wind velocity, $\dot{\alpha}_e$ is the instantaneous rate of change of the effective angle of attack and $S_{\dot{\alpha}}$ is the sign of $\dot{\alpha}_e$. The reduced frequency, $k^* = (c\dot{\alpha}_e)/(2W)$, is a dimensionless parameter commonly used to characterize the dynamic stall phenomenon.

$$\alpha_m = \alpha_e - \gamma K_1 \left| \frac{c\dot{\alpha}_e}{2W} \right|^{1/2} S_{\dot{\alpha}} \quad (3.105)$$

The value of γ is a function of the airfoil thickness-to-chord ratio (t/c) and the local blade Mach number. For $t/c > 0.10$ and low Mach numbers, the value of γ is given by Eq. (3.106).

$$\gamma = 1.4 - 6(0.06 - t/c) \quad (3.106)$$

The value of K_1 changes with the sign of the time derivative of the effective angle of attack and is calculated according to Eq. (3.107).

$$K_1 = 0.75 + 0.25S_{\dot{\alpha}} \quad (3.107)$$

Note that blades of Darrieus turbines have both positive and negative angles of attack. This has to be taken into account when calculating the lift and drag coefficients to obtain aerodynamic coefficients consistent with the dynamic stall phenomenon. The equivalence between positive and negative angle of attack and their instantaneous rate of change are shown in Eq. (3.108).

$$\alpha > 0 \wedge \dot{\alpha} > 0 \Leftrightarrow \alpha < 0 \wedge \dot{\alpha} < 0 \quad (3.108)$$

$$\alpha > 0 \wedge \dot{\alpha} < 0 \Leftrightarrow \alpha < 0 \wedge \dot{\alpha} > 0$$

The instantaneous lift, moment and drag coefficients are calculated from Eqs. (3.109) – (3.111), respectively. The term α_{e0} is the effective angle of attack for zero lift. Therefore, for symmetric airfoils, $\alpha_{e0} = 0$.

$$c_L = \left(\frac{\alpha_e}{\alpha_m - \alpha_{e0}} \right) c_L(\alpha_m) \quad (3.109)$$

$$c_D = c_D(\alpha_m) \quad (3.110)$$

$$c_M = c_M(\alpha_m) \quad (3.111)$$

It has been observed that turbulence delays the onset of dynamic stall [9]. For instance, two experiments with the same dynamic stall parameters can show very different dynamic stall behaviors if one has low turbulence and the other has high turbulence. A high turbulent flow prevents the appearance of the leading edge vortex on the upper surface of the airfoil, hence, producing less (or no) increase in the lift coefficient in comparison with the static stall condition. Also, the angle of attack changes its sign in the upstream and downstream sides of the rotor. This causes the high and low pressure sides of the blade to switch during one turbine rotation. Since the dynamic stall phenomenon

consists of the appearance and later convection of a vortex on the upper surface of the airfoil, the dynamic stall phenomenon will be different if the upper surface of the airfoil is facing the freestream velocity, U_∞ , or not.

To illustrate the influence of turbulence on dynamic stall, dye visualizations in the high-speed water tunnel of the Computational Fluid Dynamics Laboratory of the Aerospace and Mechanical Engineering Department at the University of Arizona were performed during an internship of the author of the present work. The turbine had three NACA 0012 blades with chord $c = 50.8 \text{ mm}$ and a solidity of $\sigma = 1.2$. The wake behind the blade receiving dye in Fig. 3.33 (a) is highly turbulent and therefore dynamic stall should not occur at those azimuthal angles [4]. The blade in Fig. 3.33 (b) is in a low turbulence zone, and therefore dynamic stall can happen. Vortices associated with dynamic stall are observable in the downstream streakline. The authors of [9] recommend the use of the modified Boing-Vertol dynamic stall model only in the low turbulence zones, that is, between the azimuthal angles of 195° and 315° . A detailed description of the dynamic stall phenomenon in Darrieus SB-VAWTs was performed by Fujisawa and Shibuya [91].

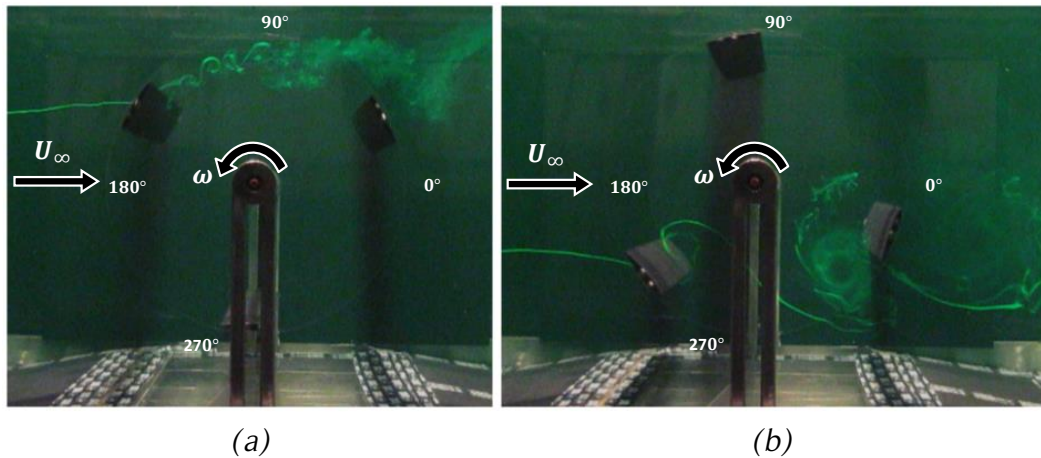


Figure 3.33. Dye visualizations of some flow structures of a Darrieus SB-VAWT.

The figures show the streaklines of the dye visualizations performed on a Darrieus SB-VAWT for $TSR = 1.85$ in the high-speed water tunnel of the Computational Fluid Dynamics Laboratory of the Aerospace and Mechanical Engineering Department at the University of Arizona, USA. Source: own elaboration during student internship.

3.8.5. Modified MIT dynamic stall model

Like the Boing-Vertol model, the MIT dynamic stall model, is not a fully unsteady aero-

dynamic model as it does not modify the aerodynamic forces on an airfoils pitching at angles below static stall (attached flow). It models the delayed stall and increased lift present in pitching airfoils. Pawsey's modification of the MIT dynamic stall model is presented below [7].

While the angle of attack is below the static stall angle, α_{SS} , the static aerodynamic coefficients are used for calculating the aerodynamic force and moment. The angle of attack at which dynamic stall occurs, α_{DS} , is found from the static angle using Eq. (3.112), where γ is an empirical constant weakly dependent on the airfoil ($\gamma = 1.6 \text{ rad}$ for a NACA 0012 airfoil and if γ is not known for a given airfoil, $\gamma = 1 \text{ rad}$ is recommended [92]), c is the chord, $\dot{\alpha}$ is the time derivative of the angle of attack and W is the relative flow velocity [7].

$$\alpha_{DS} = \alpha_{SS} + \gamma \left| \frac{\dot{\alpha}c}{2W} \right|^{1/2} \quad (3.112)$$

The main difference between the MIT model and the Boing-Vertol model is that the MIT model simulates the passing of a vortex over the upper surface of the airfoil instead of just modifying the angle of attack to use the tabulated experimental data. When the dynamic stall model is being programmed, it is useful to divide the code into the four modes that the MIT model defines. Each mode contains rules for determining the lift and drag coefficients as well as when to switch modes [92]. A diagram of the method is presented in Fig. 3.34.

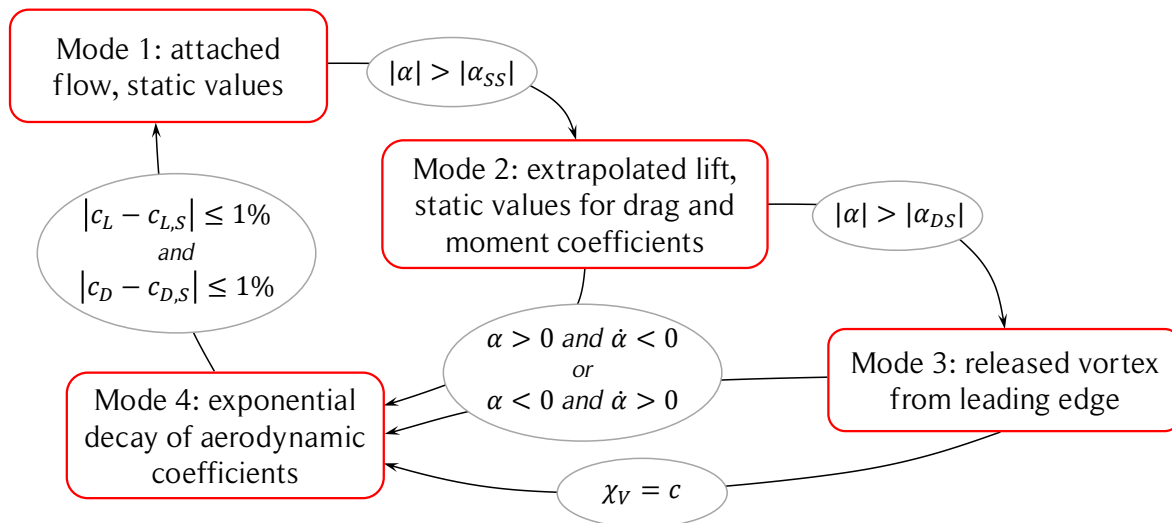


Figure 3.34. Diagram of the MIT dynamic stall model.

The figure shows the diagram of the MIT dynamic stall model and the rules to switch between the four modes. Source: own elaboration.

In Mode 1, the lift and drag coefficients are determined from the static tabulated data. The method continues in this mode until the angle of attack increases from below the static angle to above. The static stall angle of attack, α_{SS} , is defined as the angle at which the lift coefficient slope has a value of $a_0 = 0.05/1^\circ$ [92]. The static stall lift coefficient, $c_{L,SS}$, is calculated based on the static stall angle. Then the method goes to Mode 2. Note that the description presented here is for positive angles of attack. The equivalencies of Eq. (3.108) are still valid for this model.

If the angle of attack, α , exceeds the static angle, α_{SS} , but is still less than the dynamic stall angle, α_{DS} , the model switches to Mode 2 and the drag and moment coefficients are selected from the static tabulated data and the lift coefficient is estimated from Eq. (3.113), where $c_{L,SS}$ is the lift coefficient at the static stall angle and the angle of attack is measured in degrees. When the geometric angle of attack reaches the dynamic stall angle, the method switches to Mode 3. If the angle of attack starts to decrease ($\dot{\alpha} < 0$) before the peak lift is reached, the method switches to Mode 4.

$$c_L = c_{L,SS} + 0.05(\alpha - \alpha_{SS}) \quad (3.113)$$

In Mode 3, a vortex is assumed to be released from the leading edge. Then, it moves in the streamwise direction over the upper surface of the airfoil, growing in strength as it moves. Consequently, the lift continues to increase and the center of pressure moves aft, contributing to a plunging moment. The vortex is assumed to move at 50% of the blade rotational speed [92]. The maximum lift and moment coefficients are calculated based on an instantaneous pitch rate parameter, $c\dot{\alpha}/W$, from an empirically derived relation, showed in Eqs. (3.114) and (3.115), respectively.

$$c_{L,max} = \begin{cases} 1.0 + 40.0 \left| \frac{c\dot{\alpha}}{W} \right|, & 0.00 \leq \left| \frac{c\dot{\alpha}}{W} \right| \leq 0.05 \\ 3.0, & 0.05 < \left| \frac{c\dot{\alpha}}{W} \right| \end{cases} \quad (3.114)$$

$$c_{M,max} = \begin{cases} -0.15, & 0.00 \leq \left| \frac{c\dot{\alpha}}{W} \right| \leq 0.02 \\ -0.15 - 21.0 \left(\left| \frac{c\dot{\alpha}}{W} \right| - 0.02 \right), & 0.02 \leq \left| \frac{c\dot{\alpha}}{W} \right| \leq 0.05 \\ -0.78, & 0.05 < \left| \frac{c\dot{\alpha}}{W} \right| \end{cases} \quad (3.115)$$

The lift coefficient continues to be calculated from Eq. (3.113) until it reaches the maximum value given by Eq. (3.114). It is assumed that the maximum lift occurs when the dynamic stall vortex reaches the midchord, $\chi_V = c/2$, where χ_V is the position of the vortex core measured on the chord line and from the leading edge. The maximum pitching moment occurs when it reaches the 3/4-chord position. The pitching moment about the quarter chord is calculated on the basis of the position of the center of pressure, as shown in Eq. (3.116), where c_N is the normal coefficient shown in Eq. (3.117) and χ_{CP} is the position of the center of pressure measured in chords from the leading edge.

$$c_M = -c_N(\chi_{CP} - 0.25) \quad (3.116)$$

$$c_N = c_L \cos \alpha + c_D \sin \alpha \quad (3.117)$$

The rearward movement of the center of pressure is assumed to be constant and according to [7] its position is calculated from Eq. (3.118), where t is time in seconds, t_{DS} is the time at which the vortex was released from the leading edge, V is the velocity of still air relative to a rotating blade, t_L is the time when the maximum lift coefficient was reached and χ_{CPL} is the position in chords of the center of pressure where the maximum lift coefficient was reached.

$$\chi_{CP} = \begin{cases} (t - t_{DS}) \frac{V}{4c} + 0.25, & c_L \leq c_{L,max} \\ (t - t_L)(0.75 - \chi_{CPL}) \frac{2V}{c} + \chi_{CPL}, & c_L > c_{L,max} \end{cases} \quad (3.118)$$

The lift and moment coefficients increase until the vortex reaches the respective position of maximum value ($\chi_V = c/2$ for lift and $\chi_V = 3c/4$ for moment), or until the limits of Eqs. (3.114) and (3.115) are reached, whichever happens first. The MIT model holds the coefficients, c_L and c_M , at that level until the peak angle of attack is reached. The drag coefficient is calculated from Eq. (3.119) in this mode.

$$c_D = c_D(\alpha) \left| \frac{\alpha}{\alpha_{DS}} \right| \quad (3.119)$$

Pawsey states that at low TSR , the amplitude of the angle of attack oscillations may be very large for Darrieus turbines. Therefore, it is not considered a good estimation to maintain the maximum values for so long [7]. Thus, the maximum values are held constant until the dynamic stall vortex reaches the trailing edge and then the decay of the dynamic stall phenomenon begins. Since the vortex velocity is considered constant, this

time can be calculated from its position and velocity. According to [92], the vortex core velocity is assumed to be 50% of the blade velocity.

When the vortex reaches the trailing edge ($\chi_V = c$), the method switches to Mode 4. Alternatively, if the angle of attack starts to decrease ($\dot{\alpha} < 0$) before the peak lift is reached, the method switches to Mode 4 and the exponential decay of coefficients begins immediately from the reached values.

In Mode 4, the coefficients decay towards the static values at the current angle of attack, as shown in Eqs. (3.120) and (3.121), where $c_{L,s}$ and $c_{M,s}$ are the static values of the lift and moment coefficients, respectively, θ is the azimuthal angle and θ_0 is the azimuthal angle at which the decay started (when the vortex reached the trailing edge).

$$c_L = [c_{L,max} - c_{L,s}(\alpha)] \exp\left[-\frac{2R}{c} (\theta - \theta_0)\right] + c_{L,s}(\alpha) \quad (3.120)$$

$$c_M = [c_{M,max} - c_{M,s}(\alpha)] \exp\left[-\frac{2R}{2.5c} (\theta - \theta_0)\right] + c_{M,s}(\alpha) \quad (3.121)$$

According to Pawsey, the drag coefficient is calculated from Eq. (3.122) in this mode. However, in general, there will be a discontinuity of the drag coefficient when changing from Eq. (3.119) of Mode 3 to Eq. (3.122) of Mode 4. Therefore, Eq. (3.123) is used instead.

$$c_D = c_{D,s}(\alpha) \left| \frac{c_L}{c_{L,s}(\alpha)} \right| \quad (3.122)$$

$$c_D = [c_{D,max} - c_{D,s}(\alpha)] \exp\left[-\frac{2R}{c} (\theta - \theta_0)\right] + c_{D,s}(\alpha) \quad (3.123)$$

Mode 4 remains in effect until all aerodynamic coefficients are within 1% of the static values. Then, the method returns to Mode 1.

3.8.6. Tower effects

In Darrieus turbines, it is difficult to avoid the presence of a rotating central tower. The tower affects the flow at the downstream side of the turbine. Hence, it also affects the blade aerodynamics. The flow behind the tower will have a lower speed than if there

were no tower. A Gaussian distribution is commonly used to model the deceleration of the flow. The rotating tower adds additional flow perturbations. However, Paraschivoiu in [10] states that the tower rotation for the usual operating range for Darrieus turbines is almost negligible because the tower rotational ratio r_T defined in Eq. (3.124) is rather low, where ω is the rotational speed of the turbine (and tower), R_T is the tower radius and U_e is the local wind velocity at the tower. Therefore, the wake-velocity deficit is calculated using the fixed circular cylinder momentum theory.

$$r_T = \frac{\omega R_T}{U_e} \quad (3.124)$$

The tower wake flow is calculated as a linear superposition of the main flow pattern and the wake-velocity deficit, as shown in Fig. 3.35. For Reynolds numbers between 300 and 3×10^5 , the Strouhal number, St , corresponding to a free-vortex frequency, f , is calculated using Eq. (3.125) and remains nearly constant with a value of about 0.21. This frequency can be used to calculate the influence of the tower wake on the blade aerodynamics of the downstream side for time dependent models.

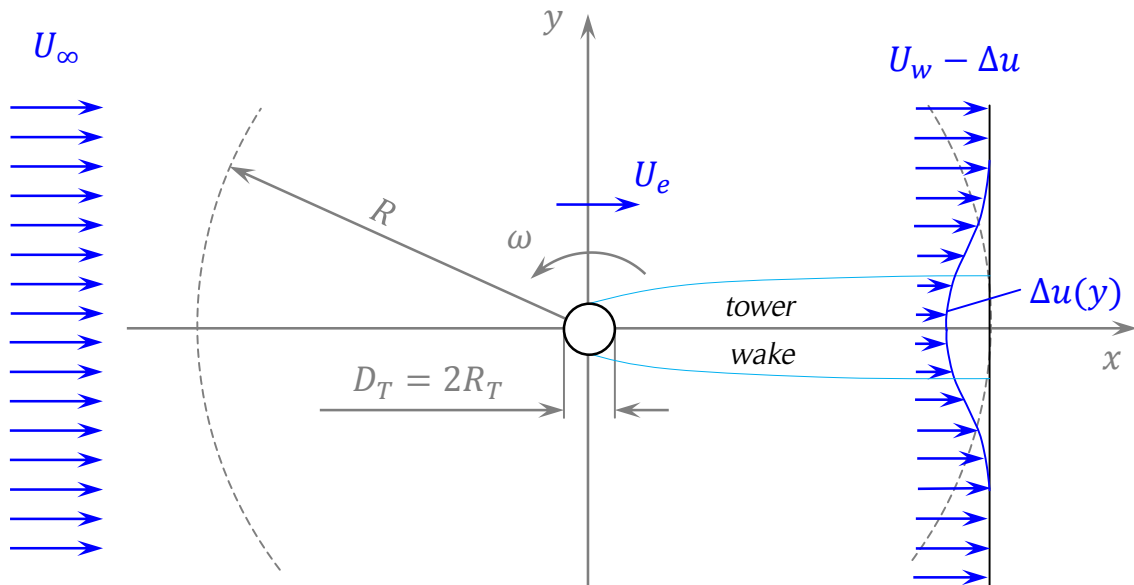


Figure 3.35. Tower wake-velocity deficit.

The figure shows the tower wake-velocity deficit produced in the downstream side of the turbine. Source: own elaboration based on [4].

$$St = \frac{f D_T}{U_e} \quad (3.125)$$

Nygaard presented an analysis of the tower wake of a HAWT [93]. Far downstream from the tower, the wake is assumed to become self-similar, i.e., the wake shape is similar to itself along the streamwise direction. Using the streamwise momentum equation and some assumptions, a relatively simple approach is obtained. The velocity profile at the wake, $U_p(y)$, is calculated from Eq. (3.126), where Δu is the wake-velocity deficit. Note that in general $U_p = U_p(x, y)$. In the context of Darrieus SB-VAWTs, the terms of Eq. (3.126) are evaluated only at $x = R$, and therefore the terms only depend on the y coordinate: $\Delta u = \Delta u(y)$ and $U_p = U_p(y)$.

$$U_p(y) = U_w - \Delta u(y) \quad (3.126)$$

The spatial distribution of Δu is calculated from Eq. (3.127), where Δu_{max} is the maximum velocity deficit, which is calculated in Eq. (3.128), where $y_{1/2}$ is the half-velocity point, which is calculated from Eq. (3.129). The momentum thickness, θ , is estimated using Eq. (3.130), where c_D is the tower drag and D_T is the tower diameter. A tower drag coefficient, c_D , of 1.15 can be used for the range of Reynolds number of the typical parameters of a Darrieus turbine [4].

$$\frac{\Delta u}{\Delta u_{max}} = \exp \left[-0.693 \left(\frac{y}{y_{1/2}} \right)^2 \right] \quad (3.127)$$

$$\Delta u_{max} = 1.75 U_e \left(\frac{\theta}{x} \right)^{1/2} \quad (3.128)$$

$$y_{1/2} = 0.275 (x\theta)^{1/2} \quad (3.129)$$

$$\theta = \frac{c_D D_T}{2} \quad (3.130)$$

3.8.7. Turbine struts losses

In general, blades are responsible for the primary drag force of the Darrieus turbines. However, other turbine parts such as the tower and struts can produce significant losses of the turbine power performance due to drag forces [4]. In Darrieus CB-VAWTs, struts are used to give rigidity to blades and reduce rotor stresses. On the other hand, struts of Darrieus SB-VAWTs are commonly the only way to transfer the forces acting on the blades to the turbine tower [4]. In some designs, the struts can be avoided using a squirrel

cage configuration. The disks at the turbine ends will still produce drag due the shear stress and the respective boundary layer formed on the disk surfaces.

In general, struts are straight structures that form an angle φ with the horizontal. They have an airfoil section (to reduce drag) of variable chord, c_s , along their span, l . The torque, $d\tau_D$, produced by the drag force acting on a strut segment, dl , can be calculated from Eq. (3.131), where ρ is the air density, W_r is the relative wind velocity, α_r is the angle of attack, and c_D is the drag coefficient of the strut cross sectional shape (see Fig. 3.36).

$$d\tau_D = \frac{1}{2} \rho c_s dl (W_r \cos \alpha_r)^2 c_D r \quad (3.131)$$

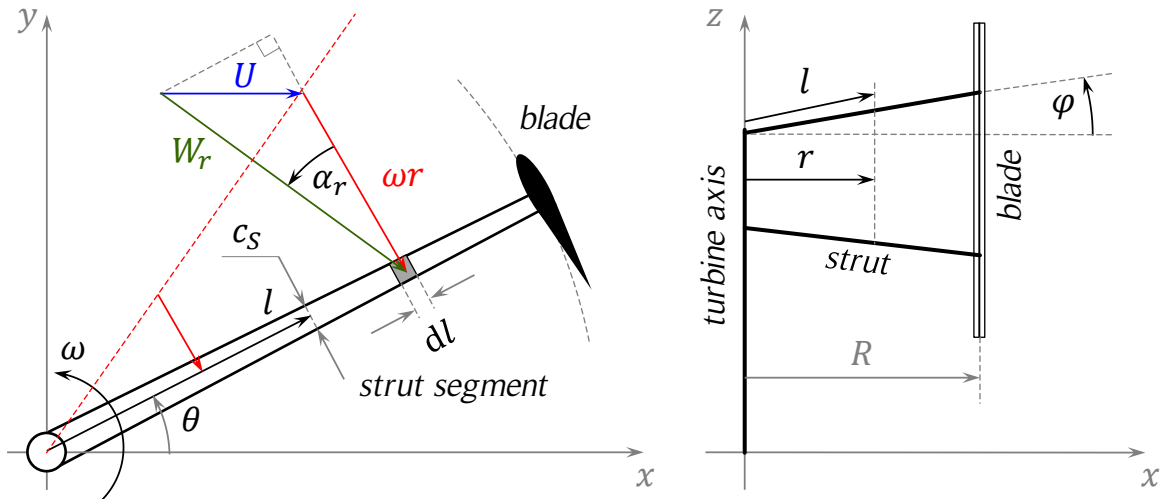


Figure 3.36. Triangle of velocities for a strut segment.

The figure shows the main parameters for the calculation of the drag force acting on a strut segment. Note that the rotational velocity depends on the radial position of the strut segment. Source: own elaboration.

The relative wind velocity, W_r , is a function of the position of the strut section, r , as shown in Eq. (3.132), where ω is the rotational speed of the turbine and U is the local wind speed. The angle of attack, α_r , is calculated from Eq. (3.133). The total power loss of one strut, \dot{W}_S , is calculated by integrating the drag torque along the strut length, from the tower radius, R_T , to the turbine radius, R , and averaging for one rotation, as shown in Eq. (3.134). Note that $r = l \cos \varphi$, therefore, $dr = dl \cos \varphi$ and that in general the strut chord, c_s , varies along the strut span, l . The drag coefficient, c_D , depends only on the strut Reynolds number, Re_s , which is calculated using Eq. (3.135).

$$W_r = [(\omega r + U \sin \theta)^2 + (U \cos \theta)^2]^{1/2} \quad (3.132)$$

$$\alpha_r = \text{sign}(\cos \theta) \arccos \left(\frac{\omega r + U \sin \theta}{W_r} \right) \quad (3.133)$$

$$\dot{W}_s = \frac{1}{4\pi \cos \varphi} \rho \omega \int_0^{2\pi} \int_{R_T}^R (W_r \cos \alpha_r)^2 c_s c_D r dr d\theta \quad (3.134)$$

$$Re_s = \frac{c_s W_r \cos \alpha_r}{\nu} \quad (3.135)$$

3.8.8. Blade tip losses

Finite blades have higher lift to drag ratio in the center than at the tips. This phenomenon is caused by the uneven pressure at both faces of the blade, which in turn causes a circulation pattern at the blade tips. In airplanes, this effect produces tip vortices and a downwash air movement in the wake [94]. A similar phenomenon happens at the blade tips of SB-VAWTs, which causes a decrease in the turbine performance. The change in the flow direction near the tips is known as vertical streamtube expansion [4].

The dependence of aerodynamic performance on spanwise location was studied by Prandtl. Based on his studies, he developed a method for screw propellers. Later, Prandtl's method was modified by Willmer for a VAWT. The upstream and downstream loss factors, L_u and L_d , are calculated from Eqs. (3.136) and (3.137), respectively. The coordinates used in [4] were changed here to match the notation of the present work. Thus, the vertical coordinate, z , varies between H_0 and $H_0 + H$, as shown in Eq. (3.138). Note that the loss factors become 1 at $z = H_0 + H/2$ (half of the blade height). The upstream and downstream factors, s_u and s_d , are calculated from Eqs. (3.139) and (3.140), where U_e is the equilibrium velocity at $z = H_0 + H/2$, N is the number of blades, and ω is the rotational speed of the turbine.

$$L_u = \frac{\arccos \left[\exp \left(-\frac{\pi Z}{s_u} \right) \right]}{\arccos \left[\exp \left(-\frac{\pi H}{2s_u} \right) \right]} \quad (3.136)$$

$$L_d = \frac{\arccos \left[\exp \left(-\frac{\pi Z}{s_d} \right) \right]}{\arccos \left[\exp \left(-\frac{\pi H}{s_d} \right) \right]} \quad (3.137)$$

$$Z = \frac{H}{2} - \left| z - H_0 - \frac{H}{2} \right| \quad (3.138)$$

$$s_u = \frac{\pi U_e}{N\omega} \quad (3.139)$$

$$s_d = \frac{\pi U_w}{N\omega} \quad (3.140)$$

The loss factors, L_u and L_d , are applied in the perpendicular component of the relative wind velocity of the blade at the calculation of the relative wind velocity, W , and the angle of attack, α , as the factor L_i , where i stands for upstream or downstream, as shown in Eqs. (3.141) and (3.142). An example of the variation of $L_u(z)$ is presented in Fig. 3.37.

$$W = [(V + U \sin \theta)^2 + (L_i U \cos \theta)^2]^{1/2} \quad (3.141)$$

$$\alpha = \text{sign}(\cos \theta) \arccos \left(\frac{V + U \sin \theta}{W} \right) \quad (3.142)$$

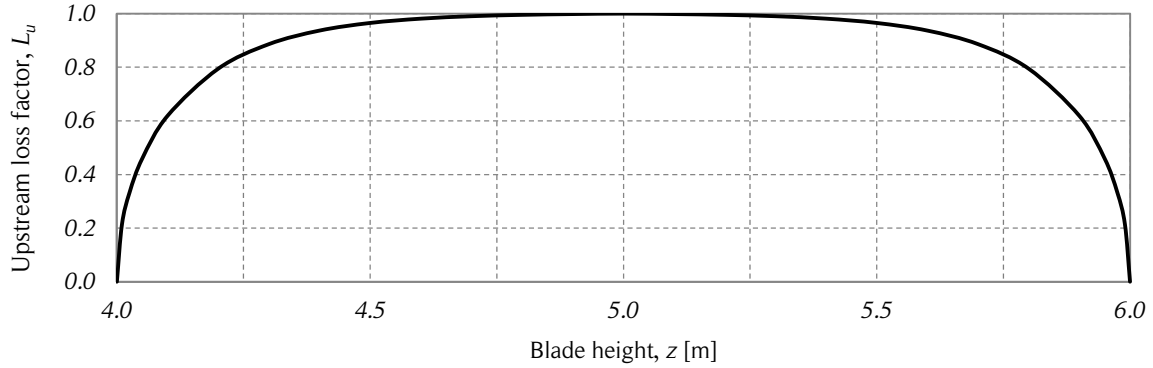


Figure 3.37. Upstream loss factor vs. blade height.

The figure shows the upstream loss factor as a function of the blade height for a three-bladed turbine of 4 m of ground clearance and blade length of 2 m. The equilibrium velocity is 7 m/s and the rotational speed is of 13.3 rad/s. Source: own elaboration.

The finite aerodynamic coefficients are calculated from the infinite lift and drag coefficients, which are evaluated at the angle of attack, α , as shown in Eq. (3.143) and (3.144), where t/c is the thickness-to-chord ratio and H/c is the blade aspect ratio [94]. The infinite lift and drag coefficients have the subscript ∞ and the finite coefficients the subscript f .

$$c_{L,f} = \frac{c_{L,\infty}}{1 + 1.8 \left(1 + 0.8 \frac{t}{c}\right) \frac{H}{c}} \quad (3.143)$$

$$c_{D,f} = c_{D,\infty} + \frac{c}{\pi H} (c_{L,f})^2 \quad (3.144)$$

With the presence of the downwash velocity, the effective angle of attack (in radians), α_e , is calculated from Eq. (3.145). However, since the expressions for the modified aerodynamic coefficients were derived from the linear theory of airfoils, they are not used in the dynamic stall calculations.

$$\alpha_e = \alpha - \frac{c}{\pi H} c_{L,f} \quad (3.145)$$

According to [4], the tip losses have a great influence on the turbine power coefficient, but little effect on structural design. This is due to the fact that the tip losses reduce the tangential forces but have little effect on the radial forces, which in general, are much larger than the tangential forces. The maximum specific power (power divided by turbine sectional area) is plotted in Fig. 3.38 for several turbines of the same solidity $\sigma = 0.0067$ (with turbine radius $R = 3 \text{ m}$). This plot was redrawn from [4] and can be useful for the design of Darrieus SB-VAWTs. For a small-scale turbine with a blade aspect ratio of $H/c = 30$, the power is reduced about 10%.

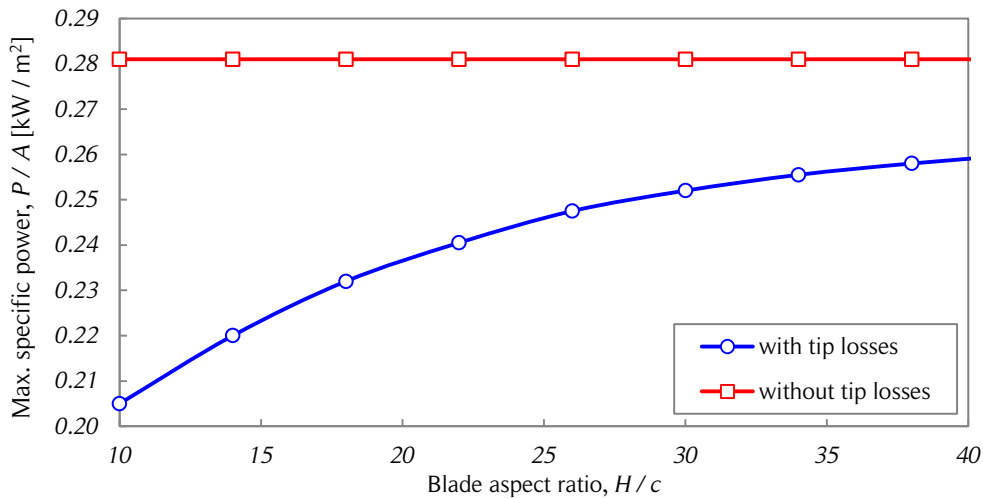


Figure 3.38. Specific power vs. blade aspect ratio.

The figure shows the specific power as a function of the blade aspect ratio with and without tip losses. A turbine with solidity of 0.0067, with radius $R=3 \text{ m}$ and operating at $TSR = 2.7$ was considered to build the curves. Source: [4].

3.9. Vortex models

3.9.1. General considerations

Streamtube momentum models predict reasonably well the overall performance of wind turbines when the rotor blades are lightly loaded (for small solidity and moderate TSR). However, streamtube models become invalid for large TSR and also for high solidity rotors because of the wake structure generated in these cases. In general, predicted blade loads are inaccurate since these models assume quasi-steady flow through the rotor.

Another class of aerodynamic predictions for Darrieus turbines is based on potential flow. This approach is based on vorticity equations in which pressure does not appear explicitly and is not needed to determine the velocity field. The vorticity regions are treated as thin sheets or points of concentrated vorticity to facilitate numerical calculation. Two-dimensional and three-dimensional models have been developed to predict the power performance of Darrieus turbines [4, 95-97]. Several studies of Darrieus turbines power performance using vortex models have been published. One of the most used models is a free-vortex model developed by Strickland et al. [4]. Only the basic principles of the free-vortex models are presented here.

The main advantage of the vortex models is that they predict the turbine wake in a better way than the BEM models. The wake structure, turbulence and their time dependency are intrinsically included in vortex models. The main drawbacks are that they require considerable more computational time than BEM models and still rely on significant simplifications such as the viscosity and pressure in the blade boundary layer, which is included through empirical aerodynamic coefficients [3].

3.9.2. Free-wake vortex model

In this model the production and convection of vortices springing from the turbine blades is used to predict the induced or perturbed velocity of the flow around the turbine. The induced velocity is calculated as the superposition of the freestream velocity and the perturbations produced by the vortex systems. The aerodynamic coefficients are obtained using airfoil data [95].

In vortex theory airfoils are commonly replaced by a bound vortex filament sometimes called a substitution vortex filament or a lifting line. To obtain better predictions, a distribution of bound vortices along the camber line can be used. However, if only one

bound vortex is used, the wake behind the airfoil at a distance larger than one chord is well represented. Therefore, to simplify the model and reduce computational time, usually only one bound vortex is used.

If the strength of the bound vortex, Γ , changes in time due to a change of the lift force acting on the airfoil, then a vortex is shed. The Kutta-Joukowski law gives a relationship between the lift force, F_L , per unit span of a blade and the bound vortex strength, Γ , as shown in Eq. (3.146). A blade that experiences lift changes over time is presented in Fig. 3.39. The strengths of the shed vortices have changed on several occasions producing different circulation values. The lift force is obtained from the tabulated aerodynamic coefficients. Unsteady aerodynamics can be included in the method applying dynamic stall models.

$$F_L = \rho U_\infty \Gamma \quad (3.146)$$

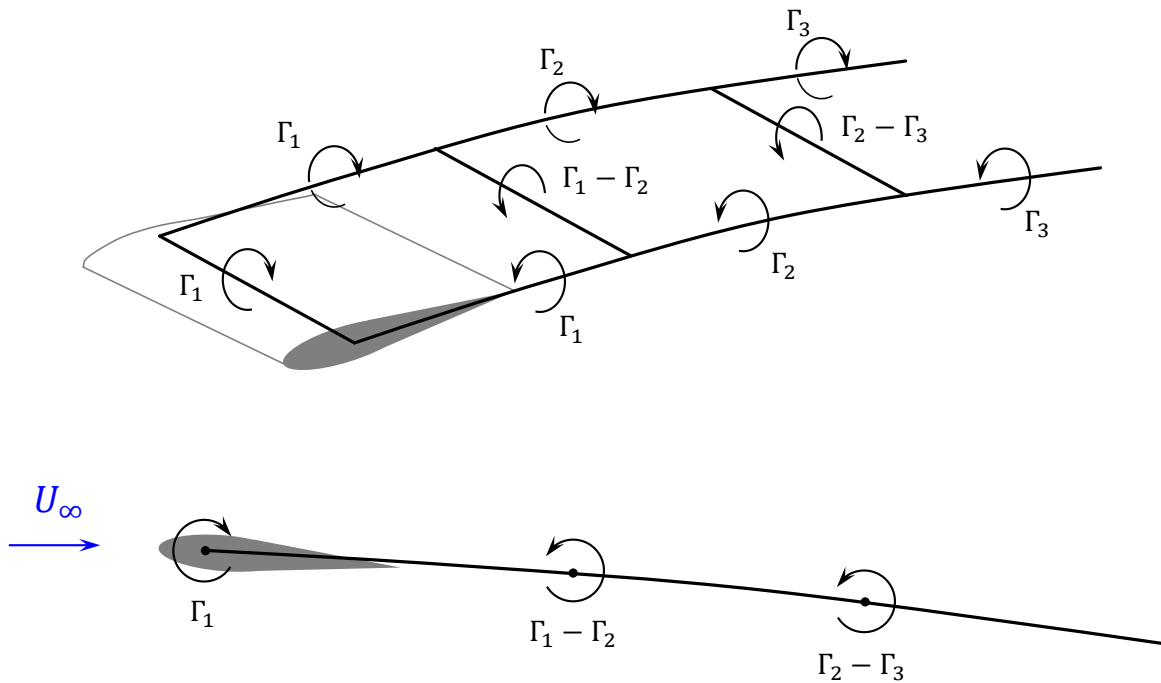


Figure 3.39. Vortex system for a single blade element.

The figure shows the three- and two-dimensional vortex systems for a single blade element that is experiencing lift changes in time, and therefore, is shedding vortices with different strengths. Source: redrawn from [4].

Each time a spanwise vortex is shed, its strength must be equal to the change in the bound vortex strength as it is stated by Kelvin's circulation theorem: the circulation around a close curve moving with the fluid remains constant in time. The mathematical expression of the theorem is presented in Eq. (3.147). Thus, if the contour encloses both the airfoil and its wake, any change in the bound circulation must be accompanied by an equal and opposite change in circulation in the wake. The center of each shed vortex is assumed to move with the fluid at the local fluid velocity.

$$\frac{D\Gamma}{Dt} = 0 \quad (3.147)$$

The velocity induced by a single vortex filament at any given point, Q , in the two-dimensional space can be obtained from the Biot-Savart law which relates the induced velocity with the filament strength, as shown in Eq. (3.148), where \vec{V}_Q is the induced velocity at a point Q , caused by a vortex filament of strength, Γ , and length, l , and \vec{r} is the position vector of points on the filament with respect to the point Q (see Fig. 3.40).

$$\vec{V}_Q = \frac{\Gamma}{4\pi} \int_0^l \frac{\vec{r} \times d\vec{l}}{r^3} \quad (3.148)$$

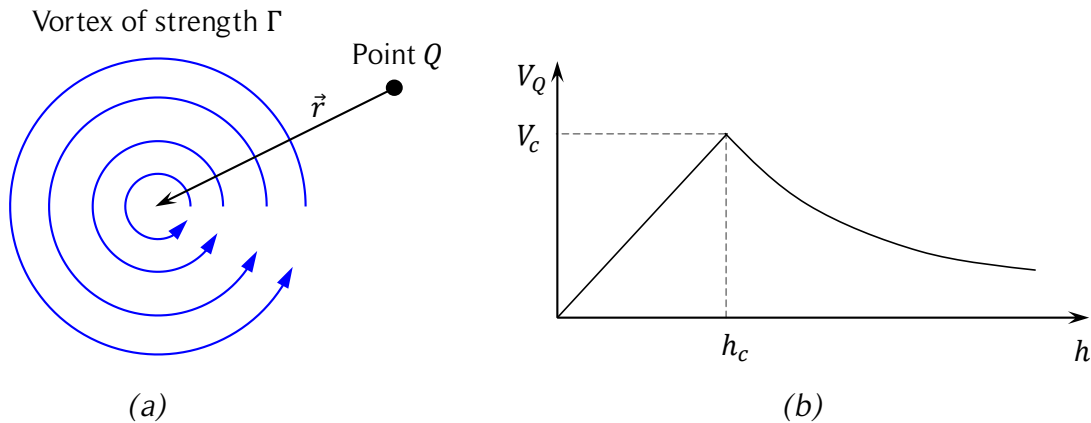


Figure 3.40. Velocity induced by a vortex.

The figure shows the velocity field in a two-dimensional space induced by a vortex of strength Γ . Source: redrawn from [95].

For an infinitely long vortex filament, Eq. (3.148) can be expressed as Eq. (3.149), where \vec{e} is in the unit vector in the direction of $\vec{r} \times d\vec{l}$ and h is the distance between the vortex filament and the point Q .

$$\vec{V}_p = \frac{\Gamma}{2\pi h} \vec{e} \quad (3.149)$$

The velocity induced by a straight vortex filament on itself is zero and therefore Eq. (3.149) is valid only outside the vortex core. The velocity induced inside the vortex core is proportional to the distance from the vortex filament and reaches a maximum value at the edge of the vortex core. According to [95], the maximum core velocity of a shed vortex, V_c , for VAWTs is calculated from Eq. (3.150), where R is the turbine radius and $\Delta\theta$ is the azimuthal distance traveled by the blade between two vortex shedding positions. The radial position of the maximum velocity of the vortex, h_c , known as the vortex core edge, is presented in Eq. (3.151). Therefore, the induced velocity caused by a vortex filament is calculated from Eq. (3.152).

$$V_c = \frac{1}{2} \frac{\Gamma}{R\Delta\theta} \quad (3.150)$$

$$h_c = \frac{R\Delta\theta}{\pi} \quad (3.151)$$

$$\vec{V}_p = \begin{cases} \frac{\pi \vec{h} \times \vec{\Gamma}}{2(R\Delta\theta)^2}, & 0 \leq h \leq h_c \\ \frac{\vec{h} \times \vec{\Gamma}}{2\pi h^2}, & h_c < h \end{cases} \quad (3.152)$$

The flow field around the turbine is constructed as the superposition of the freestream velocity and the induced velocity caused by all vortices. Once the velocity field is constructed for one time step, the turbine is rotated in a small azimuthal angle and the procedure is repeated for several time steps until convergence for an entire revolution is accomplished.

Since the calculation of the induced velocity by the vortices requires considerable resources, usually a grid of points distributed around the turbine and in the wake is considered. After some calculation time, many shed vortices should be moving along the turbine wake. To reduce computational time, some criteria can be used to neglect the effect in the turbine wake of certain vortices, for instance, the ones that are far away from the turbine and the ones that have a relative small strength. Vortices that have the same position or are very close to each other can be merged into one [95].

3.10. Computational fluid dynamics

Computational fluid dynamics (CFD) is a mixture of the two classic approaches of fluid dynamics: theoretical and experimental. CFD is based on mathematical models and equations that have to be solved. The solution is found numerically in a computational domain with the respective configuration and parameters of the situation. The obtained results commonly are a large set of data that has to be processed to get the variables of interest. For instance, the results can be the visualization of a velocity or pressure field, the visualization of streamlines around a body, or the aerodynamic coefficients of an airfoil [96]. CFD has existed for many years, but only in the recent decades the computational resources have become powerful enough to make simulations of complex problems such as the three-dimensional and transient flow around a Darrieus wind turbine. However, there are still a large set of problems that require huge human and computational efforts to be solved. In many cases, considerable simplifications are still required.

Several two-dimensional and three-dimensional CFD studies of Darrieus DB-VAWTs have been carried out [99-105]. These CFD simulations solve the governing equations (continuity, momentum and energy) using commercial softwares or own-programmed codes. Most of them are based on the finite volume method. To implement a successful simulation, several aspects have to be taken into account carefully. Some of them are: computational domain, mesh, boundary conditions, and solution methods for the pressure-velocity coupling, turbulence models, and boundary layer treatment, among others (for more details see [98]). If these considerations are carefully looked into, accurate results can be achieved. However, in general, CFD simulations require much more computational resources than BEM or vortex models.

Currently, powerful computers are affordable for almost any research center; therefore, if experimental resources such as a wind tunnel or a scale model of a wind turbine are not available, CFD simulations can present considerable lower costs than experiments. On the other hand, CFD simulations have the advantage of being portable, namely, they can be easily shared with other researches around the world through storage devices or the internet. One disadvantage of CFD is that commercial softwares are relatively expensive. Additionally, in many cases the user does not have full control on the software, which can easily lead to poor simulations if the software design and limits are not considered carefully. Own programmed codes do not have that disadvantage but require a lot of human effort to be developed.

Due to its intrinsic numerical nature, CFD simulations can produce a large amount of

information. For instance, a transient simulation of a Darrieus turbine, depending on the size of the computational domain and mesh, can easily generate many gigabytes of data for only a few seconds of real time operation of the turbine. This information can be very useful to help understanding phenomena that in general are hardly measurable in experiments such as pressure fields, turbulence distribution, and so on. Some experimental techniques can also generate large amounts of valuable data. Particle image velocimetry (PIV) and image treatment from flow visualizations such as dye or hydrogen bubbles are among these techniques.

In conclusion, CFD simulations can be very powerful and useful, but have to be used carefully to obtain accurate results. They require considerable computational resources and time. Therefore, if a large amount of design and operation cases of Darrieus wind turbines have to be studied, it could be helpful to have at disposal a faster tool such as BEM models that can make reasonably good estimations. Thus, the most relevant design and operation cases can be found without using too much time. Later, the relevant cases can be validated and studied in detail with more accurate approaches such as CFD simulations, experiments carried out in laboratories or field tests.

3.11. Dynamic effects

The performance analysis of Darrieus VAWTs usually is performed under static conditions: constant wind speed (magnitude and direction); and constant angular velocity of the turbine. Therefore, transient operational conditions of the turbine, such as its start-up or stop, are typically not modeled. However, in places where the wind resource shows large variations in time, transient conditions might be decisive for the technical and economic assessment of a wind turbine.

The angular acceleration and deceleration, $\ddot{\theta}$, of the turbine is related to the moment of inertia of the turbine-generator system, I , and the torques acting on the turbine shaft, as shown in Eq. (3.153). Commonly, the torques acting on the shaft are: the aerodynamic torque of the turbine blades, τ_T ; a resistive torque caused mainly by the drag of the blade struts and the friction of the bearings, τ_{res} ; and an electric load caused by the generator, τ_e ; as shown in Eq. (3.154) [106, 107].

$$\sum \tau = I\ddot{\theta} \quad (3.153)$$

$$\tau_T + \tau_{res} + \tau_e = I\ddot{\theta} \quad (3.154)$$

Even under steady wind conditions, the torque of the blades usually is not constant for VAWTs. This phenomenon is caused by the azimuthal dependency of the aerodynamic forces acting on the blades. Multiple blades, helical blade geometry and/or turbine tiers with the adequate angular offset can decrease the negative effect of the aforementioned phenomenon. The inertia of the system also plays an important role in the dynamic behavior of the turbine [107].

The influence of the wind resource variation in time on the Darrieus VAWTs performance has been studied by several authors. A numerical and experimental study was conducted by Danao et al. [105]. According to their results, SB-VAWTs operating under periodically fluctuating winds, overall performance can be slightly improved if a series of conditions are met. In general, large wind speed fluctuations produce a lower aerodynamic performance [105]. Another experimental study on the unsteady wind conditions influence on SB-VAWTs performance was conducted by Kooiman and Tullis [108]. Their experimental testing confirmed the independence of the direction fluctuations and quantified the impact of the wind speed fluctuations on the turbine performance. According to Kooiman and Tullis, a turbulent intensity below $TI = 0.15$ based on an averaging interval of 10 s have a minimal impact on the turbine performance. An experimental study on the influence of turbulence on lift and drag coefficients of airfoils was performed by Delnero et al. [118].

3.12. Control and optimization

Performance and safety improvements of Darrieus SB-VAWTs maintaining a simple design and low cost are key features to boost a greater use of this type of wind turbines. The aim of this section is to address a brief description of the control and optimization of Darrieus SB-VAWTs.

3.12.1. Control

Power control strategies for wind turbines are commonly classified in two types: fixed pitching and variable pitching of blades [109]. Pitch control and active stall belong to the variable pitching strategies. When wind speeds exceed a certain value, pitch control plunges the blades to decrease the angle of attack, which in turn decreases lift and power. On the other hand, under those conditions, active stall pitches the blades to make them stall. The control strategy for fixed pitch blades is called passive stall. The blades of

turbines with this control strategy take advantage of the inherent stall phenomenon that takes place for stronger winds. The aerodynamic design of the blades for this control strategy is crucial for the turbine safety. Among other reasons, these blades are slightly twisted along their longitudinal axis to produce the blades to stall gradually.

For some types of Darrieus VAWTs, such as CB-VAWTs or HB-VAWTs, it is not possible to use pitch control due to the geometric and construction characteristics of those turbines [110]. Some SB-VAWTs use pitch control. However, due to the reasons discussed below, most Darrieus VAWTs use passive stall control. This strategy is based on a powerful generator that controls the rotational speed of the turbine. At high wind speeds, if the rotational speed is kept at relative low values, the TSR decreases. This causes large variations in the angle of attack and the turbine to stall.

Darrieus VAWTs with passive stall typically use a direct driven generator [110]. The generator must meet the following characteristics to achieve good overall performance. It is desirable to have high efficiency for a large range of rotational speeds due to the variable rotational speed used in passive stall. Additionally, it requires a large overload capability to be able to stand the high turbine power generated at strong winds. According to Eriksson [109], the generator overload capability depends on the pull-out torque, which is the maximum torque that the generator can handle before becoming desynchronized. A small load angle at rated power is a good measurement of a good pull-out torque, and therefore, a good overload capability. High temperature in the generator decreases the overload capability. The generator can also be used as a motor for the start-up of the turbine.

Depending on the wind speed, Darrieus SB-VAWTs with passive stall control can be operated according to different rules. A brief example is described here and shown in Fig. 3.41 (a). Below the cut-in wind speed the turbine is not operated. For wind speeds above the cut-in wind speed but below the rated power wind speed, the turbine is operated at optimum TSR . For wind speeds above the rated power wind speed but below the cut-off wind speed, the turbine rotational speed is controlled to obtain constant power output.

A schematic plot of the turbine, P_T , and electric, P_e , power curves as a function of the rotational speed is shown in Fig. 3.41 (b). The turbine and generator are designed in such way that the powers coincide at the optimum rotational speed of the blade power curve. At low rotational speeds, when the electric power is higher than the power supplied by the blades, the rotational speed decreases and the turbine stops. When the blade power is higher than the electric power, the turbine accelerates until the equilibrium position. This

rotational speed range is known as the stable region. If the rotational speed is above the equilibrium, it will decrease until the equilibrium is met. Other control possibilities to take advantage of the power generated at low rotational speeds were discussed by Goude and Bülow [111, 112].

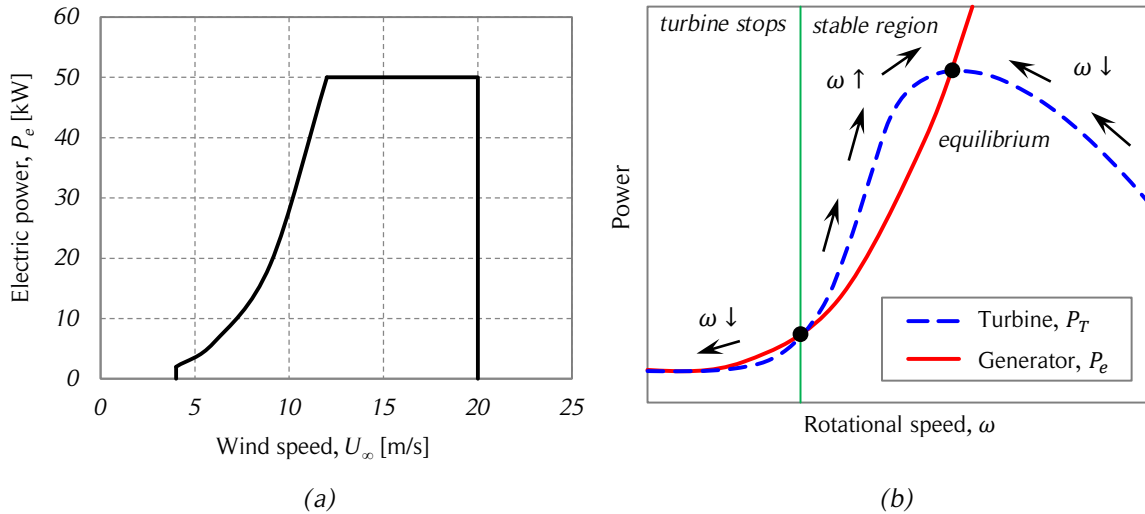


Figure 3.41. Typical power curves of a Darrieus VAWT with passive stall.

The figure shows: (a) a typical electric power curve as a function of the wind speed and (b) electric and turbine power curves as a function of the rotational speed for a Darrieus VAWT with passive stall. Source: redrawn from [109, 111].

3.12.2. Performance improvement

Several variable pitch strategies to improve performance of SB-VAWTs have been studied. They are commonly classified into active and passive variable pitch. This topic was discussed by Pawsey [7]. The aim of variable pitch is to avoid large angles of attacks, and thus, stall. Variable pitching allows comparatively higher torques at low and intermediate TSR than fixed pitch without compromising peak efficiency. It is considered not practical for $TSR < 1$ because of the large variations in the angle of attack. Active pitch is commonly performed by pneumatic or hydraulic actuators. Precise information of the wind conditions are required to operate the active variable pitch in a proper manner. Therefore, the system is comparatively more complex than a fixed pitch system and requires more maintenance. A 30% increase in annual energy production is claimed to be achievable by an optimized active pitch control proposed by Paraschivoiu et al. [66] Passive pitch allows the blades to pitch freely with the aim of pointing it into the relative

wind to avoid large angles of attack and stall. Blade inertia and aerodynamic moment are key elements in a passive pitch design. More details are available at [7].

Other approaches for improving the performance of Darrieus SB-VAWTs include the use of plasma actuators and synthetic jets. Greenblatt et al. [113] used dielectric barrier discharge plasma actuators installed at the blade leading edge of a small-scale high-solidity SB-VAWT. Overall performance improvements up to 38% were achieved. Yen and Ahmed [114] used synthetic jets to improve the aerodynamic blade performance of a NACA 0020 airfoil in a wind tunnel simulating low *TSR*. Synthetic jets are formed the ambient fluid by an oscillating piston or diaphragm enclosed within a cavity. Their experiments show that the blade performance at the downstream half can be enhanced and the turbine can generate more power.

3.12.3. Urban environment and wind farms

The control and optimization of Darrieus SB-VAWTs in urban environments and wind farms can be quite different from standalone turbines. The wind resource is affected by many elements in urban environments such as buildings, highways, street lighting, and trees, among others. SB-VAWTs can be benefitted from the concentrated and/or skewed flow caused by buildings and rooftops [30, 75]. On the other hand, the proper design of wind farms is a key feature to use the wind resource efficiently. This topic has been addressed by several authors. Dabiri states that a proper design of counter-rotating Darrieus SB-VAWTs wind farm can show an order-of-magnitude enhancement of the power density of present wind farms [82]. This is explained by the fast recovery of the turbine wakes caused by the counter-rotating SB-VAWTs. A diagram of the wind farm configuration is shown in Fig. 3.42.

In general, the flow around an operating turbine, especially for Darrieus turbines, is quite complex due its variation in time. Turbulence with several time and length scales is typically present in the wake of SB-VAWTs. One approach to describe the flow is to divide it into a time-averaged flow and a time-dependent flow. The DMS model is suitable for modeling the time-averaged flow. Other approaches, such as the vortex models, can be used to complement the time-dependency of the flow. Urban environments and wind farms in general will cause to have non-uniform velocity profiles in front of a turbine. Some examples of incoming velocity profiles are shown in Fig. 3.43. The first case, shown in Fig. 3.43 (a), can be observed if a turbine is located between two buildings or in staggered wind farms. The second case, shown in Fig. 3.43 (b), is the typical velocity profile of the wake of a Darrieus turbine and can be observed in a turbine

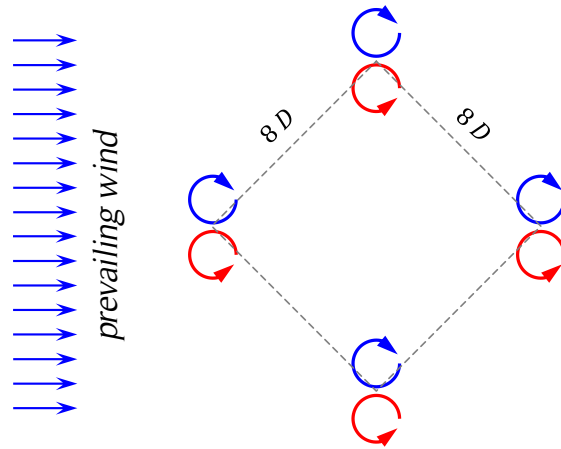


Figure 3.42. Wind farm arrangement of counter-rotating Darrieus SB-VAWTs.

The figure shows the wind farm spatial arrangement of counter-rotating Darrieus SB-VAWTs of the Graduate Aeronautical Laboratories of the California Institute of Technology. Source: redrawn from [80].

aligned behind another one. The third case, shown in Fig. 3.43 (c), can be observed in turbines located besides one building or in staggered wind farms. Calculations with these velocity profiles can be easily performed with the DMS model.

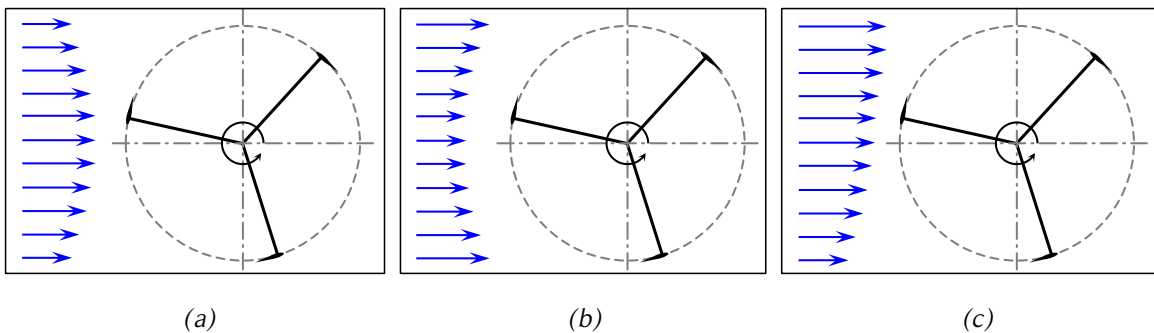


Figure 3.43. Incoming velocity profiles in urban environment or wind farms.

The figure shows three possible incoming wind velocity profiles found in urban environments or wind farms. Source: own elaboration.

4. REFERENCE CASE

The purpose of this chapter is to introduce a reference case to compare the results of the calculations performed with the variations of the DMS model presented in the following chapters. The experimental results of a field test study are presented first. Then, the results of a two-dimensional CFD simulation are shown. Three-dimensional corrections applied to the results of the simulations are able to validate the numerical study, and therefore, the numerical two-dimensional results can be used as the reference case for the calculations using the DMS model.

4.1. Uppsala University 12 kW SB-VAWT

4.1.1. General description

The reference case for this work is the Uppsala University 12 kW SB-VAWT [115], work lead by Kjellin. The turbine was built in 2006 by Uppsala University, Sweden [110]. The rotor is based on a SB-VAWT concept without blade-pitch control. The turbine is directly connected by a shaft to the electric generator located on the ground (see Fig. 4.1). The SB-VAWT operates at variable speed. Due to the fixed blades, mechanical control is not possible, thus, the turbine is controlled electrically by regulating the power from the generator. The generator is a permanent magnet synchronous generator. According to the authors of [115], protection in case of strong winds is provided by passive stall and a sufficient overload capacity of the generator.

4.1.2. Turbine specifications

The turbine was designed as a small research prototype, thus, the design parameters were chosen to obtain a relatively simple and reliable machine. Optimum energy production was not a design criterion; hence, the turbine tower was designed quite low to increase the simplicity and safety of the turbo machine. Tables 4.1 and 4.2 show the main nominal properties of the turbine and its generator, respectively.

The blades are tapered at the top and bottom. The tapering has a length of 1 m, starting at 60% of the chord on the tips, and increasing linearly up to 100% of the chord. Thus, only 3 m in the middle section of the blade has a constant chord of 250 mm. The turbine

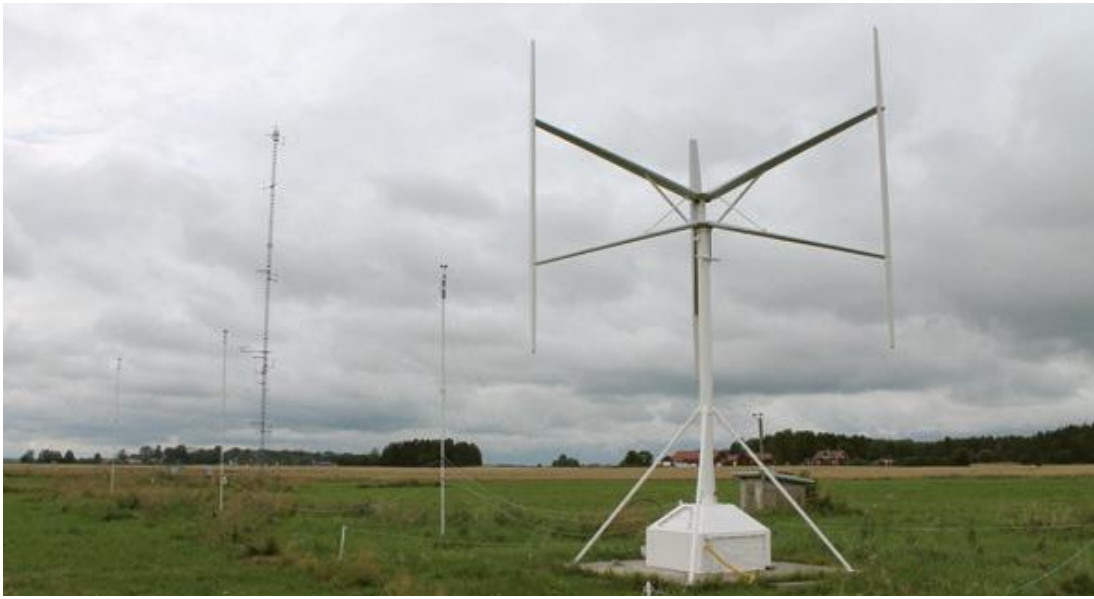


Figure 4.1. Uppsala University 12 kW SB-VAWT.

The figure shows the location site of the Uppsala University 12 kW SB-VAWT, Sweden. Source: [5.1]

Table 4.1. Nominal properties of the wind turbine.

Property	Value
Power	12 kW (at 12 m/s)
Rotational speed	127 rpm
Number of blades	3
Blade chord	0.25 m (NACA 0021)
Blade length	5 m
Turbine radius	3 m
Cross-section area	30 m ²
Hub height	6 m
Aerodynamic control	Passive stall

tower has a diameter of 200 mm. The blades are connected to the rotating shaft through two struts per blade. The struts have a NACA 0025 inspired profile that is trimmed at the trailing edge. The height of the trailing edge decreases with the distance from the hub: 38 mm close to the hub, 18 mm at the middle and 6 mm where the strut is connected to the blade. The strut chord length is 320 mm close to the hub, 280 mm at the middle and

Table 4.2. Nominal properties of the generator.

Property	Value
Power	12 kW
Phase voltage	156 V
Current	25.7 A
Electrical frequency	33.9 Hz
Efficiency	95.9 %
Number of poles	32
Load angle	5.8°

200 mm at the joint with the blade. The blade struts are at an angle of $\pm 17.6^\circ$ from the horizontal. Each pair of struts has two rods with a NACA 0025 airfoil shape that act as reinforcements. Each rod has a length of 1,000 mm, a chord of 100 mm and is at an angle of $\pm 40^\circ$ from the horizontal.

4.1.3. Experimental results

The turbine location is a well characterized wind site. Wind shear and wind distribution are known from several years of measurements (for more details see [110]). Air pressure, temperature and wind direction were collected at a meteorological measurement station located at less than 100 m from the wind turbine. The type of site is considered as ‘field’, the Weibull scale factor is 5.24 m/s and the Weibull form factor is 1.94. A cup anemometer was placed 15 m from the turbine. The power law shown in Eq. (2.10) is used to model the wind shear using a power law exponent of 0.185.

The voltage and current of the generator were measured to calculate the power output of the turbine. The data for wind speeds outside the range 3 – 17 m/s were rejected. The measurements when the anemometer was in the wake of the turbine were also rejected. Rotational speeds below 36 rpm and power less than 100 W were also not considered.

The power coefficient as a function of the tip-speed ratio is shown in Fig. 4.2. The results were obtained from a measurement campaign of two months, between March and May 2009, which produced a valid data set of 350 h.

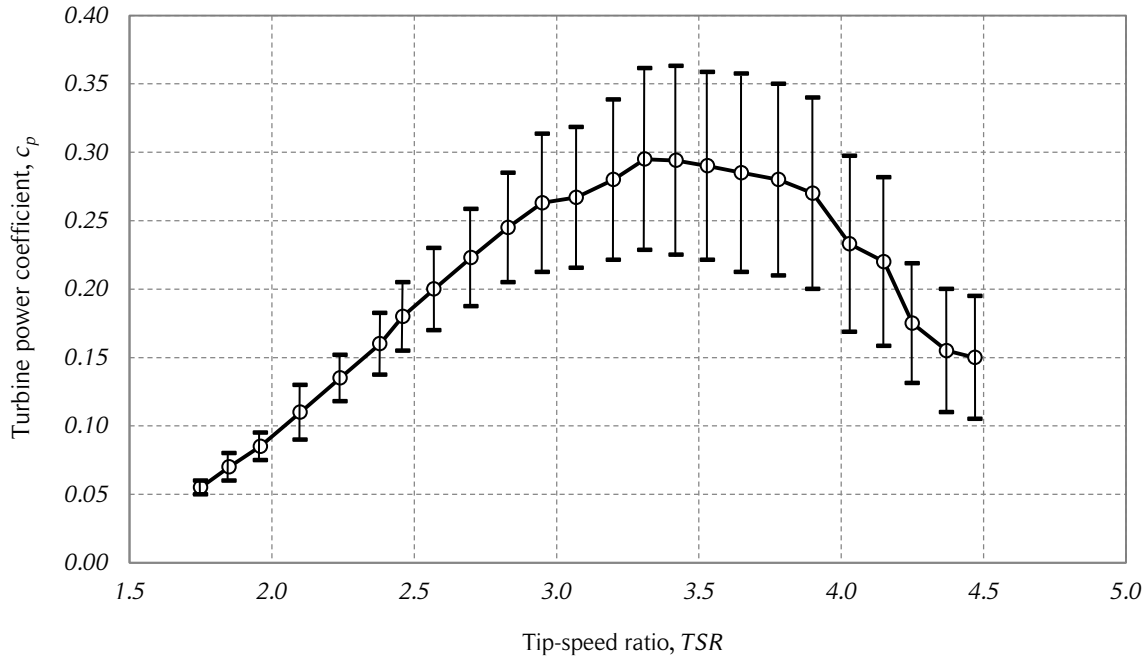


Figure 4.2. Turbine power coefficient vs. tip-speed ratio of the 12 kW SB-VAWT.

The figure shows the mean power coefficients as a function of the tip-speed ratio of the 12 kW SB-VAWT of the Uppsala University, Sweden. The estimated maximum error for each bin is shown. Source: [110].

4.2. Two-dimensional CFD simulations

The aim of this section is to show the set up and results of the two-dimensional CFD simulations performed in the present work. The computational mesh and software setup was provided by Rangel [99]. Blade and turbine aerodynamic coefficients and also information about the flow behavior are shown here because they are used as input and for comparison of the variations of the DMS model addressed in the following chapters.

4.2.1. General description

A two-dimensional CFD simulation based on the Uppsala University 12 kW SB-VAWT was performed by Rangel [99] with the aim of studying the variation of the aerodynamic performance of a SB-VAWT as a function of the blade surface temperature. The basic case considered the same temperature for both local air and blade surface, which is the configuration for the present work. The simulation was performed with the academic version of the software ANSYS Fluent v13.0. The $k - \omega$ SST (Shear Stress Transport)

turbulence model was used. The three blades and the shaft of the Darrieus SB-VAWT were considered in the two-dimensional model.

The results of the CFD simulations performed by Rangel were not suitable for the requirements of the present work mainly because of the turbine wake structure. Rangel's simulations were performed with an “outflow” boundary condition. After many turbine revolutions, the turbine wake is expected to be developed. However, the CFD simulations presented a strange behavior of the wake structure at the exit of the computational domain. According to [116], the outflow boundary condition uses an extrapolation procedure to update the velocity and pressure in a manner that is consistent with a fully-developed flow assumption. It must be noted that the gradients in the cross-stream direction may exist at an outflow boundary. Although this boundary condition at first glance may seem a proper boundary condition, [116] states that the outflow boundary may affect the convergence if there is a recirculation at the outflow boundary (particularly true for turbulent flow simulations). Therefore, in order to solve this problem, new CFD simulations were run using the same domain, mesh and maintaining the solution configurations. The only configuration changed was the boundary condition at the outlet of the computational domain (see Fig. 4.3). A “pressure-outlet” boundary condition was used instead of the “outflow” boundary condition.

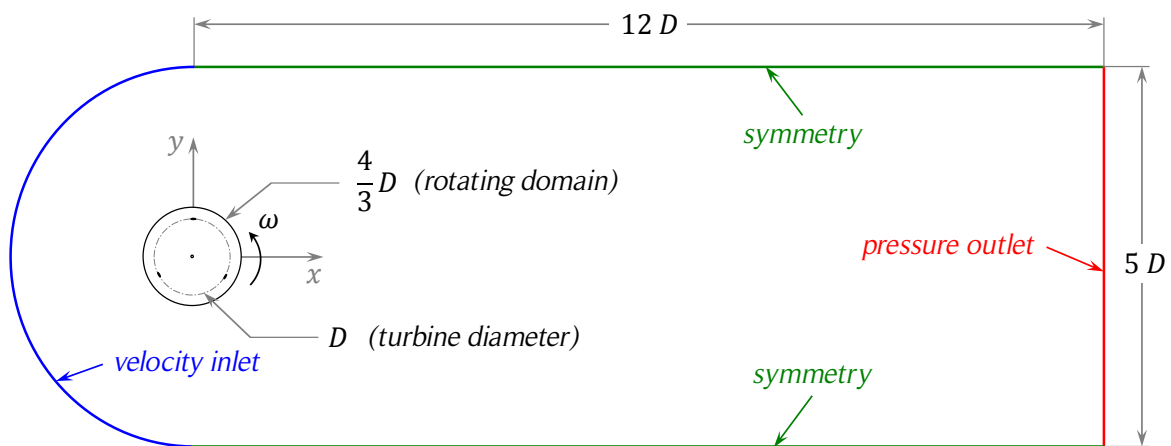


Figure 4.3. Computational domain and boundary conditions.

The figure shows the computational domain and boundary conditions of the CFD simulations performed in the present work, which are based on the simulations of Rangel's work [5.X]. Source: own elaboration.

The computational domain and boundary conditions are presented in Fig. 4.3. The element type of the two-dimensional mesh is the triangle. The mesh general information

is presented in Table 4.3. Element sizing was used near the walls to capture the boundary layer effects. More details of the computational mesh are available in [99]. The main simulation parameters are shown in Table 4.4. The local air speed was considered constant with a value of 10 m/s , which was chosen arbitrarily as a representative moderate value of the free-stream velocity at the turbine equator. Note that the turbine rated power is at 12 m/s .

Table 4.3. Mesh information.

Parameter	Value
Mesh element type	triangle
Number of nodes	277,490
Number of elements	550,881
Maximum skewness	0.7410
Minimum orthogonal quality	0.4719

Table 4.4. CFD simulation parameters.

Parameter	Nomenclature	Value
Airfoil geometry	AG	NACA 0021
Number of blades	N	3
Blade chord	c	250 mm
Turbine radius	D	6000 mm
Turbine solidity	σ	0.25
Tower diameter	D_T	200 mm
Blade fixation angle	α_0	0°
Air temperature	T	288.15 K
Air density	ρ	$1,225 \text{ kg/m}^3$
Air kinematic viscosity	ν	$1,45 \cdot 10^{-5} \text{ m}^2/\text{s}$

Six turbine rotational speeds were simulated. The rotational speeds were calculated from values of the tip-speed ratios between $TSR = 1$ and $TSR = 6$. This range encompasses the field test turbine performance curve presented in Fig. 4.2. The main solution parameters of the CFD simulations are presented in Table 4.5. A standard solution initialization was used, that is, all domain variables were set to constant initial values, in this case, the inlet values. Convergence of the solution was monitored in two ways. The

first criterion was a change smaller than 0.5% in the mean moment coefficient per rotation of each blade. The second criterion was the achievement of a fully developed wake, which was monitored quantitatively comparing the streamline shape at each revolution. Convergence was harder to achieve at high *TSR*. Convergence at *TSR* = 1 took 12 turbine revolutions. At *TSR* = 6, convergence was achieved after 60 turbine revolutions. Different time steps were used at each *TSR* case with a constant azimuthal angular discretization of $\Delta\theta = 360^\circ/1440 = 0.25^\circ$. Therefore, the fixed time step of each case was calculated from the turbine period divided by 1440, which satisfied the Courant number restriction for all cases. The relevant results of the CFD simulations of the present work such as the flow expansion, the power and force coefficients are presented in the following sub-sections of this section.

Table 4.5. Solution parameters.

Parameter	Value
Solver	2D, pressure-based, transient
Equations	Unsteady Reynolds Averaged Navier-Stokes (URANS), pressure-velocity coupling
Turbulence model	$k - \omega$ Shear Stress Transport (SST)
Solution scheme	Pressure Implicit with Splitting of Operators (PISO)
Spatial discretization gradient	Least squares cell based
Pressure	Second order
Momentum	Second order upwind
Turbulent kinetic energy	Second order upwind
Specific dissipation rate	Second order upwind
Transient formulation	First order implicit
Solution initialization	Standard
Maximum iterations per time step	10
Time step size	Depending on the <i>TSR</i> case, with $\Delta\theta = 0.25^\circ$ (satisfying the Courant number restriction in each case)

4.2.2. Blade moment coefficient

The blade moment coefficients were calculated by the software according to Eq. (2.33) using the pressure and shear stress distribution of the CFD simulations on each body of the computational domain to determine the resulting moment about the *z*-axis. This calculation was performed for the turbine tower and each blade at each time step (every

0.25°). The converged moment coefficients of one blade for each TSR case are shown in Fig. 4.4.

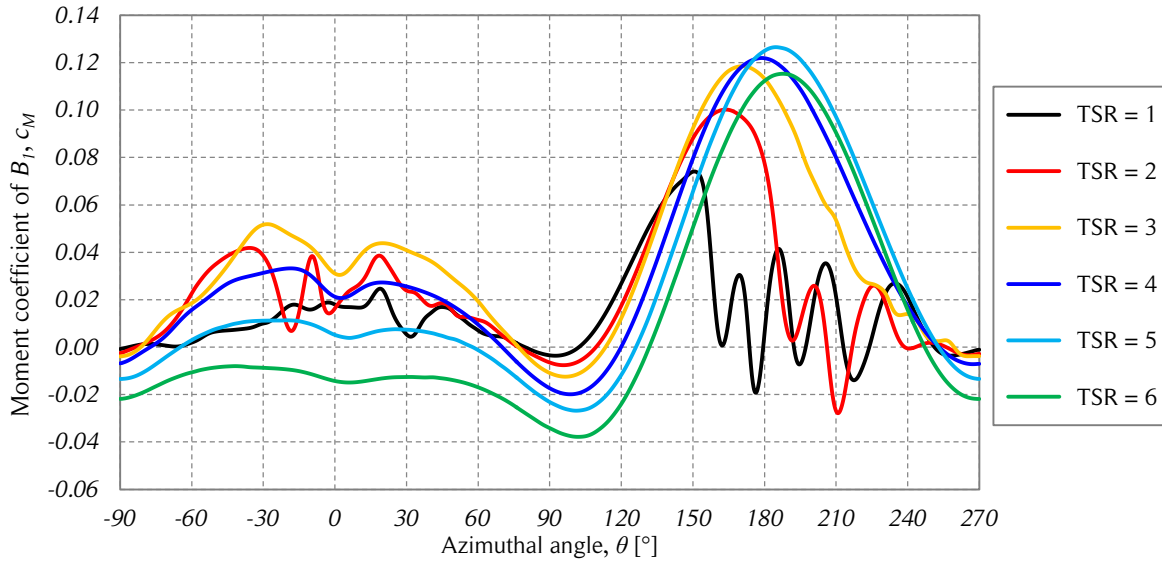


Figure 4.4. Blade moment coefficients vs. azimuthal angle.

The figure shows the moment coefficients of the blade B_1 as a function of the azimuthal angle of one blade for the six studied cases of the CFD simulations. Source: own elaboration.

4.2.3. Power coefficients

The mean power coefficients of the CFD simulations were calculated from the moment coefficients using Eqs. (2.7) and (3.38). Note that if the turbine radius is the reference length of the moment coefficient, the mean power coefficient can be obtained from the product of the mean moment coefficient of the turbine and the TSR . The available power at the turbine shaft was calculated from the sum of the resulting moments of the three blades and the turbine tower. The mean moment coefficient of the turbine tower is between four and five orders of magnitude smaller (depending on the TSR case) than the blade coefficients; therefore, it has a marginal influence in the mean power coefficient of the turbine. The mean power coefficients of the two-dimensional CFD simulations performed by Rangel [99] and the ones obtained in the present work are presented together with the experimental results of the Uppsala University SB-VAWT [115] in Fig. 4.5.

There are several reasons that explain the difference in the turbine power coefficients shown in Fig. 4.5. Probably the most obvious is that the CFD simulations are two-

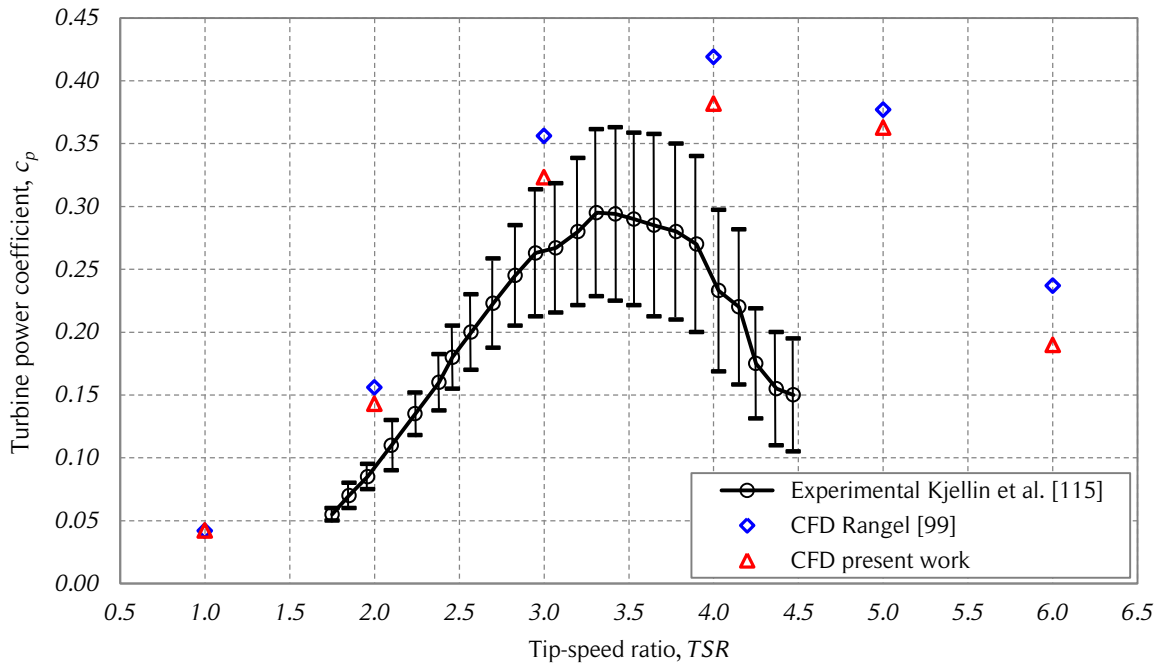


Figure 4.5. Experimental and CFD simulations turbine power coefficients.

The figure shows the experimental power coefficients as a function of the tip-speed ratio of the 12 kW SB-VAWT and both two-dimensional CFD simulations. Source: [99, 115].

dimensional and, therefore, do not take into account the three-dimensional effects such as the turbine struts, the wind shear (power law), the blade-tip losses and the tapering of the blades. In addition, the experimental results are calculated from the measured power in the generator (voltage and current); therefore, the experimental aerodynamic power coefficients should be higher due to the mechanical losses (bearings) and the generator efficiency (95.9%). Transient effects such as quick variations of the wind magnitude or/and direction may produce power losses due to the influence of the turbine inertia in the rotational speed. All these differences can be considered sufficient to explain the over-estimation of the power coefficients obtained by the CFD simulations. Similar differences in the power coefficient estimation using two-dimensional simulations and experiments were reported by Li et al. [100]. A detailed description of Darrieus SB-VAWTs three-dimensional flow is available in [120, 121].

The differences between the two CFD simulations are attributed to the change in the outlet boundary condition (from “outflow” to “pressure outlet”) and the respective wake development, because the computational domain, the mesh and solution parameters were the same for the two simulations.

4.2.4. Force coefficients

The streamwise and cross-stream force coefficients, f_x and f_y , are calculated by the software. This data was saved for each surface in the computational domain at every time step (every 0.25°). The converged streamwise and cross-stream force coefficients of the first blade for each TSR case are shown in Figs. 4.6 and 4.7.

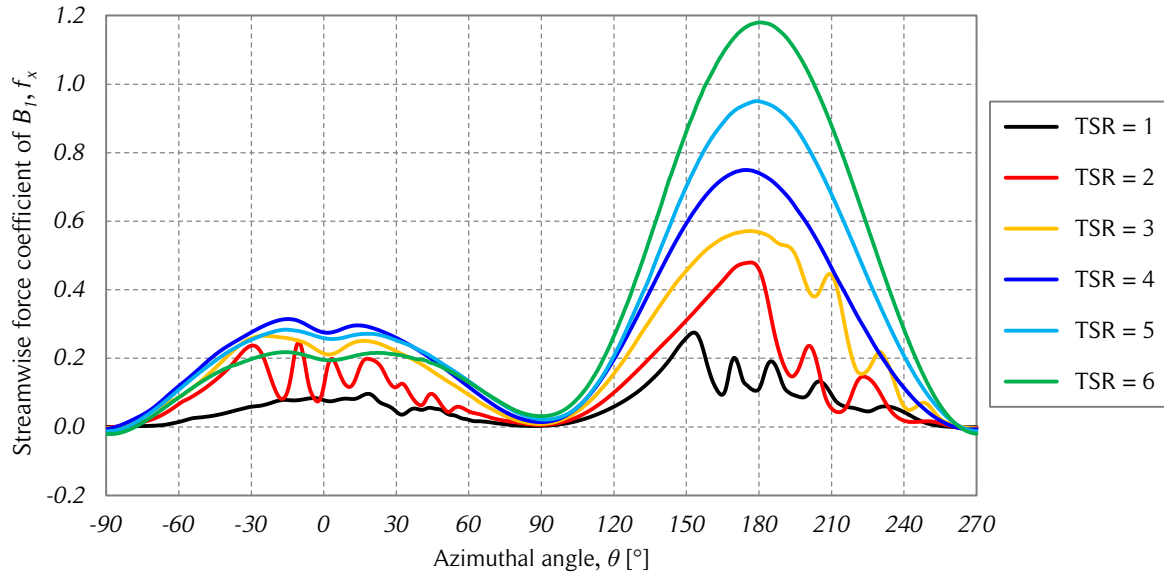


Figure 4.6. Blade streamwise force coefficients vs. azimuthal angle.

The figure shows the streamwise force coefficients of the CFD simulations as a function of the azimuthal position of the blade B_1 for the six studied cases. Source: own elaboration.

The upstream coefficients are larger than the downstream coefficients. The streamwise force coefficients are almost always positive for all the TSR cases shown in Fig. 4.6, that is, the streamwise force is in the same direction of the wind. On the other hand, the cross-stream force coefficients have four changes of sign in one rotation. The tendency in both force coefficients is the same for all the studied cases: the higher the TSR , the larger the force coefficients. In addition, the lower TSR cases show minor oscillations around the general pattern. This phenomenon is attributed to the dynamic effects which are more relevant at low rotational speeds of the turbine.

The tangential and radial force coefficients were calculated from the streamwise and cross-stream force coefficients using Eqs. (3.34) and (3.35), respectively. The results are presented in Figs. 4.8 and 4.9. The radial force coefficients show that on the

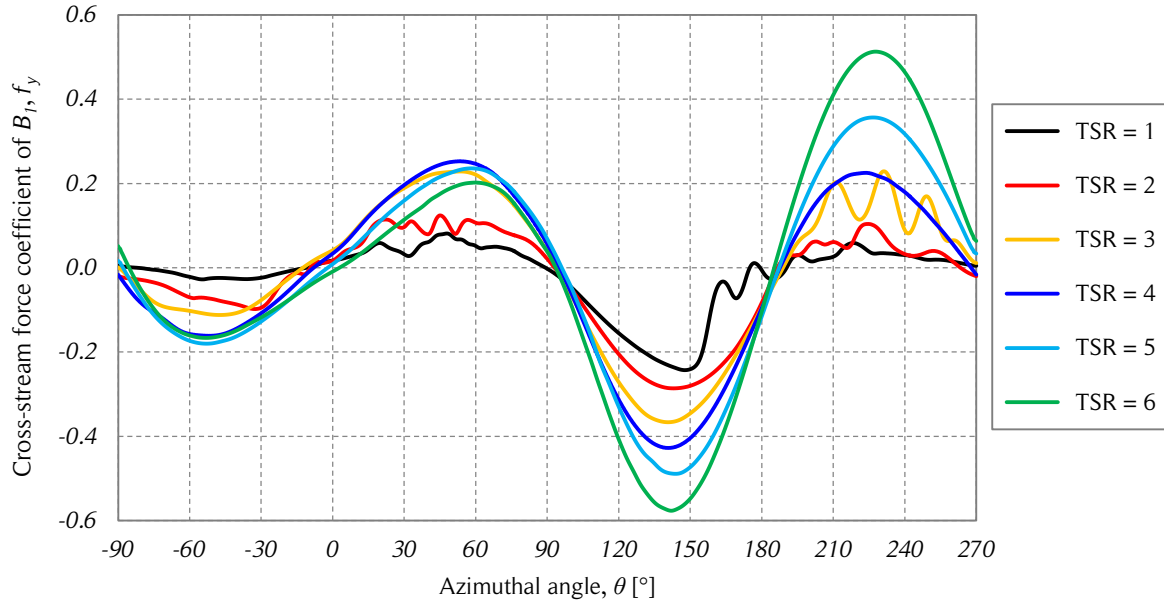


Figure 4.7. Blade cross-stream force coefficients vs. azimuthal angle.

The figure shows the cross-stream force coefficients of the CFD simulations as a function of the azimuthal position of the blade B_1 for the six studied cases. Source: own elaboration.

downwind half of the rotor the turbine struts are under traction, and on the upwind half are under compression. The magnitudes of the upstream radial force coefficients are also larger than the downstream coefficients.

The tangential force coefficients shown in Fig. 4.8 do not show self-consistent behavior as the radial force coefficients for the studied cases. The tangential force coefficient curves of Fig. 4.8 look very similar to the moment coefficients curves of Fig. 4.4. This is consistent with the fact that the aerodynamic moment acting on the blade is small in comparison with the aerodynamic forces. If both figures are compared in detail, some small differences are apparent. One simple way to demonstrate these differences is to calculate the mean power coefficient at each rotational speed, which is shown in Fig. 4.10. There are not large differences between the two. Note that both coefficients are calculated in the software using the surface pressure and shear stress distributions. However, the calculation of the power performance using only the tangential force, do not include the intrinsic moment acting on the blades, which is the cause of the difference in the power prediction. Of course, the calculations using the moment coefficients should be considered the most accurate approach. As was mentioned before, the moment coefficient acting on the aerodynamic center of thin symmetrical airfoils is assumed to be negligible [4]. In this case, Fig. 4.10 indicates that the moment

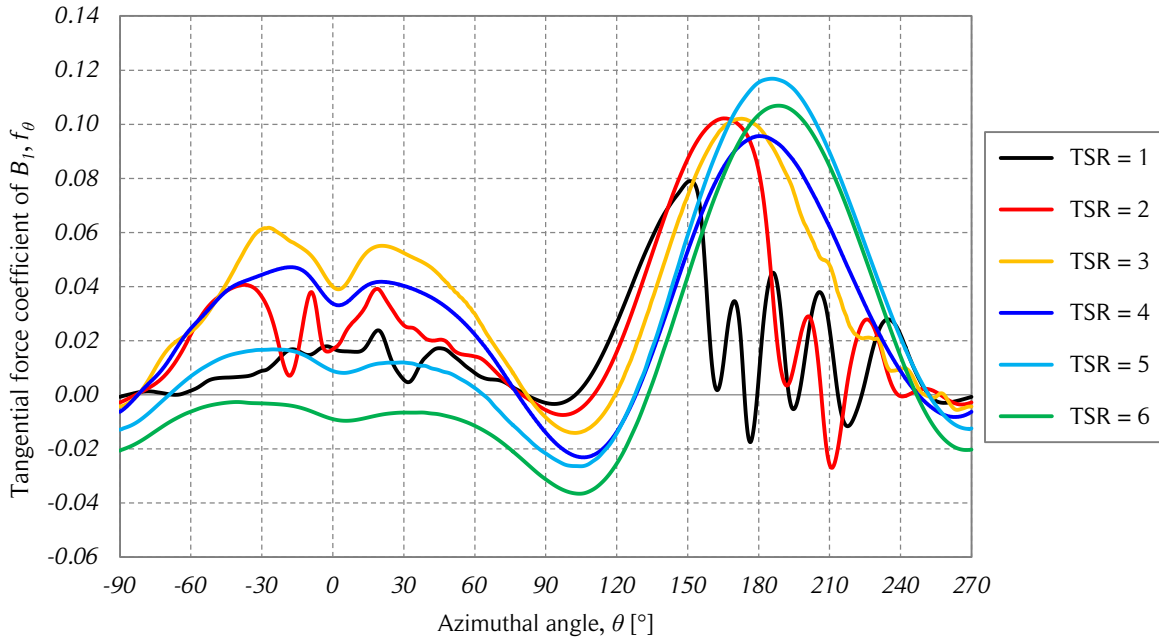


Figure 4.8. Blade tangential force coefficients vs. azimuthal angle.

The figure shows the tangential force coefficients of the CFD simulations as a function of the azimuthal position of the blade B_1 for the six studied cases. Source: own elaboration.

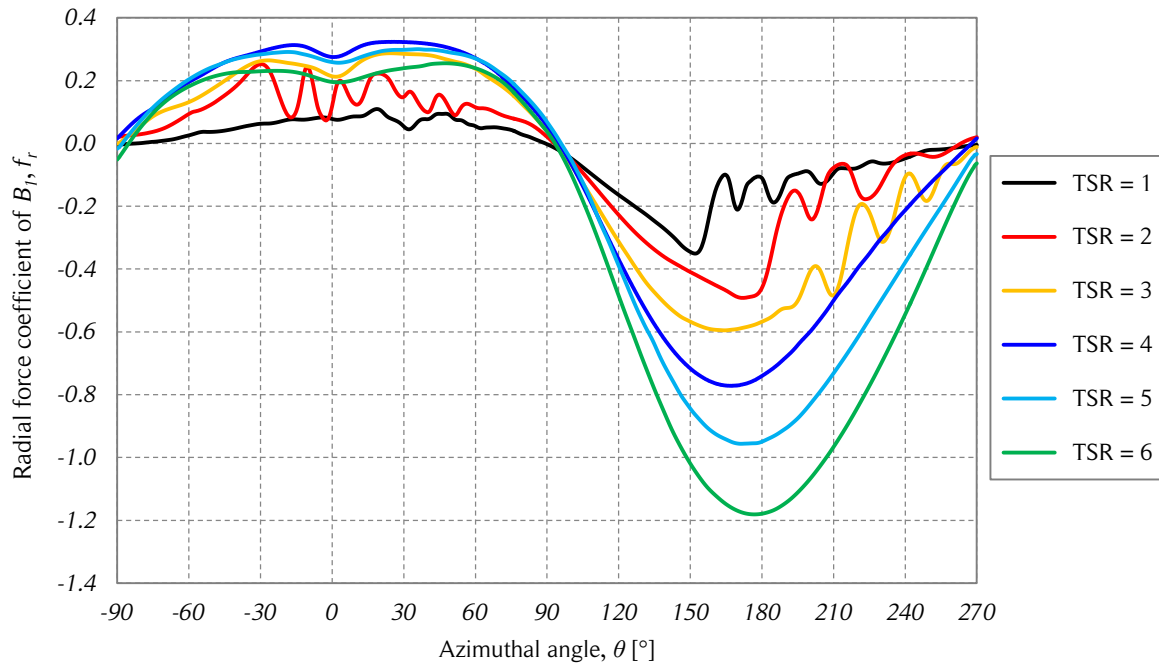


Figure 4.9. Blade radial force coefficients vs. azimuthal angle.

The figure shows the CFD simulations radial force coefficients as a function of the azimuthal position of the first blade for the six studied cases. Source: own elaboration.

coefficient acting at the quarter-chord point of each blade effectively does not have a large influence on the power coefficient, but is more noticeable for $TSR > 4$.

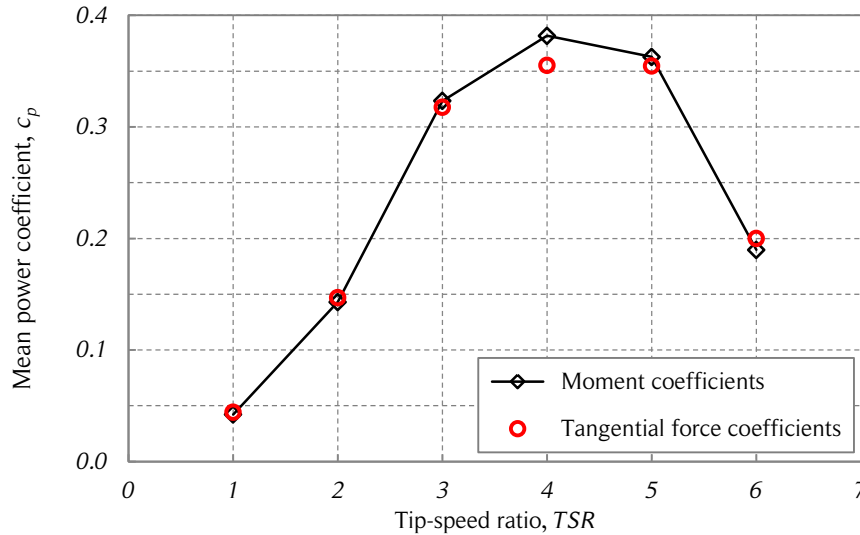


Figure 4.10. Mean power coefficients vs. tip-speed ratio.

The figure shows the CFD simulations mean power coefficients as a function of the tip-speed ratio calculated from the complete turbine moment coefficients $c_p(c_m)$, and from the longitudinal and transverse force coefficients of the blades $c_p(c_x, c_y)$. Source: own elaboration based on [5.2] data.

The total streamwise and cross-stream force coefficients acting on the turbine shaft for the studied cases are presented in Figs. 4.11 and 4.12, respectively. The blade coefficients of each blade in its respective phase were added for each azimuthal position to obtain these results. The behavior of the curves is similar for all cases. Amplitude increases with increasing TSR . The influence of the three blades is noticeable in the peaks and valleys of the plots.

4.2.5. Flow expansion around the turbine

Several measurements were performed to characterize the expansion of the flow around the turbine of the CFD simulations. Due to the conservation of mass in a streamtube, the cross-section of a two-dimensional streamtube at any position allows the calculation of the average velocity in that location. Therefore, one way to determine the flow expansion is to find the streamtube limits (streamlines). Though an automated process could have been developed to perform this task, manual measurements of the plotted streamlines

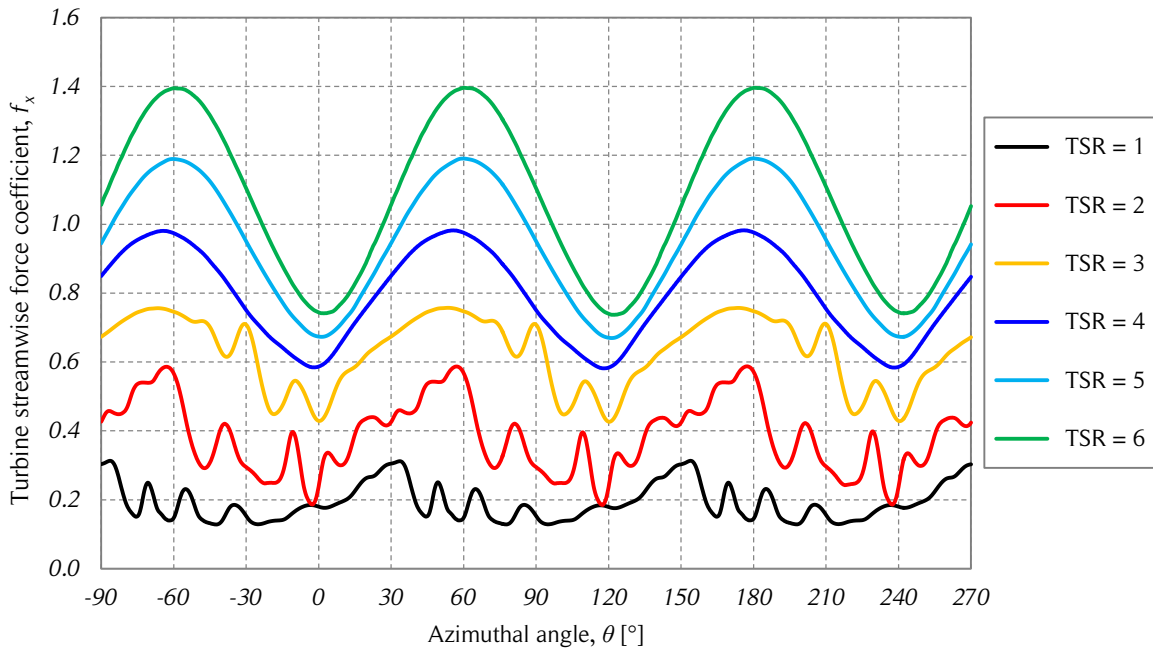


Figure 4.11. Turbine streamwise force coefficients vs. azimuthal angle.

The figure shows the total turbine streamwise force coefficients acting on the shaft as a function of the azimuthal angle for the six studied cases of the CFD simulations. Source: own elaboration.

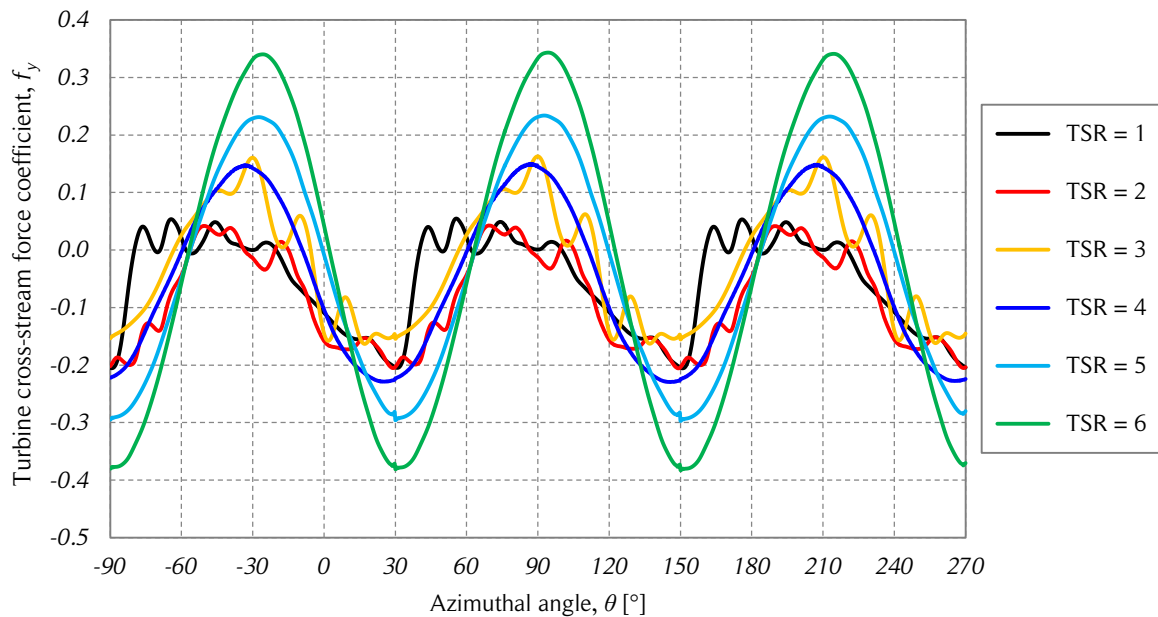


Figure 4.12. Turbine cross-stream force coefficients vs. azimuthal angle.

The figure shows the total turbine cross-stream force coefficients acting on the shaft as a function of the azimuthal angle for the six studied cases of the CFD simulations. Source: own elaboration.

were performed instead. Since the number of cases that were analyzed is small, the work of performing the manual measurements was considered smaller than the development of an automated process.

The first step of the procedure was to define a streamline density. If too many streamlines were visualized, the graphic measurements were hard to perform because it was difficult to follow each streamline without confusing it with the adjacent streamlines. If too few streamlines were visualized, the measurement accuracy decreased because of the low streamline resolution. A streamline density of 14 streamlines per turbine diameter was considered enough to perform the measurements. The second step of the procedure was to identify the streamlines that defined the streamtube limits. To accomplish this, the following criterion was used. At both the left and right sides, the lateral streamtube limits were chosen as the streamline that passes closer to the turbine diameter, but does not cross it. Then, the two chosen streamlines were followed to the upwind and downwind ends of the computational domain to determine the upwind and downwind flow expansion. Since the streamlines change in time, measurements at several different turbine positions were made. The turbine of the reference case has three blades; therefore, the flow patterns are repeated every 120° . To reduce the quantity of the measurements that had to be carried out, the measurements were performed in a swept angle of 120° for each of the six turbine rotational speeds. Based on the flow behavior, an azimuthal sampling of 15° was considered sufficient to capture the flow patterns; therefore, eight measurements at different blade positions were performed for each *TSR* case.

An instantaneous streamline visualization of the flow in the entire computational domain for the six *TSR* cases is shown in Fig. 4.13. As expected, the flow structure depends on the *TSR*: the higher the *TSR*, the larger the flow expansion of the wake behind the turbine. For low tip-speed ratios ($TSR \leq 3$), there is an oscillatory phenomenon in the wake, which decreases with increasing *TSR*. This is mainly caused by the large variations in the angle of attack of the blades and the vortex shedding described by the dynamic stall phenomenon. The instantaneous streamline visualization was chosen instead of the time average visualization to show this phenomenon.

In comparison with the low tip-speed ratio cases ($TSR < 4$), the high tip-speed ratios show a different behavior of the wake at the outlet of the computational domain. It seems that the instantaneous streamlines shown in Fig. 4.13 present an oscillatory pattern that changes in time (like a von Kármán vortex street), but in fact, the far structure of the wake does not change in time when the solution is converged. This phenomenon was also observed in the time-averaged streamline visualization presented in [117], which

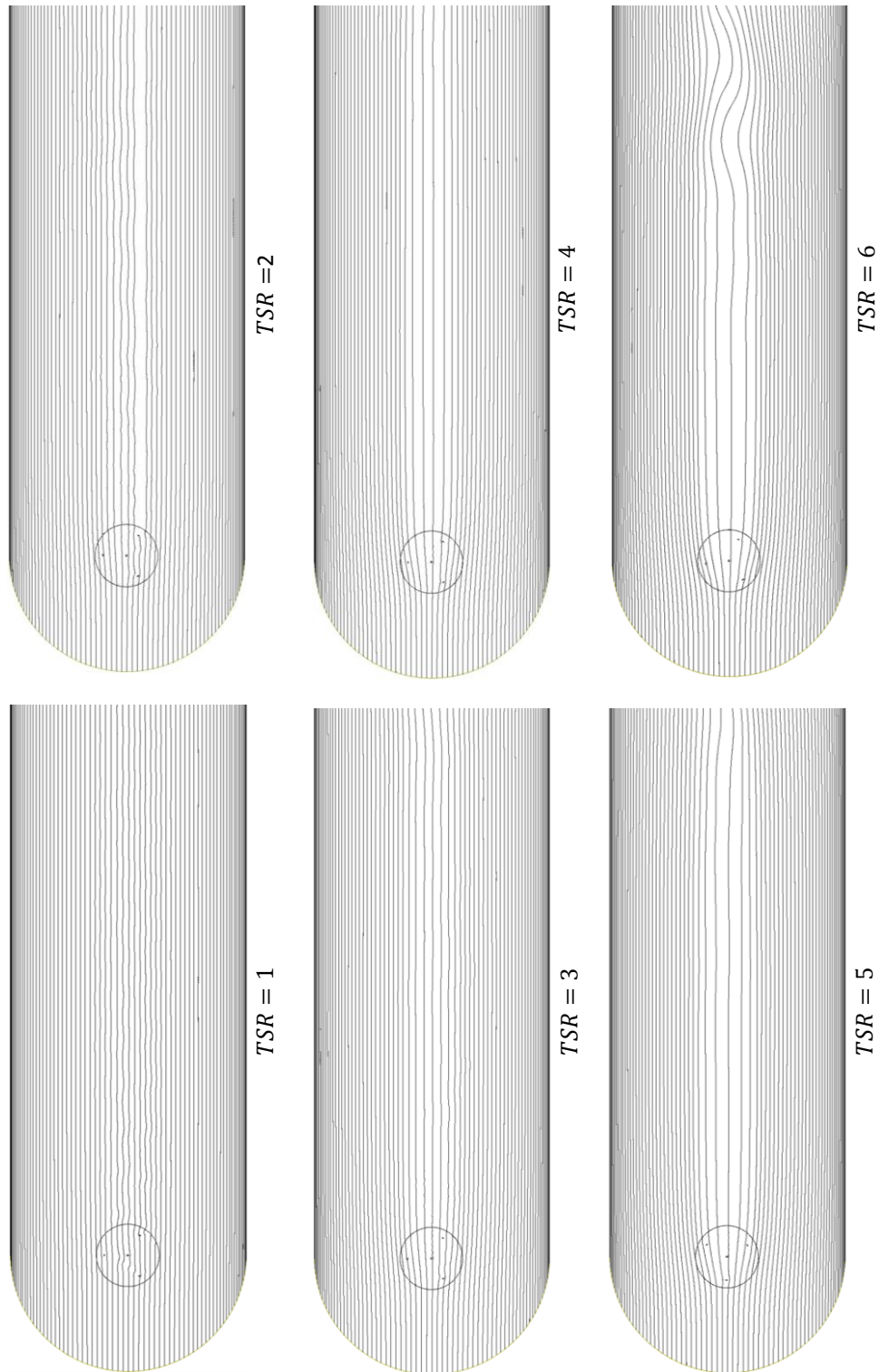


Figure 4.13. Streamline visualization of the CFD simulations.

The figure shows the instantaneous streamline visualization of the CFD simulations for the converged solution of the six studied tip-speed ratios and for $\theta = 90^\circ$. Source: own elaboration.

had a computational domain and operating conditions ($TSR = 3.5$) similar to the ones used in the present work. Time-averaged streamline visualization for three different tip-speed ratios are shown later in this chapter.

One possible reason for the wake shape at the outlet of the computational domain is the large difference between the free-stream and the wake. This produces large values of shear, which is related with vortex shedding. This behavior was discussed in Section 3.4 and is known as the turbulent wake state. However, in flow visualizations, shedding vortices are not observed. The streamwise wake velocity profiles for $TSR = 6$ at several downstream positions are presented in Fig. 4.14.

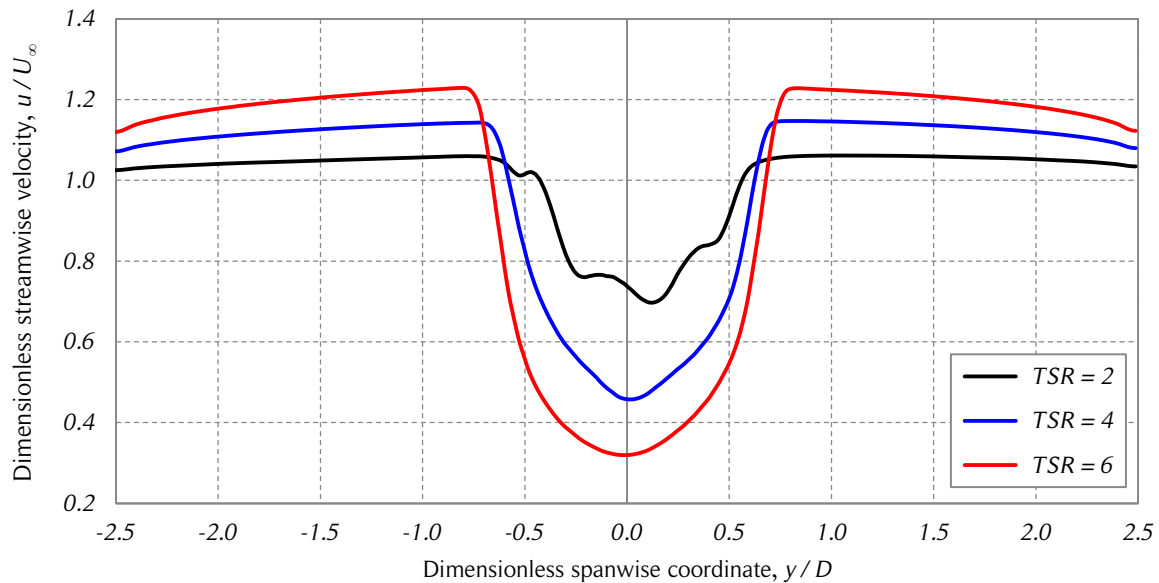


Figure 4.14. Streamwise wake velocity profiles.

The figure shows the instantaneous streamwise wake velocity profiles at a downstream position of three turbine diameters ($x = 3D$) and $\theta = 0^\circ$ for the converged solutions of three tip-speed ratios. Source: own elaboration.

The streamwise velocities at the lateral ends of the computational domain are higher than the freestream velocity, and therefore, the flow at the walls with symmetry boundary conditions do not behave as expected. The velocity profiles of [115] showed the same behavior as the ones of the present work. This phenomenon can be explained by the flow blockage produced by the turbine. The higher the turbine rotational speed, the higher the blockage of the flow. Hence, to satisfy the continuity equation, the velocity outside the wake has to become faster than the free-stream velocity. This is a phenomenon commonly discussed in wind tunnel experiments. However, since the aim of this work is

to model a stand-alone turbine, it must be noted that, to avoid the influence of the walls in the flow, a wider computational domain should be used for the higher values of the *TSR*. The recovery of the velocity profiles at the outlet of the computational domain can be explained by the pressure boundary condition used at that wall and by noting that the distance behind the wake is large enough (12 turbine diameters) to allow the development of the velocity profile. Finally, note that the simulations of the present work are two-dimensional, and thus, do not take into account the recovery effects of the wake velocity profiles caused by the exchange of momentum of the atmospheric boundary layer, a topic that was discussed in Section 3.4.

A diagram of the measured parameters of the CFD simulations is presented in Fig. 4.15. Three global parameters that allow quantification off the flow expansion are the streamtube widths at the inlet, W_∞ , at the equilibrium position ($x = 0$), W_e , and at the developed wake, W_w . The freestream distance and developed wake length, L_∞ and L_w respectively, are define as the distances from the turbine equilibrium position to the upstream and downstream locations were the streamtube width do not show any more changes with the streamwise position, x .

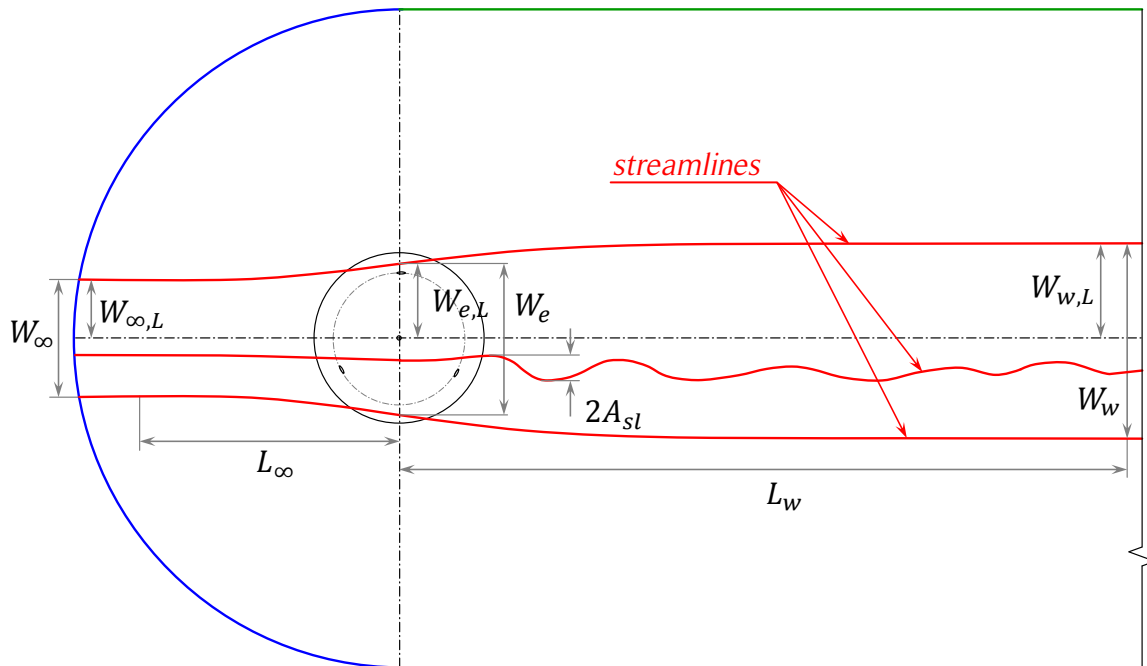


Figure 4.15. Streamline visualization of the CFD simulations.

The figure shows a diagram of the instantaneous streamline visualization and the variables that were manually measured for each case. Only three streamlines are shown to facilitate the understanding of the figure. Source: own elaboration.

For the lower TSR cases where the streamtube limits show oscillations in time, the time-averaged streamlines were used. The asymmetry of the expansion was taken into account measuring the left width of the turbine streamtube at the inlet, at the equilibrium position and at the developed wake. The variation in time of the wake streamlines inside the turbine streamtube was taken into account measuring the maximum amplitude of all streamlines in the wake, A_{sl} , which usually were found at a distance of one diameter behind the turbine and on the right side ($y < 0$).

Three dimensionless expansion ratios are defined according to [8] to account for the flow expansion: the upstream (subscript u), the downstream (subscript d) and the turbine (subscript T) expansion ratios, as shown in Eqs. (4.1) – (4.3), respectively.

$$ER_u = \frac{W_\infty}{W_e} \quad (4.1)$$

$$ER_d = \frac{W_e}{W_w} \quad (4.2)$$

$$ER_T = \frac{W_\infty}{W_w} \quad (4.3)$$

The streamtube widths were measured at each of the eight aforementioned blade azimuthal positions and averaged. The average flow expansion ratios and its dispersion are shown in Fig. 4.16. The line thickness of the streamline visualizations and the resolution of the graphic measurement tool were considered the only sources of error of the performed measurements. These errors were added as the dispersion of the ratios. The upstream, downstream and turbine flow expansion ratios decreasing with increasing TSR shown in Fig. 4.16 is consistent with Fig. 4.13 and behaves almost linearly for the three ratios.

It was difficult to identify the exact position of the upstream and downstream wake lengths, L_∞ and L_w , with the graphic measurement tool. The procedure was, for each TSR , blade position, upstream and downstream side, to choose the streamlines that have the segments farthest from the turbine center that are not parallel to the freestream velocity. Then, straight lines parallel to the freestream velocity and tangent to the chosen streamlines were drawn. Each wake length was measured as the distance between the turbine center and the intersection point of the chosen streamline and its tangent straight line. The main error sources for these measurements are the line thickness of the streamline visualization. The dimensionless wake lengths in terms of the turbine diameter are shown in Fig. 4.16. The freestream distance remains nearly constant with a value of

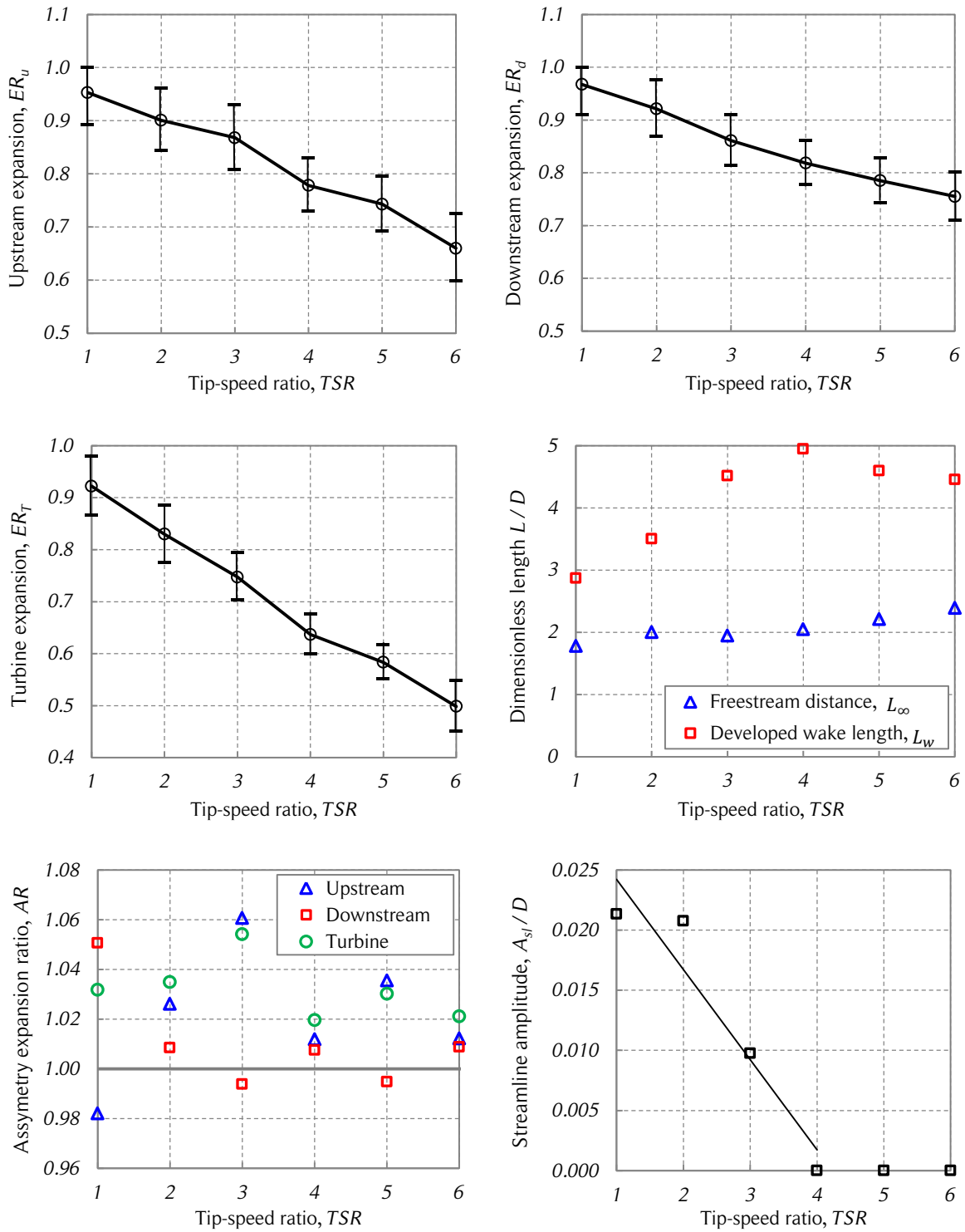


Figure 4.16. Flow expansion manual measurements from the CFD simulations.

The figure shows the manual measurements of the flow expansion parameters of the CFD simulations. Source: own elaboration.

two turbine diameters ($2D$). The downstream wake length increases with the TSR from $3D$ to about $5D$, but decreases slightly for the last two TSR cases because the streamlines exhibited fluctuations towards the end of computational domain, as shown in Fig. 4.13. The maximum dispersion of the measurements was of 29% and is not shown in the figure to facilitate the reading of the data. The downstream length of the domain seems to be large enough. However, since the curvature of the streamlines at the inlet is evident for a high TSR , the upstream length of the domain might be too short for the large turbine blockage produced at high tip-speed ratios.

Following the expansion ratio nomenclature, the upstream, downstream, and turbine asymmetry expansion ratios (AR) are defined for the left (subscript L) and right (subscript R) turbine streamtube widths, as shown in Eqs. (4.4) – (4.6). The asymmetry expansion ratios calculated from the measurements are shown in Fig. 4.16. The ratios show a rather random distribution with a tendency to the left side ($AR > 1$). In fact, the left side turbine expansion ratio is around 3% larger than the right side.

$$AR_u = \frac{\frac{W_{e,L}}{W_{\infty,L}}}{\frac{W_{e,R}}{W_{\infty,R}}} \quad (4.4)$$

$$AR_d = \frac{\frac{W_{w,L}}{W_{e,L}}}{\frac{W_{w,R}}{W_{e,R}}} \quad (4.5)$$

$$AR_T = \frac{\frac{W_{w,L}}{W_{\infty,L}}}{\frac{W_{w,R}}{W_{\infty,R}}} \quad (4.6)$$

The measurements of the maximum streamline oscillation amplitude in the wake, A_{st} , are also shown in Fig. 4.16. Only the first three TSR cases show oscillations in the wake, with a decreasing amplitude for increasing TSR . As shown in Fig. 4.13, the streamtube expansion is larger in the central streamlines and smaller in the streamlines that are far from the x -axis. To take this into account, each streamtube width (transverse distance between consecutive streamlines), w_k , was measured at the developed wake for each TSR . The results are shown in Fig. 4.17.

The streamtube numeration starts at one on the left side and at minus one on the right side. The reason for this nomenclature is explained in Section 4.3. The left and right

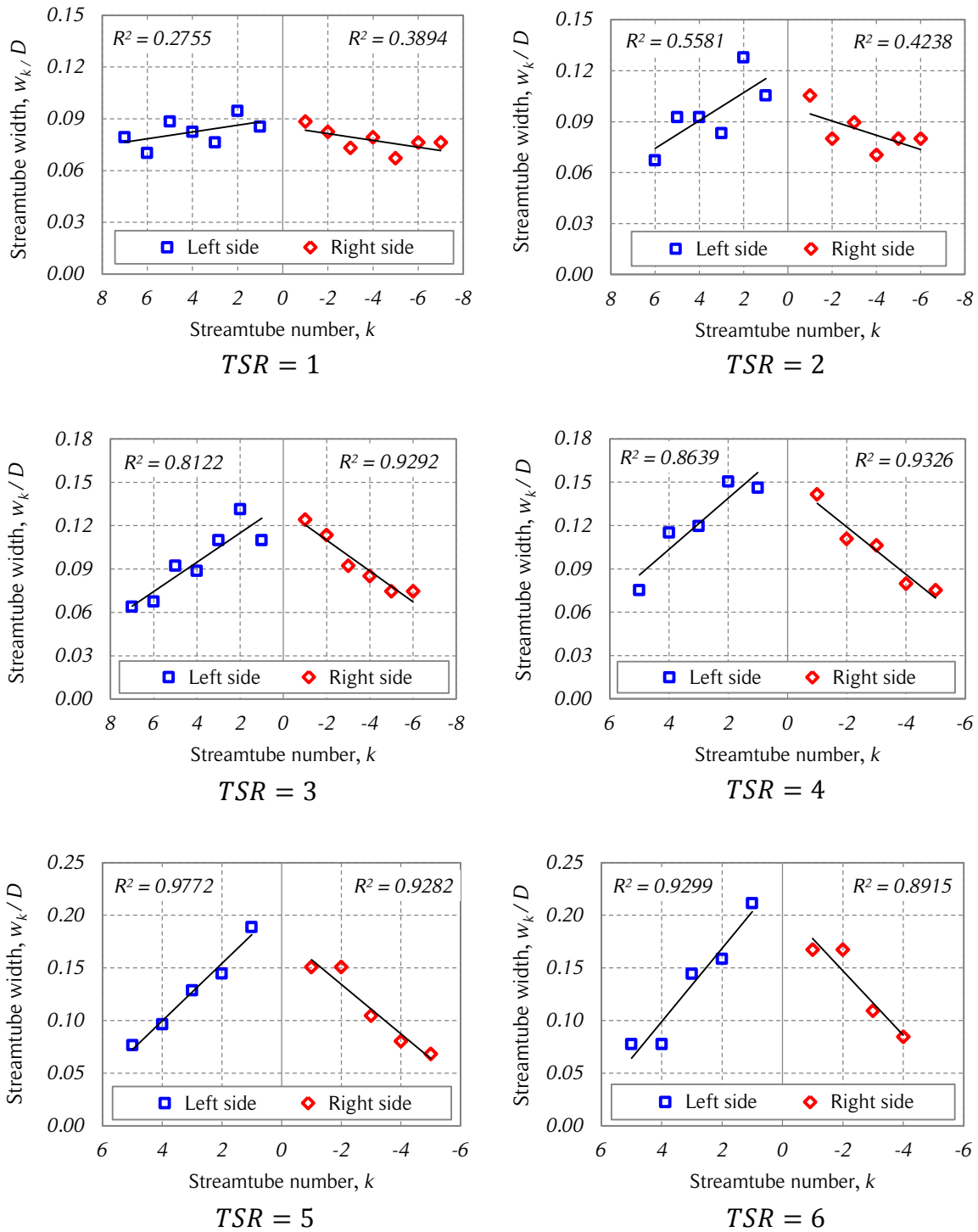


Figure 4.17. Streamtube lateral expansion.

The figure shows the left and right side lateral expansion of the streamtubes in the developed wake of the CFD simulations for the six studied tip-speed ratios. Source: own elaboration.

expansion shown in Fig. 4.17 is similar in all cases, but on the left side the difference between the first and last streamtube width is in general somewhat larger. On both sides the difference between the first and last streamtube (slope) increases with increasing *TSR*. This is consistent with increasing blockage for higher tip-speed ratios.

4.3. Mathematical representation of the flow expansion

The purpose of this section is to show the mathematical representation of the flow expansion that is required for the following section of this chapter and also useful to the modeling of Darrieus turbines. This approach is inspired by [8].

4.3.1. Time-averaged streamlines

The momentum models are based on an average formulation of the flow field around the turbine. Of course this approach does not take into account relevant transient phenomena that occur in the turbine wake such as the time dependency of the wake due to vortex shedding and other dynamic effects. However, in many cases, the time averaged flow field does not show such a large variation from the flow field at a certain time; therefore can be considered a reasonably good approximation. The time-averaged streamlines calculated from the CFD simulations are shown later in this section for some *TSR* cases.

Several approaches can be used to obtain a mathematical representation of the flow field around a wind turbine. Since the present work is based on the momentum models (particularly the DMS model) whose formulation is based on the streamtube concept, an approach focused on the modeling of the streamlines is utilized. The streamlines are parallel to the freestream velocity far upstream and downstream from the turbine, as shown in Fig. 4.13. The upstream, equilibrium and downstream widths of the streamtubes are known from the flow expansion measurements. Therefore, five conditions can be used to build a mathematical model for the streamlines: two derivatives at the ends of the streamlines and three conditions on the *y* coordinates: at the upstream wake, equilibrium position, and downstream wake. The polynomials are among the simplest mathematical formulations that allow the modeling of streamlines. In this case, due to the number of conditions, a fourth-order polynomial is the simplest. However, depending on the values of the conditions, the polynomial can misbehave and exhibit a non-physical behavior along the streamlines. Other more complex approaches can be used to obtain the splines that model the streamlines of the flow. Chen et al. suggested the use of fractal and fractional derivatives [106].

After several attempts, the following formulation was chosen: a second-order polynomial is used for the upstream side (f_1) and an exponential function with three constants for the downstream side (f_2), as shown in Eqs. (4.7) and (4.8), respectively. This formulation is applied to each streamline, as shown in Fig. 4.18. The streamlines are calculated sequentially advancing in both directions (left and right) separately, starting from the turbine center ($y = 0$) and assuming there is an undistorted streamline that coincides with the x -axis. The derivatives of Eqs. (4.7) and (4.8) are presented in Eqs. (4.9) and (4.10), respectively.

$$f_1(x) = A_1x^2 + B_1x + C_1 \quad (4.7)$$

$$f_2(x) = A_2 - B_2 \exp(-C_2x) \quad (4.8)$$

$$\frac{df_1}{dx} = 2A_1x + B_1 \quad (4.9)$$

$$\frac{df_2}{dx} = B_2C_2 \exp(-C_2x) \quad (4.10)$$

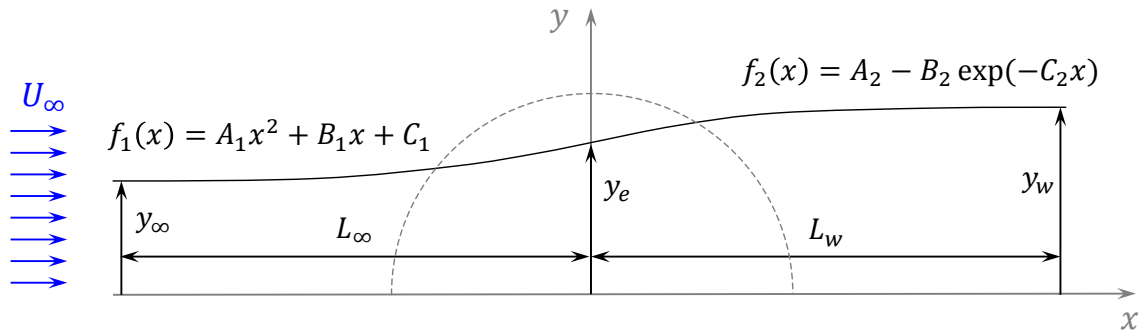


Figure 4.18. Mathematical modeling of the streamlines.

The figure shows the upstream and downstream functions used to model the streamlines. Source: own elaboration.

To ensure continuity and smoothness at the junction of the upstream and downstream functions, Eqs. (4.11) and (4.12) are imposed.

$$f_1(0) = f_2(0) \quad (4.11)$$

$$\left. \frac{df_1}{dx} \right|_{x=0} = \left. \frac{df_2}{dx} \right|_{x=0} \quad (4.12)$$

The conditions to determine the upstream function, f_1 , constants are obtained for each streamtube from the upstream wake length, L_∞ , the free-stream spanwise position, y_∞ , and the equilibrium spanwise position, y_e , as shown in Eqs. (4.13) – (4.15). Note that the same wake length is used for every streamline, which is a model simplification.

$$f_1(-L_\infty) = y_\infty \quad (4.13)$$

$$f_1(0) = y_e \quad (4.14)$$

$$\left. \frac{df_1}{dx} \right|_{x=-L_\infty} = 0 \quad (4.15)$$

Solving the three by three linear system of equations yields the constants of the upstream function shown in Eq. (4.16).

$$\begin{pmatrix} A_1 \\ B_1 \\ C_1 \end{pmatrix} = \begin{pmatrix} \frac{y_e - y_\infty}{L_\infty^2} \\ \frac{2(y_e - y_\infty)}{L_\infty} \\ y_e \end{pmatrix} \quad (4.16)$$

The conditions to find the constants of the downstream function, f_2 , are obtained from the downstream wake length, L_w , the equilibrium spanwise position, y_e , and the wake spanwise position, y_w , as it is shown in Eqs. (4.17) – (4.19). The approximation used in Eq. (4.19) is valid if the second term of the downstream function is negligible, that is if $B_2 \exp(-C_2 L_w) \approx 0$, then $f_2(L_w) \approx A_2$, condition that is satisfied for the measured data. Solving the three by three linear system of equations yields the constants of the upstream function shown in Eq. (4.20).

$$f_2(0) = y_e \quad (4.17)$$

$$\left. \frac{df_2}{dx} \right|_{x=0} = \left. \frac{df_1}{dx} \right|_{x=0} \quad (4.18)$$

$$f_2(L_w) = y_w \quad (4.19)$$

$$\begin{pmatrix} A_2 \\ B_2 \\ C_2 \end{pmatrix} = \begin{pmatrix} y_w \\ y_w - y_e \\ \frac{2(y_e - y_\infty)}{L_\infty(y_w - y_e)} \end{pmatrix} \quad (4.20)$$

4.3.2. Non-uniform spanwise streamtube expansion

According to Figs. 4.13 and 4.17, the spanwise expansion of the streamtubes is uneven. The energy extraction in the central section of the turbine ($y \approx 0$) is larger than in the lateral sections ($y \approx \pm R$); therefore, there is a larger flow deceleration in the middle section of the turbine, which means larger expansion of the central streamtubes. This uneven expansion follows a linear tendency for all studied *TSR* cases according to Fig. 4.17: the streamtube width, w_k , is a linear function of the streamtube number, k . Note that the spanwise limits of each streamtube can be calculated from the streamtube widths. The streamtube expansion is expressed as a function of the streamtube number because the mathematical representation is simpler. This is discussed below.

The unevenness of the expansion can be different at the turbine equilibrium position ($x = 0$) and at the downstream wake position ($x = L_w$). Therefore, a non-uniform expansion ratio, K , is defined at each side (left and right) and streamwise position (equilibrium or developed wake) as the ratio between the width of the first streamtube ($y \approx 0$) and the width of the last streamtube passing inside the turbine streamtube ($y \approx \pm R$), as shown in Eqs. (4.21) and (4.22). The left and right sides show a similar behavior, therefore to simplify the model, only the average non-uniform expansion ratio at the equilibrium position and developed wake are shown in Fig. 4.19. Note that both non-uniform expansion ratios (at the equilibrium position and the developed wake) follow a nearly linear behavior as a function of the *TSR*. The flow asymmetry, which is considered small (see Figure 4.17), is included in this model through the asymmetry expansion ratios, AR , and the non-uniform expansion ratios, K .

$$K_e = \frac{w_{e,k}(first)}{w_{e,k}(last)} \quad (4.21)$$

$$K_w = \frac{w_{w,k}(first)}{w_{w,k}(last)} \quad (4.22)$$

Considering that the streamtube width depends linearly on the streamtube number, two conditions permit determination of two constants of the straight line that fits the data. The idea is to obtain an expression that does not depend on the number of streamtubes. Two possible conditions are the following: the first one is the non-uniform expansion ratio, K , and the second one is the total wake width at the streamwise position of interest. The sum of all streamtube widths on each side (left or right) has to be equal to the respective total wake width at that side. It is assumed that half of the streamtubes pass at each side of the turbine (left and right). Therefore, the number of streamtubes,

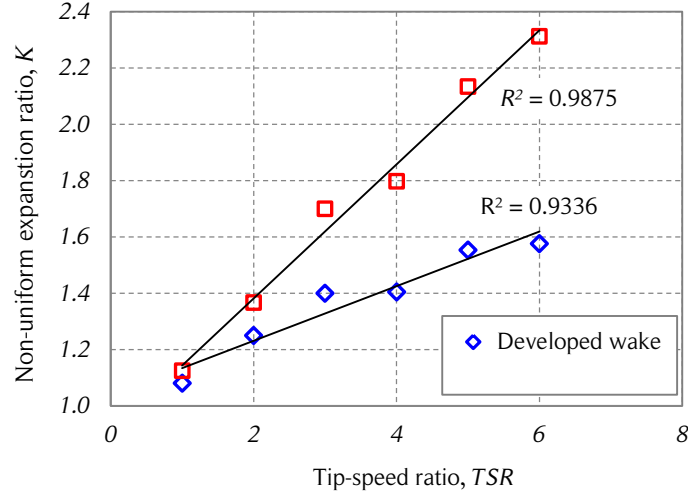


Figure 4.19. Side-averaged non-uniform expansion ratio vs. tip-speed ratio.

The figure shows the side-averaged (left and right) non-uniform expansion ratio at the equilibrium position and at the developed wake as a function of the tip-speed ratio. Source: own elaboration.

NST , has to be an even integer. Note that the asymmetry of the wake is taken into account with the aforementioned parameters. An undistorted straight streamline in the middle of the turbine that coincides with the x -axis is also assumed. This line is used as the streamtube limit for the first left and right side streamtubes. The other streamtube limits (streamlines) are calculated sequentially starting from the first left and right side streamtube, until the entire turbine is covered.

The linear expression to calculate the left side streamtube widths at the equilibrium position, $w_{e,L}(k)$, and developed wake, $w_{w,L}(k)$, are shown in Eqs. (4.23) and (4.24). The right side streamtube widths, $w_{w,R}(k)$ and $w_{e,R}(k)$, are calculated in the same way. Note that the absolute value is required for the right side because of the negative integer definition for the streamtube number, k .

$$w_{e,L}(k) = m_{e,L}|k| + n_{e,L} \quad (4.23)$$

$$w_{w,L}(k) = m_{w,L}|k| + n_{w,L} \quad (4.24)$$

The non-uniform cross-stream expansion ratios at the equilibrium position, K_e , and developed wake, K_w , for the left side are shown in Eqs. (4.25) and (4.26).

$$K_e = \frac{m_{e,L} + n_{e,L}}{m_{e,L} \frac{NST}{2} + n_{e,L}} \quad (4.25)$$

$$K_w = \frac{m_{w,L} + n_{w,L}}{m_{w,L} \frac{NST}{2} + n_{w,L}} \quad (4.26)$$

The total left side wake width at the equilibrium position, $W_{e,L}$, is calculated using Eq. (4.27). The variable change of Eq. (4.28) applied to Eq. (4.27) yields Eq. (4.29).

$$W_{e,L} = \sum_{k=1}^{NST/2} w_{e,L}(k) = m_{e,L} \sum_{k=1}^{NST/2} k + n_{e,L} \sum_{k=1}^{NST/2} 1 \quad (4.27)$$

$$S_1 = \sum_{k=1}^{NST/2} k = \frac{\left(\frac{NST}{2}\right) \left(\frac{NST}{2} + 1\right)}{2} \quad (4.28)$$

$$W_{e,L} = m_{e,L} S_1 + n_{e,L} \frac{NST}{2} \quad (4.29)$$

The left side wake width at the developed wake, $W_{w,L}$, is calculated in the same way as shown in Eq. (4.30).

$$W_{w,L} = m_{w,L} S_1 + n_{w,L} \frac{NST}{2} \quad (4.30)$$

If Eq. (4.25) is solved for $m_{e,L}$, then Eq. (4.31) is obtained. An auxiliary constant, K'_e , is defined in Eq. (4.32) to simplify the notation.

$$m_{e,L} = n_{e,L} \frac{K_e - 1}{1 - K_e \frac{NST}{2}} \quad (4.31)$$

$$K'_e = \frac{K_e - 1}{1 - K_e \frac{NST}{2}} \quad (4.32)$$

Combining Eqs. (4.29) and (4.31) yields Eq. (4.33). Then the term $m_{e,L}$ can be calculated from Eqs. (4.31) and (4.33), as shown in Eq. (4.34). This procedure has to be repeated for the right side at the equilibrium position and both sides for the developed wake. Since the equations are the same, only the subscripts e , w and L have to be replaced.

$$n_{e,L} = \frac{W_{e,L}}{K'_e S_1 + \frac{NST}{2}} \quad (4.33)$$

$$m_{e,L} = n_{e,L} K'_e \quad (4.34)$$

To illustrate the behavior of the mathematical representation of the streamlines, they were plotted using the measurements from the CFD simulations together with the time-averaged streamlines for some tip-speed ratios in Fig. 4.20. In general, the mathematical representation of the streamlines is in good agreement with the time-averaged streamlines. The main difference between the streamlines is the curvature of the lines near the turbine. This misalignment produces slightly different angular limits for the streamtubes (intersection of the streamlines and the blade path) and also a variation in the magnitude and direction of the flow velocity. Considering that the BEM models, and in particular the DMS model, are approaches based on time-averaged flow expansion, small misalignment differences in the streamtubes would not cause large losses of precision in the calculations.

4.3.3. Flow expansion and momentum theory

The aim of this section is to investigate the validity of the one-dimensional momentum theory for Darrieus VAWTs. This is carried out through the plotting of the streamwise forces (thrust) and the induction factor (or interference factor), which is a way of measuring the flow expansion, at different tip-speed ratios.

To be consistent with the previous definitions of the induction factor, the flow expansion is measured using Eq. (4.35). Note that when $W_\infty/W_w = 1$, that is $a = 0$, there is no flow expansion. If the interference factor definition of Eq. (4.35) is recalled, the turbine, upstream, and downstream induction factors can be calculated from Eqs. (4.36) – (4.38). The flow expansion (interference factors) of the turbine, upstream, and downstream halves were calculated using the average expansion ratios, ER , of Eqs. (4.1) – (4.3).

$$a = \frac{1}{2} \left(1 - \frac{U_w}{U_\infty} \right) \quad (4.35)$$

$$a_T = \frac{1}{2} \left(1 - \frac{W_\infty}{W_w} \right) \quad (4.36)$$

$$a_u = \frac{1}{2} \left(1 - \frac{W_\infty}{W_e} \right) \quad (4.37)$$

$$a_d = \frac{1}{2} \left(1 - \frac{W_e}{W_w} \right) \quad (4.38)$$

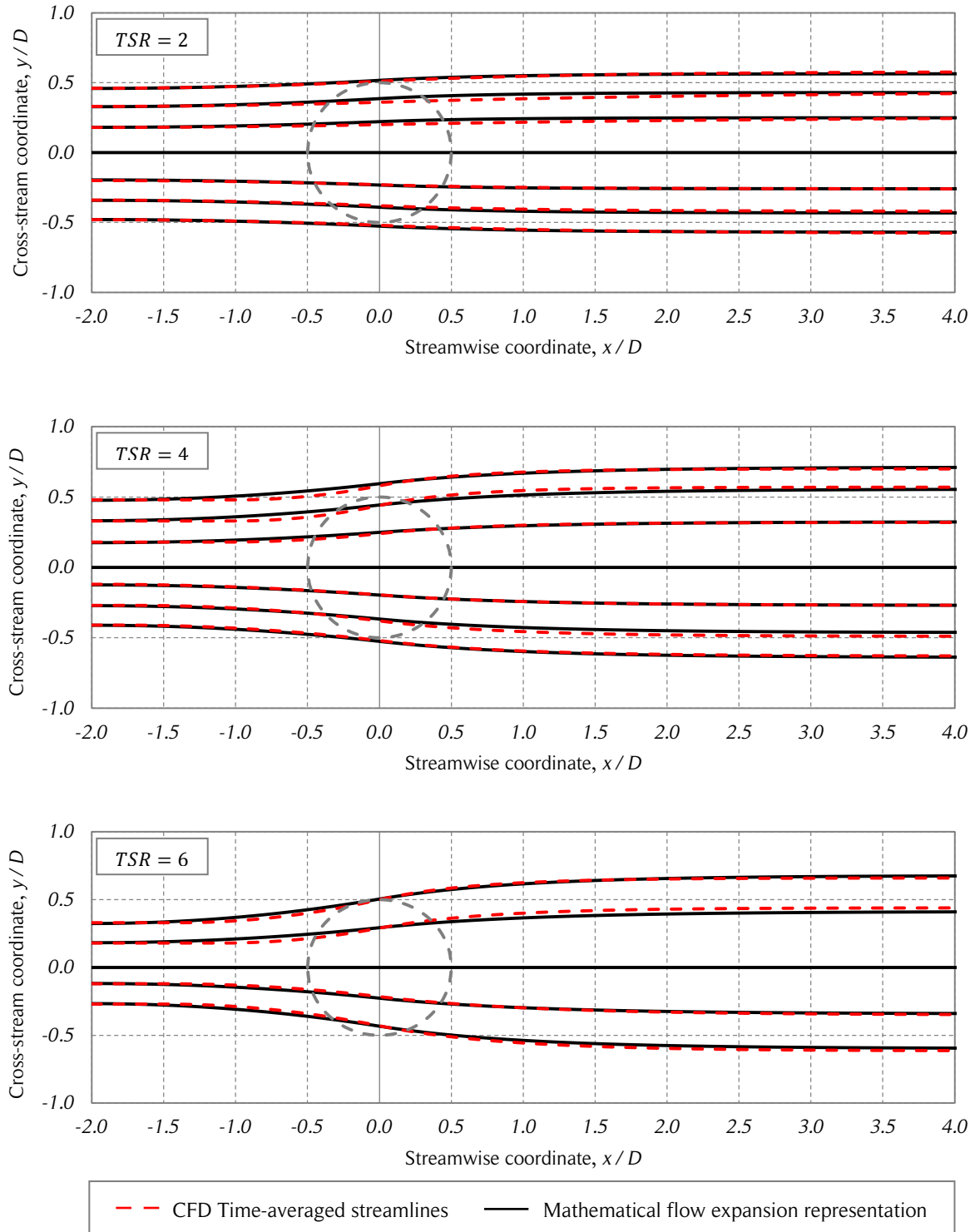


Figure 4.20. Streamline visualization comparison.

The figure shows a comparison between the CFD time-averaged streamlines and the mathematical representation of streamlines for three tip-speed ratios. The central streamline is not shown for the CFD simulations because of the influence of the turbine tower. Source: own elaboration.

The average streamwise force coefficients of the entire turbine, \bar{f}_x , and the upstream, $\bar{f}_{x,u}$, and downstream, $\bar{f}_{x,d}$, halves were calculated using Eqs. (4.39) – (4.41), where Eq. (4.42) was used to determine if the blade i was in the upstream or downstream half (N is the number of blades). The discrete streamwise force coefficient, $f_{x,i,j}$, of each blade was obtained from the CFD results shown in Fig. 4.6, where N_p is the number of discrete points in one turbine revolution. In this case, $\Delta\theta = 0.25^\circ$, and therefore, $N_p = 1440$. The results are shown in Fig. 4.21.

$$\bar{f}_x = \sum_{i=1}^N \bar{f}_{x,i} \quad (4.39)$$

$$\bar{f}_{x,u} = \sum_{i=1}^N \frac{1}{N_p} \sum_{j=1}^{N_p} f_{x,i,j} \varphi_{i,j} \quad (4.40)$$

$$\bar{f}_{x,d} = \sum_{i=1}^N \frac{1}{N_p} \sum_{j=1}^{N_p} f_{x,i,j} (1 - \varphi_{i,j}) \quad (4.41)$$

$$\varphi_{i,j} = \begin{cases} 0, & -90^\circ \leq \theta_{i,j} < 90^\circ \\ 1, & 90^\circ \leq \theta_{i,j} < 270^\circ \end{cases} \quad (4.42)$$

It can be concluded that the entire turbine has lower expansion for the same streamwise force in comparison with the one-dimensional momentum theory. The tendency of the upstream half is similar. On the other hand, the downstream half shows lower loads for the same expansion in comparison with the momentum theory. Additionally, after an induction factor near $a \approx 1$, the streamwise forces decay with larger flow expansion. The two last points of the curve correspond to the cases $TSR = 5$ and $TSR = 6$. This behavior is consistent with the results shown in Fig. 4.6.

One of the relevant results of the one-dimensional momentum theory is the determination of the induced velocity, U or U_e , which is equal to the average of the free-stream velocity and the wake velocity, as shown in Eq. (4.43).

$$U_e = \frac{U_\infty + U_w}{2} \quad (4.43)$$

With the mathematical representation of the streamlines and the available measurements of the CFD simulations, it is easier to verify if the streamtubes satisfy Eq. (4.43) in terms

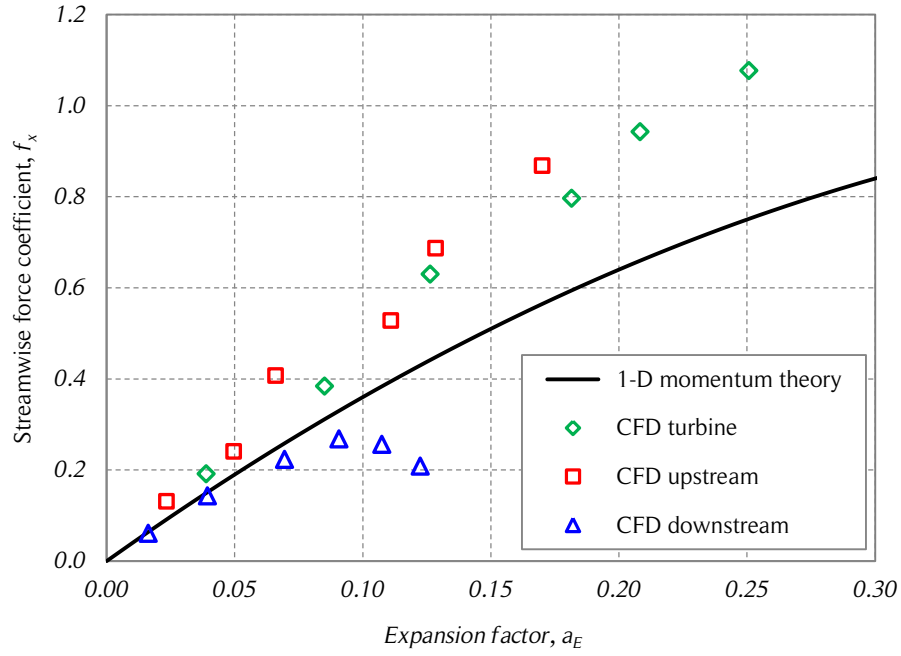


Figure 4.21. Streamwise force coefficients vs. interference factor.

The figure shows the streamwise force coefficients of the entire turbine and the upstream and downstream halves as a function of the induction factor for all the TSR cases. The momentum theory curve is shown for comparison. Source: own elaboration.

of the streamtube widths rather than the streamwise velocities. The continuity equation at any given streamtube passing through the turbine yields Eqs. (4.44) and (4.45). Substituting these equations into Eq. (4.43) and simplifying yields Eq. (4.46). Reproducing the procedure for the upstream and downstream halves yields Eqs. (4.47) and (4.48).

$$U_e = \frac{w_\infty}{w_e} U_\infty \quad (4.44)$$

$$U_w = \frac{w_\infty}{w_w} U_\infty \quad (4.45)$$

$$w_e = \frac{2w_\infty w_w}{w_\infty + w_w} \quad (4.46)$$

$$w_u = \frac{2w_\infty w_e}{w_\infty + w_e} \quad (4.47)$$

$$w_d = \frac{2w_e w_w}{w_e + w_w} \quad (4.48)$$

The predicted streamtube widths of Eqs. (4.46) – (4.48) are calculated from the measured data and the streamline mathematical representation for three tip-speed ratios. The effective streamtube widths are measured for the same cases and are shown together with the predicted values in Fig. 4.22. Note that the number of streamtubes used is $NST = 10$ and only the values from the left side are shown. The predicted and measured upstream and downstream streamtubes widths are in better agreement than the turbine streamtubes. In fact, the predicted widths of the turbine streamtubes are larger than the measured widths, with a maximum difference of about 30% for $TSR = 6$ and $k = 1$ (larger streamtube width, w_e). Although the upstream and downstream streamtubes from the streamline visualizations of Fig. 4.20 might not look like two streamtubes in tandem (see Fig. 3.29), they are in better agreement with the one-dimensional momentum theory than the turbine streamtubes.

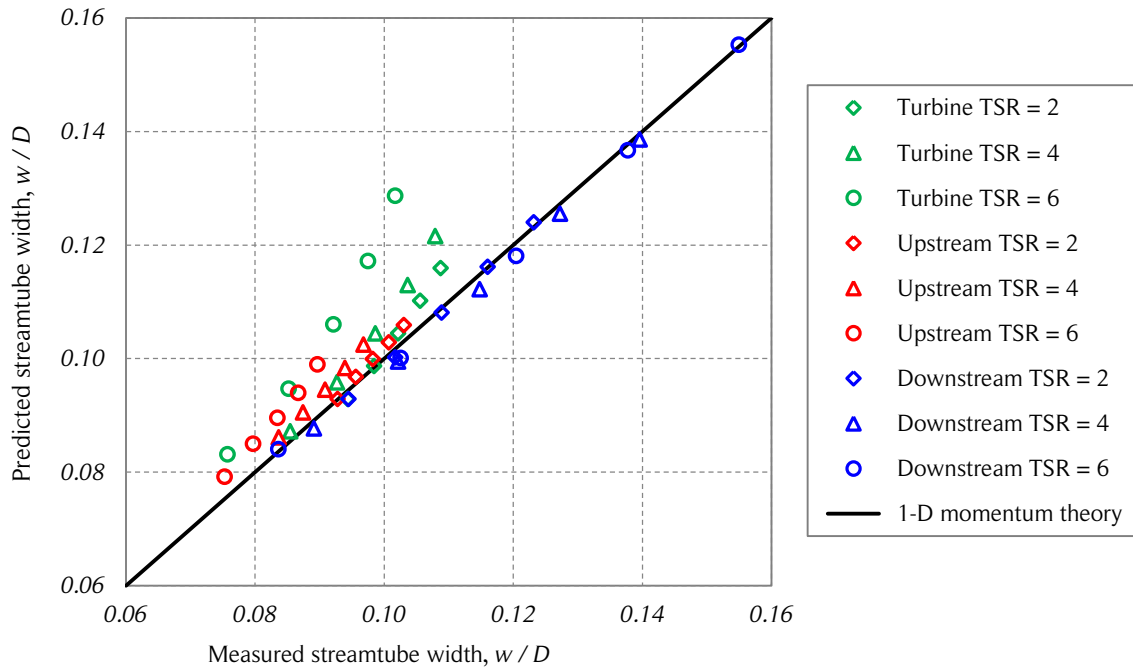


Figure 4.22. Predicted and measured streamtube widths.

The figure shows the predicted and measured left side dimensionless turbine, upstream and downstream streamtube widths for three tip-speed ratios with $NST = 10$. The data was obtained from the CFD simulations and the mathematical representation of the streamlines. Source: own elaboration.

4.4. Three-dimensional corrections of the CFD simulations

To compare the results of the CFD simulations with experimental results, it is necessary to add three-dimensional effects. This is done through corrections that include the vertical variation of the wind speed due to the atmospheric boundary layer, the finite aspect ratio of blades and the blade struts. Although the struts have airfoil shapes to reduce the aerodynamic losses, they produce a significant drag; therefore, reducing the overall performance of the turbine. The code used to calculate the three-dimensional corrections (TDC) is presented in Appendix B. Specifically, the following corrections are applied:

- The power law due to the atmospheric boundary layer is calculated based on the parameters of the field tests with $U_{\infty} = 10 \text{ m/s}$ at the half height of the blades (tower height) (see Section 2.5.2).
- The blade tapering is taken into account by applying the change of blade geometry in the vertical direction for the calculation of the forces using the respective chord length (see Section 4.1.2).
- The entire three-dimensional flow field around the turbine is reconstructed using the mathematical representation of the streamlines and the measurement of the CFD simulations. It is assumed that the power law is the only variation of the flow in the vertical direction. The flow field at each horizontal plane is weighted accordingly in respect to the reference flow field at the tower height.
- The calculation of the aerodynamic forces is performed using two corrections that are related to the finite aspect ratio of the blades. The first one modifies the relative wind velocity and angle of attack depending on the vertical location along the blades and the second one transforms the infinite blade characteristic into finite ones. See Section 3.8.8 for more details.
- Both the main and the auxiliary turbine struts are considered for the calculation of the aerodynamic losses. The joining points are not considered, that is, the drag of the struts is calculated at each spanwise position with the respective chord as an infinite blade. To decrease the computational time of the flow field determination for the strut velocity triangle, an interpolation procedure using the turbine streamtube limits is implemented. Therefore, the local wind flow field, U , is assumed to be only a function of the streamwise position, x . The drag forces of the struts are calculated at the hub height of the turbine to simplify the

calculations. Since the vertical velocity profile varies little in the vertical direction in the range of the struts, this is not considered as a large simplification. The aerodynamic coefficients of the modified airfoil geometry (trimmed airfoil at the trailing edge) of the struts are not available; thus, this can be a source of inaccuracies. See Sections 3.8.7 and 4.1.2 for more details.

The results of these corrections are shown in Fig. 4.23. The three-dimensional corrections (TDC) produce a significant decrease in the estimated two-dimensional CFD power coefficients. At tip-speed ratios below the peak performance ($TSR \approx 3.5$), the corrections seem to overestimate the losses. On the other hand, at tip-speed ratios larger than the peak performance, the corrections seem to underestimate the losses. The expected power performance can be considered to be bounded by the two-dimensional CFD simulations and the CFD simulations with the three-dimensional corrections.

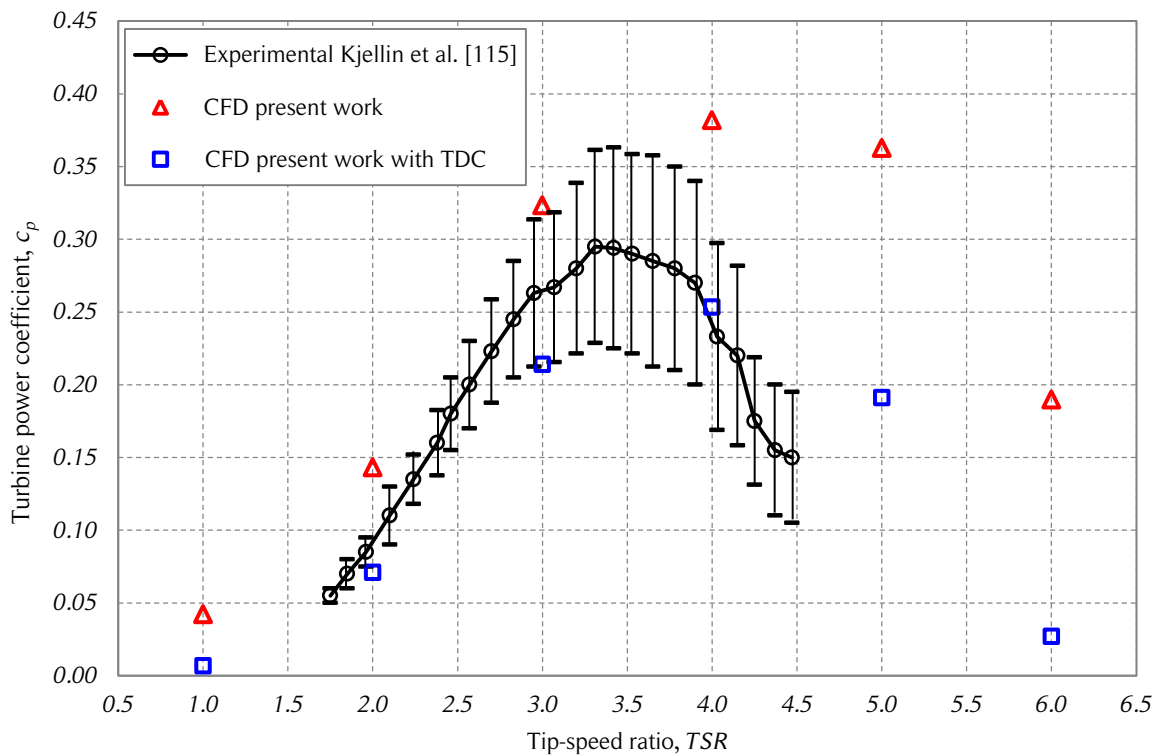


Figure 4.23. Turbine power coefficient with three-dimensional corrections.

The figure shows the turbine power coefficient as a function of the tip-speed ratio for the experimental data, the two-dimensional CFD simulations, and the simulated data with the three-dimensional corrections (TDC). Source: own elaboration.

Assuming that the CFD simulations are reasonably accurate, the inaccuracy of the corrections can be explained by the complexity of the physics involved in the three-dimensional and time-dependent flow field around the turbine. The corrections are based on empirical coefficients that do not necessarily represent the operating conditions of the studied turbine. As mentioned in Section 4.2.3, similar differences between experimental and two-dimensional simulations as the ones shown in Fig. 4.23 have been reported in the literature [100].

A breakdown of the three-dimensional corrections is shown in Fig. 4.24. The three-dimensional effects reduce the turbine power coefficient derived using the two-dimensional CFD simulations. The power loss due to the struts includes only losses from drag and not losses due to the modification of the flow around the turbine blades. This is justified because the struts are expected to influence the flow around the blades only in isolated regions near the attachment points. The strut drag has a large significant impact on the turbine performance, especially for high values of TSR .

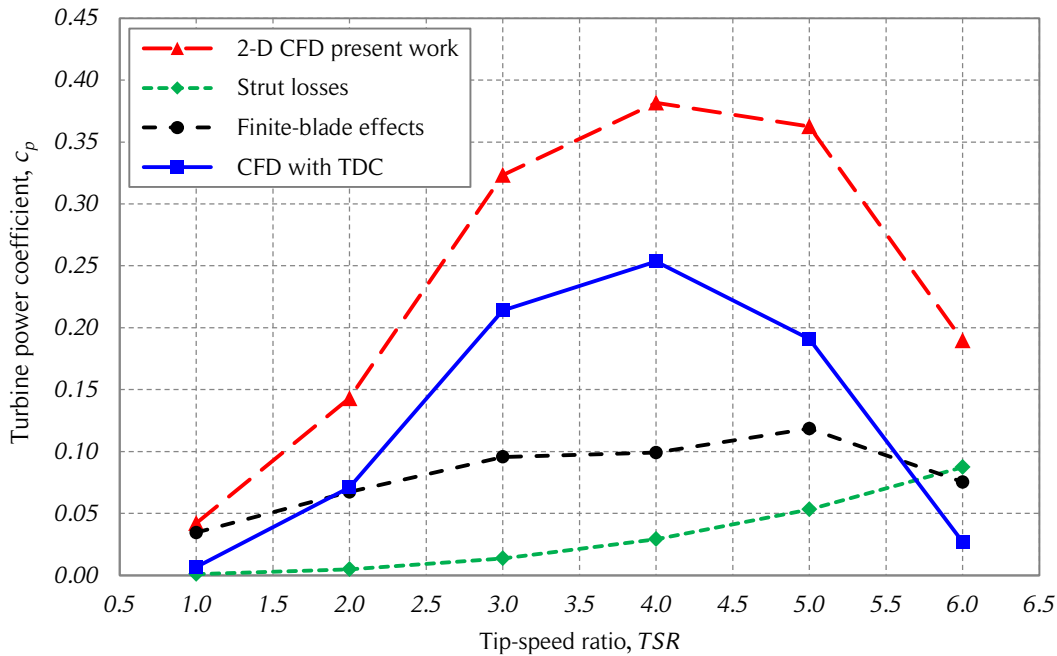


Figure 4.24. Three-dimensional corrections breakdown.

The figure shows the turbine power coefficient as a function of the tip-speed ratio and the breakdown of the three-dimensional corrections (TDC). Note that struts losses include the main and auxiliary struts of the turbine. Finite-blade effects include blade tapering and finite aspect ratio of the blades. Source: own elaboration.

Finite-blades effects have a larger impact on the power coefficient than strut losses at the tip-speed ratios studied. These effects take into account the blade tapering and the aforementioned effects related to the finite aspect ratio of the blades. Unlike strut losses, finite-blade effects do not show monotonically increase for increasing tip-speed ratios.

In summary, the three-dimensional corrections (TDC) applied to the two-dimensional CFD simulations are considered in good agreement with experimental results. Many simplifications and assumptions are used in the three-dimensional corrections. These are able to explain the differences observed in the power coefficient estimation. Since the corrected CFD simulations are considered a good representation of the experiments, it can be inferred that the two-dimensional CFD simulations are also in good agreement with experimental results. The two-dimensional CFD simulations are used as the reference case to simplify the validation of the DMS model variations addressed in the following chapters of the present work.

5. VARIATIONS OF THE DMS MODEL

Several variations of the double-multiple streamtube (DMS) model intended to improve estimation of power performance and flow expansion commonly found in the literature are presented in this chapter. The variations of the DMS model are the following. First, a modified DMS model with no flow expansion (MDMSM-NFE) is implemented. One of the dynamic stall models addressed in Chapter 3 is chosen to be used in the variations of the DMS model. Secondly, a modified DMS model with flow expansion (MDMSM-WFE) is implemented to take into account the expansion of the flow through the mathematical representation of streamlines discussed in Chapter 4. The computer codes are written in MATLAB.

5.1. Modified DMS model – no flow expansion

The DMS model without flow expansion has been widely used because the streamtube limits are chosen beforehand by the user and do not change with each iteration performed to find the streamwise velocities in the streamtubes (see Section 3.8.1). However, the decelerating wind velocities and the constant width of streamtubes do not satisfy the continuity equation. This issue is discussed later in this section.

Typically, in the DMS model without flow expansion the streamtube widths are determined by the equally-spaced arcs of the azimuthal angle obtained from the chosen number of streamtubes (NST). When many streamtubes are used, the width of the streamtubes at both sides of the turbine (left and right) tend to zero, and thus numerical divergence in the calculations appears.

A different approach was developed for the present work, where the streamtube widths are chosen first and the azimuthal arcs are determined afterwards. This new approach is called modified DMS model – no flow expansion (MDMSM-NFE). Thus, for a large NST , the width of the streamtubes at the turbine sides can be controlled and the numerical divergence problem can be avoided. Additionally, if all streamtubes are chosen to have the same width, the utilization and visualization of non-uniform free-stream velocity profiles become easier. Since the azimuthal arcs in this approach do not have the same length, the values calculated at each streamtube have to be weighted to obtain the results for the entire turbine. This issue is taken into account through a linear interpolation from the discrete data to a higher resolution equally-spaced azimuthal partition of a whole

turbine rotation, a procedure which gives smoother curves in the plotting of the results.

5.1.1. Implementation

The equations for the MDMSM-NFE of the present work are the same ones that were used in previous works except for the calculation of the streamtube widths and angular limits. A diagram of the uniform streamtube width of the MDMSM-NFE is presented in Fig. 5.1. The uniform streamtube width, w_{ST} , is calculated from the turbine diameter, D , and the number of streamtubes, NST , as shown in Eq. 5.1. The spanwise coordinates of the streamtubes for the left side of the turbine are obtained from the streamtube number, k , and the streamtube widths, w_{ST} , as shown in Eqs. (5.2) and (5.3).

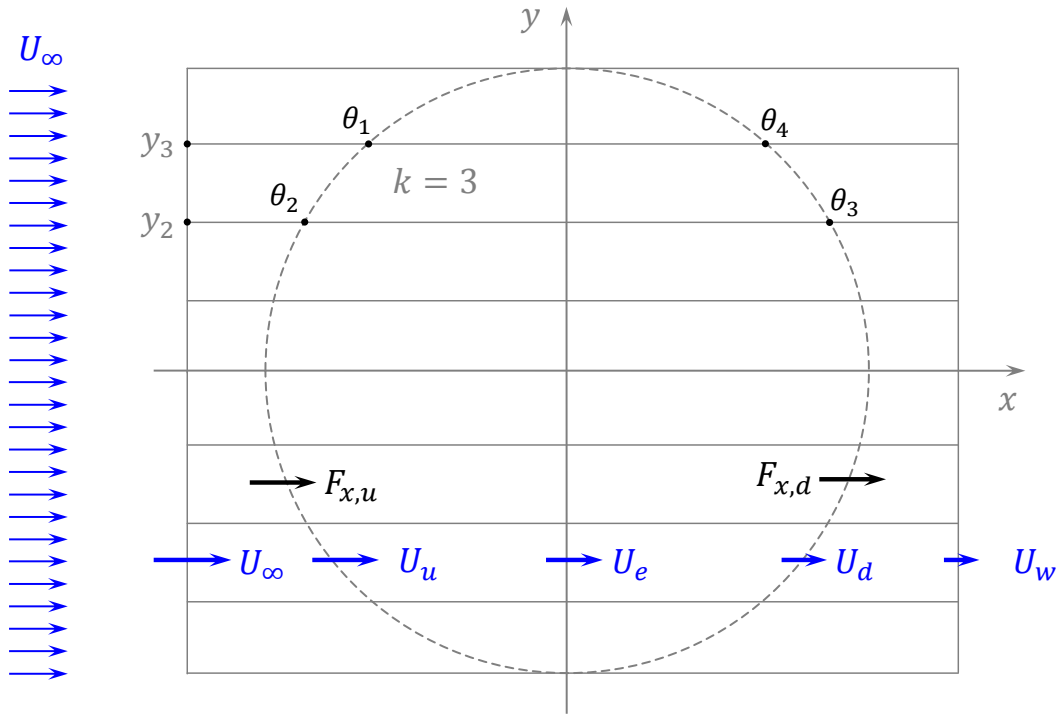


Figure 5.1. Diagram of the MDMSM-NFE with uniform streamtube width.

The figure shows a diagram of the modified DMS model – no flow expansion with uniform streamtube width and $NST = 8$. Source: own elaboration.

$$w_{ST} = \frac{D}{NST} \quad (5.1)$$

$$y_k = k w_{ST} \quad (5.2)$$

$$y_{k-1} = (k - 1) w_{ST} \quad (5.3)$$

For a given streamtube, k , with spanwise coordinates, y_k and y_{k-1} , the angular limits, $\theta_{1,k}$ and $\theta_{2,k}$, are calculated from Eqs. (5.4) and (5.5). The left side upstream angular limits and all the downstream angular limits, θ_3 and θ_4 , are obtained applying the respective azimuthal offsets. Note that $y_{k-1} = 0$ when $k = 1$.

$$\theta_{1,k} = 180^\circ - \arcsin\left(\frac{y_k}{R}\right) \quad (5.4)$$

$$\theta_{2,k} = 180^\circ - \arcsin\left(\frac{y_{k-1}}{R}\right) \quad (5.5)$$

Due to the model restrictions to find solution in some turbine geometry and operational conditions, the iterative procedure presented in Section 3.8.1 is replaced by the following procedure. A resolution of the interference factor, u , is defined by the number of iterations, NI , as shown in Eq. (5.6), where the number i starts at 1 and goes up to NI . The upstream dimensionless momentum equation, MOM_u , is shown in Eq. (5.7) and is defined for the upstream and downstream halves. The upstream dimensionless aerodynamic force coefficients, AFC_u , are calculated from Eq. (5.8). Since the iterative process starts from a no-load state (there is no streamwise force and no flow deceleration), thus, $u_u = 1$ and MOM_u starts at zero. To start at a positive value, the upstream difference, DIF_u , is calculated as the subtraction of MOM_u from AFC_u , as shown in Eq. (5.9).

$$u_i = 1 - \frac{i - 1}{NI} \quad (5.6)$$

$$MOM_u = u_u(1 - u_u) \quad (5.7)$$

$$AFC_u = \frac{Nc}{8\pi U_\infty^2 w_{ST}} \int_{\theta_1}^{\theta_2} (c_r \cos \theta - c_\theta \sin \theta) W^2 d\theta \quad (5.8)$$

$$DIF_u = AFC_u - MOM_u \quad (5.9)$$

The converged upstream interference factor, u_u , is the one that satisfies $DIF_u = 0$. To improve the accuracy of the discretization, NI , a linear interpolation between the iteration i and $i - 1$ is performed when $DIF_{u,i} \leq 0$, as shown in Eq. (5.10).

$$u_u = u_{u,i-1} + \frac{DIF_{u,i-1}}{DIF_{u,i} - DIF_{u,i-1}} (u_{u,i-1} - u_{u,i}) \quad (5.10)$$

This procedure has to be repeated for the downstream half of the turbine until the induced velocity is known for all the azimuthal angles. Note that a linear interpolation from the discrete data to a higher resolution equally-spaced azimuthal partition of a whole turbine revolution is performed. With this information, the dynamic stall model is applied to obtain the blade aerodynamic coefficients.

5.1.2. Dynamic stall model

The two dynamic stall models modified for Darrieus VAWTs presented in Sections 3.8.4 and 3.8.5 were implemented to choose the most suitable one for the present work. The modified Boing-Vertol dynamic stall model (MBVDSM) is based on the modification of the angle of attack used to read the empirical aerodynamic coefficients and is quite simple to implement. The modified MIT dynamic stall model (MMITDSM) consists of four modes which are inspired in the physical phenomena of a vortex shedding and is not just based on empirical coefficients. This causes it to be more complex than the MBVDSM, but the information of the dynamic stall phenomenon is more complete, which gives flexibility to adjust the model parameters.

The models were compared using the following model geometry and operating conditions:

- Geometric parameters of reference [9]: turbine diameter $D = 6 \text{ m}$, blade chord $c = 0.2 \text{ m}$, airfoil geometry NACA 0015.
- Free-stream velocity for all turbine domain: $U(\theta) = U_\infty = 10 \text{ m/s}$; and constant air physical properties: density of $\rho = 1.225 \text{ kg/m}^3$, kinematic viscosity of $\nu = 1.46 \times 10^{-5} \text{ m}^2/\text{s}$. A constant turbine rotational speed: $\omega = 10.00 \text{ rad/s}$ ($TSR = 3$).

Note that the typical dynamic stall experiments and simulations have a constant free-stream velocity, commonly denoted U_∞ , and therefore the only variable that changes in time is the angle of attack, α . In the aerodynamics of Darrieus VAWTs the relative wind velocity, W , changes its magnitude and orientation and therefore the Reynolds number also varies. This implies a change in the typical lift and drag coefficient curves plotted as a function of the angle of attack available in the literature. For instance, the static stall angle can be different at the onset and offset of the dynamic stall phenomenon due to the variation in the Reynolds number. The tip-speed ratio, $TSR = 3$, was chosen as a representative for this part of the study because for low tip-speed ratios, the power

coefficient is low and at higher tip-speed ratios, dynamic stall does not occur. The blade Reynolds number is in the range 274,000 and 548,000 in this case. The moment coefficients were not included in this analysis because experimental data is not always available and also because according to Fig. 4.10, the moment coefficients do not have a large impact on the power performance at low tip-speed ratios and no influence on the streamwise momentum balance. For reference, the angle of attack as a function of the azimuthal angle is shown in Fig. 5.2. It is the same for both MBVDSM and MMITDSM.

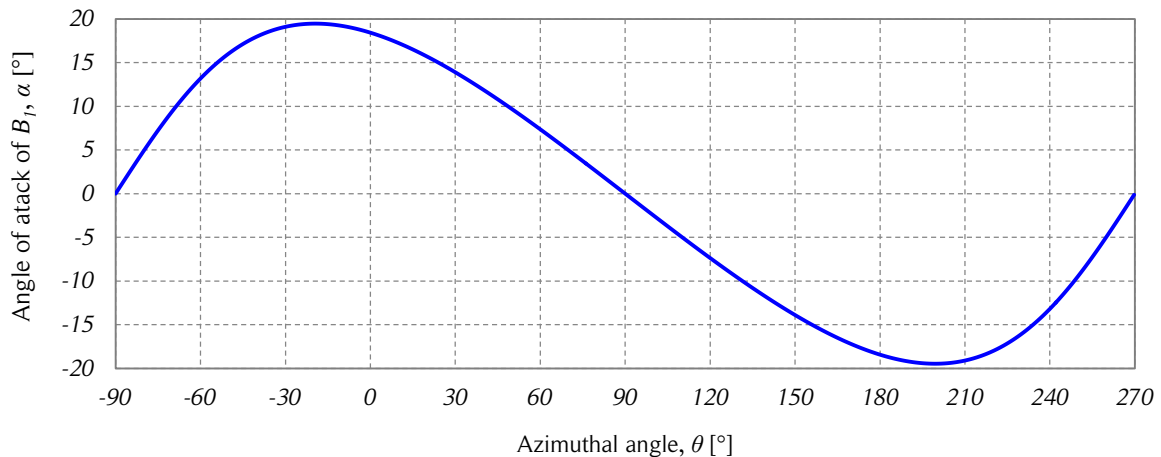


Figure 5.2. Angle of attack vs. azimuthal angle.

The figure shows the angle of attack as a function of the azimuthal angle for the geometric and operational parameters of reference [9] ($TSR = 3$) and no flow interference. Source: own elaboration.

The MBVDSM and the MBVDSM with the azimuthal restriction of Paraschivoiu et al. (MBVDSM-AR) are presented in Figs. 5.3 – 5.6. There is a dynamic stall effect on the downstream ($\alpha > 0$) and upstream ($\alpha < 0$) sides of the turbine. The restriction of the azimuthal angles ($195^\circ - 315^\circ$) limits the range where the dynamic stall model can be applied (see Section 3.8.4). This is noticeable in the discontinuities of the curves due to formulation of the model of Figs. 5.3 and 5.4. When the static stall angle of attack, α_{SS} , is reached, a small leap in the curve is observed. This leap becomes larger when α becomes lower than α_{SS} again. These leaps are explained the aerodynamic coefficients modifications (offset and change in amplitude). The leaps are larger especially for the flow reattachment, where the parameters $\dot{\alpha}$, W and Re can be quite different from the ones where the dynamic stall phenomenon started at α_{SS} . Another reason for this is that machines with dynamic stall effects where the angle of attack range is controlled (helicopters for instance), the angle of attack usually does not go far above the static stall angle to optimize the lift to drag ratios. In this case the angle of attack can go far above

the static stall angle and for relatively long periods of time, which is able to explain the discontinuities of the curves of the MBVDSM and MBVDSM-AR.

The MMITDSM is also shown in Figs. 5.3 – 5.6. The four modes of the MIT model can be identified in the figures from the lift curves and are shown explicitly in Fig. 5.7. The MMITDSM lift curve has a smaller slope than the MBVDSM. According to [92], the static stall angle of attack is defined as the point with a slope of $0.05/1^\circ$, and therefore, that slope is maintained in the Mode 1 of the dynamic stall model. The reattachment of the flow in the downstream half for this dynamic stall model coincides with the azimuthal restriction of Paraschivoiu. However, on the upstream half, the MMITDSM allows the dynamic stall phenomenon to occur at an azimuthal angle smaller than the one allowed by the MBVDSM-AR. Since the dynamic stall has to start with the shedding of a vortex from the leading edge, the dynamic stall can start at $\theta \approx 130^\circ$ because the upper side of the airfoil is “hidden” from the relative wind (inner side of the blade). According to MBVDSM-AR this is not possible because of the high turbulence. One advantage of the MMITDSM is that it does not result in the discontinuities of the MBVDSM-AR. The constant lift zones or plateaus of the MMITDSM below $c_{L,max} = 3$ are explained by the relatively small dynamic stall parameter, in other words, $\dot{\alpha}$ is small in comparison with W . The MMITDSM modes and the reduced frequency are shown in Figs. 5.7 and 5.8, respectively. Note that for this part of the study, perturbation of the flow is not considered, $U(\theta) = U_\infty$, and yet, large differences are noticeable for the upstream and downstream halves due to the asymmetry in VAWT aerodynamics.

The drag coefficients of the MBVDSM-AR shown in Figs. 5.5 and 5.6 have zones with large increases and decreases in comparison with the static data. This is easier to notice in Fig. 5.6. In addition to the curve shape modification, the dynamic stall produces an offset of the drag coefficients with respect to the azimuthal angle. This does not happen in the MMITDSM, for which the zones where the drag is modified are quite small (only modes 3 and 4). The drag modifications of the MMITDSM are barely noticeable in the upstream half. This can be attributed to the shape difference in the angle of attack curve in the onset zone of the dynamic stall: the downstream slope of the curve is steeper than the upstream slope (see Figs. 5.2 and 5.8). Both models have results similar to the ones presented in [7]. Since both models are based on empirical constants deduced from experiments with different conditions, it cannot be concluded which model is more accurate only with this information.

To summarize, the MMITDSM has a better behavior than the MBVDSM in the lift and drag curves because it does not have any unphysical discontinuities. With the information available for this comparison, it is not clear whether the MBVDSM-AR is overestimating

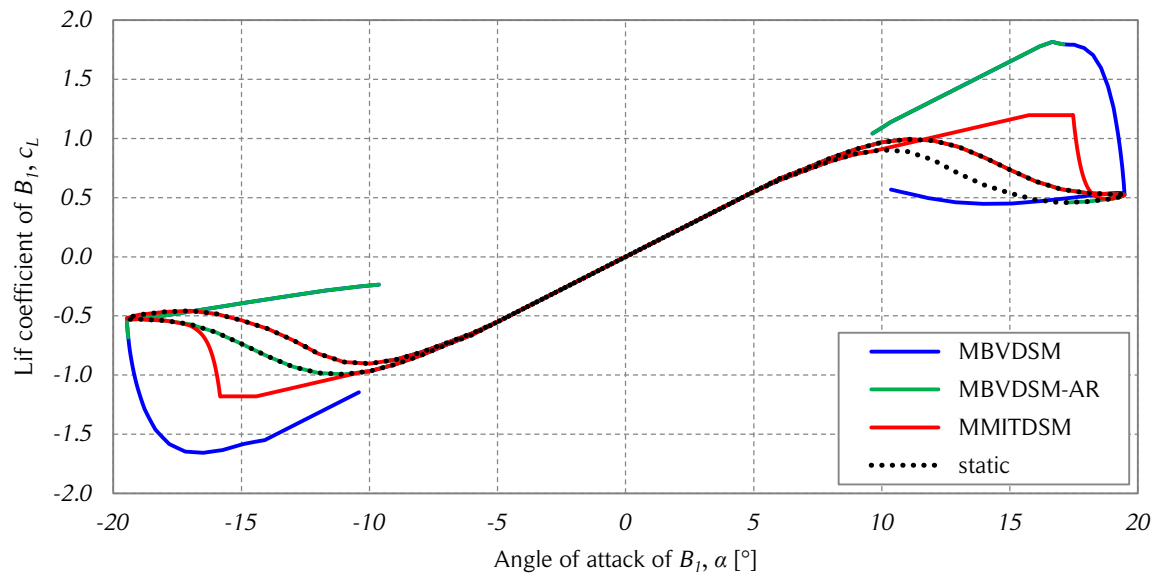


Figure 5.3. Dynamic stall lift coefficients vs. angle of attack.

The figure shows the lift coefficient as a function of the angle of attack using the two dynamic stall models tested for the present work. Geometric and operational parameters of reference [9] were used ($TSR = 3$). Source: own elaboration.

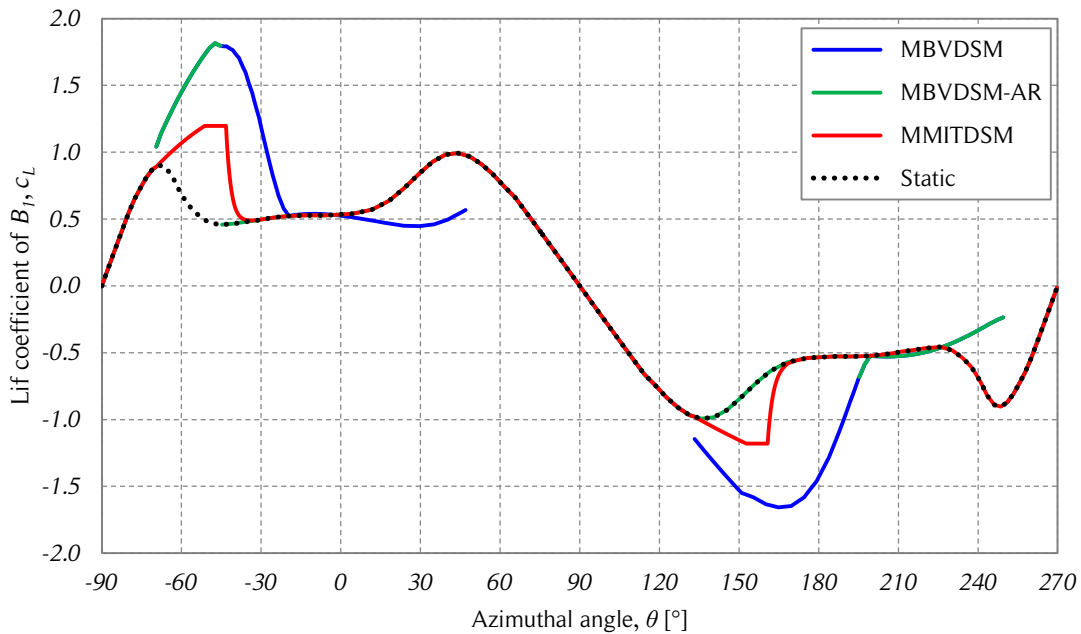


Figure 5.4. Dynamic stall lift coefficients vs. azimuthal angle.

The figure shows the lift coefficient as a function of the azimuthal angle using the two dynamic stall models tested for the present work. Geometric and operational parameters of reference [9] were used ($TSR = 3$). Source: own elaboration.

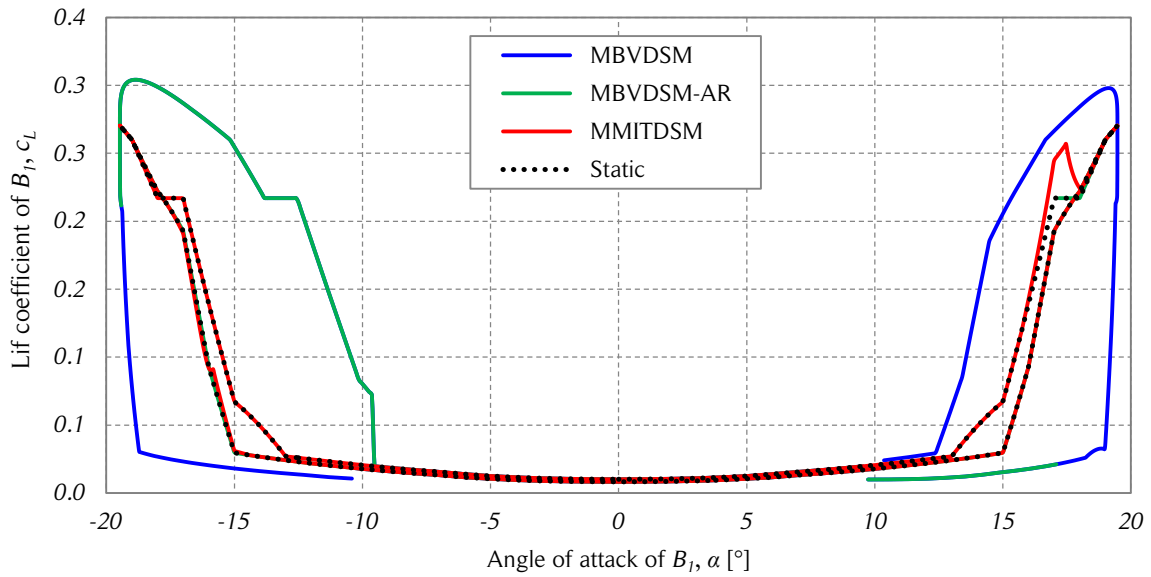


Figure 5.5. Dynamic stall drag coefficients vs. angle of attack.

The figure shows the lift coefficient as a function of the angle of attack using the two dynamic stall models tested for the present work. Geometric and operational parameters of reference [9] were used ($TSR = 3$). Source: own elaboration.

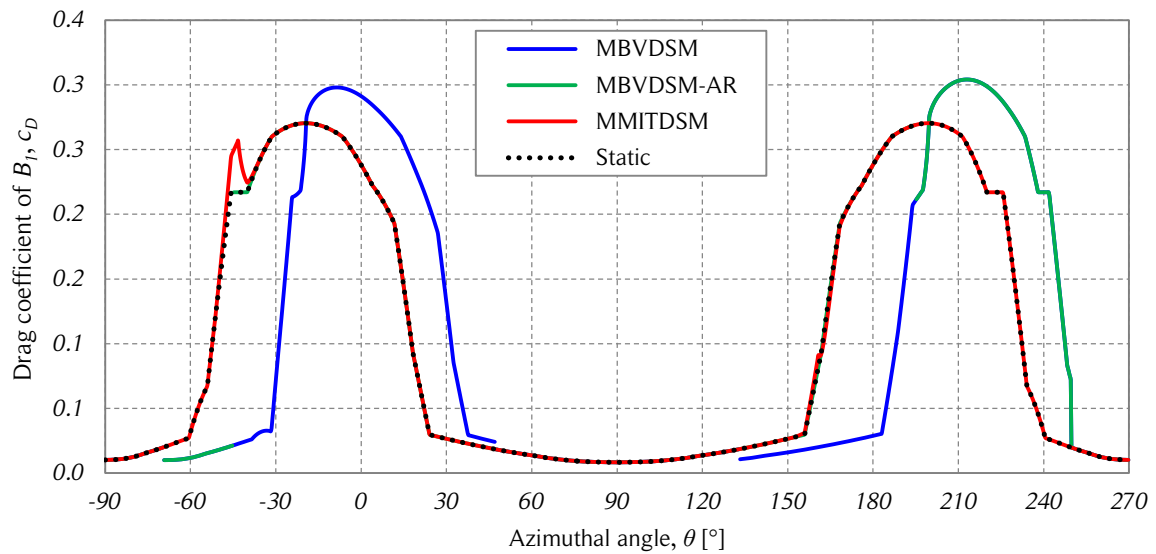


Figure 5.6. Dynamic stall drag coefficients vs. azimuthal angle.

The figure shows the lift coefficient as a function of the azimuthal angle using the two dynamic stall models tested for the present work. Geometric and operational parameters of reference [9] were used ($TSR = 3$). Source: own elaboration.

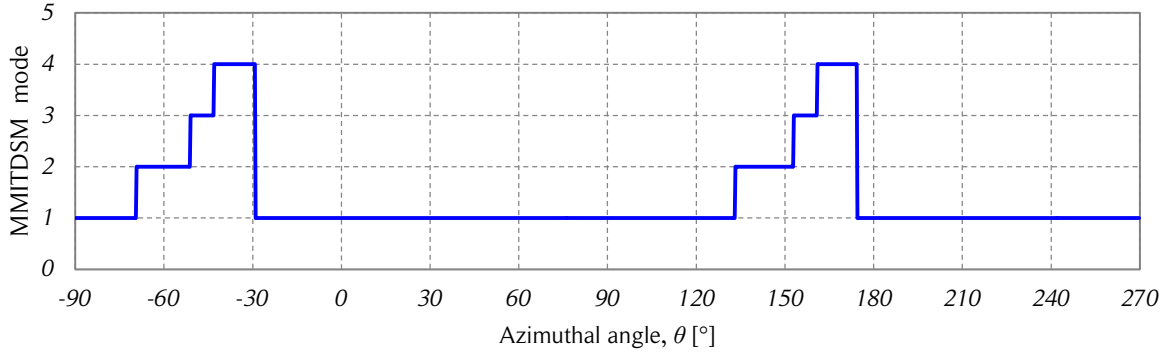


Figure 5.7. Modified MIT dynamic stall model modes vs. azimuthal angle.

The figure shows the modes of the modified MIT dynamic stall model (MMITDSM) as a function of the azimuthal angle. Source: own elaboration.

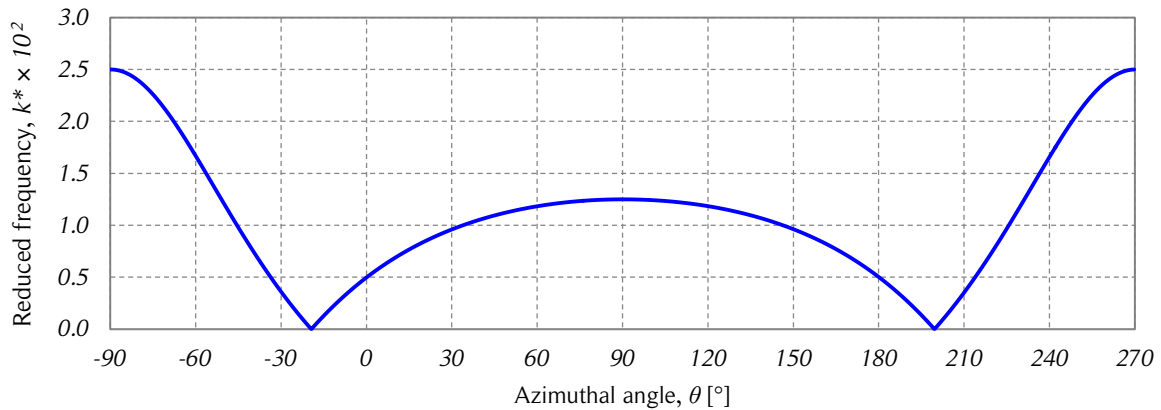


Figure 5.8. Reduced frequency vs. azimuthal angle.

The figure shows the reduced frequency as a function of the azimuthal angle for the studied case, where $TSR = 3$. Source: own elaboration.

the aerodynamic coefficients or whether the MMITDSM is underestimating them. Since there are several empirical coefficients in each dynamic stall model, this has to be analyzed separately for each situation. Due to the possibility of implementing modifications in the MMITDSM based on physical phenomena such as the convection velocity of the dynamic stall vortex, it is considered more suitable for the modified DMS models of the present work.

5.1.3. Verification of the model

The performance of the DMS model with the MMITDSM presented in this section is verified by comparing its results with the DMSV model results from reference [9]. The

turbine parameters are: turbine diameter $D = 6\text{ m}$, blade chord $c = 0.2\text{ m}$, airfoil geometry NACA 0015, and constant rotational speed $\omega = 125\text{ rpm}$. The number of streamtubes used for the calculations is twelve, which is close to the number of streamtubes commonly used in the DMS models found in the literature ($NST \approx 10$).

The tangential force coefficient is shown as a function of the azimuthal angle for $TSR = 5.2$ in Fig. 5.9 for no flow expansion (MDMSM-NFE). The present approach is in good agreement with the results from reference [9]. The larger differences at the peak values in the upstream and downstream halves can be attributed to the different approaches of the DMS model used to calculate the interference factors and also to the source of the tabulated aerodynamic coefficients used in the calculations. The dynamic stall model does not play any role at this TSR because the operation conditions cause the angle of attack to be within the range $-9.3^\circ \leq \alpha \leq 6.3^\circ$, which is below the static stall angle for the respective Reynolds number range, which is $430,000 \leq Re \leq 640,000$ ($\alpha_{SS} \geq 10^\circ$ when $Re \geq 360,000$).

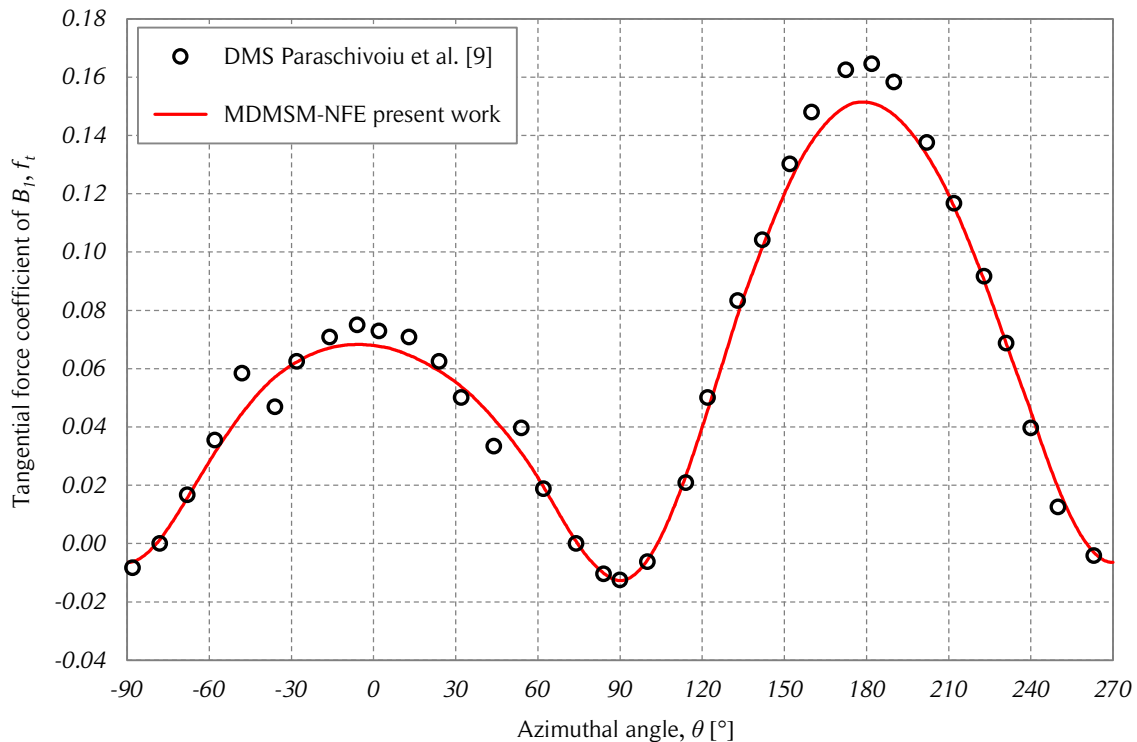


Figure 5.9. Tangential force coefficient verification.

The figure shows the tangential force coefficient as a function of the azimuthal angle of the MDMSM-NFE and the results of [9], for the case $TSR = 5.2$. Source: own elaboration and [9].

The turbine performance prediction is compared in Fig. 5.10. In general, the results are in good agreement with the results from reference [9]. For low tip-speed ratios ($TSR < 3$), the present model predicts a lower turbine performance. For tip-speed ratios between $TSR = 3$ and $TSR = 4.5$, the present model predicts slightly higher power coefficients. These differences occur in the operational range of the turbine where dynamic stall still has a relevant influence on the aerodynamics and are attributed to the different dynamic stall models used. This issue was addressed in the previous subsection. For higher tip-speed ratios, the present work predicts again a slightly lower turbine performance than [9]. This can be attributed to the already discussed differences noticeable in Fig. 5.9. Note that the dynamic stall phenomenon increases slightly the estimated power coefficient. For $TSR > 4$, dynamic stall has no influence on the power coefficient.

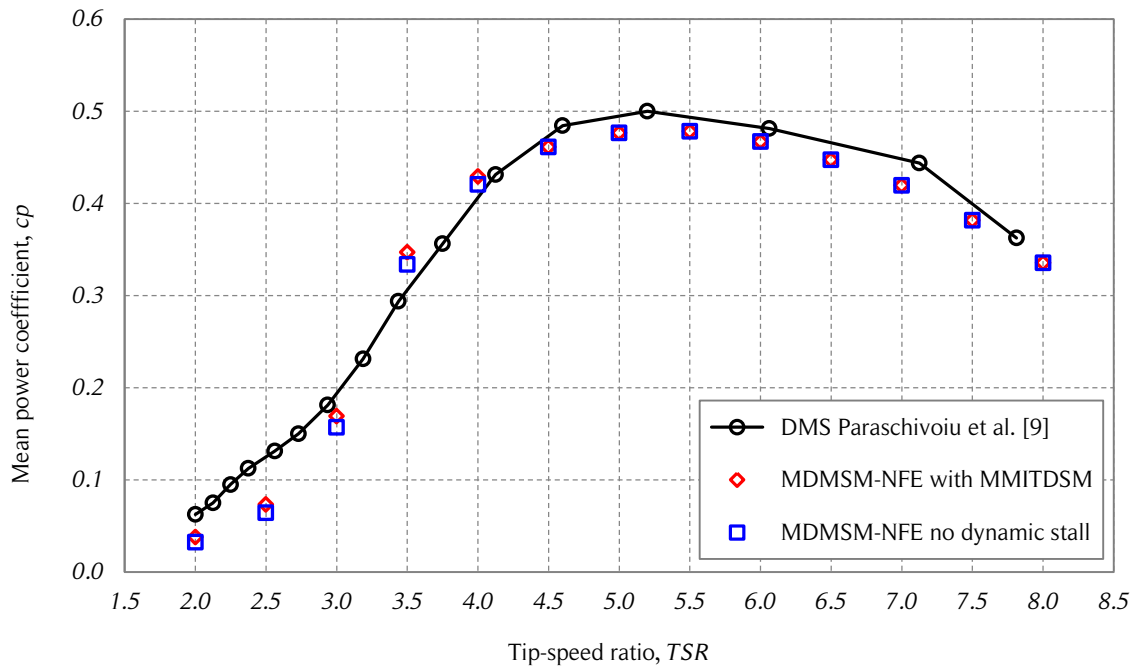


Figure 5.10. Power coefficient verification.

The figure shows the power coefficient as a function of the tip-speed ratio of the MDMSM-NFE and the results of the DMSV model [9]. Source: own elaboration and [9].

Based on the aforementioned results, it can be concluded that the MDMSM-NFE implemented in the present work is in good agreement with the DMS model typically available in the VAWT literature. The main differences are attributed to the dynamic stall model used here. The empirical parameters of the MMITDSM can be adjusted depending on the available experimental data, which is not available for this verification.

5.1.4. Comparison with the two-dimensional reference case

The MDMSM-NFE is used to compare the turbine performance with the two-dimensional reference case (CFD simulations). Since the MDMSM-NFE does not satisfy the continuity equation, the flow deceleration predicted by the model is used to estimate the flow expansion. Some of the parameters of the MMITDSM previously discussed were changed to follow the physical phenomena observed in the CFD simulations. The turbine tower wake was included in the calculations of the induced velocity. The magnitude of the velocity deficit calculated according to [93] was changed to be in good agreement with the CFD simulations. The calculations use twelve streamtubes.

According to the CFD simulations, the average velocity deficit due to the tower wake for all of the tip-speed ratios studied is shown in Eq. (5.11). According to the theoretical derivation and empirical parameters discussed in Section 3.8.6, the velocity deficit of Eq. (3.128) should be of $\Delta u_{max}/U_e = 0.3426$ at a downstream distance of one turbine radius ($x = 3m$) from the tower. The deficit velocity factor, 1.75, was multiplied by a factor of 0.4 to have a better agreement between the MDMSM-NFE and the CFD simulations. The tower wake shape factor of Eq. (3.129), 0.275, was multiplied by 3. One possible explanation for these modifications is that the empirical parameters of the tower wake modeled in [9] were adjusted for a HAWT. Therefore, the distance from the tower to the point where the aerodynamic forces are calculated is shorter than the distance in VAWTs in terms of the tower diameter.

$$\frac{\Delta u_{max}}{U_e} = 0.1319 \pm 0.0151 \quad (5.11)$$

Since the behavior of the lift and drag coefficients amongst the NACA 00XX airfoils is similar, the parameter γ of Eq. (3.112) was changed to 1.6 rad. The convection velocity of the dynamic stall vortex was changed from 50% of the rotational blade velocity (according to [92] for a HAWT) to a 22% (for general dynamic stall according to [4]). These changes meant larger lift and drag coefficients and a better agreement with the CFD results.

The power coefficients of the MDMSM-NFE and the CFD simulations are compared in Fig. 5.11. For low tip-speed ratios there is an underestimation of the power performance and there is an overestimation for high tip-speed ratios. These results are consistent with tangential force coefficients shown in Fig. 5.12. At low tip-speed ratios, the agreement between the MDMSM-NFE and the CFD simulations is not very good, especially where the dynamic stall effect has a large influence in the tangential force. This happens for

both the upstream and downstream halves. The shape of the curves for higher tip-speed ratios is in good agreement with the CFD results but in general there is an overestimation of the tangential force coefficients by the model at the upstream half and an underestimation at the downstream half.

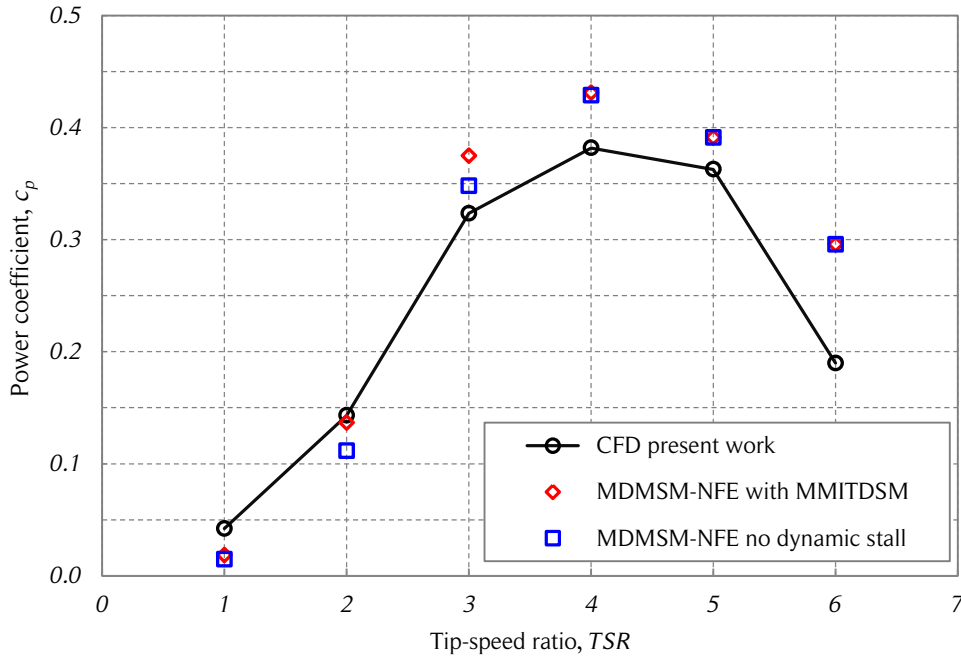


Figure 5.11. Turbine power coefficient comparison.

The figure shows the power coefficient as a function of the tip-speed ratio of the two-dimensional CFD simulations and the MDMSM-NFE. The six studied tip-speed ratios of the reference case are shown. Source: own elaboration.

The cases with $TSR \leq 3$ of Fig. 5.12 show an oscillatory behavior after the peak tangential force coefficient in the upstream half. A similar behavior has not been found in the literature. Additionally, according to the physical nature of the dynamic stall phenomenon described in Section 3.8.3-3.8.5, the oscillations can be considered as a non-physical phenomenon. To study this behavior in detail, the instantaneous pressure field and streamlines close to a blade are shown in Fig. 5.13 for various azimuthal positions and with $TSR = 2$. A flow visualization of the entire rotating domain is shown in Fig. 5.14 for the same operating conditions.

In Fig. 5.13, the flow is attached at $\theta = 105^\circ$. The flow becomes separated at $\theta = 135^\circ$. At $\theta = 165^\circ$ and $\theta = 180^\circ$ the dynamic stall vortex is moving from the leading edge to the trailing edge on the low-pressure surface of the airfoil. At $\theta = 195^\circ$ and $\theta = 225^\circ$

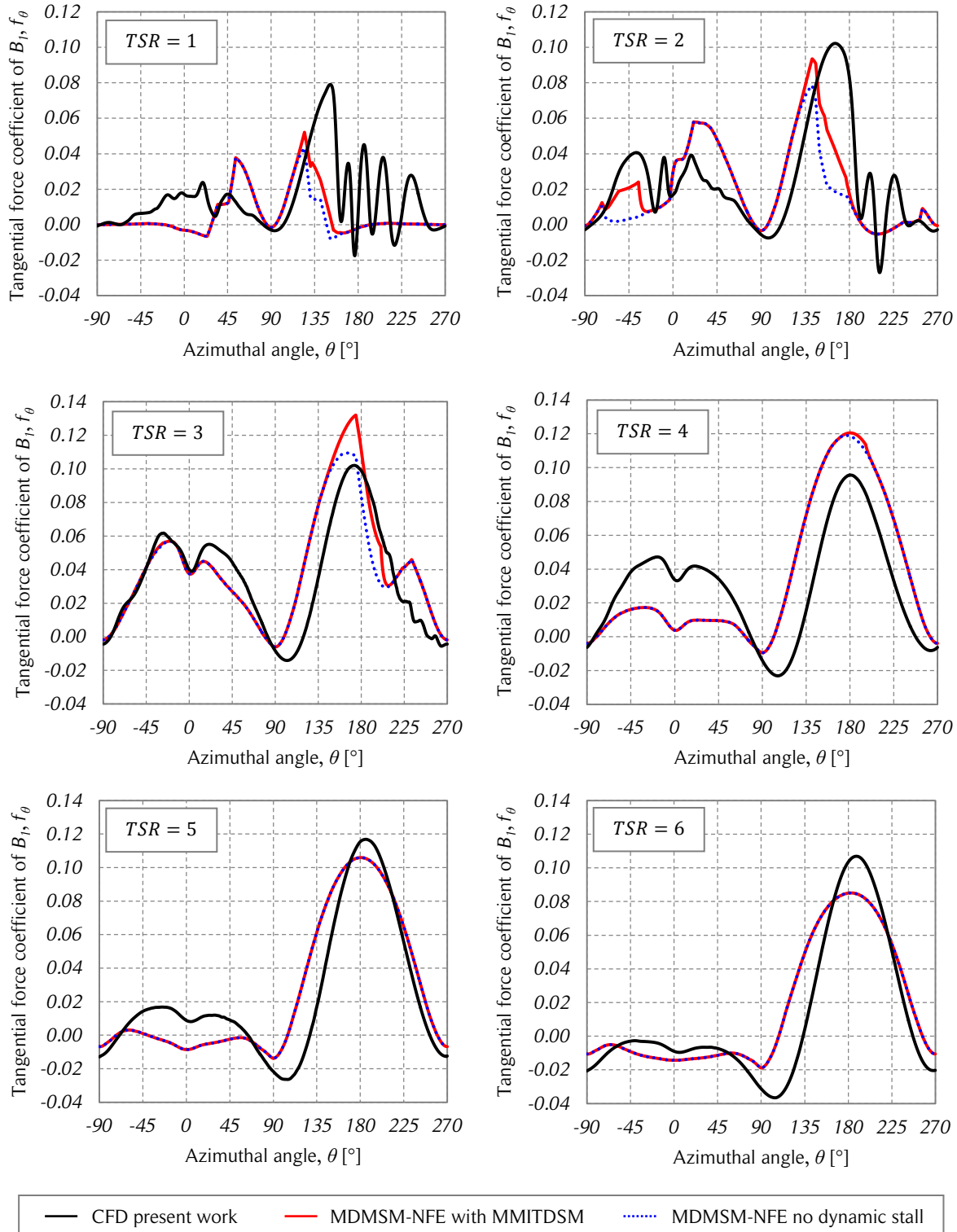


Figure 5.12. Tangential force coefficient comparison.

The figure shows the tangential force coefficients as a function of the azimuthal angle of the CFD simulations and the MDMSM-NFE for the six tip-speed ratios of the reference case. Source: own elaboration.

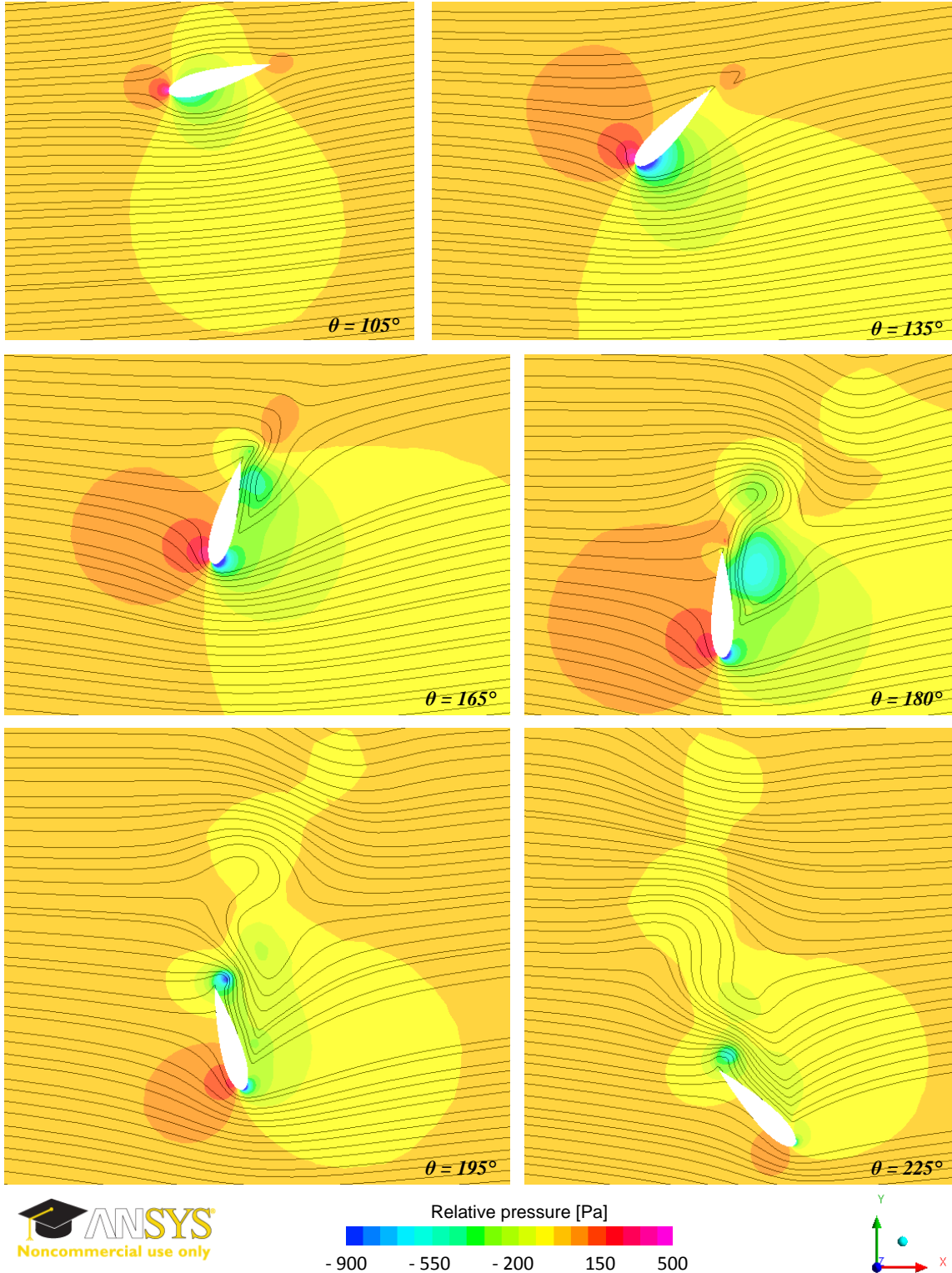


Figure 5.13. Instantaneous flow visualizations for blade under dynamic stall.

The figure shows the instantaneous pressure and streamline visualizations for a blade under dynamic stall at various azimuthal angles and $TSR = 2$. Source: own elaboration.

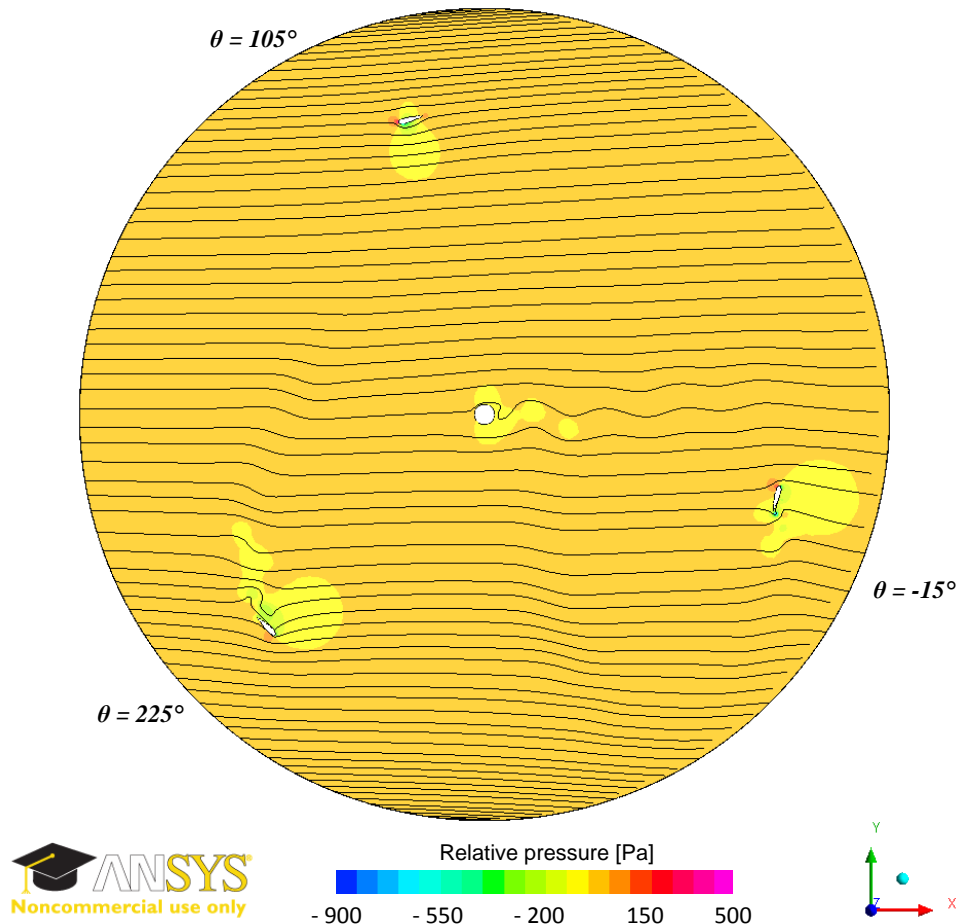


Figure 5.14. Instantaneous flow visualization of the rotating domain.

The figure shows the instantaneous pressure and streamline visualizations of the rotating computational domain with $TSR = 2$. Source: own elaboration.

the vortex has already been shed from the airfoil, which produces an important flow disturbance behind the blade. This description is consistent with the characteristic behavior of dynamic stall and the tangential force coefficient curves of Fig. 5.12. However, the oscillations of the tangential force coefficient are not in accordance with the expected behavior. Note that the oscillations are repeated almost exactly for each blade and for all the simulated revolutions of the turbine (for the converged solution) and that the magnitude of the oscillations decreases with increasing TSR . Two possible reasons for these oscillations are the computational mesh and the turbulence model. This phenomenon should be studied in detail to find out if it is a physical phenomenon or a modeling error of the CFD simulations.

The interference factor as a function of the azimuthal angle for all studied tip-speed ratios are shown in Fig. 5.15. Note that the interference factors at the turbine sides ($\theta = -90^\circ$

and $\theta = 90^\circ$) is imposed to be one. The interference factors at the downstream half are lower than the ones of the upstream halves for the same TSR . The interference factors are always lower at the center of the turbine than at the sides. A slight asymmetry with lower interference factors at the left side of the turbine can be noted. This asymmetry is consistent with the streamwise force coefficients shown in Fig. 4.6.

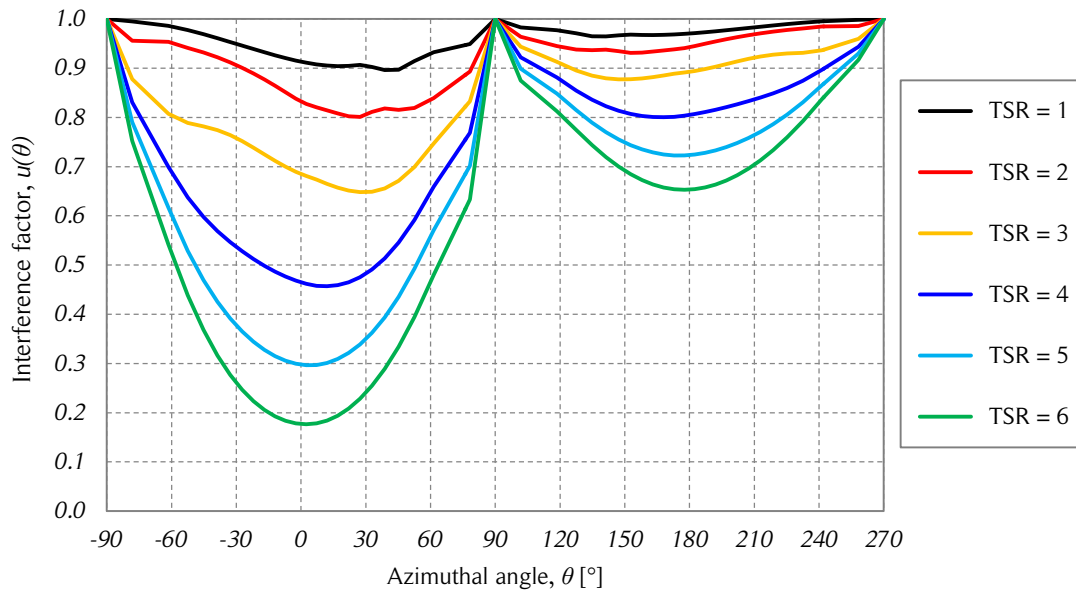


Figure 5.15. Interference factor vs. azimuthal angle.

The figure shows the interference factor as a function of the azimuthal angle using the MDMSM-NFE for the six studied tip-speed ratios of the reference case. Source: own elaboration.

A flow expansion estimation based on the flow deceleration predicted by the MDMSM-NFE using Eqs. (4.36) – (4.38) is shown in Fig. 5.16. The estimated expansion ratios are compared with the flow expansion of the two-dimensional CFD. The upstream and turbine expansion ratios are for $TSR \leq 2$. For higher tip-speed ratios, the difference becomes larger with increasing TSR . The downstream expansion ratio of the MDMSM-NFE is much smaller than the one from the CFD simulations, even reaching negative values. This is due to the interference factors below 0.5 found in the iterative process. According to [86] and Fig. 3.25, this is physically possible, but according to the CFD simulations, that is not the actual flow expansion corresponding to the operational conditions of the turbine.

In summary, the MDMSM-NFE gives relatively accurate predictions of the power performance of the turbine. The shape of the force coefficients is in good agreement with

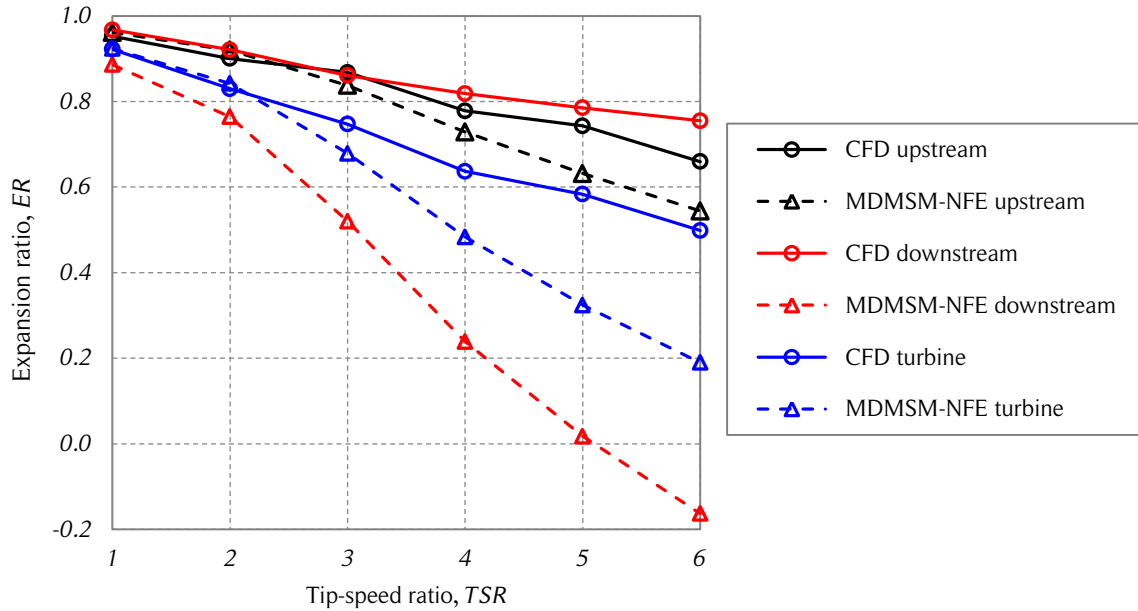


Figure 5.16. MDMSM-NFE flow expansion comparison.

The figure shows the upstream, downstream and turbine expansion ratios of the CFD simulations and the MDMSM-NFE for the six studied tip-speed ratios of the reference case. Note that the expansion ratios of the MDMSM-NFE are estimated from the interference factors. Source: own elaboration.

the CFD simulations but there are amplitude differences in the upstream and downstream halves. The flow expansion estimation based on the flow deceleration is considerably overestimated by the MDMSM-NFE relative to the CFD simulations.

5.2. Modified DMS model – with flow expansion

Although the MDMSM-NFE estimates the power performance of the Darrieus SB-VAWT in a relatively good manner, the flow expansion estimation is inadequate. Therefore, a modified DMS model with flow expansion (MDMSM-WFE) is implemented to improve the flow expansion estimation. This is done with the mathematical representation of streamlines addressed in Section 4.3.

5.2.1. Implementation

The MDMSM-WFE is based on the DMS model addressed in Section 3.8.2. The principle of the momentum balance is maintained. The modifications to the flow expansion

calculation are shown below. In Section 4.3, the streamtube widths at the equilibrium ($x = 0$) and developed wake positions were known from the manual measurements of the CFD simulations. In general, this information is not available, and therefore, the streamtube widths are determined from an iterative process of the streamwise momentum balance for each streamtube.

Due to the flow expansion, the time-averaged wind velocity, U , has both a streamwise and a spanwise component. According to Fig. 4.20, this is especially noticeable at the equilibrium position, where the maximum slope of the streamlines occurs. This is taken into account in the MDMSM-WFE through the modification of some of the expressions used in Section 4.3, as shown in Fig. 5.17.

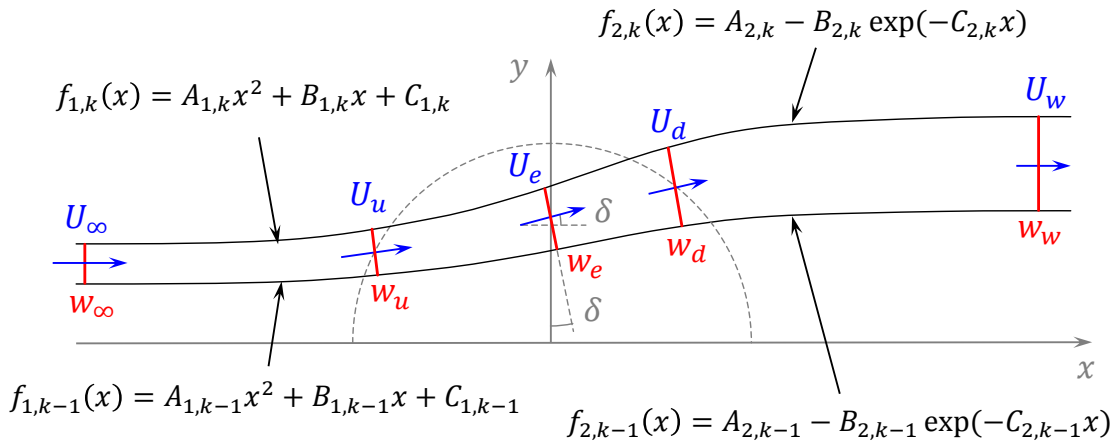


Figure 5.17. Streamtube expansion.

The figure shows a diagram of the streamtube expansion along the streamwise coordinate. The wind velocity and streamtube width at the five relevant locations of the MDMSM-WFE are shown. Source: own elaboration.

The streamtube slope at the equilibrium position of a streamtube can be approximated by the average of the two streamlines that define it. Although the equilibrium position width, $w_{e,k}$, of a given streamtube k is not known beforehand, the iteration process over the interference factor for each streamtube enables the determination of the streamlines for each iteration. Therefore, the streamtube width at the equilibrium position, $w_{e,k}$, is estimated from the slope, δ_k , of the lower streamtube limit (higher limit of the previous streamtube) as a first approach, as shown in Eqs. (5.12) – (5.14). This calculation is updated with each iteration of the interference factor.

$$f_{1,k}(0) = y_{e,k-1} + w_{e,k} \cos(\delta_k) \quad (5.12)$$

$$\left. \frac{df_{1,k-1}}{dx} \right|_{x=0} = B_{1,k-1} \quad (5.13)$$

$$\delta_k \approx \arctan(B_{1,k-1}) \quad (5.14)$$

The expressions of the angle of attack, α , and the relative wind velocity, W , also change when the flow expansion is considered. This is shown in Fig. 5.18 and Eqs. (5.15) – (5.18).

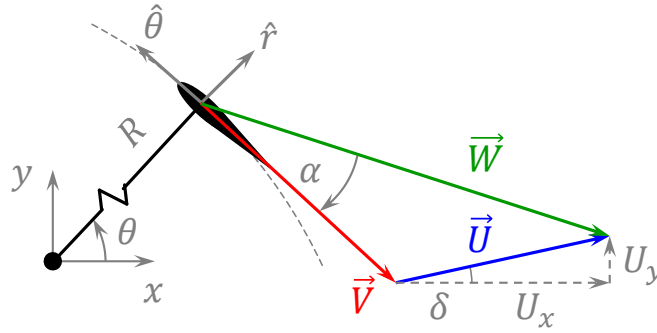


Figure 5.18. Triangle of velocities with streamtube expansion.

The figure shows a diagram of the triangle of velocities considering the spanwise component of the streamtube expansion. Source: own elaboration.

$$\vec{U} = U_x \hat{i} + U_y \hat{j} = U \cos \delta \hat{i} + U \sin \delta \hat{j} \quad (5.15)$$

$$\vec{W} = U_x \hat{i} + U_y \hat{j} - \omega R \hat{\theta} \quad (5.16)$$

$$W = \left[(U_x + \omega R \sin \theta)^2 + (U_y - \omega R \cos \theta)^2 \right]^{1/2} \quad (5.17)$$

$$\alpha_B = \text{sign}(U_x \cos \theta - U_y \sin \theta) \arccos \left(\frac{U_x \sin \theta + \omega R - U_y \cos \theta}{W} \right) \quad (5.18)$$

The expressions of the streamwise momentum balance considering flow expansion are presented below. The definitions of the upstream and downstream interference factors remain unchanged, which gives the equilibrium and wake velocities, as shown in Eqs. (5.19) and (5.20).

$$U_e = U_\infty (2u_u - 1) \quad (5.19)$$

$$U_w = U_e (2u_d - 1) \quad (5.20)$$

The streamwise momentum equation are slightly modified according to the slope of the streamtube at the equilibrium position, as shown in Eqs. (5.21) – (5.23). Replacing Eqs. (5.19) and (5.20) in the streamwise momentum expressions yields Eqs. (5.24) and (5.25). The streamtube number, k , is not shown in the following equations to simplify the notation.

$$F_{x,u} = \rho w_{\infty} U_{\infty} (U_{\infty} - U_{e,x}) \quad (5.21)$$

$$F_{x,d} = \rho w_w U_w (U_{e,x} - U_w) \quad (5.22)$$

$$U_{e,x} = U_e \cos \delta \quad (5.23)$$

$$F_{x,u} = \rho w_{\infty} U_{\infty}^2 [1 - (2u_u - 1) \cos \delta] \quad (5.24)$$

$$F_{x,d} = \rho w_e U_e^2 (1 + \cos \delta - 2u_d) \quad (5.25)$$

The average streamwise force expressions remain unchanged, as shown in Eqs. (5.26) and (5.27). Hence, the non-dimensional expressions for the streamwise momentum balance can be expressed as shown in Eqs. (5.28) and (5.29). Note that for moderate values of the slope at the equilibrium, δ , the terms MOM_u and MOM_d are lower than one.

$$\bar{F}_{x,u} = \frac{1}{2} \rho c \frac{N \Delta \theta}{2\pi} \frac{1}{\Delta \theta} \int_{\theta_1}^{\theta_2} (c_r \cos \theta - c_{\theta} \sin \theta) W^2 d\theta \quad (5.26)$$

$$\bar{F}_{x,d} = \frac{1}{2} \rho c \frac{N \Delta \theta}{2\pi} \frac{1}{\Delta \theta} \int_{\theta_3}^{\theta_4} (c_r \cos \theta - c_{\theta} \sin \theta) W^2 d\theta \quad (5.27)$$

$$\underbrace{1 + \cos \delta - 2u_u \cos \delta}_{MOM_u} = \underbrace{\frac{Nc}{4\pi w_{\infty}} \int_{\theta_1}^{\theta_2} (c_r \cos \theta - c_{\theta} \sin \theta) \left(\frac{W}{U_{\infty}}\right)^2 d\theta}_{AFC_u} \quad (5.28)$$

$$\underbrace{1 + \cos \delta - 2u_d}_{MOM_d} = \underbrace{\frac{Nc}{4\pi w_e} \int_{\theta_3}^{\theta_4} (c_r \cos \theta - c_{\theta} \sin \theta) \left(\frac{W}{U_e}\right)^2 d\theta}_{AFC_d} \quad (5.29)$$

To determine the angular limits of the streamtubes (azimuthal angles θ_1 , θ_2 , θ_3 and θ_4), the intersections between the streamlines and the blade trajectory have to be found. There are three possibilities for the intersection in the upstream half: no intersection, one intersection or two intersections. This is shown in Fig. 5.19. Due to the mathematical nature of the downstream streamlines, there are only two cases for the intersections: no intersection and one intersection. The mathematical problem of finding the intersections is equivalent to finding the roots of the expression $g(x) = 0$ in the respective Cartesian quadrant, as shown in Eq. 5.30.

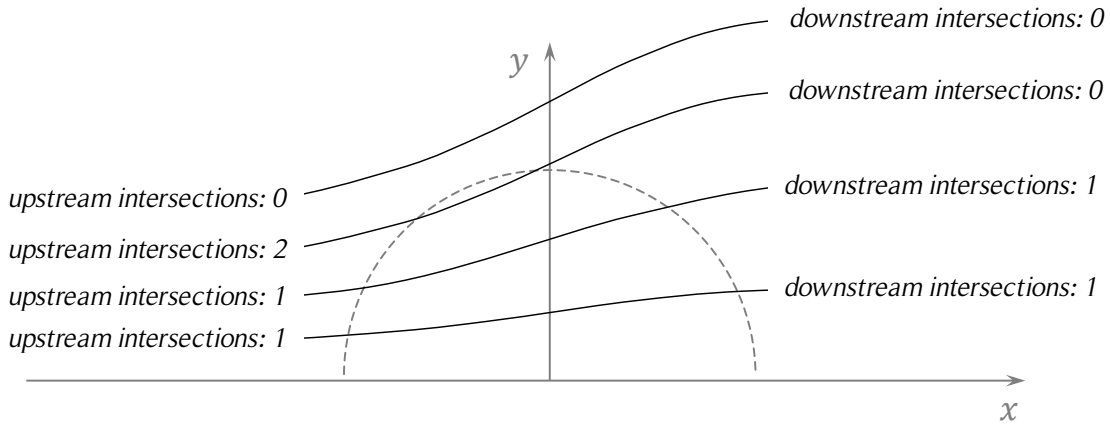


Figure 5.19. Upstream and downstream intersection possibilities.

The figure shows a diagram of the upstream and downstream intersection possibilities between the streamlines and the blade trajectory. Source: own elaboration.

$$g(x) = \begin{cases} A_1x^2 + B_1x + C_1 + \sqrt{R^2 - x^2}, & x \leq 0, y \leq 0 \\ A_1x^2 + B_1x + C_1 - \sqrt{R^2 - x^2}, & x \leq 0, y > 0 \\ A_2 - B_2 \exp(-C_2x) + \sqrt{R^2 - x^2}, & x > 0, y \leq 0 \\ A_2 - B_2 \exp(-C_2x) - \sqrt{R^2 - x^2}, & x > 0, y > 0 \end{cases} \quad (5.30)$$

The Newton-Raphson and the Halley's root-finding methods were implemented to find the solutions of Eq. 5.30 when $g(x) = 0$. However, the initial guesses of the numerical schemes showed problems to find the roots for the cases with two intersections in the upstream half. Additionally, the derivative of the square root term near $x = \pm R$ diverges. Considering that the domain to find the roots is well defined, the following alternative

method is used. The upstream and downstream domains, $[-R, 0]$ and $[0, R]$ respectively, are discretized in a vector, x_i . Then, the $g(x)$ function is calculated for each location in the respective discrete domain. The intersections are found from the changes in sign of $g(x)$, as shown in Eq. (5.31). The condition of Eq. (5.32) has to be satisfied to have two intersections in the upstream half. The x -coordinate of an intersection, x_{int} , is estimated as the average of two successive discrete locations, x_i and x_{i-1} , that meet Eq. (5.31) or (5.32), as shown in Eq. (5.33).

$$\text{sign}[g(x_i)g(x_{i-1})] \leq 0 \quad (5.31)$$

$$\text{sign}[g(x_i)g(x_{i-1})] \leq 0 \quad \wedge \quad |C_1| \geq R \quad (5.32)$$

$$x_{int} = \frac{1}{2}(x_i + x_{i-1}) \quad (5.33)$$

5.2.2. Results with empirical aerodynamic coefficients

Twelve streamtubes are used for the calculations of the MDMSM-WFE with empirical aerodynamic coefficients. The tangential force coefficients as a function of the azimuthal angle are shown in Fig. 5.20. Note that only the first four tip-speed ratios of the reference case are plotted because convergence for the higher tip-speed ratios was not achieved. This is discussed below.

Similar to the no flow expansion case, at low tip-speed ratios, the agreement between the MDMSM-WFE and the CFD simulations of the tangential force coefficients of Fig. 5.20 is not very good, especially where the dynamic stall effect has a large influence on the tangential force. This is the case for both the upstream and downstream halves. The shape of the curves for higher tip-speed ratios is in good agreement with the CFD results but in general there is an overestimation of the tangential force coefficients. These results are consistent with the power coefficients of Fig. 5.21. For low tip-speed ratios there is an underestimation of the power performance and for high tip-speed ratios there is an overestimation.

A comparison between the measured flow expansion of the CFD simulations and the expansion obtained from the MDMSM-WFE is shown in Fig. 5.22. All three upstream, downstream and turbine expansion ratios are similar to the equivalent ratios of the CFD simulations for $TSR \leq 2$. For higher tip-speed ratios, the difference becomes larger with increasing TSR .

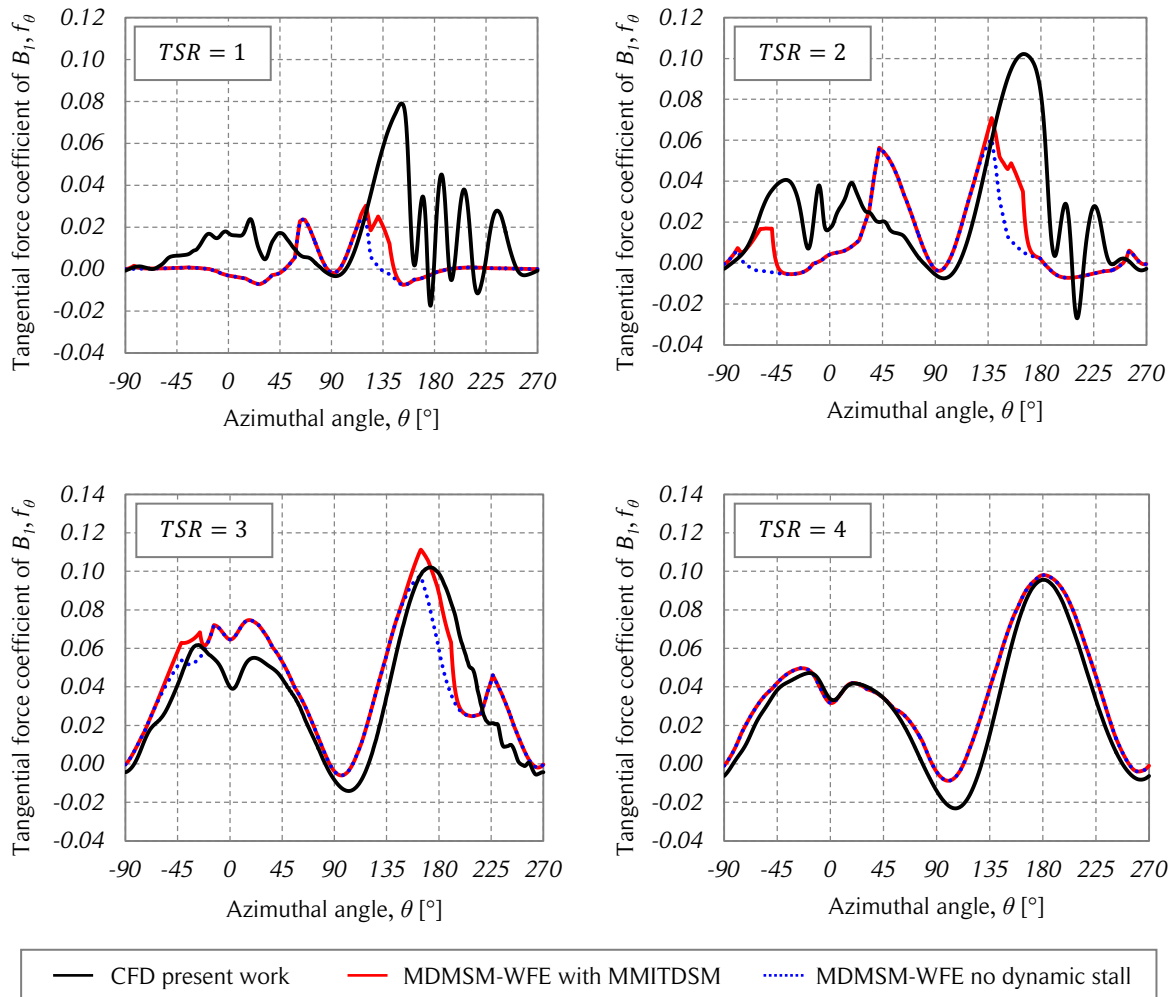


Figure 5.20. Tangential force coefficient comparison.

The figure shows the tangential force coefficients as a function of the azimuthal angle of the CFD simulations and the MDMSM-WFE for the four tip-speed ratios where convergence is achieved. Source: own elaboration.

Considering that flow reversals do not happen in the CFD simulations of the reference case, the interference factors of the MDMSM-WFE are not allowed be smaller than $u = 0.5$ because it would mean that the streamwise velocity changes its direction. Due to the sequential calculation of the streamtubes, if the first one does not converge, the following streamtubes cannot be determined. The same happens with the upstream and downstream halves.

For the case with $TSR = 5$ and $NST = 12$, the first left side upstream streamtube ($k = 1$) converges, as shown in Fig. 5.23. However, the downstream dimensionless momentum expression (MOM_d) does not reach the value of the average aerodynamic force

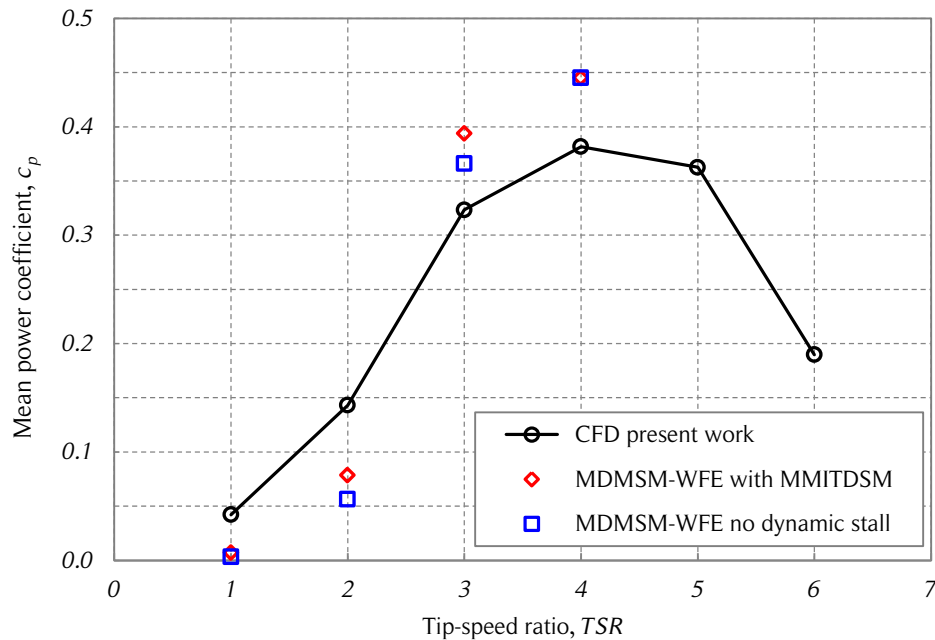


Figure 5.21. Power coefficient comparison.

The figure shows the power coefficient as a function of the tip-speed ratio of the CFD simulations and of the DMSM-WFE for the four tip-speed ratios where convergence is achieved. Source: own elaboration.

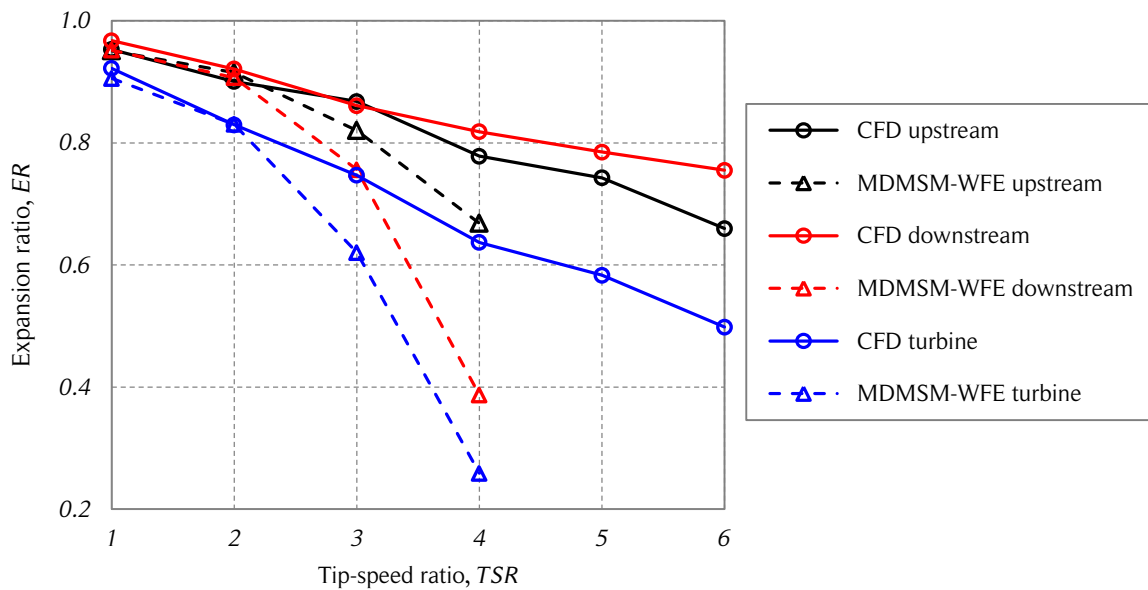


Figure 5.22. MDMSM-WFE with empiric coefficients flow expansion comparison.

The figure shows the upstream, downstream, and turbine expansion ratios of the CFD simulations and the MDMSM-WFE for the four tip-speed ratios where convergence is achieved. Source: own elaboration.

coefficients (AFC_d) for an interference factor larger than 0.5. Note that the dimensionless momentum expression (MOM) of Eqs. (5.28) and (5.29) can be different for each case due to the respective streamtube slope at the equilibrium position, δ . The calculations are repeated for $NST = 2$. In this case, the first left side downstream streamtube ($k = 1$) converges for an interference factor larger than 0.5.

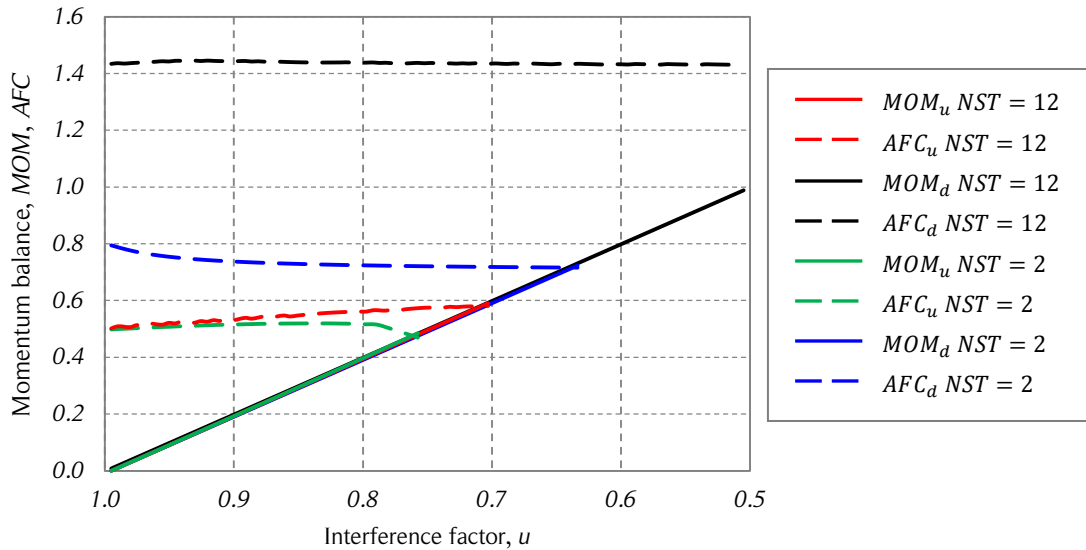


Figure 5.23. Momentum balance convergence curves.

The figure shows the upstream and downstream convergence curves of the dimensionless momentum and average aerodynamic force coefficients of the first left side streamtube ($k = 1$) with $TSR = 5$ for the cases $NST = 12$ and $NST = 2$. Source: own elaboration.

A sensitivity analysis of the impact of the number of streamtubes on the behavior of the streamtube limits, the streamtube width, the average streamwise force coefficient obtained from the aerodynamic forces acting on the blades, and the interference factor is shown in Table 5.1 for $TSR = 5$. The fewer the number of streamtubes, the larger the streamtube width and the smaller the streamwise force coefficient. The combination of these parameters and the azimuthal limits are shown in Eqs. (5.28) and (5.29), expressions that establish whether convergence can be achieved or not. In general, for moderate values of δ , the dimensionless momentum term, MOM , cannot be greater than 1.0. The upstream streamtube reaches convergence for all the streamtube numbers. The downstream streamtube only reaches convergence for the case $NST = 2$. Note that when convergence is not achieved, the values are still calculated for the smallest value of the interference factor greater than 0.5. For the discretization used in this study, the smallest possible value of the interference factor is 0.5050.

Table 5.1. Streamtube number convergence sensitivity for $TSR = 5$.

upstream side, first streamtube, left side ($k = 1$)						
NST	θ_1 [°]	θ_2 [°]	w_∞ [m]	$\bar{f}_{x,u}$	u_u	Convergence
12	162.2	180.0	0.50	1.98	0.7093	YES
8	152.7	180.0	0.75	1.91	0.7140	YES
4	132.5	180.0	1.20	1.74	0.7253	YES
2	90.0	180.0	1.80	1.10	0.7644	YES
downstream side, first streamtube, left side ($k = 1$)						
NST	θ_3 [°]	θ_4 [°]	w_e [m]	$\bar{f}_{x,d}$	u_d	Convergence
12	0.0	30.6	1.22	1.12	0.5050	NO
8	0.0	45.7	1.79	1.10	0.5050	NO
4	0.0	73.4	2.67	1.02	0.5050	NO
2	0.0	90.0	3.46	0.90	0.6373	YES

When convergence is not achieved, the values are calculated for the smallest interference factor of the discretization, in this case, $u = 0.5050$.

Table 5.1 also shows that the interference factor increases (smaller flow expansion) when the number of streamtubes decreases. This phenomenon is similar to the noticeable difference when using multiple streamtubes versus using a single one. Usually, the interference factors at the center of the turbine are smaller than the ones closer to the lateral ends (which are closer one). A single streamtube has an interference factor similar to the average interference factor of multiple streamtubes.

One of the objectives of the DMS model is to have enough streamtubes in the cross-stream direction to have an accurate representation of the flow. To illustrate this, the tangential force coefficients as a function of the azimuthal angle with $TSR = 4$ for the cases $NST = 12$ and $NST = 2$ are shown in Fig. 5.24. Note that, for this case, the tangential force coefficient estimation using $NST = 12$ is slightly improved in respect of $NST = 2$. However, the general description of the flow with $NST = 2$ is less accurate than with $NST = 12$.

5.2.3. Results with aerodynamic coefficients from CFD simulations

Considering that the results of the MDMSM-WFE using the empirical aerodynamic coefficients are not satisfactory, the calculations were repeated using the aerodynamic

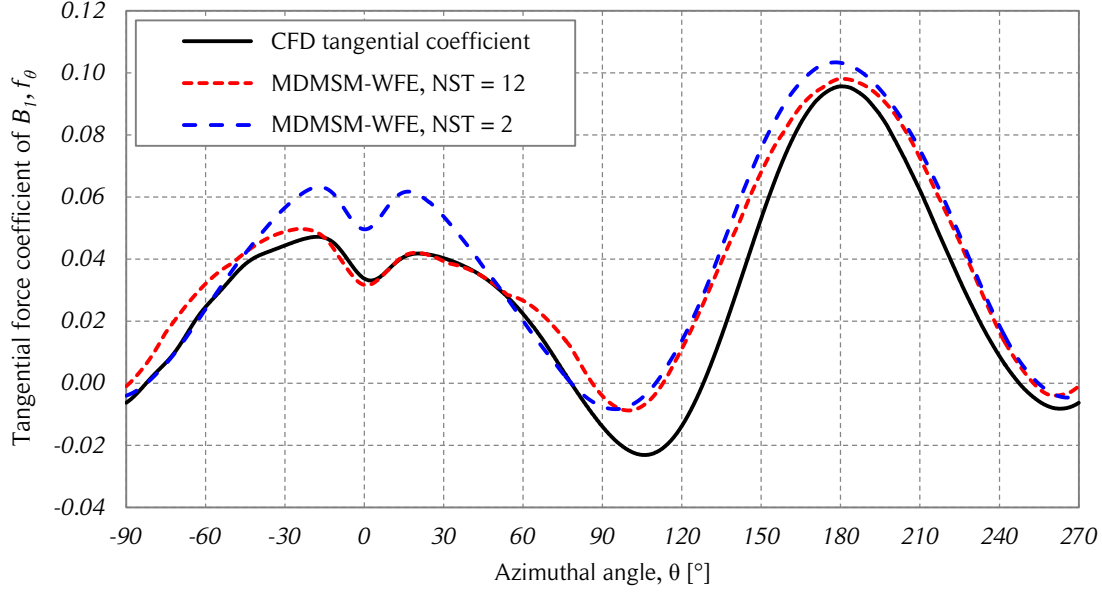


Figure 5.24. Tangential force coefficient comparison.

The figure shows a comparison of the tangential force coefficients of the CFD simulations and the MDMSM-WFE for the cases $NST = 12$ and $NST = 2$ with $TSR = 4$. Source: own elaboration.

coefficients from the CFD simulations of the reference case. The expressions of the momentum balance only suffer small changes due to the difference in the calculation of the average streamwise forces from the CFD simulations, as shown in Eqs. (5.34) – (5.37). The aerodynamic forces calculated from the CFD simulations are non-dimensional. The dimensional factor in this case is $\rho D U_\infty^2 / 2$.

$$\bar{F}_{x,u} = \frac{N\Delta\theta}{2\pi} \left(\frac{1}{2} \rho D U_\infty^2 \right) \left(\frac{1}{\Delta\theta} \int_{\theta_1}^{\theta_2} f_x(\theta) d\theta \right) \quad (5.34)$$

$$\bar{F}_{x,d} = \frac{N\Delta\theta}{2\pi} \left(\frac{1}{2} \rho D U_\infty^2 \right) \left(\frac{1}{\Delta\theta} \int_{\theta_3}^{\theta_4} f_x(\theta) d\theta \right) \quad (5.35)$$

$$\underbrace{1 - (2u_u - 1) \cos \delta}_{MOM_u} = \frac{\bar{F}_{x,u}}{\underbrace{\rho w_\infty U_\infty^2}_{AFC_u}} \quad (5.36)$$

$$\underbrace{1 + \cos \delta - 2u_d}_{MOM_d} = \frac{\bar{F}_{x,d}}{\underbrace{\rho w_e U_e^2}_{AFC_d}} \quad (5.37)$$

In this case, the tangential force coefficients and power performance of the CFD simulations and of the MDMSM-WFE are not compared. The reason for this is that the coefficients of the CFD simulations are used as an input of the MDMSM-WFE. A comparison of the flow expansion is shown in Fig. 5.25.

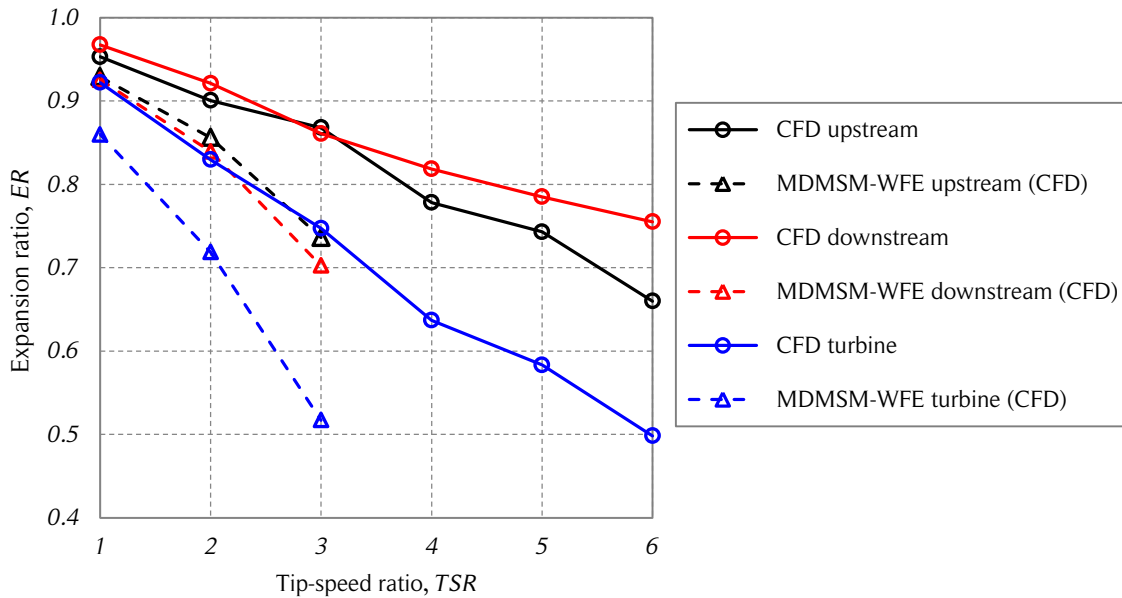


Figure 5.25. MDMSM-WFE with CFD coefficients flow expansion comparison.

The figure shows the upstream, downstream and turbine expansion ratios of the CFD simulations and the MDMSM-WFE for the three tip-speed ratios where convergence is achieved. Note that the flow expansion of the MDMSM-WFE is calculated with the aerodynamic coefficients of the CFD simulations. Source: own elaboration.

All three upstream, downstream, and turbine expansion ratios are below the respective expansion ratios of the CFD simulations. In other words, the flow expansion is considerably overestimated. Convergence is achieved only up to $TSR = 3$. According to Fig. 5.20, the tangential force coefficients of the empirical data are larger than the CFD simulations for high tip-speed ratios. It could be argued that the streamwise force coefficients behave in the same way. Based on this, the MDMSM-WFE using force coefficients of the CFD simulation can be expected to converge for higher tip-speed ratios than when using empirical aerodynamic coefficients, or at least, converge for the same tip-speed ratio ($TSR = 4$). However, the results of Fig. 5.25 show that is not true. There are two reasons that explain this phenomenon. The first one is that the streamwise force coefficients are not as similar as the tangential force coefficients for $TSR = 4$, as shown in Fig. 5.26. The CFD coefficients have larger values for the upstream half and

lower values for the downstream half. The second reason is the asymmetry in the left and right sides of the upstream half. The left side has values slightly higher than the right side. To illustrate the influence of the asymmetry of the aerodynamic coefficients on the interference factor calculation and convergence of the MDMSM-WFE, the momentum convergence curves are shown in Fig. 5.27. Since convergence is not achieved for $TSR = 4$ and $NST = 12$, the calculation is performed for a lower number of streamtubes ($NST = 8$) which allows convergence of the model.

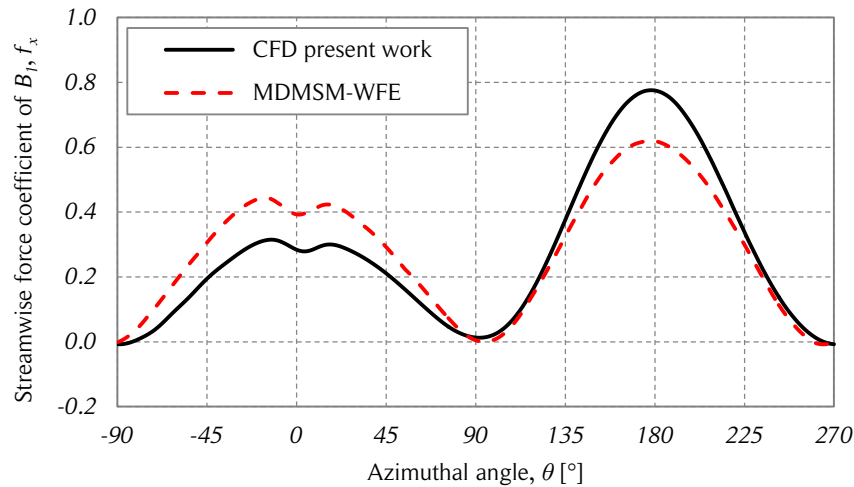


Figure 5.26. Streamwise force coefficient comparison.

The figure shows the streamwise force coefficient as a function of the azimuthal angle of the CFD simulation of the present work and the MDMSM-WFE using empirical aerodynamic coefficients from the CFD simulations with $TSR = 4$. Source: own elaboration.

Convergence for the first upstream left-side streamtube ($k = 1$) is shown in Fig. 5.27. The shape of the AFC_u curve is caused by the large expansion of the streamtube required to achieve convergence, which is achieved through successive increases in the streamtube width. A plateau in the AFC_u curve starts at $u_u \approx 0.65$. At that flow expansion, the turbine streamtube covers the entire left-side quadrant, and therefore, the average streamwise force does not change any more. The first upstream right-side streamtube ($k = 5$) achieves convergence without requiring a small interference factor.

5.3. Discussion

Aerodynamic performance predictions are better with the MDMSM-NFE than with the MDMSM-WFE. However, the shape of the tangential force coefficient curves of the

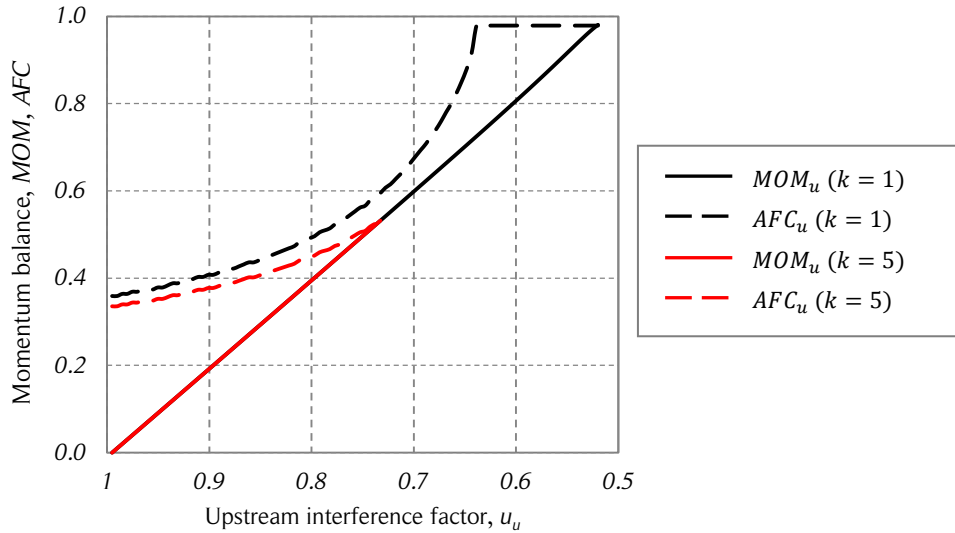


Figure 5.27. Upstream momentum balance convergence curves.

The figure shows the upstream convergence curves of the dimensionless momentum and average aerodynamic force coefficients of the first streamtube of the left ($k = 1$) and right ($k = 5$) sides for the case $NST = 8$. Source: own elaboration.

MDMSM-WFE are in better agreement with the CFD simulations than the ones from the MDMSM-NFE. The reason for the differences in the tangential forces predicted by the two versions of the DMS model and the CFD simulations are attributed to the inability of the model to represent the dynamic effects properly. Turbulence is not taken into account in the calculation. According to Delnero et al. [118], turbulence has a large influence on the aerodynamic coefficients. Lift coefficients are higher for turbulent flows than for laminar flows. However, drag coefficients can experience even larger increases due to turbulence. In other words, the lift to drag ratio is decreased, which directly affects the turbine aerodynamic performance. In addition, the empirical aerodynamic coefficients used here might not be representing the NACA 0021 airfoil adequately [119].

Predictions of the MDMSM-NFE flow expansion are inaccurate. The MDMSM-WFE better predicts the flow expansion but the model does not converge for all cases. This problem occurs for the MDMSM-WFE using both empirical and CFD-based aerodynamic coefficients. This is due to the large average streamwise forces in relation to the momentum equation predicted by the one-dimensional, steady and frictionless linear momentum theory.

6. ENERGY-BASED DMS MODEL

All modifications of the DMS model discussed in the previous chapter are based on a streamwise linear momentum balance. A novel approach based on an energy balance is presented in this chapter. The deduction of the energy-based DMS model (EB-DMSM) is very similar to the momentum-based model (MB-DMSM). The main difference between the approaches is that the EB-DMSM employs the tangential force coefficients instead of the streamwise force coefficients to find the interference factors in the iteration process. This is discussed below.

6.1. Formulation

The mechanical energy equation for incompressible flows applied in a control volume with one inlet (*in*) and one outlet (*out*) in terms of energy per unit volume is shown in Eq. (6.1), where P is the static pressure at the point of interest, ρ is the fluid density, U is the flow velocity, g is the acceleration of gravity, z is the elevation at the point of interest, w_{shaft} is the net available energy per unit mass on the turbine shaft and w_{losses} are the energy losses per unit mass due to friction.

$$\frac{P_{in}}{\rho} + \frac{U_{in}^2}{2} + gz_{in} = \frac{P_{out}}{\rho} + \frac{U_{out}^2}{2} + gz_{out} + w_{shaft} + w_{losses} \quad (6.1)$$

If the inlet and outlet of the control volume are far enough from the turbine, the inlet and outlet pressures will be equal to the ambient pressure, P_{∞} , and therefore do not play any role in Eq. (6.1). The elevation terms, z_{in} and z_{out} , can be removed from Eq. (6.1) if the elevation remains constant. If the friction losses are neglected and the net available power on the shaft is expressed as $\Delta\dot{W} = \dot{m} w_{shaft}$, Eq. (6.2) is obtained.

$$\frac{1}{2}\dot{m}U_{in}^2 = \frac{1}{2}\dot{m}U_{out}^2 + \Delta\dot{W} \quad (6.2)$$

In this approach, the control volume needed for application of the mechanical energy equation is chosen to match the upstream and downstream streamtubes, as shown in Fig. 6.1. Therefore, Eq. (6.2) can be applied at each upstream and downstream streamtubes of the DMS model, which yields Eqs. (6.3) and (6.4), respectively.

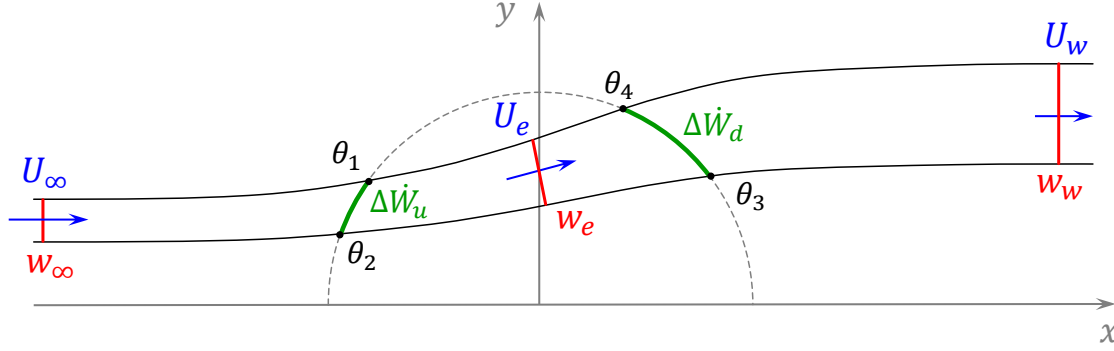


Figure 6.1. Diagram of energy-based DMS model.

The figure shows a diagram of a turbine streamtube (upstream and downstream streamtubes in tandem) and its main parameters for the energy-based DMS model formulation. Source: own elaboration.

$$\frac{1}{2} \dot{m} U_\infty^2 = \frac{1}{2} \dot{m} U_e^2 + \Delta \dot{W}_u \quad (6.3)$$

$$\frac{1}{2} \dot{m} U_e^2 = \frac{1}{2} \dot{m} U_w^2 + \Delta \dot{W}_d \quad (6.4)$$

The upstream and downstream net available powers are calculated using Eqs. (6.5) and (6.6), where N is the number of blades, ω is the angular velocity of the turbine, R is the turbine radius, θ_1 and θ_2 are the angular limits of the upstream tube, θ_3 and θ_4 are the angular limits of the downstream tube and F_θ is the tangential force acting on one blade. Note that each net available power on the shaft is weighted by the fraction of the blade trajectory contained inside the streamtube.

$$\Delta \dot{W}_u = N \omega R \frac{\theta_2 - \theta_1}{2\pi} \frac{1}{\theta_2 - \theta_1} \int_{\theta_1}^{\theta_2} F_\theta(\theta) d\theta \quad (6.5)$$

$$\Delta \dot{W}_d = N \omega R \frac{\theta_4 - \theta_3}{2\pi} \frac{1}{\theta_4 - \theta_3} \int_{\theta_3}^{\theta_4} F_\theta(\theta) d\theta \quad (6.6)$$

To obtain a definition of the upstream and downstream interference factors, u_u and u_d respectively, consistent with the ones used in the previous chapter, the interference factors of the EB-DMSM are defined as shown in Eqs. (6.7) – (6.10).

$$u_u = \frac{1}{2} \left(1 + \frac{U_e}{U_\infty} \right) \quad (6.7)$$

$$u_d = \frac{1}{2} \left(1 + \frac{U_w}{U_e} \right) \quad (6.8)$$

$$U_e = U_\infty (2u_u - 1) \quad (6.9)$$

$$U_w = U_e (2u_d - 1) \quad (6.10)$$

Substituting Eqs. (6.9) and (6.10) into Eqs. (6.3) – (6.6) yields Eqs. (6.11) – (6.14).

$$(2u_u - 1)^2 = 1 - \frac{2\Delta\dot{W}_u}{\rho w_\infty U_\infty^3} \quad (6.11)$$

$$(2u_d - 1)^2 = 1 - \frac{2\Delta\dot{W}_d}{\rho w_e U_e^3} \quad (6.12)$$

$$(2u_u - 1)^2 = 1 - \frac{N\omega R}{\pi\rho w_\infty U_\infty^3} \int_{\theta_1}^{\theta_2} F_\theta(\theta) d\theta \quad (6.13)$$

$$(2u_d - 1)^2 = 1 - \frac{N\omega R}{\pi\rho w_e U_e^3} \int_{\theta_3}^{\theta_4} F_\theta(\theta) d\theta \quad (6.14)$$

Following the notation of the previous chapter, the dimensionless energy quantities are defined according to Eqs. (6.15) – (6.18).

$$ENE_u = (2u_u - 1)^2 \quad (6.15)$$

$$ENE_d = (2u_d - 1)^2 \quad (6.16)$$

$$AFC_u = 1 - \frac{N\omega R}{\pi\rho w_\infty U_\infty^3} \int_{\theta_1}^{\theta_2} F_\theta(\theta) d\theta \quad (6.17)$$

$$AFC_d = 1 - \frac{N\omega R}{\pi\rho w_e U_e^3} \int_{\theta_3}^{\theta_4} F_\theta(\theta) d\theta \quad (6.18)$$

Note that the use of the Bernoulli equation in the deduction of the one-dimensional momentum theory for an ideal wind turbine (see Section 3.4) is equivalent to the

mechanical energy equation of Eq. (6.1) when frictional losses are neglected. The thrust force in the streamwise direction caused by the pressure difference at the rotor (one-dimensional momentum theory) can be transformed to power units if it is multiplied by the induced velocity, U_e , as shown in Eq. (6.19).

$$\Delta\dot{W} = F_x U_e = \frac{1}{2} \rho A U_e (U_\infty^2 - U_w^2) \quad (6.19)$$

The latter expression is equivalent to Eq. (6.2). Therefore, there are only two differences between the MB-DMSM and the EB-DMSM. The first one involves the mathematical expressions used to find the interference factors, which are explicitly shown in Eqs. (5.28), (5.29), (6.13), and (6.14). The second one is the nature of the aerodynamic force coefficients utilized to determine the interference factors: the MB-DMSM uses the streamwise force and the EB-DMSM the tangential forces. Note that the EB-DMSM uses the same mathematical representation of the streamlines for the flow expansion.

6.2. Results with aerodynamic coefficients from CFD simulations

Since the results of the MDMSM-WFE using empirical aerodynamic coefficients are not satisfactory, the calculations of the EB-DMSM are performed with aerodynamic coefficients from the CFD simulations of the present work. The force coefficients of the CFD simulations are considered more accurate than the empirical coefficients because the latter do not include the dynamic effects properly. Twelve streamtubes are used for the calculations.

A comparison between the measured flow expansion of the CFD simulations and the expansion obtained from the EB-DMSM-WFE is shown in Fig. 6.2. The upstream, downstream, and turbine expansion ratios are quite similar to the equivalent ratios of the CFD simulations for $TSR \leq 2$. For higher tip-speed ratios, the difference becomes larger with increasing TSR .

Convergence is not achieved for the first streamtubes of the left and right side for tip-speed ratios larger than $TSR > 4$. This is caused by the low values of AFC_u in comparison with ENE_u . The low values of AFC_u are caused by the high values of tangential forces. In other words, the energy balance of Eq. (6.13) states that the time-averaged difference between the kinetic energy of the flow entering the streamtube and the power extracted by the blades between the angular limits of the turbine is larger than the kinetic energy of the flow exiting the streamtube. The convergence curves for $TSR = 5$ are shown in Fig. 6.3.

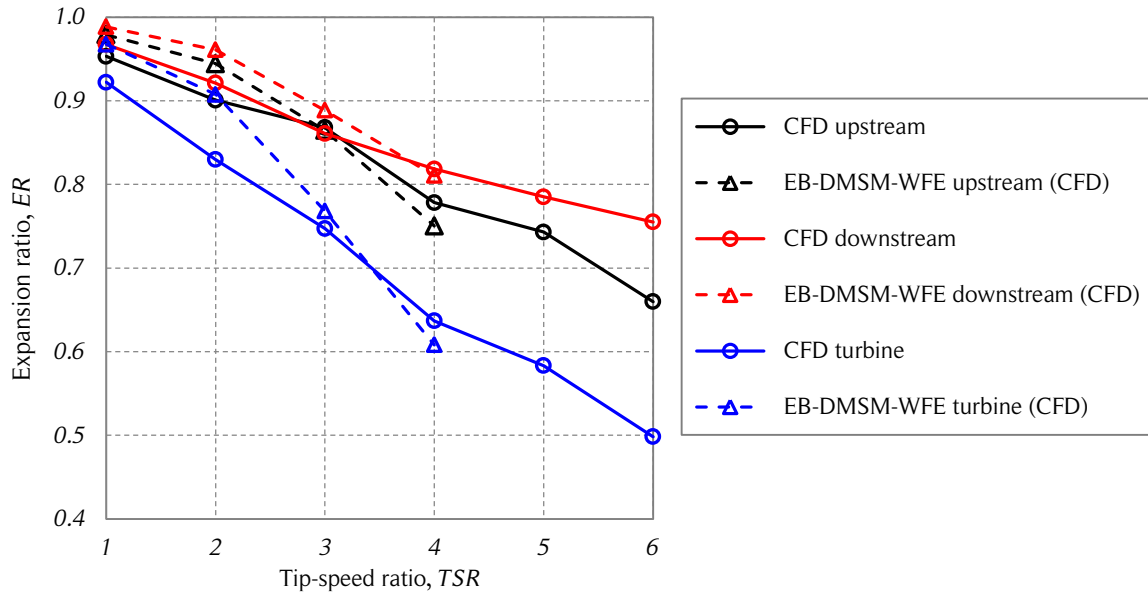


Figure 6.2. Energy-based DMS model flow expansion comparison.

The figure shows the upstream, downstream and turbine expansion ratios of the CFD simulations and the EB-DMSM for the four tip-speed ratios where convergence is achieved. Note that the flow expansion of the EB-DMSM-WFE is calculated with the aerodynamic coefficients of the CFD simulations. Source: own elaboration.

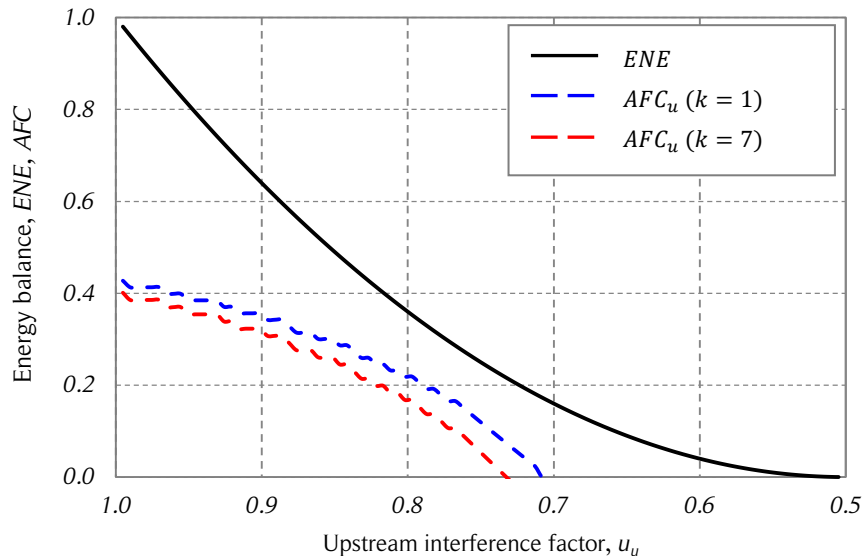


Figure 6.3. Energy balance convergence curves.

The figure shows the upstream convergence curves of the dimensionless energy (ENE) and average aerodynamic force coefficients (AFC) of the first upstream left-side ($k=1$) and right-side ($k=7$) streamtubes for the case $NST=12$ and $TSR=5$. Source: own elaboration.

The dimensionless momentum expression, MOM , of Eqs. (5.28) and (5.29) is almost linear. On the other hand, the dimensionless energy expression, ENE , of Eqs. (6.13) and (6.14) is quadratic. Therefore, when convergence is achieved, it is more likely to have more than one intersection for the EB-DMSM than for the M-DMSM. If a double intersection is found (two solutions), the larger interference factor (u closer to one) is assumed to represent the actual physical solution. However, the interference factor that corresponds to the actual physical solution depends on the actual operating conditions of the turbine. At a certain instant, the angular speed of the turbine, its inertia, the aerodynamic torque on the turbine shaft due to the blade loading, and the load due to the electric generator determine the acceleration or deceleration of the rotational speed of the turbine (see Section 3.12), which in turn determines the momentum transferred from the wind to the turbine, and thus, the interference factor and actual flow expansion.

6.3. Discussion

The EB-DMSM-WFE shows a better prediction of the flow expansion than the MDMSM-WFE when the aerodynamic coefficients from CFD simulations are used. However, convergence problems do not allow the flow expansion to be calculated at high tip-speed ratios. The reasons for this are similar to the ones addressed in Chapter 5. The average aerodynamic force that determine the turbine power is larger than the difference between the power (energy per unit time) entering and exiting the streamtubes, balance dictated by a one-dimensional theory for steady, frictionless flows.

7. FLOW EXPANSION CORRECTIONS

The purpose of this chapter is to address the flow expansion corrections which improve the DMS models of the present work. Using the mathematical representation of streamlines and flow expansion from CFD simulations, the first task is to quantify the dimensionless momentum and energy needed to find convergence in the MDMSM-WFE and the EB-DMSM-WFE. The momentum and energy corrections are functions of the streamtube azimuthal coordinate and of the TSR . These corrections are analyzed to investigate whether they have a physical explanation or not. Then, a correction to the momentum balance equation that improves the prediction of flow expansion is proposed.

7.1. Corrections of the DMS models

The dimensionless momentum flow expansion corrections ($MFEC$) are based on a force correction, F' , as shown in Eq. (7.1). The dimensionless upstream and downstream streamtubes momentum corrections are shown in Eqs. (7.2) and (7.3) and a general expression for $MFEC$ is shown in Eq. (7.4).

$$\dot{m}\Delta U + F' = \bar{F}_x \quad (7.1)$$

$$MOM_u + MFEC_u = AFC_u \quad (7.2)$$

$$MOM_d + MFEC_d = AFC_d \quad (7.3)$$

$$MFEC(\theta, TSR) = AFC - MOM \quad (7.4)$$

The dimensionless energy flow expansion corrections ($EFEC$) are based on a power correction (energy per unit time), E' , as shown in Eq. (7.5). The dimensionless upstream and downstream streamtubes energy corrections are shown in Eqs. (7.6) and (7.7) and a general expression for $EFEC$ is shown in Eq. (7.8).

$$\frac{1}{2}\dot{m}U_\infty^3 - \Delta\dot{W} = \frac{1}{2}\dot{m}U_w^3 + E' \quad (7.5)$$

$$AFC_u = ENE_u + EFEC_u \quad (7.6)$$

$$AFC_d = ENE_d + EFEC_d \quad (7.7)$$

$$EFEC(\theta, TSR) = AFC - ENE \quad (7.8)$$

The corrections $MFEC(\theta, TSR)$ and $EFEC(\theta, TSR)$ are calculated using $NST = 12$ and imposing the flow expansion from the CFD simulations. The corrections using the CFD aerodynamic coefficients are shown in Figs. 7.1 and 7.2.

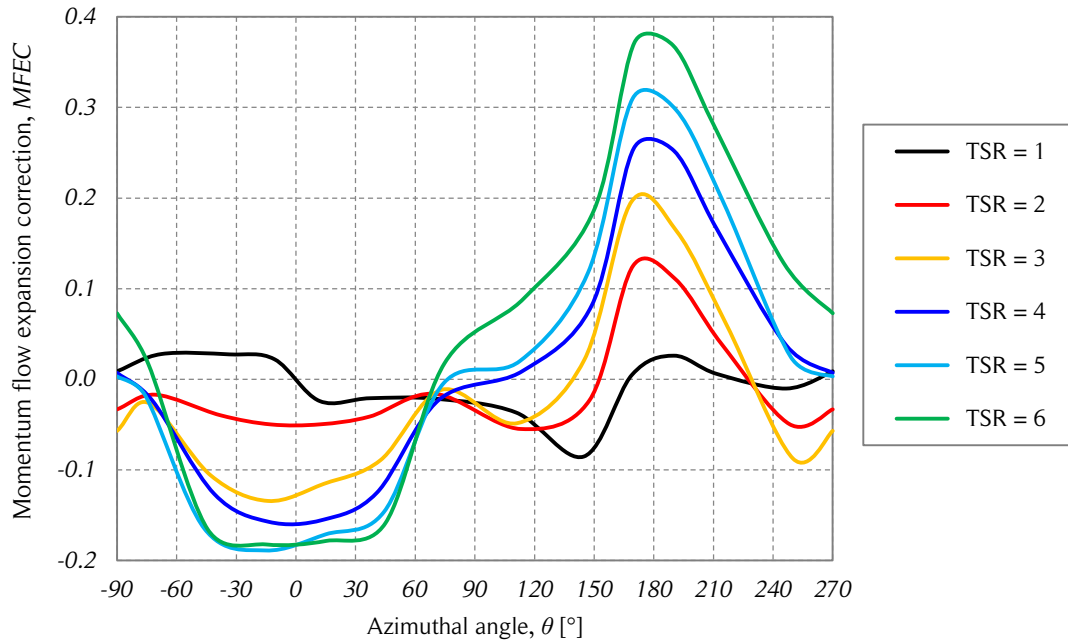


Figure 7.1. Momentum flow expansion corrections with CFD coefficients.

The figure shows the momentum flow expansion corrections as a function of the azimuthal angle for the six studied tip-speed ratios using CFD aerodynamic coefficients and when the CFD flow expansion is imposed. Source: own elaboration.

Assuming that the loads from the CFD simulations represent in a good manner the aerodynamic forces and the flow expansion, then, the results of Figs. 7.1 and 7.2 can be interpreted as physical corrections to the MB-DMSM and the EB-DMSM. These models are based on one-dimensional theories for stationary, frictionless flows.

Positive dimensionless momentum flow expansion corrections mean that the momentum predicted by the one-dimensional momentum theory (that considers stationary flow and neglects friction losses) underestimates the actual momentum transfer from the wind to the blades at the actual flow expansion. For low tip-speed ratios, the momentum transferred from the wind to the turbine is overestimated at some azimuthal positions and underestimated for other positions. For low tip-speed ratios, this does not shown a clear

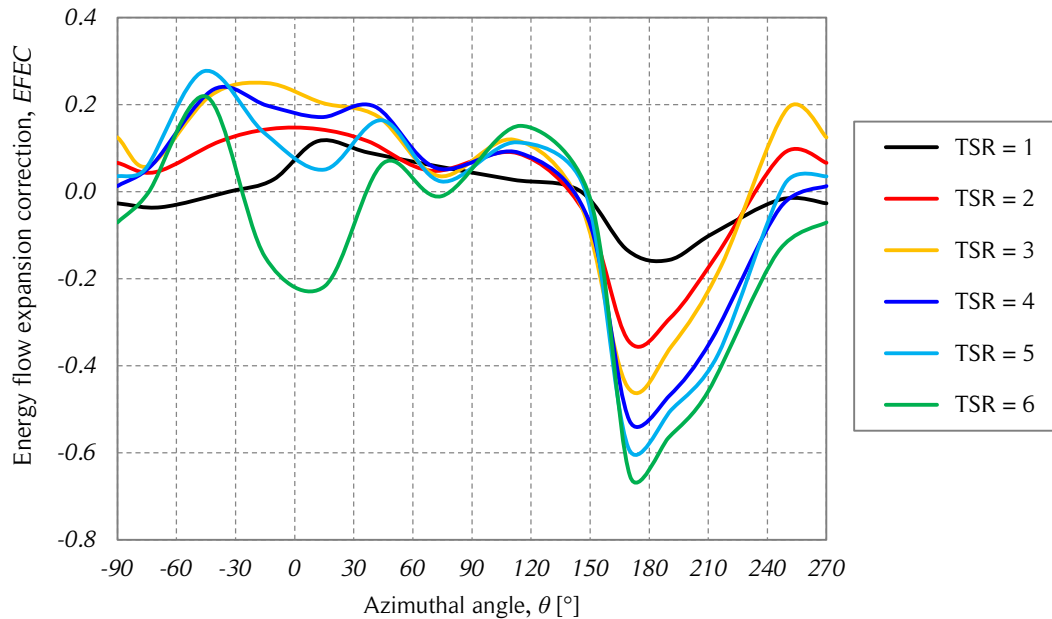


Figure 7.2. Energy flow expansion corrections with CFD coefficients.

The figure shows the energy flow expansion corrections as a function of the azimuthal angle for the six studied tip-speed ratios using CFD aerodynamic coefficients and when the CFD flow expansion is imposed. Source: own elaboration.

tendency for the left, right, upstream, and downstream quadrants. The changes in sign of the corrections can be attributed to the large variations in the blade loading caused by dynamic stall. The magnitude of the corrections is rather small. However, for higher tip-speed ratios, the magnitude of the corrections increases, especially for the central streamtubes. The corrections of the upstream half are larger than the downstream half corrections. Negative energy flow expansion corrections are needed when the difference between the flow kinetic energy entering the streamtube and the turbine power is smaller than flow kinetic energy exiting the streamtube.

It must be noted that the corrections discussed here are based on the time-average flow expansion. Therefore, the results cannot be interpreted directly. However, it can be said that the blades have a larger influence on the flow at the central part of the turbine. Additionally, since the streamtubes limits are streamlines, there should not be any mass flow through its lateral limits. If the time-averaged streamtubes are compared with instantaneous flow visualizations, it can be shown that actually there is mass flow through the streamtube limits. In addition to this, momentum and energy is transferred between streamtubes due to the convection of large-scale and small-scale eddies.

The momentum-based and energy-based corrections using the empirical aerodynamic coefficients are shown in Figs. 7.3 and 7.4. Since the results using empirical aerodynamic coefficients are not considered physically accurate, the corrections presented in Figs. 7.3 and 7.4 cannot be physically interpreted. However, these corrections can be useful for the modeling of Darrieus SB-VAWTs because they quantify the error committed when using the momentum-based and energy-based DMS models with empirical aerodynamic coefficients. Note that the shapes of the curves are very different from Figs. 7.1 and 7.2. This is attributed to the differences between the calculated aerodynamic forces by the DMS models when using empirical aerodynamic coefficients and CFD results.

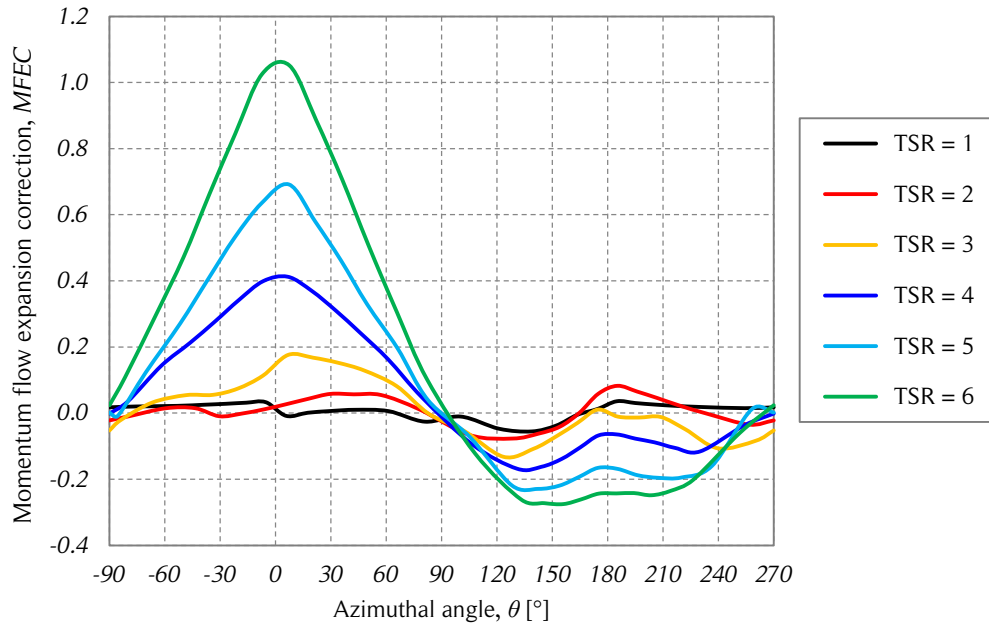


Figure 7.3. Momentum flow expansion corrections with CFD coefficients.

The figure shows the momentum flow expansion corrections as a function of the azimuthal angle for the six studied tip-speed ratios using empirical aerodynamic coefficients and when the CFD flow expansion is imposed. Source: own elaboration.

7.2. Corrections based on regressions

The upstream streamwise momentum expressions of the MDMSM-WFE are shown in Eqs. (7.9) – (7.11).

$$\rho w_{\infty} U_{\infty}^2 [1 - (2u_u - 1) \cos \delta] = \bar{F}_{x,u} \quad (7.9)$$

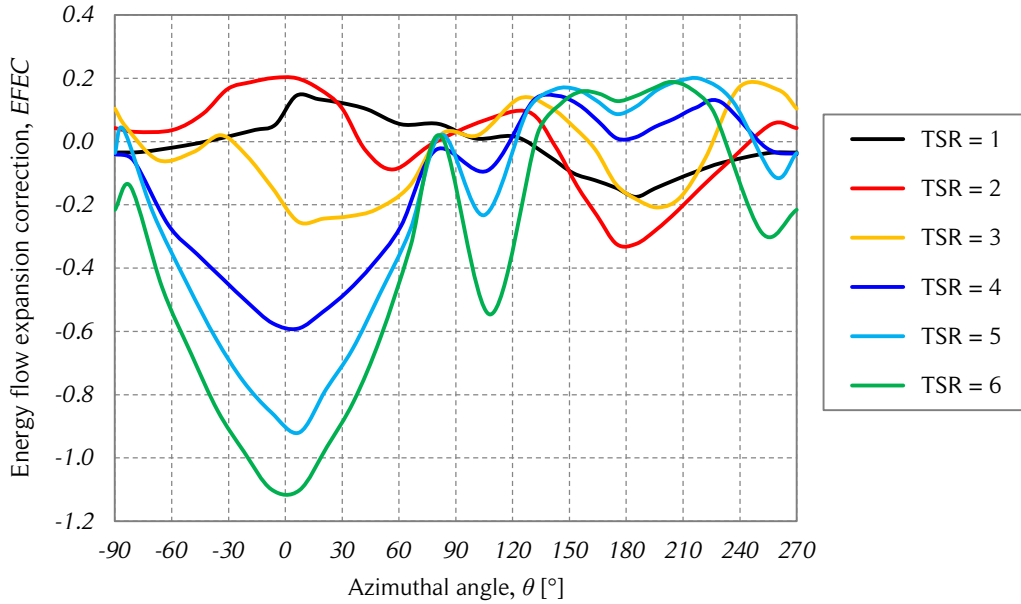


Figure 7.4. Energy flow expansion corrections with CFD coefficients.

The figure shows the energy flow expansion corrections as a function of the azimuthal angle for the six studied tip-speed ratios using empirical aerodynamic coefficients and when the CFD flow expansion is imposed. Source: own elaboration.

$$\bar{F}_{x,u} = \frac{N\Delta\theta}{2\pi} \left(\frac{1}{\Delta\theta} \int_{\theta_1}^{\theta_2} \frac{1}{2} \rho c (c_r \cos \theta - c_\theta \sin \theta) W^2 d\theta \right) \quad (7.10)$$

$$f_x = \frac{\bar{F}_{x,u}}{\frac{1}{2} \rho D U_\infty} \quad (7.11)$$

The slope of the streamwise force coefficient, f_x , depends on whether the angular weighting, $N\Delta\theta/2\pi$, is considered or not. This is shown in Fig. 7.5 for three different number of streamtubes (12, 24 and 36). The streamwise momentum expressions without the angular weighting are shown in Eqs. (7.12) and (7.13).

$$\bar{F}_{x,u}^* = N \left(\frac{1}{\Delta\theta} \int_{\theta_1}^{\theta_2} \frac{1}{2} \rho c (c_r \cos \theta - c_\theta \sin \theta) W^2 d\theta \right) \quad (7.12)$$

$$\bar{f}_x^* = \frac{\bar{F}_{x,u}^*}{\frac{1}{2} \rho D U_\infty} \quad (7.13)$$

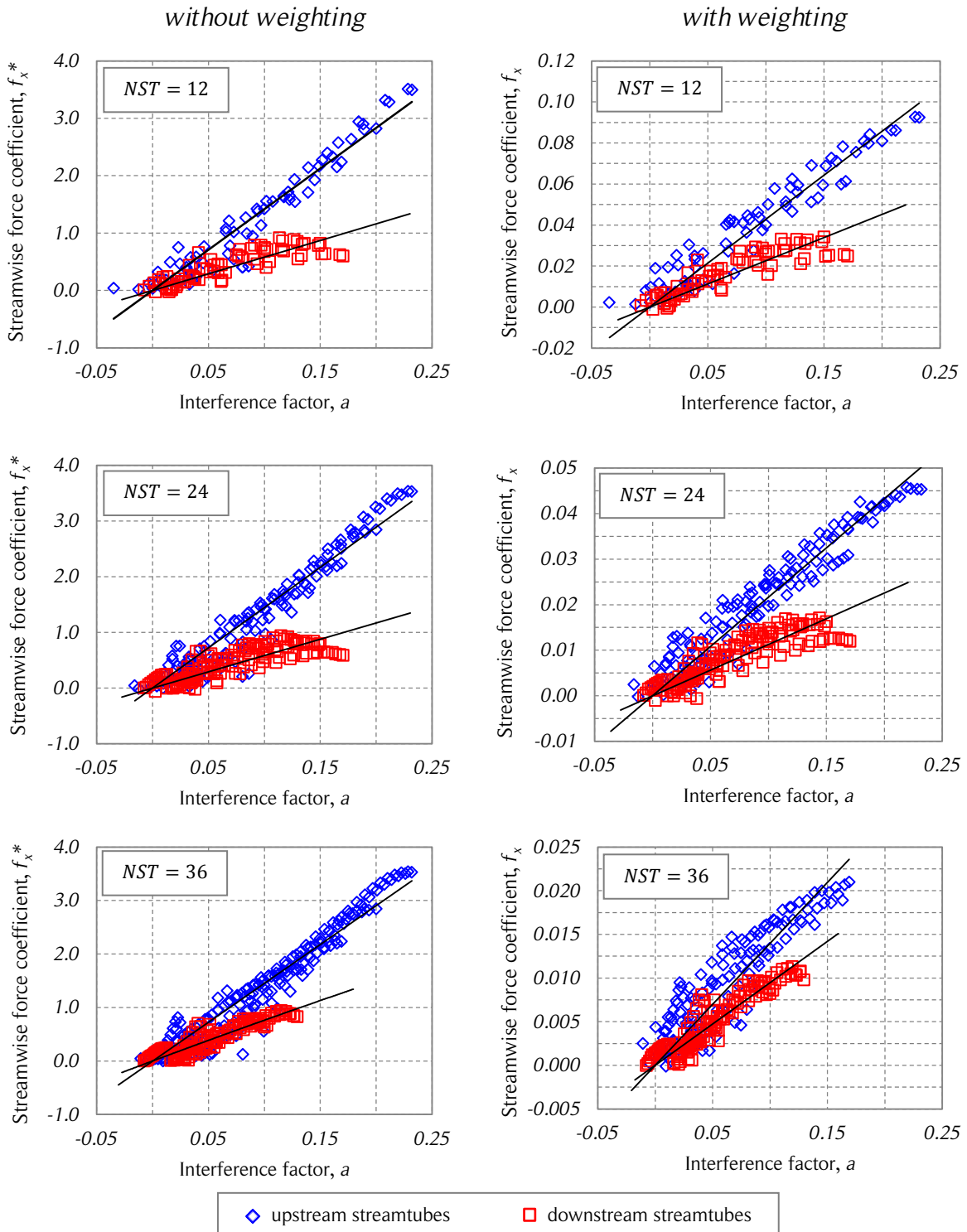


Figure 7.5. Streamwise force coefficient vs. interference factor.

The figure shows the streamwise force coefficients (with and without angular weighting) as a function of the interference factor for three different number of streamtubes. Source: own elaboration.

Regressions using linear functions are performed for the upstream and downstream streamtubes. In both cases, the fitting constraint $f_x = 0$ when $a = 0$ is imposed to force the model to have physical consistency. The mathematical expressions of the fittings are shown in Table 7.1. Note that the coefficient of determination, R^2 , is higher for the upstream streamtubes.

Table 7.1. CFD simulation parameters.

Number of streamtubes		Mathematical expression	R^2
without weighting			
$NST = 12$	upstream	$f_{x,u}^* = 14.172a$	0.9337
	downstream	$f_{x,d}^* = 5.7392a$	0.7136
$NST = 24$	upstream	$f_{x,u}^* = 14.448a$	0.9329
	downstream	$f_{x,d}^* = 5.8403a$	0.6578
$NST = 36$	upstream	$f_{x,u}^* = 14.533a$	0.9339
	downstream	$f_{x,d}^* = 7.6407a$	0.8274
with weighting			
$NST = 12$	upstream	$f_{x,u} = 0.4287a$	0.9123
	downstream	$f_{x,d} = 0.2259a$	0.7590
$NST = 24$	upstream	$f_{x,u} = 0.2163a$	0.9175
	downstream	$f_{x,d} = 0.1128a$	0.7156
$NST = 36$	upstream	$f_{x,u} = 0.1397a$	0.8009
	downstream	$f_{x,d} = 0.0946a$	0.8649

The average streamwise force coefficient of the streamtubes without weighting, \bar{f}_x^* , can be expressed as a linear function in terms of the streamwise force coefficients, $f_x^*(a)$, as shown in Eq. (7.14). Note that $a = 1 - u$. For the upstream streamtubes, the slope is nearly constant and has a value close to $m^* = 14.2$ for all the cases. For the downstream streamtubes, the slope is nearly constant for the cases $NST = 12$ and $NST = 24$ and has a value close to $m^* = 5.8$. Note that the fitting constraint $f_x = 0$ when $a = 0$ forces $n^* = 0$. The following calculations are performed with $NST = 12$ because is the number of streamtubes closer to the streamline density used in the CFD simulations.

$$\bar{f}_x^* = f_x^*(a) = m^*a + n^* \quad (7.14)$$

The accuracy of the flow expansion predictions using mathematical expressions from regressions is studied with the MDMSM-WFE. This approach is denoted DMSM model with flow expansion corrections (DMSM-FEC). Convergence is achieved for all tip-speed ratios with a relatively good accuracy. The main discrepancies are in the downstream flow expansion predictions for $TSR > 4$, as shown in Fig. 7.6.

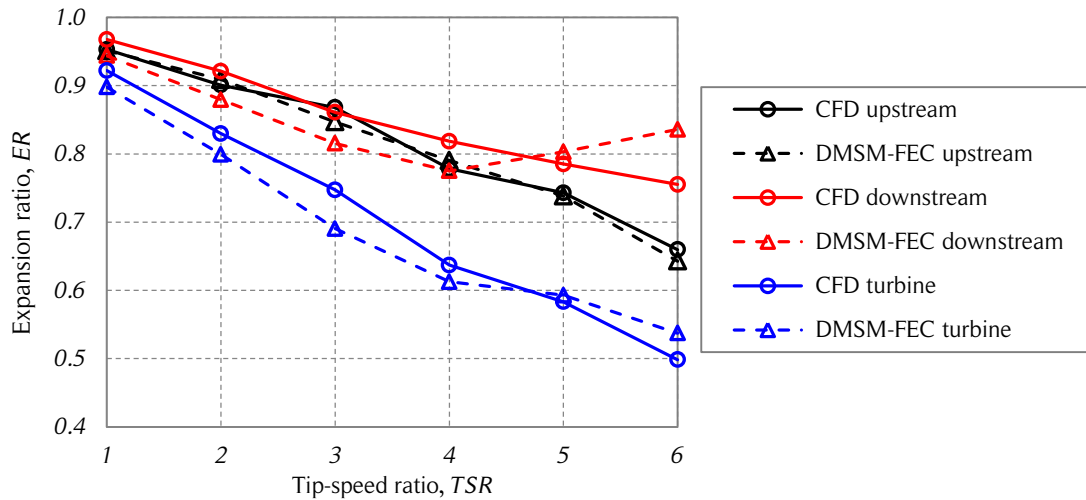


Figure 7.6. DMSM-FEC flow expansion comparison.

The figure shows the upstream, downstream, and turbine expansion ratios of the CFD simulations and the DMSM-FEC for the six studied tip-speed ratios. Source: own elaboration.

The upstream and downstream streamtubes have similar streamwise force coefficient behavior. Since flow expansion is taken into account through the mathematical representation of streamlines, a multiple streamtube model with flow expansion corrections (MSM-FEC) is studied to determine if it is able to predict the flow expansion accurately. As in the previous case, the calculations are performed using the aerodynamic coefficients from the CFD simulations.

The streamwise force coefficients without weighting as a function of the interference factor for each streamtube using the MSM-FEC with $NST = 12$ are presented in Fig. 7.7. The average turbine streamwise force coefficients from the CFD simulations are also shown for comparison (black dots). Note that the linear relation is shared by all tip-speed ratios. When the relation is calculated for the entire turbine ($NST = 1$), the relation has a slightly lower slope (not shown in the figure). This is attributed to the average of the streamwise force coefficients for an entire turbine revolution. The flow expansion prediction of the MSM-FEC is shown in Fig. 7.8.

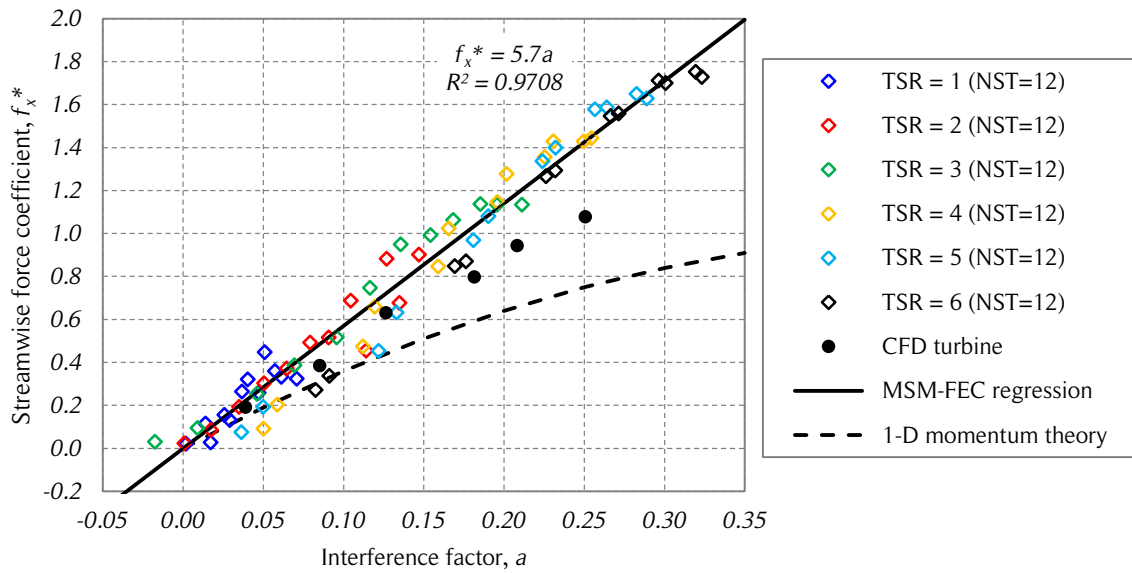


Figure 7.7. Streamwise force coefficient vs. interference factor of the MSM-FEC.

The figure shows the streamwise force coefficient without angular weighting as a function of the interference factor of the multiple streamtube model with flow expansion corrections and $NST = 12$. Source: own elaboration.

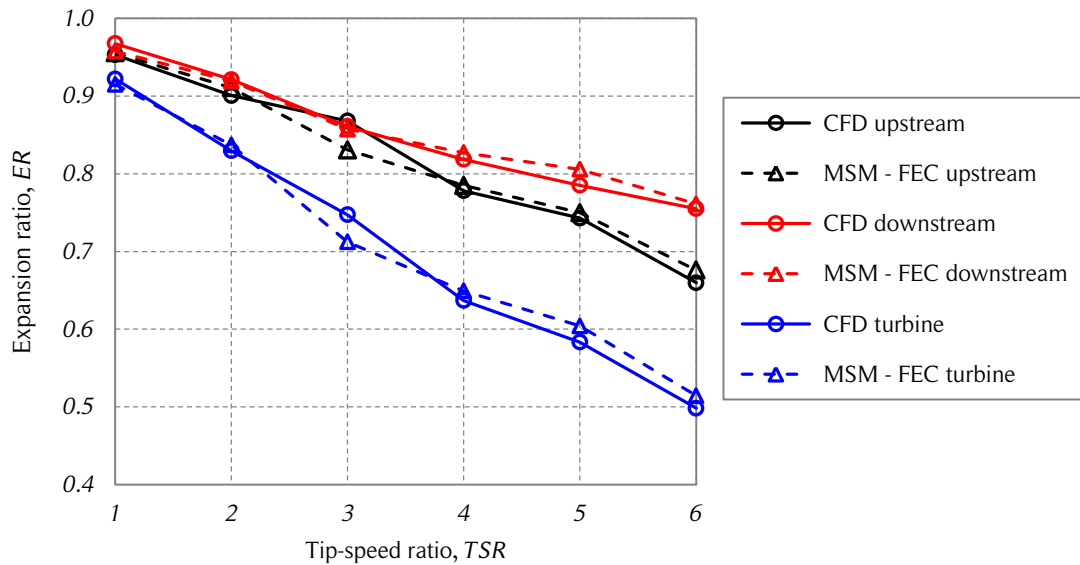


Figure 7.8. MSM-FEC flow expansion comparison.

The figure shows the upstream, downstream, and turbine expansion ratios of the CFD simulations and the MSM-FEC for the six studied tip-speed. Source: own elaboration.

The streamwise force coefficients of the streamtubes follow a linear relation with respect to the interference factors when using a multiple streamtube model (see Fig. 7.8). This approach uses the same mathematical representation of streamlines addressed in the previous chapters. The flow expansion of the MSM-FEC is in good agreement with the flow expansion of the CFD simulations. The regression coefficient, $m^* = 5.7$, is weakly dependent on the number of streamtubes for values of NST around 12.

A validation of the flow expansion corrections proposed in the present work cannot be achieved because of the lack of numerical and experimental studies available in the literature that take into account both aerodynamic forces and flow expansion of Darrieus turbines. Some studies present experimental data of flow expansion, but the aerodynamic forces for the respective cases is not available [4]. On the other hand, several experimental and numerical studies that present the aerodynamic forces acting on Darrieus SB-VAWTs have been carried out [99-115]. However, complete information of the flow expansion is not available.

7.3. Discussion

The MSM-FEC is able to perform accurate predictions of the flow expansion if the aerodynamic forces used for the calculations are accurate enough (in this case the CFD results). Convergence problems for high tip-speed ratios do not appear when using the MSM-FEC. The flow expansion correction addressed in this chapter is similar to the Glauert correction discussed in Section 3.4. The higher slope of the linear correction is due to the higher streamwise force acting on VAWTs compared to HAWTs for a same interference factor (flow expansion).

The challenge to improve the aerodynamic performance and flow expansion predictions using BEM models lies in the accurate calculation of the aerodynamic forces. With that information, the aforementioned predictions could be performed accurately using the new model with corrections. Future work should address this topic through a more accurate prediction of the influence of dynamic effects and turbulence in the determination of aerodynamic coefficients.

8. CONCLUSIONS AND FUTURE WORK

8.1. Conclusions

The conclusions of the present work are the following:

- Two-dimensional CFD simulations of the reference case (a 6 m diameter 12 kW SB-VAWT) are performed. Three dimensional corrections are applied to the results of the CFD simulations and are validated with experimental data from the literature.
- The DMS model for Darrieus SB-VAWTs is implemented and verified with cases from the literature.
- There are some cases for which the DMS model cannot achieve convergence. The inability of the model to converge is attributed to:
 - Underestimation of the momentum balance predicted by the one-dimensional theory for stationary, frictionless flows.
 - The overestimation of aerodynamic forces based on empirical data under dynamic conditions.
- Several modifications to improve the predictions of aerodynamic performance and flow expansion of the DMS model are addressed.
 - A new mathematical representation of streamlines is implemented. A third-order polynomial and an exponential function with three constants are used for the upstream and downstream halves, respectively. The flow expansion estimation of this approach is in good agreement with the CFD simulations.
 - A modified DMS model with flow expansion (MDMSM-WFE) and a modified MIT dynamic stall model (MMITDSM) are implemented. Power performance predictions are close to the CFD results. Flow expansion is inaccurate. The model does not converge for all the studied cases.

- An energy-based DMS model (EB-DMSM) is implemented. The calculations of the interference factor are based on the tangential coefficients instead of the streamwise coefficients. The flow expansion estimation is similar to the MDMSM-WFE. Converge is also not achieved for all studied tip-speed ratios.
- A multiple streamtube model with flow expansion correction (MSM-FEC) is implemented. It allows precise predictions of flow expansion when accurate aerodynamic force coefficients are available.
- The validation of the proposed model enhancement is limited to the reference case of the present work because of the lack of numerical and experimental studies available in the literature that address the flow expansion of SB-VAWTs and aerodynamic coefficients simultaneously.

Thus, the MSM-FEC is a low-cost computational tool able to perform accurate flow expansion predictions if reliable aerodynamic force coefficients are available. This BEM model is suitable to replace the DMS models described in the present work.

8.2. Future work

The aforementioned conclusions lead to the following recommendations and future work:

- The mathematical representation of streamlines should be validated for other geometric and operational parameters of Darrieus SB-VAWTs.
- The flow expansion correction proposed in the present work (MSM-FEC) should be validated with numerical and experimental studies for Darrieus turbines with different solidities and operating conditions.
- Studies concerning dynamic effects of Darrieus SB-VAWTs should be carried out to improve the prediction of aerodynamic forces acting on the turbine blades. This could be performed through the incorporation of unsteady flow effects obtained from potential flow and vortex models. For instance, the velocity field produced by the vortex shedding of blades and tower can be superimposed with the flow expansion calculated from the MSM-FEC.

- The MSM-FEC should be extended for other type of Darrieus VAWTs such as HB-VAWTs and CB-VAWTs.
- The effects of the atmospheric boundary layer in the two-dimensional models should be studied to improve the prediction of the development and recovery of the wake behind Darrieus SB-VAWTs.
- Studies with incoming non-uniform freestream velocity profiles should be carried out to investigate the behavior of flow expansion and the validity of an undisturbed streamline at the turbine center of Darrieus VAWTs for those cases.

If these recommendations are carried out, a low-cost computational tool would be available for predicting performance of Darrieus VAWTs in urban environments and wind farms.

NOMENCLATURE

The present work uses the International System of Units (SI).

Scalars

a	Interference factor.
A	Reference area, m^2 .
AG	Airfoil geometry.
AR	Flow expansion asymmetry ratio.
A_{sl}	Maximum streamline oscillation amplitude in the wake, m .
c	Blade chord length, m .
c_D	Drag coefficient.
c_f	Skin friction coefficient.
c_L	Lift coefficient.
$c_{L,max}$	Maximum lift coefficient.
c_M	Moment coefficient.
c_p	Power coefficient.
c_P	Pressure coefficient.
c_s	Strut chord length, m .
cc	Convergence criteria.
CS	Control surface.
CV	Control volume.
D	Turbine diameter, m .
D_T	Tower diameter, m .
ER	Flow expansion ratio.
f	Probability density function.
f_1	Upstream mathematical representation of streamlines.
f_2	Downstream mathematical representation of streamlines.
f_x	Streamwise force coefficient or axial force coefficient.
f_x^*	Streamwise force coefficient without angular weighting.
f_y	Cross-stream force coefficient.
f_θ	Tangential force coefficient.
f_r	Radial force coefficient.

F	Cumulative distribution function or aerodynamic force, N .
h	Tier height, m .
H	Turbine height, m .
H_0	Ground clearance, m .
I	Moment of inertia of the turbine-generator system, $kg \cdot m^2$.
k	Shape factor of the Weibull probability density function or streamtube number.
k^*	Dynamic stall reduced frequency.
K	Non-uniform expansion ratio.
L	Tip-loss factor.
L_∞	Freestream distance, m .
L_w	Developed wake length, m .
m	Maximum airfoil camber, hundredths of chords.
\dot{m}	Mass flow rate, kg/s .
M	Aerodynamic moment, $N \cdot m$.
Ma	Mach number.
N	Number of blades.
NI	Number of iterations.
NST	Number of streamtubes.
P	Pressure, Pa .
q_∞	Dynamic pressure, $kg/(m \cdot s^2)$.
R	Turbine radius, m .
R_T	Tower radius, m .
Re	Blade Reynolds number.
Re_T	Turbine Reynolds number.
Re_s	Strut Reynolds number.
s	Scale factor of the Weibull probability density function, m/s or blade span, m .
t	Airfoil thickness, hundredths of chords or time, s .
T	Number of vertical tiers or temperature, K or $^\circ C$.
TI	Turbulence intensity.
TSR	Tip-speed ratio.
u	Interference factor.
\tilde{u}	Fluctuating wind speed with zero mean, m/s .
\bar{u}	Short-term mean wind speed, m/s .
U	Local wind speed, m/s .
U_∞	Freestream wind speed, m/s .

V	Speed of still air relative to a rotating blade, m/s .
w	Streamtube width, m .
W	Relative wind speed, m/s or turbine streamtube width, m .
\dot{W}_A	Available power in the wind resource, W .
\dot{W}_T	Turbine power, W .
x	Coordinate in the x -axis, m .
y	Coordinate in the y -axis, m .
z	Coordinate in the z -axis, m .

Vectors

\vec{F}_L	Lift force, N .
\vec{F}_D	Drag force, N .
\vec{F}	Aerodynamic force, N .
\vec{F}_T	Tangential force, N .
\vec{F}_R	Radial force, N .
\vec{F}_x	Thrust force in the x -axis direction, N .
\hat{i}	Unit vector in the x -axis, Cartesian coordinates.
\hat{j}	Unit vector in the y -axis, Cartesian coordinates.
\hat{k}	Unit vector in the z -axis, Cartesian coordinates.
\hat{r}	Unit vector in the radial direction, polar coordinates.
\vec{U}	Local perturbed wind velocity, m/s .
\vec{V}	Velocity of still air relative to a rotating blade, m/s .
\vec{W}	Blade relative wind velocity, m/s .
$\hat{\theta}$	Unit vector in the tangential direction, polar coordinates.

Greek

α	Angle of attack, deg.
$\dot{\alpha}$	Instantaneous rate of change of the angle of attack, deg/s.
α_0	Blade fixation angle, deg or lift slope, deg^{-1} .
α_B	Blade angle of attack, deg or lift slope, deg^{-1} .
α_{DS}	Dynamic stall angle of attack, deg.
α_{SS}	Static stall angle of attack, deg.
Γ	Vortex strength, m^3/s .
δ	Cross-stream expansion angle, deg.

Δu	Wake velocity deficit of the tower, m .
θ	Azimuthal angle, deg.
λ	Tier angle offset, deg.
μ	Local air dynamic viscosity, $Pa \cdot s$.
ν	Local air kinematic viscosity, m^2/s .
ρ	Local air density, kg/m^3 .
σ	Turbine solidity.
σ_u	Standard deviation of the wind speed, m/s .
τ	Shear stress, Pa or torque, $N \cdot m$.
ω	Angular speed, rad/s .

Subscripts

d	Downstream.
e	Equilibrium position.
f	Finite airfoil.
k	Streamtube number.
L	Left side.
R	Right side.
u	Upstream.
w	Developed wake.
∞	Freestream or infinite airfoil.

Abbreviations

AEO: actual energy output.

AFC: dimensionless aerodynamic force coefficients.

AoA: angle of attack.

BEM: blade element momentum

CB-VAWT: curved-bladed vertical-axis wind turbine.

CDEC: *Centro de Despacho Económico de Carga* (center of economic load dispatch).

CF: capacity factor.

CFD: computational fluid dynamics.

CNE: *Comisión Nacional de Energía* (National Energy Commission).

CSP: concentrating solar power.

DIF: difference between dimensionless aerodynamic coefficients and momentum (or energy).

DMS: double-multiple streamtube.

DMSM-FEC: double-multiple streamtube model with flow expansion corrections.
DMSV: double-multiple streamtube model with angular dependency of the interference factor.
EB-DMSM: energy-based DMS model.
EFEC: energy flow expansion correction.
ENE: dimensionless energy due to deceleration of the flow.
ERNC: *energías renovables no convencionales* (central interconnected system).
EU: European Union.
FiT: feed in tariff
HAWT: horizontal-axis wind turbine.
HB-VAWT: helical-bladed vertical-axis wind turbine.
IGCC: Integrated gasification combined cycle.
ITCZ: intertropical convergence zone.
LCOE: levelized cost of energy.
MB-DMSM: momentum-based DMS model.
MBVDSM: modified Boing-Vertol dynamic stall model.
MBVDSM-AR: modified Boing-Vertol dynamic stall model with azimuthal restriction.
MDMSM-FEC: modified DMS model – flow expansion correction.
MDMSM-NFE: modified DMS model – no flow expansion.
MDMSM-WFE: modified DMS model – with flow expansion.
MFEC: momentum flow expansion correction.
MIT: Massachusetts Institute of Technology.
MMITDSM: modified MIT dynamic stall model.
MSM-FEC: modified multiple streamtube model – flow expansion correction.
MOM: dimensionless momentum due to deceleration of the flow.
MPEO: maximum potential energy output.
NACA: National Advisory Committee for Aeronautics of the United States of America.
NASA: National Aeronautics and Space Administration of the United States of America.
NPV: net present value.
NRC: National Research Council of Canada.
O&M: operation and maintenance.
PV: photovoltaic power.
RCA: *Resolución de Calificación Ambiental* (Environmental Qualification Resolution).
RES-E: renewable energy source for electricity generation.
RET: renewable energy technology.
SB-VAWT: straight-bladed vertical-axis wind turbine.

SIC: *Sistema Interconectado Central* (Central Interconnected System).

SING: *Sistema Interconectado del Norte Grande* (Northern Interconnected System).

SNL: Sandia National Laboratories of the United States of America.

TDC: three-dimensional correction.

TOU: time of use.

UK: United Kingdom.

USA: United States of America.

USD: U.S. dollars.

VAWT: vertical-axis wind turbine.

REFERENCES

- [1] **T. Burton, N. Jenkins, D. Sharpe and E. Bossanyi** (2011). *Wind Energy Handbook* (2nd edition). John Wiley and Sons, Ltd.
 - [2] **R. Gasch and J. Twele** (2011). *Wind Power Plants: Fundamentals, Design, Construction and Operation* (1st edition). Springer.
 - [3] **M. Islam, D. Ting and A. Fartaj**. *Aerodynamic models for the Darrieus-type straight-bladed vertical axis wind turbines*. *Renewable and Sustainable Energy Reviews*, 12 (2008).
 - [4] **I. Paraschivoiu** (2002). *Wind Turbine Design: With Emphasis on Darrieus Concept* (1st edition). Press Internationales Polytechnique.
 - [5] **D. Spera** (2009). *Wind Turbine Technology: Fundamental Concepts of Wind Turbine Engineering* (2nd edition). ASME Press.
 - [6] **M.C. Cervarich, S.B. Roy and L. Zhou**. *Spatiotemporal Structure of Wind Farm-atmospheric Boundary Layer Interactions*. *Energy Procedia*, 40 (2013), pp. 530-536.
 - [7] **N.C.K. Pawsey**. *Development and Evaluation of Passive Variable-Pitch Vertical Axis Wind Turbines*. Ph. D. thesis, University of New South Wales, 2002.
 - [8] **I. Paraschivoiu, P. Fraunié and C. Béguier**. *Streamtube Expansion Effects on the Darrieus Wind Turbine*. *Journal of Propulsion*, Vol. 1, No. 2 (1985), pp. 150-155.
 - [9] **I. Paraschivoiu, P. Désy and C. Masson**. *Blade Tip, Finiste Aspect Ratio, and Dynamic Stall Effects on the Darrieus Rotor*. *Journal of Propulsion*, Vol. 4, No. 1 (1988), pp. 73-80.
 - [10] **I. Paraschivoiu**. *Double-Multiple Streamtube Model for Studying Vertical-Axis Wind Turbines*. *Journal of Propulsion*, Vol. 4, No. 4 (1988), pp. 370-377.
 - [11] **R. Serway and J. Jewett** (2004). *Physics for Scientists and Engineers* (6th edition). Brooks/Cole.
 - [12] **Comisión Nacional de Energía (CNE), Gobierno de Chile**. *Fuentes de Energía [Energy Sources]*. Online 11/15/2013 at <http://www.cne.cl/energias/fuentes-energeticas/introduccion>.
 - [13] **M. Leijon, A. Skoglund, R. Waters, A. Rehn and M. Lindahl**. *On the physics of power, energy and economics of renewable electric energy sources – Part I*. *Renewable Energy* 35 (2010), pp. 1729-1734.
 - [14] **Lazard Ltd**. *Levelized Cost of Energy Analysis – Version 6.0*. June 2012.
 - [15] **Centro de Energías Renovables (CER), Ministerio de Energía, Gobierno de Chile**. *Libro de Energía Hidroeléctrica [Book of Hydroelectric Energy]*. Online 11/19/2013 at <http://cer.gob.cl/sobre-las-ernc/fuentes>.
 - [16] **Centro de Energías Renovables (CER), Ministerio de Energía, Gobierno de Chile**. *Libro de Energía Marina [Book of Marine Energy]*. Online 11/19/2013 at <http://cer.gob.cl/sobre-las-ernc/fuentes>.
 - [17] **Centro de Energías Renovables (CER), Ministerio de Energía, Gobierno de Chile**. *Libro de Energía Geotérmica [Book of Geothermal Energy]*. Online 11/19/2013 at <http://cer.gob.cl/sobre-las-ernc/fuentes>.
-

-
- [18] **I. Fridleifsson, R. Bertani, J. Lund and L. Rybach.** *The possible role and contribution of geothermal energy to the mitigation of climate change.* Proceedings of the IPCC Scoping Meeting on Renewable Energy Sources, Germany (2008).
- [19] **Centro de Energías Renovables (CER), Ministerio de Energía, Gobierno de Chile.** *Libro de Energía Solar [Book of Solar Energy].* Online 11/19/2013 at <http://cer.gob.cl/sobre-las-ernc/fuentes>.
- [20] **Centro de Energías Renovables (CER), Ministerio de Energía, Gobierno de Chile.** *Libro de Energía Eólica [Book of Wind Energy].* Online 11/19/2013 at <http://cer.gob.cl/sobre-las-ernc/fuentes>.
- [21] **Centro de Energías Renovables (CER), Ministerio de Energía, Gobierno de Chile.** *Libro de Biomasa [Book of Biomass].* Online 11/19/2013 at <http://cer.gob.cl/sobre-las-ernc/fuentes>.
- [22] **W. Hermann.** *Quantifying global exergy resources.* Energy 31 (2006), pp. 1685-1702.
- [23] **Enerdata.** *Global Energy Statistical Yearbook 2013.* Online 04/03/2014 at <http://yearbook.enerdata.net/#energy-consumption-data.html>.
- [24] **U.S. Energy Information Administration.** *Levelized Cost of New Generation Resources in the Annual Energy Outlook 2013.* EIA Independent Statistics & Analysis, January 2013.
- [25] **GREENERENERGY.ca.** *List of Helix Wind Inc. products.* Online 05/22/2014 at http://www.greenerenergy.ca/Wind%20Turbines_HELIX_WIND.html
- [26] **Tienda Solar Profesional.** *List of small scale wind turbines products.* Online 05/22/2014 at <http://www.tiendasolarprofesional.com/38-eolica-aerogeneradores>.
- [27] **Global Wind Energy Council (GWEC).** *Global wind statistics 2012.* Online 22/05/2014 at http://www.gwec.net/wp-content/uploads/2013/02/GWEC-PRstats-2012_english.pdf.
- [28] **European Photovoltaic Industry Association (EPIA).** *Global Market Outlook for Photovoltaics 2013 – 2017.* Online 22/05/2014 at http://www.epia.org/fileadmin/user_upload/Publications/GMO_2013_-_Final_PDF.pdf.
- [29] **European Commission.** *Communication from the Commission – Energy efficiency: delivering the 20% target.* Online 04/07/2014 at <http://eur-lex.europa.eu/legal-content/EN/ALL/?uri=CELEX:52008DC0772>.
- [30] **S. Mertens, G. van Kuik and G. van Bussel.** *Performance of an H-Darrieus in the Skewed Flow on a Roof.* Journal of Solar Energy Engineering, Vol. 125 (2003), pp. 433-440.
- [31] **S. Luthra, S. Kumar, R. Kharb, M.F. Ansari, S.L. Shimmi.** *Adoption of smart grid technologies: An analysis of interactions among barriers.* Renewable and Sustainable Energy Reviews 33 (2014), pp. 554-565.
- [32] **Renewable UK.** *Small and Medium Wind UK Market Report, October 2013.* Online 06/04/2014 at <http://www.renewableuk.com/en/publications/index.cfm/Small-and-Medium-Wind-UK-Market-Report-2013>.
- [33] **B. Greening and A. Azapagic.** *Environmental impacts of micro-wind turbines and their potential to contribute to UK climate change targets.* Energy 59 (2013), pp. 454-466.
- [34] **J.L. Acosta, K. Combe, S.Ž. Djokić and I. Hernando-Gil.** *Performance Assessment of Micro and Small-Scale Wind Turbines in Urban Areas.* IEEE Systems Journal, Vol. 6, No. 1 (2012), pp. 152-163.
-

-
- [35] **A. Poullikkas**. *A comparative assessment of net metering and feed in tariff schemes for residential PV systems*. Sustainable Energy Technologies and Assessments 3 (2013), pp. 1-8.
- [36] **U.S. Energy Information Administration (EIA)**. *Country Data: Chile*. Online 04/09/2014 at <http://www.eia.gov/countries/country-data.cfm?fips=ci>.
- [37] **Ministerio de Energía, Gobierno de Chile**. *Balance Energético BNE 2012 [National Energy Balance 2012]*. Online 05/22/2014 at <http://www.minenergia.cl/documentos/balance-energetico.html>.
- [38] **Comisión Nacional de Energía (CNE) de Chile and Deutsche Gesellschaft für Technische Zusammenarbeit (GTZ) GmbH**. *Non-Conventional Renewable Energy in the Chilean Electricity Market*. Online 04/09/2014 at http://www.cne.cl/images/stories/public%20estudios/raiz/ERNCMercadoElectrico_Bilingue_WEB.pdf.
- [39] **Central Energía**. *Centrales de Chile [Chilean Power Plants]*. Online 05/22/2014 at <http://www.centralenergia.cl/centrales/>.
- [40] **Ministerio de Energía**. *Ley Núm. 20.698 Propicia la ampliación de la matriz energética, mediante fuentes renovables no convencionales [Law 20.698 of Non-Conventional Renewable Energies]*. Online 04/09/2014 at <http://bcn.cl/1gsls>.
- [41] **Ministerio de Energía**. *Ley Núm. 20.571 Regula el pago de las tarifas eléctricas de las generadoras residenciales [Law 20.571: Electricity Rates and Net-metering]*. Online 04/09/2014 at <http://bcn.cl/7gy1>.
- [42] **Centro de Energías Renovables (CER), Ministerio de Energía, Gobierno de Chile**. *Reporte CER Marzo 2013 [Center of Renewable Energies: March 2013]*. Online 05/22/2014 at <http://cer.gob.cl/boletin/marzo2013/Reporte-20121.pdf>.
- [43] **Centro de Energías Renovables (CER), Ministerio de Energía, Gobierno de Chile**. *Reporte CER Febrero 2014 [Center of Renewable Energies: February 2014]*. Online 05/22/2014 at http://cer.gob.cl/mailling/2014/febrero/Reporte CER_Feb2014_dise%20V1.pdf.
- [44] **J.F. Manwell, J.G. McGowan and A.L. Rogers** (2009). *Wind Energy Explained: Theory, Design and Application* (2nd edition). John Wiley and Sons, Ltd.
- [45] **W.F. Ruddiman** (2000). *Earth's Climate: Past and Future* (1st edition). WH Freeman & Co.
- [46] **Ministerio de Energía de Chile and Deutsche Gesellschaft für Internationale Zusammenarbeit (GIZ) GmbH**. *Energías Renovables en Chile: El potencial eólico, solar e hidroeléctrico de Arica a Chiloé [Renewable Energies in Chile: wind, solar and hydroelectric potential from Arica to Chiloé]*. Online 04/09/2014 at http://www.minenergia.cl/archivos_bajar/Estudios/Potencial_ER_en_Chile_AC.pdf.
- [47] **D. Watts and D. Jara**. *Statistical analysis of wind energy in Chile*. Renewable Energy 36 (2011), pp. 1603-1613.
- [48] **C.L. Archer and M.Z. Jacobson**. *Evaluation of global wind power*. Journal of Geophysical Research, Vol. 110, D12110 (2005).
- [49] **J.D. Anderson Jr.** (2001). *Fundamentals of Aerodynamics* (3rd edition). The McGraw-Hill Companies, Inc.
- [50] **E.N. Jacobs, K.E. Ward and R.M. Pinkerton**. *Report No. 460 The Characteristics of 78*
-

-
- Related Airfoil Sections from Tests in the Variable-Density Wind Tunnel*. National Advisory Committee for Aeronautics (NACA), 1933.
- [51] **G.M. Ferrari**. *Development of an Aeroelastic Simulation for the Analysis of Vertical-Axis Wind Turbines*. Ph. D. thesis, The University of Auckland, 2012.
- [52] **S. Sarkar and K. Venkatraman**. *Influence of pitching angle of incidence on the dynamic stall behavior of a symmetric airfoil*. *European Journal of Mechanics B/Fluids* 27 (2008), pp. 219-238.
- [53] **S. Wang, D.B. Ingham, L. Ma, M. Pourkashanian and Z. Tao**. *Turbulence modeling of deep dynamic stall at relatively low Reynolds number*. *Journal of Fluids and Structures* 33 (2012), pp. 191-209.
- [54] **S. Wang, D.B. Ingham, L. Ma, M. Pourkashanian and Z. Tao**. *Numerical investigations on dynamic stall of low Reynolds number flow around oscillating airfoils*. *Computers & Fluids* 39 (2010), pp. 1529-1541.
- [55] **P. Jamieson** (2011). *Innovation in Wind Turbine Design* (1st edition). John Wiley & Sons, Ltd.
- [56] **Wind Power Monthly**. *The 10 Biggest Turbines in the World*. Online 04/15/2014 at <http://www.windpowermonthly.com/10-biggest-turbines>.
- [57] **V.L. Okulov and G.A.M. van Kuik**. *The Betz-Joukowski limit: on the contribution to rotor aerodynamics by the British, German and Russian scientific schools*. *Wind Energy* 15 (2012), pp. 335-344.
- [58] **R. Carriveau, M. Ragheb and A.M. Ragheb** (2011). *Fundamental and Advanced Topics in Wind Power*, Chapter 2 (1st edition). InTech.
- [59] **M.M.A. Bhutta, N. Hayat, A.U. Farooq, Z. Ali, S.R. Jamil and Z. Hussain**. *Vertical axis wind turbine – A review of various configurations and design techniques*. *Renewable and Sustainable Energy Reviews* 16 (2012), pp. 1926-1939.
- [60] **D. Ayhan and Ş. Sağlam**. *A technical review of building-mounted wind power systems and sample simulation model*. *Renewable and Sustainable Energy Reviews* 16 (2012), pp. 1040-1049.
- [61] **H. Riegler**. *HAWT versus VAWT: Small VAWTs find a clear niche*. *REFOCUS* July/August 2003, pp. 44-46.
- [62] **F. Toja-Silva, A. Colmenar-Santos and M. Castro-Gil**. *Urban wind energy exploitation systems: Behaviour under multidirectional flow conditions – Opportunities and challenges*. *Renewable and Sustainable Energy Reviews* 24 (2013), pp. 364-378.
- [63] **B.G. Newman**. *Multiple Actuator-Disc Theory for Wind Turbines*. *Journal of Wind Engineering and Industrial Aerodynamics*, 24 (1986), pp. 215-225.
- [64] **R. Howell, N. Qin, J. Edwards and N. Durrani**. *Wind tunnel and numerical study of a small vertical axis wind turbine*. *Renewable Energy* 35 (2010), pp. 412-422.
- [65] **Y. Li, K. Tagawa and W. Liu**. *Performance effects on attachment on blade on a straight-bladed vertical axis wind turbine*. *Current Applied Physics* 10 (2010), pp. 335-338.
- [66] **I. Paraschivoiu, O. Trifu and F. Saeed**. *H-Darrieus Wind Turbine with Blade Pitch Control*. *International Journal of Rotating Machinery* (2009), Article ID 505343 (7 p.).
-

-
- [67] **J. DeCoste, A. Smith, D. White, D. Berkvens and J. Crawford.** *Self-Starting Darrieus Wind Turbine*. Design Project Final Report, Department of Mechanical Engineering, Dalhousie University, 2004.
- [68] **D.N. Gorelov and V.P. Krivospitsky.** *Prospects for development of wind turbines with orthogonal rotor*. *Thermophysics and Aeromechanics*, Vol. 15, No. 1 (2008), pp. 153-157.
- [69] **J. Furze.** *Stealth wind turbines: Design and technologies to reduce visual pollution*. *REFOCUS* March/April 2002, pp. 18-20.
- [70] **M.H. Mohamed.** *Aero-acoustics noise evaluation of H-rotor Darrieus wind turbines*. *Energy* 65 (2014), pp. 596-604.
- [71] **T. Göçmen and B. Özerdem.** *Airfoil optimization for noise emission problem and aerodynamic performance criterion on small scale wind turbines*. *Energy* 46 (2012), pp. 62-71.
- [72] **Renewable UK.** *Planning Guidance: Small Wind – Appendices, November 2011*. Online 06/05/2014 at <http://www.renewableuk.com/en/publications/guides.cfm/Small-Wind-Planning-Guidance-Appendices>.
- [73] **T. Sharpe and G. Proven.** *Crossflex: Concept and early development of a true building integrated wind turbine*. *Energy and Buildings* 42 (2010), pp. 2365-2375.
- [74] **W.T. Chong, S.C. Poh, A. Fazlizan, S.Y. Yip, C.K. Chang and W.P. Hew.** *Early development of an energy recovery wind turbine generator for exhaust air system*. *Applied Energy* 112 (2013), pp. 568-575.
- [75] **F. Balduzzi, A. Bianchini, E.A. Carnevale, L. Ferrari and S. Magnani.** *Feasibility analysis of a Darrieus vertical-axis wind turbine installation in the rooftop of a building*. *Applied Energy* 97 (2012), pp. 921-929.
- [76] **Altaeros Energy.** *Altaeros Buoyant Airborne Turbine (BAT)*. Online 04/19/2014 at <http://www.altaerosenergies.com/index.html>.
- [77] **Z. Simic, J.G. Havelka and M.B. Vrhovcak.** *Small wind turbines – A unique segment of the wind power market*. *Renewable Energy* 50 (2013), pp. 1027-1036.
- [78] **H. Sutherland, D.E. Berg and T.D. Ashwill.** *A Retrospective of VAWT Technology*. Sandia National Laboratories, Report SAND2012-0304 (2012).
- [79] **X. Sun, D. Huang and G. Wu.** *The current state of offshore wind energy technology development*. *Energy* 41 (2012), pp. 298-312.
- [80] **M. Kinzel, Q. Mulligan and J.O. Dabiri.** *Energy exchange in an array of vertical-axis wind turbines*. *Journal of Turbulence* Vol. 13, No. 38 (2012), pp. 1-13.
- [81] **R.W. Whittlesey, S. Liska and J.O. Dabiri.** *Fish schooling as a basis for vertical axis wind turbine farm design*. *Bioinspiration & Biomimetics* 5 (2010), Article ID 035005 (6 pp.).
- [82] **J.O. Dabiri.** *Potential order-of-magnitude enhancement of wind farm power density via counter-rotating vertical-axis wind turbine arrays*. *Journal of Renewable and Sustainable Energy* 3 (2011), Article ID 043104-1.
- [83] **A.K. Prasad.** *Analytical Solution for the Optimal Spacing of Wind Turbines*. *Journal of Fluids Engineering*, Vol. 136 (2014). Article ID 011107-1.
-

-
- [84] **J. Meyers and C. Meneveau.** *Optimal turbine spacing in fully developed wind farm boundary layers.* Wind Energy, Vol. 15 (2012), pp. 305-317.
- [85] **M.C. Classens.** *The Design and Testing of Airfoils for Application in Small Vertical Axis Wind Turbines.* M. Sc. thesis, Delft University of Technology, 2006.
- [86] **M.O.L. Hansen** (2008). *Aerodynamics of Wind Turbines* (2nd edition). Earthscan.
- [87] **S.C. McIntosh and H. Babinsky.** *Convergence Failure and Stall Hysteresis in Actuator-Disk Momentum Models Applied to Vertical Axis Wind Turbines.* Journal of Solar Energy Engineering, Vol. 131 (2009). Article ID 034502-1.
- [88] **I. Paraschivoiu.** *Double-Multiple Streamtube Model for Darrieus Wind Turbines.* DOE/NASA Wind Turbines Dynamics Workshop, NASA CP-2185, Cleveland, Ohio, February 1981, pp. 19-25.
- [89] **W. Tjiu, T. Marnoto, S. Mat, M.H. Ruslan and K. Sopian.** *Darrieus vertical axis wind turbine for power generation I: Assessment of Darrieus VAWT configurations.* Renewable Energy, Vol. 75 (2015), pp. 50-67.
- [90] **I. Paraschivoiu and F. Delclaux.** *Double Multiple Streamtube Model with Recent Improvements.* Journal of Energy, Vol. 7, No. 3 (1983), pp. 250-255.
- [91] **N. Fujisawa and S. Shibuya.** *Observations of dynamic stall on Darrieus wind turbine blades.* Journal of Wind Engineering and Industrial Aerodynamics, Vol. 89 (2001), pp. 201-214.
- [92] **B.D. Hibbs.** *HAWT Performance With Dynamic Stall. A Subcontract Report.* AeroVironment, Inc. Monrovia, California. SERI/STR-217-2732. DE86004428. February 1986.
- [93] **Ø.V. Nygard.** *Wake behind a horizontal-axis wind turbine.* M. Sc. thesis, Norwegian University of Science and Technology, 2011.
- [94] **K. Karamcheti** (1980). *Principles of Ideal-Fluid Aerodynamics* (2nd edition). Krieger Pub Co.
- [95] **T. van Nguyen.** *A vortex model of the Darrieus turbine.* M. Sc. thesis, Texas Tech University, 1978.
- [96] **A. Zanon, P. Giannattasio and C.J.S. Ferreira.** *A vortex panel model for the simulation of the wake past a vertical axis wind turbine in dynamic stall.* Wind Energy, Vol. 16 (2013), pp. 661-680.
- [97] **P. Deglaire, S. Engblom, O. Ågren and H. Bernhoff.** *Analytical solutions for a single blade in vertical axis turbine motion in two-dimensions.* European Journal of Mechanics B/Fluids, Vol. 28 (2009), pp. 506-520.
- [98] **J.D. Anderson, Jr** (1995). *Computational Fluid Dynamics. The Basics with Applications.* McGraw-Hill, Inc.
- [99] **C. Rangel.** *Desempeño Aerodinámico de Turbinas Eólicas de Eje Vertical en Función de Temperatura de Superficie de Álabes [Aerodynamic Performance of Vertical-Axis Wind Turbines as a Function of Blade Surface Temperature].* M. Sc. thesis, Universidad de Chile, 2012.
- [100] **C. Li, S. Zhu, Y. Xu and Y. Xiao.** *2.5 large eddy simulation of vertical axis wind turbine in*
-

- consideration of high angle of attack flow*. Renewable Energy, Vol. 51 (2013), pp. 317-330.
- [101] **A. Rossetti and G. Pavesi**. *Comparison of different numerical approaches to the study of the H-Darrieus turbines start-up*. Renewable Energy, Vol. 50 (2013), pp. 7-19.
- [102] **K. McLaren, S. Tullis and S. Ziada**. *Computational fluid dynamics simulation of the aerodynamics of a high solidity, small-scale vertical axis wind turbine*. Wind Energy, Vol. 15 (2012), pp. 349-361.
- [103] **M.R. Castelli, G. Grandi and E. Benini**. *Numerical Analysis of the Performance of the DU91-W2-250 Airfoil for Straight-Bladed Vertical-Axis Wind Turbine Application*. World Academy of Science, Engineering and Technology, Vol. 63 (2012), pp. 855-860.
- [104] **M.R. Castelli, A. Englaro and E. Benini**. *The Darrieus wind turbine: Proposal for a new performance prediction model based on CFD*. Energy, Vol. 36 (2011), pp. 4919-4934.
- [105] **L.A. Danao, J. Edwards, O. Eboibi and R. Howell**. *A numerical investigation into the influence of unsteady wind on the performance and aerodynamics of a vertical-axis wind turbine*. Applied Energy, Vol. 116 (2014), pp. 111-124.
- [106] **W. Chen, H. Sun, X. Zhang and D. Korošak**. *Anomalous diffusion modeling by fractal and fractional derivatives*. Computers and Mathematics with Applications, Vol. 59 (2010), pp. 1754-1758.
- [107] **Y. Hara, K. Hara and T. Hayashi**. *Moment of Inertia Dependence of Vertical Axis Wind Turbines in Pulsating Winds*. International Journal of Rotating Machinery, Vol. 2012. Article ID 910940, p. 12.
- [108] **S.J. Kooiman and S.W. Tullis**. *Response of a Vertical Axis Wind Turbine to Time Varying Wind Conditions found within the Urban Environment*. Wind Engineering, Vol. 34, No. 4 (2010), pp. 389-401.
- [109] **S. Eriksson**. *Direct Driven Generators for Vertical Axis Wind Turbines*. Ph. D. thesis, Uppsala University, 2008.
- [110] **J. Kjellin**. *Vertical Axis Wind Turbines. Electrical Systems and Experimental Results*. Ph. D. thesis, Uppsala University, 2012.
- [111] **A. Goude and F. Bülow**. *Robust VAWT control system evaluation by coupled aerodynamic and electrical simulations*. Renewable Energy, Vol. 59 (2013), pp. 193-201.
- [112] **A. Goude and F. Bülow**. *Aerodynamic and electrical evaluation of a VAWT farm control system with passive rectifiers and mutual DC-bus*. Renewable Energy, Vol. 60 (2013), pp. 284-292.
- [113] **D. Greenblatt, M. Shculman and A. Ben-Harav**. *Vertical axis wind turbine performance enhancement using plasma actuators*. Renewable Energy, Vol. 37 (2012), pp. 345-354.
- [114] **J. Yen and N.A. Ahmed**. *Enhancing vertical axis wind turbine by dynamic stall control using synthetic jets*. Journal of Wind Engineering and Industrial Aerodynamics, Vol. 114 (2013), pp. 12-17.
- [115] **J. Kjellin, F. Bülow, S. Eriksson, P. Deglaire, M. Leijon and H. Bernhoff**. *Power coefficient measurement on a 12 kW straight bladed vertical axis wind turbine*. Renewable Energy, Vol. 36 (2011), pp. 3050-3053.

- [116] **ANSYS, Inc.** *ANSYS FLUENT User's Guide. Release 13.0.* November 2010.
- [117] **P. Deglaire.** *Analytical Aerodynamic Simulation Tools for Vertical Axis Wind Turbines.* Ph. D. thesis, Uppsala University, 2010.
- [118] **J.S. Delnero, J. Marañon di Leo, F.A. Bacchi, J. Colman and U. Boldes.** *Experimental determination of the influence of turbulent scale on the lift and drag coefficients of low Reynolds number airfoils.* Latin American Applied Research, Vol. 35 (2005), pp. 183-188.
- [119] **G. Bedon, E.G.A. Antonini, S. de Betta, M.R. Castelli and E. Benini.** *Evaluation of different aerodynamic databases for vertical axis wind turbine simulations.* Renewable and Sustainable Energies Reviews, Vol. 40 (2014), pp. 386-399.
- [120] **C.S. Ferreira.** *The near wake of the VAWT – 2D and 3D views of the VAWT.* Ph. D. thesis, Delft University of Technology, 2009.
- [121] **M. Nini, V. Motta, G. Bindolino and A. Guardone.** *Three-dimensional simulation of a complete Vertical Axis Wind Turbine using overlapping grids.* Journal of Computational and Applied Mathematics, Vol. 270 (2014), pp. 78-87.
- [122] **R.E. Sheldahl and P.C. Klimas.** *Aerodynamic Characteristics of Seven Symmetrical Airfoil Sections Through 180-Degree Angle of Attack for Use in Aerodynamic Analysis of Vertical Axis Wind Turbines.* Sandia National Laboratories – energy report, SAND80-2114 (1981).

APPENDIX A. AERODYNAMIC COEFFICIENTS

A1. Subsonic lift coefficients of the airfoil NACA 0012

Source: [4]. Note that some coefficients from [4] were considered typographical errors and were replaced by interpolated coefficients (in red) to obtain smooth curves.

α [°]	Re=1.0E4	Re=2.0E4	Re=4.0E4	Re=8.0E4	Re=1.6E5	Re=3.6E5	Re=7.0E5	Re=1.0E6	Re=2.0E6	Re=5.0E6
0	0.0000	0.0000	0.0000	0.0000	0.0000	0.0000	0.0000	0.0000	0.0000	0.0000
1	0.0830	0.1057	0.1100	0.1100	0.1100	0.1100	0.1100	0.1100	0.1100	0.1100
2	0.1534	0.2072	0.2200	0.2200	0.2200	0.2200	0.2200	0.2200	0.2200	0.2200
3	0.2009	0.3032	0.3376	0.3300	0.3300	0.3300	0.3300	0.3300	0.3300	0.3300
4	0.2003	0.3929	0.4464	0.4400	0.4400	0.4400	0.4400	0.4400	0.4400	0.4400
5	0.0328	0.4781	0.5726	0.5500	0.5500	0.5500	0.5500	0.5500	0.5500	0.5500
6	-0.1413	-0.0928	0.6115	0.6384	0.6600	0.6600	0.6600	0.6600	0.6600	0.6600
7	-0.1142	-0.1089	-0.0212	0.7227	0.7460	0.7700	0.7700	0.7700	0.7700	0.7700
8	-0.0703	-0.0699	-0.0615	0.6930	0.8274	0.8542	0.8800	0.8800	0.8800	0.8800
9	-0.0215	-0.0198	-0.0160	-0.0010	0.8527	0.9352	0.9598	0.9661	0.9900	0.9900
10	0.0311	0.0320	0.0344	0.0413	0.1325	0.9811	1.0343	1.0512	1.0727	1.1000
11	0.0848	0.0856	0.0869	0.0911	0.1095	0.9132	1.0749	1.1097	1.1539	1.1842
12	0.1387	0.1395	0.1406	0.1430	0.1533	0.4832	1.0390	1.1212	1.2072	1.2673
13	0.1928	0.1934	0.1945	0.1966	0.2030	0.2759	0.8737	1.0487	1.2169	1.3242
14	0.2468	0.2474	0.2484	0.2504	0.2546	0.2893	0.6284	0.8846	1.1614	1.3423
15	0.3008	0.3014	0.3024	0.3043	0.3082	0.3306	0.4907	0.7108	1.0478	1.3093
16	0.3468	0.3554	0.3563	0.3582	0.3620	0.3792	0.4696	0.6060	0.9221	1.2195
17	0.4079	0.4089	0.4107	0.4139	0.4200	0.4455	0.5195	0.5906	0.7826	1.0365
18	0.4606	0.4620	0.4644	0.4689	0.4768	0.5047	0.5584	0.6030	0.7163	0.9054
19	0.5121	0.5147	0.5178	0.5232	0.5322	0.5591	0.6032	0.6334	0.7091	0.8412
20	0.5838	0.5663	0.5708	0.5770	0.5870	0.6120	0.6474	0.6716	0.7269	0.8233
21	0.6161	0.6184	0.6232	0.6305	0.6414	0.6643	0.6949	0.7162	0.7595	0.8327
22	0.6687	0.6709	0.6755	0.6839	0.6956	0.7179	0.7446	0.7613	0.7981	0.8563
23	0.7216	0.7238	0.7283	0.7373	0.7497	0.7715	0.7948	0.8097	0.8429	0.8903
24	0.7744	0.7765	0.7809	0.7902	0.8034	0.8246	0.8462	0.8589	0.8882	0.9295
25	0.8276	0.8297	0.8340	0.8432	0.8572	0.8780	0.8984	0.9093	0.9352	0.9718
26	0.8810	0.8831	0.8873	0.8963	0.9109	0.9313	0.9506	0.9618	0.9842	1.0193
27	0.9345	0.9365	0.9407	0.9496	0.9646	0.9846	1.0029	1.0144	1.0355	1.0680
30	0.9150	0.9150	0.9150	0.9150	0.9150	0.9150	0.9150	0.9150	0.9150	0.9150
35	1.0200	1.0200	1.0200	1.0200	1.0200	1.0200	1.0200	1.0200	1.0200	1.0200

$\alpha [^\circ]$	Re=1.0E4	Re=2.0E4	Re=4.0E4	Re=8.0E4	Re=1.6E5	Re=3.6E5	Re=7.0E5	Re=1.0E6	Re=2.0E6	Re=5.0E6
40	1.0750	1.0750	1.0750	1.0750	1.0750	1.0750	1.0750	1.0750	1.0750	1.0750
45	1.0850	1.0850	1.0850	1.0850	1.0850	1.0850	1.0850	1.0850	1.0850	1.0850
50	1.0400	1.0400	1.0400	1.0400	1.0400	1.0400	1.0400	1.0400	1.0400	1.0400
55	0.9650	0.9650	0.9650	0.9650	0.9650	0.9650	0.9650	0.9650	0.9650	0.9650
60	0.8750	0.8750	0.8750	0.8750	0.8750	0.8750	0.8750	0.8750	0.8750	0.8750
65	0.7650	0.7650	0.7650	0.7650	0.7650	0.7650	0.7650	0.7650	0.7650	0.7650
70	0.6500	0.6500	0.6500	0.6500	0.6500	0.6500	0.6500	0.6500	0.6500	0.6500
75	0.5150	0.5150	0.5150	0.5150	0.5150	0.5150	0.5150	0.5150	0.5150	0.5150
80	0.3700	0.3700	0.3700	0.3700	0.3700	0.3700	0.3700	0.3700	0.3700	0.3700
85	0.2200	0.2200	0.2200	0.2200	0.2200	0.2200	0.2200	0.2200	0.2200	0.2200
90	0.0700	0.0700	0.0700	0.0700	0.0700	0.0700	0.0700	0.0700	0.0700	0.0700
95	-0.0700	-0.0700	-0.0700	-0.0700	-0.0700	-0.0700	-0.0700	-0.0700	-0.0700	-0.0700
100	-0.2200	-0.2200	-0.2200	-0.2200	-0.2200	-0.2200	-0.2200	-0.2200	-0.2200	-0.2200
105	-0.3700	-0.3700	-0.3700	-0.3700	-0.3700	-0.3700	-0.3700	-0.3700	-0.3700	-0.3700
110	-0.5100	-0.5100	-0.5100	-0.5100	-0.5100	-0.5100	-0.5100	-0.5100	-0.5100	-0.5100
115	-0.6250	-0.6250	-0.6250	-0.6250	-0.6250	-0.6250	-0.6250	-0.6250	-0.6250	-0.6250
120	-0.7350	-0.7350	-0.7350	-0.7350	-0.7350	-0.7350	-0.7350	-0.7350	-0.7350	-0.7350
125	-0.8400	-0.8400	-0.8400	-0.8400	-0.8400	-0.8400	-0.8400	-0.8400	-0.8400	-0.8400
130	-0.9100	-0.9100	-0.9100	-0.9100	-0.9100	-0.9100	-0.9100	-0.9100	-0.9100	-0.9100
135	-0.9450	-0.9450	-0.9450	-0.9450	-0.9450	-0.9450	-0.9450	-0.9450	-0.9450	-0.9450
140	-0.9450	-0.9450	-0.9450	-0.9450	-0.9450	-0.9450	-0.9450	-0.9450	-0.9450	-0.9450
145	-0.9100	-0.9100	-0.9100	-0.9100	-0.9100	-0.9100	-0.9100	-0.9100	-0.9100	-0.9100
150	-0.8500	-0.8500	-0.8500	-0.8500	-0.8500	-0.8500	-0.8500	-0.8500	-0.8500	-0.8500
155	-0.7400	-0.7400	-0.7400	-0.7400	-0.7400	-0.7400	-0.7400	-0.7400	-0.7400	-0.7400
160	-0.6600	-0.6600	-0.6600	-0.6600	-0.6600	-0.6600	-0.6600	-0.6600	-0.6600	-0.6600
165	-0.6750	-0.6750	-0.6750	-0.6750	-0.6750	-0.6750	-0.6750	-0.6750	-0.6750	-0.6750
170	-0.8500	-0.8500	-0.8500	-0.8500	-0.8500	-0.8500	-0.8500	-0.8500	-0.8500	-0.8500
175	-0.6900	-0.6900	-0.6900	-0.6900	-0.6900	-0.6900	-0.6900	-0.6900	-0.6900	-0.6900
180	0.0000	0.0000	0.0000	0.0000	0.0000	0.0000	0.0000	0.0000	0.0000	0.0000

A2. Subsonic drag coefficients of the airfoil NACA 0012

Source: [4]. Note that some coefficients from [4] were considered typographical errors and were replaced by interpolated coefficients (in red) to obtain smooth curves.

α [°]	Re=1.0E4	Re=2.0E4	Re=4.0E4	Re=8.0E4	Re=1.6E5	Re=3.6E5	Re=7.0E5	Re=1.0E6	Re=2.0E6	Re=5.0E6
0	0.0337	0.0245	0.0175	0.0133	0.0103	0.0079	0.0067	0.0065	0.0064	0.0064
1	0.0338	0.0247	0.0177	0.0134	0.0104	0.0080	0.0068	0.0066	0.0064	0.0064
2	0.0343	0.0251	0.0181	0.0138	0.0108	0.0084	0.0070	0.0068	0.0066	0.0066
3	0.0351	0.0259	0.0189	0.0145	0.0114	0.0089	0.0075	0.0071	0.0069	0.0068
4	0.0359	0.0270	0.0199	0.0155	0.0124	0.0098	0.0083	0.0078	0.0073	0.0072
5	0.0351	0.0282	0.0218	0.0170	0.0140	0.0113	0.0097	0.0091	0.0081	0.0076
6	0.0460	0.0460	0.0232	0.0189	0.0152	0.0125	0.0108	0.0101	0.0090	0.0081
7	0.0580	0.0580	0.0580	0.0204	0.0170	0.0135	0.0118	0.0110	0.0097	0.0086
8	0.0720	0.0720	0.0720	0.0222	0.0185	0.0153	0.0128	0.0119	0.0105	0.0092
9	0.0860	0.0860	0.0860	0.0600	0.0203	0.0167	0.0144	0.0134	0.0113	0.0098
10	0.1010	0.1010	0.1010	0.0900	0.0188	0.0184	0.0159	0.0147	0.0128	0.0106
11	0.1170	0.1170	0.1170	0.1170	0.0760	0.0204	0.0175	0.0162	0.0140	0.0118
12	0.1340	0.1340	0.1340	0.1340	0.1340	0.0217	0.0195	0.0180	0.0155	0.0130
13	0.1520	0.1520	0.1520	0.1520	0.1520	0.0222	0.0216	0.0200	0.0172	0.0143
14	0.1710	0.1710	0.1710	0.1710	0.1710	0.1060	0.0236	0.0222	0.0191	0.0159
15	0.1900	0.1900	0.1900	0.1900	0.1900	0.1900	0.1170	0.0245	0.0213	0.0177
16	0.2100	0.2100	0.2100	0.2100	0.2100	0.2100	0.2100	0.1280	0.0237	0.0198
17	0.2310	0.2310	0.2310	0.2310	0.2310	0.2310	0.2310	0.2310	0.1380	0.0229
18	0.2520	0.2520	0.2520	0.2520	0.2520	0.2520	0.2520	0.2520	0.2520	0.1480
19	0.2740	0.2740	0.2740	0.2740	0.2740	0.2740	0.2740	0.2740	0.2740	0.2740
20	0.2970	0.2970	0.2970	0.2970	0.2970	0.2970	0.2970	0.2970	0.2970	0.2970
21	0.3200	0.3200	0.3200	0.3200	0.3200	0.3200	0.3200	0.3200	0.3200	0.3200
22	0.3440	0.3440	0.3440	0.3440	0.3440	0.3440	0.3440	0.3440	0.3440	0.3440
23	0.3690	0.3690	0.3690	0.3690	0.3690	0.3690	0.3690	0.3690	0.3690	0.3690
24	0.3940	0.3940	0.3940	0.3940	0.3940	0.3940	0.3940	0.3940	0.3940	0.3940
25	0.4200	0.4200	0.4200	0.4200	0.4200	0.4200	0.4200	0.4200	0.4200	0.4200
26	0.4460	0.4460	0.4460	0.4460	0.4460	0.4460	0.4460	0.4460	0.4460	0.4460
27	0.4730	0.4730	0.4730	0.4730	0.4730	0.4730	0.4730	0.4730	0.4730	0.4730
30	0.5700	0.5700	0.5700	0.5700	0.5700	0.5700	0.5700	0.5700	0.5700	0.5700
35	0.7450	0.7450	0.7450	0.7450	0.7450	0.7450	0.7450	0.7450	0.7450	0.7450
40	0.9200	0.9200	0.9200	0.9200	0.9200	0.9200	0.9200	0.9200	0.9200	0.9200
45	1.0750	1.0750	1.0750	1.0750	1.0750	1.0750	1.0750	1.0750	1.0750	1.0750
50	1.2150	1.2150	1.2150	1.2150	1.2150	1.2150	1.2150	1.2150	1.2150	1.2150
55	1.3450	1.3450	1.3450	1.3450	1.3450	1.3450	1.3450	1.3450	1.3450	1.3450

α [°]	Re=1.0E4	Re=2.0E4	Re=4.0E4	Re=8.0E4	Re=1.6E5	Re=3.6E5	Re=7.0E5	Re=1.0E6	Re=2.0E6	Re=5.0E6
60	1.4700	1.4700	1.4700	1.4700	1.4700	1.4700	1.4700	1.4700	1.4700	1.4700
65	1.5750	1.5750	1.5750	1.5750	1.5750	1.5750	1.5750	1.5750	1.5750	1.5750
70	1.6650	1.6650	1.6650	1.6650	1.6650	1.6650	1.6650	1.6650	1.6650	1.6650
75	1.7350	1.7350	1.7350	1.7350	1.7350	1.7350	1.7350	1.7350	1.7350	1.7350
80	1.7800	1.7800	1.7800	1.7800	1.7800	1.7800	1.7800	1.7800	1.7800	1.7800
85	1.8000	1.8000	1.8000	1.8000	1.8000	1.8000	1.8000	1.8000	1.8000	1.8000
90	1.8000	1.8000	1.8000	1.8000	1.8000	1.8000	1.8000	1.8000	1.8000	1.8000
95	1.7800	1.7800	1.7800	1.7800	1.7800	1.7800	1.7800	1.7800	1.7800	1.7800
100	1.7500	1.7500	1.7500	1.7500	1.7500	1.7500	1.7500	1.7500	1.7500	1.7500
105	1.7000	1.7000	1.7000	1.7000	1.7000	1.7000	1.7000	1.7000	1.7000	1.7000
110	1.6350	1.6350	1.6350	1.6350	1.6350	1.6350	1.6350	1.6350	1.6350	1.6350
115	1.5550	1.5550	1.5550	1.5550	1.5550	1.5550	1.5550	1.5550	1.5550	1.5550
120	1.4650	1.4650	1.4650	1.4650	1.4650	1.4650	1.4650	1.4650	1.4650	1.4650
125	1.3500	1.3500	1.3500	1.3500	1.3500	1.3500	1.3500	1.3500	1.3500	1.3500
130	1.2250	1.2250	1.2250	1.2250	1.2250	1.2250	1.2250	1.2250	1.2250	1.2250
135	1.0850	1.0850	1.0850	1.0850	1.0850	1.0850	1.0850	1.0850	1.0850	1.0850
140	0.9250	0.9250	0.9250	0.9250	0.9250	0.9250	0.9250	0.9250	0.9250	0.9250
145	0.7550	0.7550	0.7550	0.7550	0.7550	0.7550	0.7550	0.7550	0.7550	0.7550
150	0.5750	0.5750	0.5750	0.5750	0.5750	0.5750	0.5750	0.5750	0.5750	0.5750
155	0.4200	0.4200	0.4200	0.4200	0.4200	0.4200	0.4200	0.4200	0.4200	0.4200
160	0.3200	0.3200	0.3200	0.3200	0.3200	0.3200	0.3200	0.3200	0.3200	0.3200
165	0.2300	0.2300	0.2300	0.2300	0.2300	0.2300	0.2300	0.2300	0.2300	0.2300
170	0.1400	0.1400	0.1400	0.1400	0.1400	0.1400	0.1400	0.1400	0.1400	0.1400
175	0.0550	0.0550	0.0550	0.0550	0.0550	0.0550	0.0550	0.0550	0.0550	0.0550
180	0.0250	0.0250	0.0250	0.0250	0.0250	0.0250	0.0250	0.0250	0.0250	0.0250

A3. Subsonic lift coefficients of the airfoil NACA 0015

Source: [4]. Note that some coefficients from [4] were considered typographical errors and were replaced by interpolated coefficients (in red) to obtain smooth curves.

α [°]	Re=1.0E4	Re=2.0E4	Re=4.0E4	Re=8.0E4	Re=1.6E5	Re=3.6E5	Re=7.0E5	Re=1.0E6	Re=2.0E6	Re=5.0E6
0	0.0000	0.0000	0.0000	0.0000	0.0000	0.0000	0.0000	0.0000	0.0000	0.0000
1	0.0434	0.0891	0.1054	0.1100	0.1100	0.1100	0.1100	0.1100	0.1100	0.1100
2	0.0715	0.1740	0.2099	0.2200	0.2200	0.2200	0.2200	0.2200	0.2200	0.2200
3	0.0725	0.2452	0.3078	0.3300	0.3300	0.3300	0.3300	0.3300	0.3300	0.3300
4	0.0581	0.3041	0.4186	0.4400	0.4400	0.4400	0.4400	0.4400	0.4400	0.4400
5	0.0162	0.3359	0.4871	0.5180	0.5500	0.5500	0.5500	0.5500	0.5500	0.5500
6	-0.0781	0.3001	0.5551	0.6044	0.6299	0.6600	0.6600	0.6600	0.6600	0.6600
7	-0.1517	0.0570	0.5730	0.6760	0.7150	0.7390	0.7483	0.7700	0.7700	0.7700
8	-0.1484	-0.1104	0.4663	0.7189	0.7851	0.8240	0.8442	0.8504	0.8800	0.8800
9	-0.1194	-0.1050	0.0433	0.6969	0.8311	0.8946	0.9260	0.9387	0.9574	0.9900
10	-0.0791	-0.0728	-0.0413	0.5122	0.8322	0.9440	0.9937	1.0141	1.0433	1.0685
11	-0.0348	-0.0300	-0.0144	0.1642	0.7623	0.9572	1.0363	1.0686	1.1138	1.1553
12	0.0138	0.0173	0.0261	0.0749	0.5936	0.9285	1.0508	1.0971	1.1667	1.2290
13	0.0649	0.0678	0.0741	0.0967	0.3548	0.8562	1.0302	1.0957	1.1949	1.2847
14	0.1172	0.1193	0.1244	0.1382	0.2371	0.7483	0.9801	1.0656	1.1962	1.3187
15	0.1706	0.1721	0.1756	0.1861	0.2376	0.6350	0.9113	1.0145	1.1744	1.3298
16	0.2242	0.2256	0.2280	0.2364	0.2665	0.5384	0.8401	0.9567	1.1356	1.3186
17	0.2780	0.2792	0.2815	0.2873	0.3098	0.4851	0.7799	0.8996	1.0921	1.2917
18	0.3319	0.3331	0.3351	0.3393	0.3567	0.4782	0.7305	0.8566	1.0510	1.2576
19	0.3859	0.3869	0.3889	0.3927	0.4066	0.4908	0.7041	0.8226	1.0173	1.2242
20	0.4399	0.4409	0.4427	0.4463	0.4575	0.5247	0.6990	0.8089	0.9954	1.1965
21	0.4939	0.4949	0.4966	0.5001	0.5087	0.5616	0.7097	0.8063	0.9837	1.1771
22	0.5479	0.5489	0.5506	0.5539	0.5611	0.6045	0.7298	0.8189	0.9827	1.1647
23	0.6019	0.6029	0.6045	0.6078	0.6148	0.6528	0.7593	0.8408	0.9910	1.1611
24	0.6559	0.6569	0.6585	0.6617	0.6685	0.7017	0.7961	0.8668	1.0078	1.1563
25	0.7099	0.7109	0.7125	0.7156	0.7224	0.7511	0.8353	0.9023	1.0317	1.1322
26	0.7639	0.7649	0.7666	0.7700	0.7771	0.8055	0.8838	0.9406	1.0591	1.1268
27	0.8174	0.8191	0.8222	0.8277	0.8382	0.8788	0.9473	0.9912	1.0810	1.1397
30	0.8550	0.8550	0.8550	0.8550	0.8550	0.8550	0.8550	0.8550	0.8550	0.8550
35	0.9800	0.9800	0.9800	0.9800	0.9800	0.9800	0.9800	0.9800	0.9800	0.9800
40	1.0350	1.0350	1.0350	1.0350	1.0350	1.0350	1.0350	1.0350	1.0350	1.0350
45	1.0500	1.0500	1.0500	1.0500	1.0500	1.0500	1.0500	1.0500	1.0500	1.0500
50	1.0200	1.0200	1.0200	1.0200	1.0200	1.0200	1.0200	1.0200	1.0200	1.0200
55	0.9550	0.9550	0.9550	0.9550	0.9550	0.9550	0.9550	0.9550	0.9550	0.9550

α [°]	Re=1.0E4	Re=2.0E4	Re=4.0E4	Re=8.0E4	Re=1.6E5	Re=3.6E5	Re=7.0E5	Re=1.0E6	Re=2.0E6	Re=5.0E6
60	0.8750	0.8750	0.8750	0.8750	0.8750	0.8750	0.8750	0.8750	0.8750	0.8750
65	0.7600	0.7600	0.7600	0.7600	0.7600	0.7600	0.7600	0.7600	0.7600	0.7600
70	0.6300	0.6300	0.6300	0.6300	0.6300	0.6300	0.6300	0.6300	0.6300	0.6300
75	0.5000	0.5000	0.5000	0.5000	0.5000	0.5000	0.5000	0.5000	0.5000	0.5000
80	0.3650	0.3650	0.3650	0.3650	0.3650	0.3650	0.3650	0.3650	0.3650	0.3650
85	0.2300	0.2300	0.2300	0.2300	0.2300	0.2300	0.2300	0.2300	0.2300	0.2300
90	0.0900	0.0900	0.0900	0.0900	0.0900	0.0900	0.0900	0.0900	0.0900	0.0900
95	-0.0500	-0.0500	-0.0500	-0.0500	-0.0500	-0.0500	-0.0500	-0.0500	-0.0500	-0.0500
100	-0.1850	-0.1850	-0.1850	-0.1850	-0.1850	-0.1850	-0.1850	-0.1850	-0.1850	-0.1850
105	-0.3200	-0.3200	-0.3200	-0.3200	-0.3200	-0.3200	-0.3200	-0.3200	-0.3200	-0.3200
110	-0.4500	-0.4500	-0.4500	-0.4500	-0.4500	-0.4500	-0.4500	-0.4500	-0.4500	-0.4500
115	-0.5750	-0.5750	-0.5750	-0.5750	-0.5750	-0.5750	-0.5750	-0.5750	-0.5750	-0.5750
120	-0.6700	-0.6700	-0.6700	-0.6700	-0.6700	-0.6700	-0.6700	-0.6700	-0.6700	-0.6700
125	-0.7600	-0.7600	-0.7600	-0.7600	-0.7600	-0.7600	-0.7600	-0.7600	-0.7600	-0.7600
130	-0.8500	-0.8500	-0.8500	-0.8500	-0.8500	-0.8500	-0.8500	-0.8500	-0.8500	-0.8500
135	-0.9300	-0.9300	-0.9300	-0.9300	-0.9300	-0.9300	-0.9300	-0.9300	-0.9300	-0.9300
140	-0.9800	-0.9800	-0.9800	-0.9800	-0.9800	-0.9800	-0.9800	-0.9800	-0.9800	-0.9800
145	-0.9000	-0.9000	-0.9000	-0.9000	-0.9000	-0.9000	-0.9000	-0.9000	-0.9000	-0.9000
150	-0.7700	-0.7700	-0.7700	-0.7700	-0.7700	-0.7700	-0.7700	-0.7700	-0.7700	-0.7700
155	-0.6700	-0.6700	-0.6700	-0.6700	-0.6700	-0.6700	-0.6700	-0.6700	-0.6700	-0.6700
160	-0.6350	-0.6350	-0.6350	-0.6350	-0.6350	-0.6350	-0.6350	-0.6350	-0.6350	-0.6350
165	-0.6800	-0.6800	-0.6800	-0.6800	-0.6800	-0.6800	-0.6800	-0.6800	-0.6800	-0.6800
170	-0.8500	-0.8500	-0.8500	-0.8500	-0.8500	-0.8500	-0.8500	-0.8500	-0.8500	-0.8500
175	-0.6600	-0.6600	-0.6600	-0.6600	-0.6600	-0.6600	-0.6600	-0.6600	-0.6600	-0.6600
180	0.0000	0.0000	0.0000	0.0000	0.0000	0.0000	0.0000	0.0000	0.0000	0.0000

A4. Subsonic drag coefficients of the airfoil NACA 0015

Source: [4]. Note that some coefficients from [4] were considered typographical errors and were replaced by interpolated coefficients (in red) to obtain smooth curves.

α [°]	Re=1.0E4	Re=2.0E4	Re=4.0E4	Re=8.0E4	Re=1.6E5	Re=3.6E5	Re=7.0E5	Re=1.0E6	Re=2.0E6	Re=5.0E6
0	0.0360	0.0265	0.0196	0.0147	0.0116	0.0091	0.0077	0.0074	0.0070	0.0068
1	0.0362	0.0267	0.0198	0.0148	0.0117	0.0092	0.0078	0.0075	0.0071	0.0069
2	0.0366	0.0271	0.0202	0.0151	0.0120	0.0094	0.0080	0.0076	0.0072	0.0070
3	0.0373	0.0279	0.0209	0.0156	0.0124	0.0098	0.0083	0.0079	0.0075	0.0073
4	0.0383	0.0290	0.0219	0.0168	0.0132	0.0105	0.0089	0.0083	0.0078	0.0075
5	0.0393	0.0303	0.0232	0.0181	0.0142	0.0114	0.0098	0.0091	0.0083	0.0080
6	0.0400	0.0410	0.0249	0.0197	0.0160	0.0126	0.0108	0.0101	0.0090	0.0084
7	0.0510	0.0510	0.0267	0.0214	0.0176	0.0143	0.0122	0.0111	0.0098	0.0089
8	0.0640	0.0640	0.0520	0.0234	0.0193	0.0157	0.0135	0.0126	0.0108	0.0095
9	0.0770	0.0770	0.0770	0.0255	0.0212	0.0173	0.0149	0.0138	0.0121	0.0102
10	0.0910	0.0910	0.0910	0.0277	0.0233	0.0191	0.0164	0.0152	0.0133	0.0113
11	0.1070	0.1070	0.1070	0.0760	0.0256	0.0211	0.0182	0.0168	0.0146	0.0124
12	0.1230	0.1230	0.1230	0.1230	0.0281	0.0233	0.0200	0.0186	0.0161	0.0136
13	0.1400	0.1400	0.1400	0.1400	0.0302	0.0257	0.0221	0.0205	0.0177	0.0149
14	0.1580	0.1580	0.1580	0.1580	0.1040	0.0283	0.0244	0.0225	0.0195	0.0164
15	0.1770	0.1770	0.1770	0.1770	0.1770	0.0312	0.0269	0.0249	0.0202	0.0180
16	0.1960	0.1960	0.1960	0.1960	0.1960	0.1240	0.0297	0.0275	0.0237	0.0198
17	0.2170	0.2170	0.2170	0.2170	0.2170	0.2170	0.1340	0.0303	0.0261	0.0218
18	0.2380	0.2380	0.2170	0.2170	0.2170	0.2170	0.2380	0.1450	0.0288	0.0240
19	0.2600	0.2600	0.2600	0.2600	0.2600	0.2600	0.2600	0.2600	0.1550	0.0265
20	0.2820	0.2820	0.2820	0.2820	0.2820	0.2820	0.2820	0.2820	0.2820	0.1660
21	0.3050	0.3050	0.3050	0.3050	0.3050	0.3050	0.3050	0.3050	0.3050	0.3050
22	0.3290	0.3290	0.3290	0.3290	0.3290	0.3290	0.3290	0.3290	0.3290	0.3290
23	0.3540	0.3540	0.3540	0.3540	0.3540	0.3540	0.3540	0.3540	0.3540	0.3540
24	0.3790	0.3790	0.3790	0.3790	0.3790	0.3790	0.3790	0.3790	0.3790	0.3790
25	0.4050	0.4050	0.4050	0.4050	0.4050	0.4050	0.4050	0.4050	0.4050	0.4050
26	0.4320	0.4320	0.4320	0.4320	0.4320	0.4320	0.4320	0.4320	0.4320	0.4320
27	0.4600	0.4600	0.4600	0.4600	0.4600	0.4600	0.4600	0.4600	0.4600	0.4600
30	0.5700	0.5700	0.5700	0.5700	0.5700	0.5700	0.5700	0.5700	0.5700	0.5700
35	0.7450	0.7450	0.7450	0.7450	0.7450	0.7450	0.7450	0.7450	0.7450	0.7450
40	0.9200	0.9200	0.9200	0.9200	0.9200	0.9200	0.9200	0.9200	0.9200	0.9200
45	1.0750	1.0750	1.0750	1.0750	1.0750	1.0750	1.0750	1.0750	1.0750	1.0750
50	1.2150	1.2150	1.2150	1.2150	1.2150	1.2150	1.2150	1.2150	1.2150	1.2150
55	1.3450	1.3450	1.3450	1.3450	1.3450	1.3450	1.3450	1.3450	1.3450	1.3450

α [°]	Re=1.0E4	Re=2.0E4	Re=4.0E4	Re=8.0E4	Re=1.6E5	Re=3.6E5	Re=7.0E5	Re=1.0E6	Re=2.0E6	Re=5.0E6
60	1.4700	1.4700	1.4700	1.4700	1.4700	1.4700	1.4700	1.4700	1.4700	1.4700
65	1.5750	1.5750	1.5750	1.5750	1.5750	1.5750	1.5750	1.5750	1.5750	1.5750
70	1.6650	1.6650	1.6650	1.6650	1.6650	1.6650	1.6650	1.6650	1.6650	1.6650
75	1.7350	1.7350	1.7350	1.7350	1.7350	1.7350	1.7350	1.7350	1.7350	1.7350
80	1.7800	1.7800	1.7800	1.7800	1.7800	1.7800	1.7800	1.7800	1.7800	1.7800
85	1.8000	1.8000	1.8000	1.8000	1.8000	1.8000	1.8000	1.8000	1.8000	1.8000
90	1.8000	1.8000	1.8000	1.8000	1.8000	1.8000	1.8000	1.8000	1.8000	1.8000
95	1.7800	1.7800	1.7800	1.7800	1.7800	1.7800	1.7800	1.7800	1.7800	1.7800
100	1.7500	1.7500	1.7500	1.7500	1.7500	1.7500	1.7500	1.7500	1.7500	1.7500
105	1.7000	1.7000	1.7000	1.7000	1.7000	1.7000	1.7000	1.7000	1.7000	1.7000
110	1.6350	1.6350	1.6350	1.6350	1.6350	1.6350	1.6350	1.6350	1.6350	1.6350
115	1.5550	1.5550	1.5550	1.5550	1.5550	1.5550	1.5550	1.5550	1.5550	1.5550
120	1.4650	1.4650	1.4650	1.4650	1.4650	1.4650	1.4650	1.4650	1.4650	1.4650
125	1.3500	1.3500	1.3500	1.3500	1.3500	1.3500	1.3500	1.3500	1.3500	1.3500
130	1.2250	1.2250	1.2250	1.2250	1.2250	1.2250	1.2250	1.2250	1.2250	1.2250
135	1.0850	1.0850	1.0850	1.0850	1.0850	1.0850	1.0850	1.0850	1.0850	1.0850
140	0.9250	0.9250	0.9250	0.9250	0.9250	0.9250	0.9250	0.9250	0.9250	0.9250
145	0.7550	0.7550	0.7550	0.7550	0.7550	0.7550	0.7550	0.7550	0.7550	0.7550
150	0.5750	0.5750	0.5750	0.5750	0.5750	0.5750	0.5750	0.5750	0.5750	0.5750
155	0.4200	0.4200	0.4200	0.4200	0.4200	0.4200	0.4200	0.4200	0.4200	0.4200
160	0.3200	0.3200	0.3200	0.3200	0.3200	0.3200	0.3200	0.3200	0.3200	0.3200
165	0.2300	0.2300	0.2300	0.2300	0.2300	0.2300	0.2300	0.2300	0.2300	0.2300
170	0.1400	0.1400	0.1400	0.1400	0.1400	0.1400	0.1400	0.1400	0.1400	0.1400
175	0.0550	0.0550	0.0550	0.0550	0.0550	0.0550	0.0550	0.0550	0.0550	0.0550
180	0.0250	0.0250	0.0250	0.0250	0.0250	0.0250	0.0250	0.0250	0.0250	0.0250

A5. Subsonic lift coefficients of the airfoil NACA 0018

Source: [4]. Note that some coefficients from [4] were considered typographical errors and were replaced by interpolated coefficients (in red) to obtain smooth curves.

α [°]	Re=1.0E4	Re=2.0E4	Re=4.0E4	Re=8.0E4	Re=1.6E5	Re=3.6E5	Re=7.0E5	Re=1.0E6	Re=2.0E6	Re=5.0E6
0	0.0000	0.0000	0.0000	0.0000	0.0000	0.0000	0.0000	0.0000	0.0000	0.0000
1	-0.0045	0.0607	0.0936	0.0889	0.1100	0.1100	0.1100	0.1100	0.1100	0.1100
2	-0.0154	0.1135	0.1833	0.1935	0.2200	0.2200	0.2200	0.2200	0.2200	0.2200
3	-0.0233	0.1550	0.2688	0.2924	0.3088	0.3300	0.3300	0.3300	0.3300	0.3300
4	-0.0368	0.1788	0.3495	0.3880	0.4114	0.4400	0.4400	0.4400	0.4400	0.4400
5	-0.0577	0.1788	0.4117	0.4753	0.5068	0.5240	0.5500	0.5500	0.5500	0.5500
6	-0.0838	0.1582	0.4573	0.5615	0.5960	0.6228	0.6328	0.6600	0.6600	0.6600
7	-0.1182	0.1161	0.4758	0.6224	0.6724	0.7100	0.7291	0.7362	0.7449	0.7700
8	-0.1501	0.0214	0.4428	0.6589	0.7373	0.7879	0.8156	0.8256	0.8439	0.8538
9	-0.1584	-0.0682	0.3544	0.6606	0.7781	0.8526	0.8904	0.9067	0.9314	0.9525
10	-0.1423	-0.1003	0.2108	0.6248	0.7949	0.8983	0.9541	0.9751	1.0111	1.0404
11	-0.1095	-0.0812	0.1124	0.5328	0.7719	0.9131	0.9893	1.0206	1.0704	1.1144
12	-0.0767	0.0602	0.0139	0.4408	0.7488	0.9279	1.0245	1.0664	1.1296	1.1884
13	-0.0341	0.0202	0.0313	0.3332	0.6863	0.9011	1.0210	1.0729	1.1555	1.2346
14	0.0085	0.0172	0.0489	0.2256	0.6237	0.8803	1.0175	1.0793	1.1813	1.2808
15	0.0568	0.0643	0.0888	0.2142	0.5567	0.8405	0.9912	1.0598	1.1754	1.2938
16	0.1051	0.1114	0.1287	0.2027	0.4896	0.8007	0.9648	1.0402	1.1695	1.3067
17	0.1561	0.1617	0.1754	0.2315	0.4549	0.7663	0.9399	0.9981	1.1539	1.3014
18	0.2070	0.2120	0.2228	0.2603	0.4202	0.7319	0.9150	0.9559	1.1383	1.2960
19	0.2591	0.2636	0.2731	0.3038	0.4292	0.7158	0.9014	0.9633	1.1278	1.2864
20	0.3111	0.3151	0.3236	0.3472	0.4382	0.6997	0.8877	0.9707	1.1172	1.2768
21	0.3642	0.3675	0.3751	0.3951	0.4704	0.7024	0.8872	0.9702	1.1150	1.2741
22	0.4172	0.4198	0.4265	0.4430	0.5026	0.7050	0.8867	0.9696	1.1127	1.2714
23	0.4706	0.4731	0.4790	0.4941	0.5458	0.7275	0.9020	0.9833	1.1241	1.2784
24	0.5241	0.5265	0.5315	0.5452	0.5889	0.7499	0.9173	0.9970	1.1354	1.2855
25	0.5775	0.5798	0.5840	0.5963	0.6321	0.7724	0.9326	1.0107	1.1468	1.2925
26	0.6330	0.6348	0.6382	0.6480	0.6767	0.7889	0.9171	0.9796	1.1088	1.2050
27	0.6885	0.6899	0.6924	0.6998	0.7213	0.8054	0.9016	0.9484	1.0301	1.1175
30	0.8550	0.8550	0.8550	0.8550	0.8550	0.8550	0.8550	0.8550	0.8550	0.8550
35	0.9800	0.9800	0.9800	0.9800	0.9800	0.9800	0.9800	0.9800	0.9800	0.9800
40	1.0350	1.0350	1.0350	1.0350	1.0350	1.0350	1.0350	1.0350	1.0350	1.0350
45	1.0500	1.0500	1.0500	1.0500	1.0500	1.0500	1.0500	1.0500	1.0500	1.0500
50	1.0200	1.0200	1.0200	1.0200	1.0200	1.0200	1.0200	1.0200	1.0200	1.0200
55	0.9550	0.9550	0.9550	0.9550	0.9550	0.9550	0.9550	0.9550	0.9550	0.9550

α [°]	Re=1.0E4	Re=2.0E4	Re=4.0E4	Re=8.0E4	Re=1.6E5	Re=3.6E5	Re=7.0E5	Re=1.0E6	Re=2.0E6	Re=5.0E6
60	0.8750	0.8750	0.8750	0.8750	0.8750	0.8750	0.8750	0.8750	0.8750	0.8750
65	0.7600	0.7600	0.7600	0.7600	0.7600	0.7600	0.7600	0.7600	0.7600	0.7600
70	0.6300	0.6300	0.6300	0.6300	0.6300	0.6300	0.6300	0.6300	0.6300	0.6300
75	0.5000	0.5000	0.5000	0.5000	0.5000	0.5000	0.5000	0.5000	0.5000	0.5000
80	0.3650	0.3650	0.3650	0.3650	0.3650	0.3650	0.3650	0.3650	0.3650	0.3650
85	0.2300	0.2300	0.2300	0.2300	0.2300	0.2300	0.2300	0.2300	0.2300	0.2300
90	0.0900	0.0900	0.0900	0.0900	0.0900	0.0900	0.0900	0.0900	0.0900	0.0900
95	-0.0500	-0.0500	-0.0500	-0.0500	-0.0500	-0.0500	-0.0500	-0.0500	-0.0500	-0.0500
100	-0.1850	-0.1850	-0.1850	-0.1850	-0.1850	-0.1850	-0.1850	-0.1850	-0.1850	-0.1850
105	-0.3200	-0.3200	-0.3200	-0.3200	-0.3200	-0.3200	-0.3200	-0.3200	-0.3200	-0.3200
110	-0.4500	-0.4500	-0.4500	-0.4500	-0.4500	-0.4500	-0.4500	-0.4500	-0.4500	-0.4500
115	-0.5750	-0.5750	-0.5750	-0.5750	-0.5750	-0.5750	-0.5750	-0.5750	-0.5750	-0.5750
120	-0.6700	-0.6700	-0.6700	-0.6700	-0.6700	-0.6700	-0.6700	-0.6700	-0.6700	-0.6700
125	-0.7600	-0.7600	-0.7600	-0.7600	-0.7600	-0.7600	-0.7600	-0.7600	-0.7600	-0.7600
130	-0.8500	-0.8500	-0.8500	-0.8500	-0.8500	-0.8500	-0.8500	-0.8500	-0.8500	-0.8500
135	-0.9300	-0.9300	-0.9300	-0.9300	-0.9300	-0.9300	-0.9300	-0.9300	-0.9300	-0.9300
140	-0.9800	-0.9800	-0.9800	-0.9800	-0.9800	-0.9800	-0.9800	-0.9800	-0.9800	-0.9800
145	-0.9000	-0.9000	-0.9000	-0.9000	-0.9000	-0.9000	-0.9000	-0.9000	-0.9000	-0.9000
150	-0.7700	-0.7700	-0.7700	-0.7700	-0.7700	-0.7700	-0.7700	-0.7700	-0.7700	-0.7700
155	-0.6700	-0.6700	-0.6700	-0.6700	-0.6700	-0.6700	-0.6700	-0.6700	-0.6700	-0.6700
160	-0.6350	-0.6350	-0.6350	-0.6350	-0.6350	-0.6350	-0.6350	-0.6350	-0.6350	-0.6350
165	-0.6800	-0.6800	-0.6800	-0.6800	-0.6800	-0.6800	-0.6800	-0.6800	-0.6800	-0.6800
170	-0.8500	-0.8500	-0.8500	-0.8500	-0.8500	-0.8500	-0.8500	-0.8500	-0.8500	-0.8500
175	-0.6600	-0.6600	-0.6600	-0.6600	-0.6600	-0.6600	-0.6600	-0.6600	-0.6600	-0.6600
180	0.0000	0.0000	0.0000	0.0000	0.0000	0.0000	0.0000	0.0000	0.0000	0.0000

A6. Subsonic drag coefficients of the airfoil NACA 0018

Source: [4]. Note that some coefficients from [4] were considered typographical errors and were replaced by interpolated coefficients (in red) to obtain smooth curves.

α [°]	Re=1.0E4	Re=2.0E4	Re=4.0E4	Re=8.0E4	Re=1.6E5	Re=3.6E5	Re=7.0E5	Re=1.0E6	Re=2.0E6	Re=5.0E6
0	0.0385	0.0286	0.0214	0.0162	0.0110	0.0101	0.0085	0.0082	0.0077	0.0073
1	0.0387	0.0288	0.0215	0.0163	0.0129	0.0102	0.0087	0.0082	0.0077	0.0073
2	0.0391	0.0292	0.0219	0.0167	0.0131	0.0104	0.0088	0.0083	0.0078	0.0075
3	0.0399	0.0299	0.0225	0.0172	0.0137	0.0107	0.0091	0.0086	0.0080	0.0077
4	0.0410	0.0310	0.0235	0.0181	0.0144	0.0112	0.0096	0.0089	0.0084	0.0079
5	0.0425	0.0323	0.0247	0.0192	0.0153	0.0121	0.0102	0.0095	0.0087	0.0083
6	0.0443	0.0339	0.0263	0.0206	0.0166	0.0132	0.0112	0.0102	0.0093	0.0087
7	0.0463	0.0358	0.0285	0.0223	0.0181	0.0145	0.0123	0.0115	0.0101	0.0093
8	0.0489	0.0376	0.0303	0.0242	0.0198	0.0159	0.0136	0.0126	0.0111	0.0100
9	0.0525	0.0396	0.0327	0.0264	0.0217	0.0176	0.0150	0.0139	0.0122	0.0108
10	0.0574	0.0630	0.0620	0.0288	0.0238	0.0194	0.0166	0.0154	0.0134	0.0117
11	0.0902	0.0930	0.0915	0.0544	0.0263	0.0215	0.0184	0.0171	0.0149	0.0129
12	0.1230	0.1230	0.1230	0.0800	0.0288	0.0235	0.0202	0.0187	0.0163	0.0140
13	0.1405	0.1405	0.1395	0.1190	0.0934	0.0588	0.0224	0.0207	0.0180	0.0150
14	0.1580	0.1580	0.1580	0.1580	0.1580	0.0940	0.0245	0.0227	0.0197	0.0168
15	0.1770	0.1770	0.1770	0.1770	0.1770	0.1450	0.1103	0.0654	0.0219	0.0182
16	0.1960	0.1960	0.1960	0.1960	0.1960	0.1960	0.1960	0.1080	0.0240	0.0203
17	0.2170	0.2170	0.2170	0.2170	0.2170	0.2170	0.2170	0.1730	0.1310	0.0224
18	0.2380	0.2380	0.2380	0.2380	0.2380	0.2380	0.2380	0.2380	0.2380	0.0244
19	0.2600	0.2600	0.2600	0.2600	0.2600	0.2600	0.2600	0.2600	0.2600	0.1532
20	0.2820	0.2820	0.2820	0.2820	0.2820	0.2820	0.2820	0.2820	0.2820	0.2820
21	0.3055	0.3055	0.3055	0.3055	0.3055	0.3055	0.3055	0.3055	0.3055	0.3055
22	0.3290	0.3290	0.3290	0.3290	0.3290	0.3290	0.3290	0.3290	0.3290	0.3290
23	0.3543	0.3543	0.3543	0.3543	0.3543	0.3543	0.3543	0.3543	0.3543	0.3543
24	0.3797	0.3797	0.3797	0.3797	0.3797	0.3797	0.3797	0.3797	0.3797	0.3797
25	0.4050	0.4050	0.4050	0.4050	0.4050	0.4050	0.4050	0.4050	0.4050	0.4050
26	0.4380	0.4380	0.4380	0.4380	0.4380	0.4380	0.4380	0.4380	0.4380	0.4380
27	0.4710	0.4710	0.4710	0.4710	0.4710	0.4710	0.4710	0.4710	0.4710	0.4710
30	0.5700	0.5700	0.5700	0.5700	0.5700	0.5700	0.5700	0.5700	0.5700	0.5700
35	0.7450	0.7450	0.7450	0.7450	0.7450	0.7450	0.7450	0.7450	0.7450	0.7450
40	0.9200	0.9200	0.9200	0.9200	0.9200	0.9200	0.9200	0.9200	0.9200	0.9200
45	1.0750	1.0750	1.0750	1.0750	1.0750	1.0750	1.0750	1.0750	1.0750	1.0750
50	1.2150	1.2150	1.2150	1.2150	1.2150	1.2150	1.2150	1.2150	1.2150	1.2150
55	1.3450	1.3450	1.3450	1.3450	1.3450	1.3450	1.3450	1.3450	1.3450	1.3450

α [°]	Re=1.0E4	Re=2.0E4	Re=4.0E4	Re=8.0E4	Re=1.6E5	Re=3.6E5	Re=7.0E5	Re=1.0E6	Re=2.0E6	Re=5.0E6
60	1.4700	1.4700	1.4700	1.4700	1.4700	1.4700	1.4700	1.4700	1.4700	1.4700
65	1.5750	1.5750	1.5750	1.5750	1.5750	1.5750	1.5750	1.5750	1.5750	1.5750
70	1.6650	1.6650	1.6650	1.6650	1.6650	1.6650	1.6650	1.6650	1.6650	1.6650
75	1.7350	1.7350	1.7350	1.7350	1.7350	1.7350	1.7350	1.7350	1.7350	1.7350
80	1.7800	1.7800	1.7800	1.7800	1.7800	1.7800	1.7800	1.7800	1.7800	1.7800
85	1.8000	1.8000	1.8000	1.8000	1.8000	1.8000	1.8000	1.8000	1.8000	1.8000
90	1.8000	1.8000	1.8000	1.8000	1.8000	1.8000	1.8000	1.8000	1.8000	1.8000
95	1.7800	1.7800	1.7800	1.7800	1.7800	1.7800	1.7800	1.7800	1.7800	1.7800
100	1.7500	1.7500	1.7500	1.7500	1.7500	1.7500	1.7500	1.7500	1.7500	1.7500
105	1.7000	1.7000	1.7000	1.7000	1.7000	1.7000	1.7000	1.7000	1.7000	1.7000
110	1.6350	1.6350	1.6350	1.6350	1.6350	1.6350	1.6350	1.6350	1.6350	1.6350
115	1.5550	1.5550	1.5550	1.5550	1.5550	1.5550	1.5550	1.5550	1.5550	1.5550
120	1.4650	1.4650	1.4650	1.4650	1.4650	1.4650	1.4650	1.4650	1.4650	1.4650
125	1.3500	1.3500	1.3500	1.3500	1.3500	1.3500	1.3500	1.3500	1.3500	1.3500
130	1.2250	1.2250	1.2250	1.2250	1.2250	1.2250	1.2250	1.2250	1.2250	1.2250
135	1.0850	1.0850	1.0850	1.0850	1.0850	1.0850	1.0850	1.0850	1.0850	1.0850
140	0.9250	0.9250	0.9250	0.9250	0.9250	0.9250	0.9250	0.9250	0.9250	0.9250
145	0.7550	0.7550	0.7550	0.7550	0.7550	0.7550	0.7550	0.7550	0.7550	0.7550
150	0.5750	0.5750	0.5750	0.5750	0.5750	0.5750	0.5750	0.5750	0.5750	0.5750
155	0.4200	0.4200	0.4200	0.4200	0.4200	0.4200	0.4200	0.4200	0.4200	0.4200
160	0.3200	0.3200	0.3200	0.3200	0.3200	0.3200	0.3200	0.3200	0.3200	0.3200
165	0.2300	0.2300	0.2300	0.2300	0.2300	0.2300	0.2300	0.2300	0.2300	0.2300
170	0.1400	0.1400	0.1400	0.1400	0.1400	0.1400	0.1400	0.1400	0.1400	0.1400
175	0.0550	0.0550	0.0550	0.0550	0.0550	0.0550	0.0550	0.0550	0.0550	0.0550
180	0.0250	0.0250	0.0250	0.0250	0.0250	0.0250	0.0250	0.0250	0.0250	0.0250

A7. Subsonic lift coefficients of the airfoil NACA 0021

Source: [122]. Note that some coefficients from [122] were considered typographical errors and were replaced by interpolated coefficients (in red) to obtain smooth curves.

α [°]	Re=1.0E4	Re=2.0E4	Re=4.0E4	Re=8.0E4	Re=1.6E5	Re=3.6E5	Re=7.0E5	Re=1.0E6	Re=2.0E6	Re=5.0E6
0	0.0000	0.0000	0.0000	0.0000	0.0000	0.0000	0.0000	0.0000	0.0000	0.0000
1	-0.0320	0.0243	0.0752	0.0921	0.0842	0.1100	0.1100	0.1100	0.1100	0.1100
2	-0.0631	0.0393	0.1465	0.1839	0.1879	0.2200	0.2200	0.2200	0.2200	0.2200
3	-0.0854	0.0472	0.2103	0.2731	0.2861	0.3024	0.3300	0.3300	0.3300	0.3300
4	-0.0995	0.0619	0.2730	0.3564	0.3800	0.4044	0.4128	0.4400	0.4400	0.4400
5	-0.1156	0.0505	0.3086	0.4324	0.4687	0.4998	0.5146	0.5192	0.5500	0.5500
6	-0.1240	0.0475	0.3382	0.4953	0.5486	0.5891	0.6100	0.6191	0.6268	0.6600
7	-0.1400	0.0266	0.3427	0.5445	0.6209	0.6728	0.6988	0.7102	0.7254	0.7354
8	-0.1475	0.0120	0.3420	0.5751	0.6745	0.7434	0.7802	0.7939	0.8143	0.8334
9	-0.1581	-0.0190	0.3162	0.5874	0.7148	0.8026	0.8498	0.8694	0.8986	0.9222
10	-0.1581	-0.0506	0.2691	0.5780	0.7374	0.8500	0.9091	0.9364	0.9739	1.0049
11	-0.1429	-0.0610	0.2176	0.5564	0.7443	0.8779	0.9543	0.9862	1.0398	1.0787
12	-0.1276	-0.0713	0.1660	0.5228	0.7363	0.8938	0.9843	1.0257	1.0906	1.1453
13	-0.0967	-0.0538	0.1247	0.4762	0.7255	0.8973	1.0020	1.0492	1.1305	1.1979
14	-0.0658	-0.0362	0.0833	0.4296	0.6993	0.8937	1.0122	1.0657	1.1580	1.2410
15	-0.0268	-0.0016	0.0907	0.3898	0.6740	0.8840	1.0106	1.0709	1.1747	1.2680
16	0.0123	0.0331	0.0981	0.3499	0.6487	0.8717	1.0056	1.0690	1.1823	1.2860
17	0.0579	0.0756	0.1300	0.3360	0.6293	0.8603	0.9973	1.0641	1.1824	1.2977
18	0.1035	0.1180	0.1619	0.3221	0.6098	0.8489	0.9911	1.0588	1.1814	1.3031
19	0.1521	0.1652	0.2017	0.3348	0.6009	0.8443	0.9885	1.0571	1.1797	1.3066
20	0.2006	0.2124	0.2414	0.3475	0.5920	0.8397	0.9858	1.0554	1.1812	1.3054
21	0.2504	0.2614	0.2880	0.3783	0.5972	0.8425	0.9899	1.0599	1.1853	1.3092
22	0.3002	0.3103	0.3345	0.4091	0.6023	0.8453	0.9940	1.0644	1.1893	1.3130
25	0.4539	0.4618	0.4802	0.5297	0.6664	0.8866	1.0350	1.1018	1.2230	1.3476
30	0.8550	0.8550	0.8550	0.8550	0.8550	0.8550	0.8550	0.8550	0.8550	0.8550
35	0.9800	0.9800	0.9800	0.9800	0.9800	0.9800	0.9800	0.9800	0.9800	0.9800
40	1.0350	1.0350	1.0350	1.0350	1.0350	1.0350	1.0350	1.0350	1.0350	1.0350
45	1.0500	1.0500	1.0500	1.0500	1.0500	1.0500	1.0500	1.0500	1.0500	1.0500
50	1.0200	1.0200	1.0200	1.0200	1.0200	1.0200	1.0200	1.0200	1.0200	1.0200
55	0.9550	0.9550	0.9550	0.9550	0.9550	0.9550	0.9550	0.9550	0.9550	0.9550
60	0.8750	0.8750	0.8750	0.8750	0.8750	0.8750	0.8750	0.8750	0.8750	0.8750
65	0.7600	0.7600	0.7600	0.7600	0.7600	0.7600	0.7600	0.7600	0.7600	0.7600
70	0.6300	0.6300	0.6300	0.6300	0.6300	0.6300	0.6300	0.6300	0.6300	0.6300
75	0.5000	0.5000	0.5000	0.5000	0.5000	0.5000	0.5000	0.5000	0.5000	0.5000

$\alpha [^\circ]$	Re=1.0E4	Re=2.0E4	Re=4.0E4	Re=8.0E4	Re=1.6E5	Re=3.6E5	Re=7.0E5	Re=1.0E6	Re=2.0E6	Re=5.0E6
80	0.3650	0.3650	0.3650	0.3650	0.3650	0.3650	0.3650	0.3650	0.3650	0.3650
85	0.2300	0.2300	0.2300	0.2300	0.2300	0.2300	0.2300	0.2300	0.2300	0.2300
90	0.0900	0.0900	0.0900	0.0900	0.0900	0.0900	0.0900	0.0900	0.0900	0.0900
95	-0.0500	-0.0500	-0.0500	-0.0500	-0.0500	-0.0500	-0.0500	-0.0500	-0.0500	-0.0500
100	-0.1850	-0.1850	-0.1850	-0.1850	-0.1850	-0.1850	-0.1850	-0.1850	-0.1850	-0.1850
105	-0.3200	-0.3200	-0.3200	-0.3200	-0.3200	-0.3200	-0.3200	-0.3200	-0.3200	-0.3200
110	-0.4500	-0.4500	-0.4500	-0.4500	-0.4500	-0.4500	-0.4500	-0.4500	-0.4500	-0.4500
115	-0.5750	-0.5750	-0.5750	-0.5750	-0.5750	-0.5750	-0.5750	-0.5750	-0.5750	-0.5750
120	-0.6700	-0.6700	-0.6700	-0.6700	-0.6700	-0.6700	-0.6700	-0.6700	-0.6700	-0.6700
125	-0.7600	-0.7600	-0.7600	-0.7600	-0.7600	-0.7600	-0.7600	-0.7600	-0.7600	-0.7600
130	-0.8500	-0.8500	-0.8500	-0.8500	-0.8500	-0.8500	-0.8500	-0.8500	-0.8500	-0.8500
135	-0.9300	-0.9300	-0.9300	-0.9300	-0.9300	-0.9300	-0.9300	-0.9300	-0.9300	-0.9300
140	-0.9800	-0.9800	-0.9800	-0.9800	-0.9800	-0.9800	-0.9800	-0.9800	-0.9800	-0.9800
145	-0.9000	-0.9000	-0.9000	-0.9000	-0.9000	-0.9000	-0.9000	-0.9000	-0.9000	-0.9000
150	-0.7700	-0.7700	-0.7700	-0.7700	-0.7700	-0.7700	-0.7700	-0.7700	-0.7700	-0.7700
155	-0.6700	-0.6700	-0.6700	-0.6700	-0.6700	-0.6700	-0.6700	-0.6700	-0.6700	-0.6700
160	-0.6350	-0.6350	-0.6350	-0.6350	-0.6350	-0.6350	-0.6350	-0.6350	-0.6350	-0.6350
165	-0.6800	-0.6800	-0.6800	-0.6800	-0.6800	-0.6800	-0.6800	-0.6800	-0.6800	-0.6800
170	-0.8500	-0.8500	-0.8500	-0.8500	-0.8500	-0.8500	-0.8500	-0.8500	-0.8500	-0.8500
175	-0.6600	-0.6600	-0.6600	-0.6600	-0.6600	-0.6600	-0.6600	-0.6600	-0.6600	-0.6600
180	0.0000	0.0000	0.0000	0.0000	0.0000	0.0000	0.0000	0.0000	0.0000	0.0000

A8. Subsonic drag coefficients of the airfoil NACA 0021

Source: [122]. Note that some coefficients from [122] were considered typographical errors and were replaced by interpolated coefficients (in red) to obtain smooth curves.

α [°]	Re=1.0E4	Re=2.0E4	Re=4.0E4	Re=8.0E4	Re=1.6E5	Re=3.6E5	Re=7.0E5	Re=1.0E6	Re=2.0E6	Re=5.0E6
0	0.0413	0.0309	0.0232	0.0177	0.0139	0.0111	0.0094	0.0089	0.0082	0.0078
1	0.0414	0.0310	0.0233	0.0178	0.0140	0.0111	0.0094	0.0089	0.0083	0.0078
2	0.0420	0.0314	0.0237	0.0181	0.0143	0.0113	0.0096	0.0090	0.0084	0.0079
3	0.0429	0.0321	0.0243	0.0186	0.0148	0.0117	0.0098	0.0092	0.0086	0.0081
4	0.0441	0.0332	0.0253	0.0194	0.0155	0.0122	0.0103	0.0096	0.0089	0.0083
5	0.0459	0.0345	0.0264	0.0204	0.0163	0.0129	0.0109	0.0101	0.0092	0.0086
6	0.0480	0.0362	0.0279	0.0217	0.0174	0.0138	0.0117	0.0108	0.0098	0.0091
7	0.0507	0.0382	0.0297	0.0233	0.0187	0.0149	0.0126	0.0117	0.0105	0.0097
8	0.0538	0.0407	0.0319	0.0252	0.0204	0.0163	0.0138	0.0128	0.0114	0.0104
9	0.0575	0.0435	0.0343	0.0273	0.0222	0.0178	0.0152	0.0140	0.0124	0.0112
10	0.0750	0.0362	0.0620	0.0297	0.0243	0.0195	0.0166	0.0154	0.0135	0.0121
11	0.0990	0.0796	0.0925	0.0700	0.0266	0.0215	0.0184	0.0170	0.0148	0.0132
12	0.1230	0.1230	0.1230	0.1230	0.0292	0.0237	0.0202	0.0187	0.0162	0.0143
13	0.1405	0.1405	0.1405	0.1405	0.0860	0.0260	0.0223	0.0206	0.0179	0.0156
14	0.1580	0.1580	0.1580	0.1580	0.1580	0.0286	0.0244	0.0226	0.0196	0.0170
15	0.1770	0.1770	0.1770	0.1770	0.1770	0.1040	0.0269	0.0248	0.0215	0.0186
16	0.1960	0.1960	0.1960	0.1960	0.1960	0.1960	0.0295	0.0273	0.0236	0.0205
17	0.2170	0.2170	0.2170	0.2170	0.2170	0.2170	0.1250	0.0300	0.0260	0.0224
18	0.2380	0.2380	0.2380	0.2380	0.2380	0.2380	0.2380	0.1350	0.0285	0.0245
19	0.2600	0.2600	0.2600	0.2600	0.2600	0.2600	0.2600	0.2085	0.1450	0.0268
20	0.2820	0.2820	0.2820	0.2820	0.2820	0.2820	0.2820	0.2820	0.2820	0.0293
21	0.3055	0.3055	0.3055	0.3055	0.3055	0.3055	0.3055	0.3055	0.3055	0.1792
22	0.3290	0.3290	0.3290	0.3290	0.3290	0.3290	0.3290	0.3290	0.3290	0.3290
25	0.4050	0.4050	0.4050	0.4050	0.4050	0.4050	0.4050	0.4050	0.4050	0.4050
30	0.5700	0.5700	0.5700	0.5700	0.5700	0.5700	0.5700	0.5700	0.5700	0.5700
35	0.7450	0.7450	0.7450	0.7450	0.7450	0.7450	0.7450	0.7450	0.7450	0.7450
40	0.9200	0.9200	0.9200	0.9200	0.9200	0.9200	0.9200	0.9200	0.9200	0.9200
45	1.0750	1.0750	1.0750	1.0750	1.0750	1.0750	1.0750	1.0750	1.0750	1.0750
50	1.2150	1.2150	1.2150	1.2150	1.2150	1.2150	1.2150	1.2150	1.2150	1.2150
55	1.3450	1.3450	1.3450	1.3450	1.3450	1.3450	1.3450	1.3450	1.3450	1.3450
60	1.4700	1.4700	1.4700	1.4700	1.4700	1.4700	1.4700	1.4700	1.4700	1.4700
65	1.5750	1.5750	1.5750	1.5750	1.5750	1.5750	1.5750	1.5750	1.5750	1.5750
70	1.6650	1.6650	1.6650	1.6650	1.6650	1.6650	1.6650	1.6650	1.6650	1.6650
75	1.7350	1.7350	1.7350	1.7350	1.7350	1.7350	1.7350	1.7350	1.7350	1.7350

α [°]	Re=1.0E4	Re=2.0E4	Re=4.0E4	Re=8.0E4	Re=1.6E5	Re=3.6E5	Re=7.0E5	Re=1.0E6	Re=2.0E6	Re=5.0E6
80	1.7800	1.7800	1.7800	1.7800	1.7800	1.7800	1.7800	1.7800	1.7800	1.7800
85	1.8000	1.8000	1.8000	1.8000	1.8000	1.8000	1.8000	1.8000	1.8000	1.8000
90	1.8000	1.8000	1.8000	1.8000	1.8000	1.8000	1.8000	1.8000	1.8000	1.8000
95	1.7800	1.7800	1.7800	1.7800	1.7800	1.7800	1.7800	1.7800	1.7800	1.7800
100	1.7500	1.7500	1.7500	1.7500	1.7500	1.7500	1.7500	1.7500	1.7500	1.7500
105	1.7000	1.7000	1.7000	1.7000	1.7000	1.7000	1.7000	1.7000	1.7000	1.7000
110	1.6350	1.6350	1.6350	1.6350	1.6350	1.6350	1.6350	1.6350	1.6350	1.6350
115	1.5550	1.5550	1.5550	1.5550	1.5550	1.5550	1.5550	1.5550	1.5550	1.5550
120	1.4650	1.4650	1.4650	1.4650	1.4650	1.4650	1.4650	1.4650	1.4650	1.4650
125	1.3500	1.3500	1.3500	1.3500	1.3500	1.3500	1.3500	1.3500	1.3500	1.3500
130	1.2250	1.2250	1.2250	1.2250	1.2250	1.2250	1.2250	1.2250	1.2250	1.2250
135	1.0850	1.0850	1.0850	1.0850	1.0850	1.0850	1.0850	1.0850	1.0850	1.0850
140	0.9250	0.9250	0.9250	0.9250	0.9250	0.9250	0.9250	0.9250	0.9250	0.9250
145	0.7550	0.7550	0.7550	0.7550	0.7550	0.7550	0.7550	0.7550	0.7550	0.7550
150	0.5750	0.5750	0.5750	0.5750	0.5750	0.5750	0.5750	0.5750	0.5750	0.5750
155	0.4200	0.4200	0.4200	0.4200	0.4200	0.4200	0.4200	0.4200	0.4200	0.4200
160	0.3200	0.3200	0.3200	0.3200	0.3200	0.3200	0.3200	0.3200	0.3200	0.3200
165	0.2300	0.2300	0.2300	0.2300	0.2300	0.2300	0.2300	0.2300	0.2300	0.2300
170	0.1400	0.1400	0.1400	0.1400	0.1400	0.1400	0.1400	0.1400	0.1400	0.1400
175	0.0550	0.0550	0.0550	0.0550	0.0550	0.0550	0.0550	0.0550	0.0550	0.0550
180	0.0250	0.0250	0.0250	0.0250	0.0250	0.0250	0.0250	0.0250	0.0250	0.0250

A9. Subsonic lift coefficients of the airfoil NACA 0025

Source: [122]. Note that some coefficients from [122] were considered typographical errors and were replaced by interpolated coefficients (in red) to obtain smooth curves.

α [°]	Re=1.0E4	Re=2.0E4	Re=4.0E4	Re=8.0E4	Re=1.6E5	Re=3.6E5	Re=7.0E5	Re=1.0E6	Re=2.0E6	Re=5.0E6
0	0.0000	0.0000	0.0000	0.0000	0.0000	0.0000	0.0000	0.0000	0.0000	0.0000
1	-0.0434	-0.0223	0.0411	0.0743	0.0875	0.0982	0.0817	0.1100	0.1100	0.1100
2	-0.0807	-0.0376	0.0821	0.1487	0.1745	0.1721	0.1851	0.1890	0.2200	0.2200
3	-0.1151	-0.0509	0.1167	0.2198	0.2613	0.2682	0.2861	0.2917	0.2978	0.3300
4	-0.1403	-0.0550	0.1479	0.2832	0.3400	0.3608	0.3811	0.3900	0.4000	0.4078
5	-0.1585	-0.0589	0.1693	0.3413	0.4170	0.4495	0.4743	0.4844	0.4977	0.5097
6	-0.1723	-0.0650	0.1778	0.3866	0.4831	0.5295	0.5627	0.5757	0.5913	0.6076
7	-0.1799	-0.0690	0.1856	0.4215	0.5263	0.6062	0.6444	0.6622	0.6810	0.6997
8	-0.1797	-0.0683	0.1929	0.4503	0.5916	0.6701	0.7194	0.7387	0.7664	0.7886
9	-0.1776	-0.0635	0.1942	0.4656	0.6271	0.7256	0.7852	0.8117	0.8415	0.8730
10	-0.1747	-0.0635	0.1915	0.4749	0.6539	0.7713	0.8405	0.8710	0.9135	0.9472
11	-0.1647	-0.0607	0.1889	0.4797	0.6720	0.8039	0.8873	0.9228	0.9723	1.0177
12	-0.1512	-0.0572	0.1813	0.4783	0.6811	0.8295	0.9230	0.9656	1.0245	1.0750
13	-0.1323	-0.0475	0.1783	0.4754	0.6866	0.8471	0.9491	0.9960	1.0672	1.1270
14	-0.1134	-0.0377	0.1753	0.4713	0.6886	0.8565	0.9685	1.0192	1.0989	1.1717
15	-0.0869	-0.0202	0.1711	0.4651	0.6906	0.8656	0.9820	1.0382	1.1258	1.2065
16	-0.0604	-0.0027	0.1669	0.4588	0.6921	0.8742	0.9944	1.0522	1.1488	1.2358
17	-0.0261	0.0243	0.1747	0.4555	0.6935	0.8821	1.0052	1.0654	1.1654	1.2617
18	0.0082	0.0512	0.1824	0.4522	0.6945	0.8890	1.0157	1.0774	1.1806	1.2790
19	0.0483	0.0863	0.2004	0.4535	0.7006	0.8992	1.0276	1.0896	1.1953	1.2952
20	0.0883	0.1213	0.2183	0.4547	0.7069	0.9114	1.0403	1.1031	1.2094	1.3121
21	0.1334	0.1642	0.2513	0.4687	0.7164	0.9216	1.0521	1.1151	1.2220	1.3257
22	0.1785	0.2071	0.2843	0.4826	0.7289	0.9381	1.0678	1.1294	1.2350	1.3378
25	0.3205	0.3435	0.4026	0.5574	0.7840	0.8866	1.1223	1.1856	1.2890	1.3960
30	0.8550	0.8550	0.8550	0.8550	0.8550	0.8550	0.8550	0.8550	0.8550	0.8550
35	0.9800	0.9800	0.9800	0.9800	0.9800	0.9800	0.9800	0.9800	0.9800	0.9800
40	1.0350	1.0350	1.0350	1.0350	1.0350	1.0350	1.0350	1.0350	1.0350	1.0350
45	1.0500	1.0500	1.0500	1.0500	1.0500	1.0500	1.0500	1.0500	1.0500	1.0500
50	1.0200	1.0200	1.0200	1.0200	1.0200	1.0200	1.0200	1.0200	1.0200	1.0200
55	0.9550	0.9550	0.9550	0.9550	0.9550	0.9550	0.9550	0.9550	0.9550	0.9550
60	0.8750	0.8750	0.8750	0.8750	0.8750	0.8750	0.8750	0.8750	0.8750	0.8750
65	0.7600	0.7600	0.7600	0.7600	0.7600	0.7600	0.7600	0.7600	0.7600	0.7600
70	0.6300	0.6300	0.6300	0.6300	0.6300	0.6300	0.6300	0.6300	0.6300	0.6300
75	0.5000	0.5000	0.5000	0.5000	0.5000	0.5000	0.5000	0.5000	0.5000	0.5000

α [°]	Re=1.0E4	Re=2.0E4	Re=4.0E4	Re=8.0E4	Re=1.6E5	Re=3.6E5	Re=7.0E5	Re=1.0E6	Re=2.0E6	Re=5.0E6
80	0.3650	0.3650	0.3650	0.3650	0.3650	0.3650	0.3650	0.3650	0.3650	0.3650
85	0.2300	0.2300	0.2300	0.2300	0.2300	0.2300	0.2300	0.2300	0.2300	0.2300
90	0.0900	0.0900	0.0900	0.0900	0.0900	0.0900	0.0900	0.0900	0.0900	0.0900
95	-0.0500	-0.0500	-0.0500	-0.0500	-0.0500	-0.0500	-0.0500	-0.0500	-0.0500	-0.0500
100	-0.1850	-0.1850	-0.1850	-0.1850	-0.1850	-0.1850	-0.1850	-0.1850	-0.1850	-0.1850
105	-0.3200	-0.3200	-0.3200	-0.3200	-0.3200	-0.3200	-0.3200	-0.3200	-0.3200	-0.3200
110	-0.4500	-0.4500	-0.4500	-0.4500	-0.4500	-0.4500	-0.4500	-0.4500	-0.4500	-0.4500
115	-0.5750	-0.5750	-0.5750	-0.5750	-0.5750	-0.5750	-0.5750	-0.5750	-0.5750	-0.5750
120	-0.6700	-0.6700	-0.6700	-0.6700	-0.6700	-0.6700	-0.6700	-0.6700	-0.6700	-0.6700
125	-0.7600	-0.7600	-0.7600	-0.7600	-0.7600	-0.7600	-0.7600	-0.7600	-0.7600	-0.7600
130	-0.8500	-0.8500	-0.8500	-0.8500	-0.8500	-0.8500	-0.8500	-0.8500	-0.8500	-0.8500
135	-0.9300	-0.9300	-0.9300	-0.9300	-0.9300	-0.9300	-0.9300	-0.9300	-0.9300	-0.9300
140	-0.9800	-0.9800	-0.9800	-0.9800	-0.9800	-0.9800	-0.9800	-0.9800	-0.9800	-0.9800
145	-0.9000	-0.9000	-0.9000	-0.9000	-0.9000	-0.9000	-0.9000	-0.9000	-0.9000	-0.9000
150	-0.7700	-0.7700	-0.7700	-0.7700	-0.7700	-0.7700	-0.7700	-0.7700	-0.7700	-0.7700
155	-0.6700	-0.6700	-0.6700	-0.6700	-0.6700	-0.6700	-0.6700	-0.6700	-0.6700	-0.6700
160	-0.6350	-0.6350	-0.6350	-0.6350	-0.6350	-0.6350	-0.6350	-0.6350	-0.6350	-0.6350
165	-0.6800	-0.6800	-0.6800	-0.6800	-0.6800	-0.6800	-0.6800	-0.6800	-0.6800	-0.6800
170	-0.8500	-0.8500	-0.8500	-0.8500	-0.8500	-0.8500	-0.8500	-0.8500	-0.8500	-0.8500
175	-0.6600	-0.6600	-0.6600	-0.6600	-0.6600	-0.6600	-0.6600	-0.6600	-0.6600	-0.6600
180	0.0000	0.0000	0.0000	0.0000	0.0000	0.0000	0.0000	0.0000	0.0000	0.0000

A10. Subsonic drag coefficients of the airfoil NACA 0025

Source: [122]. Note that some coefficients from [122] were considered typographical errors and were replaced by interpolated coefficients (in red) to obtain smooth curves.

α [°]	Re=1.0E4	Re=2.0E4	Re=4.0E4	Re=8.0E4	Re=1.6E5	Re=3.6E5	Re=7.0E5	Re=1.0E6	Re=2.0E6	Re=5.0E6
0	0.0455	0.0341	0.0258	0.0197	0.0155	0.0121	0.0104	0.0097	0.0090	0.0084
1	0.0457	0.0342	0.0259	0.0198	0.0156	0.0122	0.0104	0.0098	0.0090	0.0084
2	0.0463	0.0346	0.0263	0.0201	0.0158	0.0125	0.0105	0.0098	0.0091	0.0085
3	0.0474	0.0354	0.0269	0.0207	0.0163	0.0129	0.0109	0.0101	0.0093	0.0087
4	0.0488	0.0365	0.0278	0.0214	0.0169	0.0135	0.0113	0.0105	0.0096	0.0089
5	0.0508	0.0379	0.0290	0.0214	0.0177	0.0141	0.0119	0.0110	0.0100	0.0092
6	0.0532	0.0397	0.0304	0.0224	0.0187	0.0149	0.0126	0.0116	0.0106	0.0097
7	0.0562	0.0419	0.0322	0.0236	0.0201	0.0159	0.0134	0.0124	0.0112	0.0103
8	0.0597	0.0445	0.0343	0.0250	0.0213	0.0170	0.0144	0.0133	0.0120	0.0110
9	0.0638	0.0476	0.0367	0.0268	0.0230	0.0185	0.0156	0.0144	0.0129	0.0117
10	0.0686	0.0511	0.0396	0.0288	0.0250	0.0200	0.0170	0.0157	0.0140	0.0126
11	0.0820	0.0810	0.0428	0.0311	0.0272	0.0219	0.0185	0.0171	0.0151	0.0137
12	0.1230	0.1230	0.0850	0.0338	0.0296	0.0239	0.0202	0.0187	0.0165	0.0148
13	0.1405	0.1405	0.1215	0.0401	0.0324	0.0261	0.0222	0.0205	0.0165	0.0161
14	0.1580	0.1580	0.1580	0.1010	0.0355	0.0286	0.0244	0.0225	0.0197	0.0175
15	0.1770	0.1770	0.1770	0.1485	0.0389	0.0314	0.0267	0.0246	0.0215	0.0190
16	0.1960	0.1960	0.1960	0.1960	0.0426	0.0343	0.0293	0.0269	0.0235	0.0207
17	0.2170	0.2170	0.2170	0.2170	0.0466	0.0375	0.0319	0.0294	0.0257	0.0225
18	0.2380	0.2380	0.2380	0.2380	0.0510	0.0411	0.0349	0.0322	0.0280	0.0245
19	0.2600	0.2600	0.2600	0.2600	0.0558	0.0448	0.0381	0.0351	0.0305	0.0267
20	0.2820	0.2820	0.2820	0.2820	0.0610	0.0489	0.0415	0.0382	0.0332	0.0290
21	0.3055	0.3055	0.3055	0.3055	0.0668	0.0534	0.0453	0.0417	0.0362	0.0316
22	0.3290	0.3290	0.3290	0.3290	0.0730	0.0582	0.0493	0.0454	0.0394	0.0344
25	0.4050	0.4050	0.4050	0.4050	0.0947	0.0750	0.0632	0.0581	0.0428	0.0436
30	0.5700	0.5700	0.5700	0.5700	0.5700	0.5700	0.5700	0.5700	0.5700	0.5700
35	0.7450	0.7450	0.7450	0.7450	0.7450	0.7450	0.7450	0.7450	0.7450	0.7450
40	0.9200	0.9200	0.9200	0.9200	0.9200	0.9200	0.9200	0.9200	0.9200	0.9200
45	1.0750	1.0750	1.0750	1.0750	1.0750	1.0750	1.0750	1.0750	1.0750	1.0750
50	1.2150	1.2150	1.2150	1.2150	1.2150	1.2150	1.2150	1.2150	1.2150	1.2150
55	1.3450	1.3450	1.3450	1.3450	1.3450	1.3450	1.3450	1.3450	1.3450	1.3450
60	1.4700	1.4700	1.4700	1.4700	1.4700	1.4700	1.4700	1.4700	1.4700	1.4700
65	1.5750	1.5750	1.5750	1.5750	1.5750	1.5750	1.5750	1.5750	1.5750	1.5750
70	1.6650	1.6650	1.6650	1.6650	1.6650	1.6650	1.6650	1.6650	1.6650	1.6650
75	1.7350	1.7350	1.7350	1.7350	1.7350	1.7350	1.7350	1.7350	1.7350	1.7350

α [°]	Re=1.0E4	Re=2.0E4	Re=4.0E4	Re=8.0E4	Re=1.6E5	Re=3.6E5	Re=7.0E5	Re=1.0E6	Re=2.0E6	Re=5.0E6
80	1.7800	1.7800	1.7800	1.7800	1.7800	1.7800	1.7800	1.7800	1.7800	1.7800
85	1.8000	1.8000	1.8000	1.8000	1.8000	1.8000	1.8000	1.8000	1.8000	1.8000
90	1.8000	1.8000	1.8000	1.8000	1.8000	1.8000	1.8000	1.8000	1.8000	1.8000
95	1.7800	1.7800	1.7800	1.7800	1.7800	1.7800	1.7800	1.7800	1.7800	1.7800
100	1.7500	1.7500	1.7500	1.7500	1.7500	1.7500	1.7500	1.7500	1.7500	1.7500
105	1.7000	1.7000	1.7000	1.7000	1.7000	1.7000	1.7000	1.7000	1.7000	1.7000
110	1.6350	1.6350	1.6350	1.6350	1.6350	1.6350	1.6350	1.6350	1.6350	1.6350
115	1.5550	1.5550	1.5550	1.5550	1.5550	1.5550	1.5550	1.5550	1.5550	1.5550
120	1.4650	1.4650	1.4650	1.4650	1.4650	1.4650	1.4650	1.4650	1.4650	1.4650
125	1.3500	1.3500	1.3500	1.3500	1.3500	1.3500	1.3500	1.3500	1.3500	1.3500
130	1.2250	1.2250	1.2250	1.2250	1.2250	1.2250	1.2250	1.2250	1.2250	1.2250
135	1.0850	1.0850	1.0850	1.0850	1.0850	1.0850	1.0850	1.0850	1.0850	1.0850
140	0.9250	0.9250	0.9250	0.9250	0.9250	0.9250	0.9250	0.9250	0.9250	0.9250
145	0.7550	0.7550	0.7550	0.7550	0.7550	0.7550	0.7550	0.7550	0.7550	0.7550
150	0.5750	0.5750	0.5750	0.5750	0.5750	0.5750	0.5750	0.5750	0.5750	0.5750
155	0.4200	0.4200	0.4200	0.4200	0.4200	0.4200	0.4200	0.4200	0.4200	0.4200
160	0.3200	0.3200	0.3200	0.3200	0.3200	0.3200	0.3200	0.3200	0.3200	0.3200
165	0.2300	0.2300	0.2300	0.2300	0.2300	0.2300	0.2300	0.2300	0.2300	0.2300
170	0.1400	0.1400	0.1400	0.1400	0.1400	0.1400	0.1400	0.1400	0.1400	0.1400
175	0.0550	0.0550	0.0550	0.0550	0.0550	0.0550	0.0550	0.0550	0.0550	0.0550
180	0.0250	0.0250	0.0250	0.0250	0.0250	0.0250	0.0250	0.0250	0.0250	0.0250

A11. Lift and drag coefficients of the airfoil NACA 0021

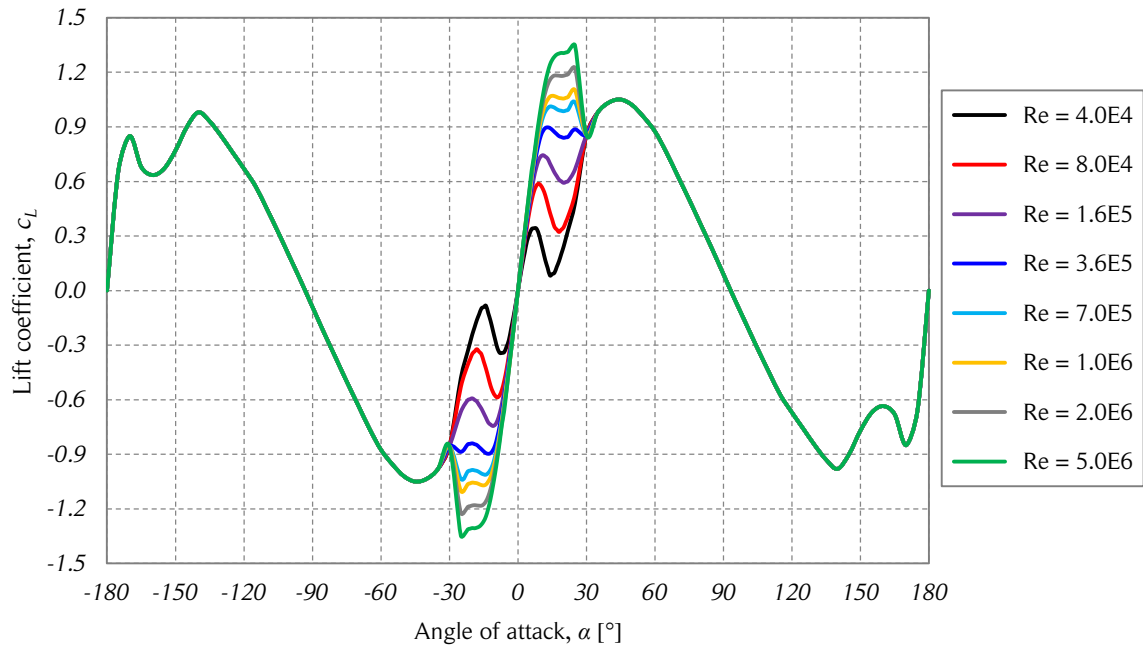


Figure A.1. Lift coefficient vs. angle of attack.

The figure shows the lift coefficient as a function of the angle of attack for various values of the Reynolds number. Source: [4].

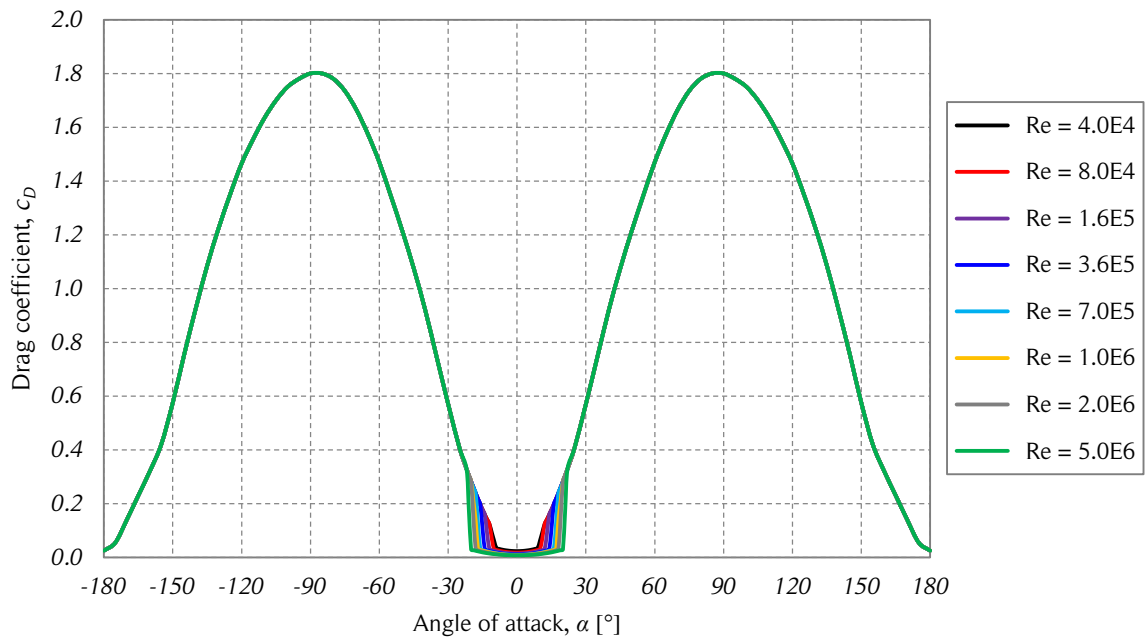


Figure A.2. Drag coefficient vs. angle of attack.

The figure shows the drag coefficient as a function of the angle of attack for various values of the Reynolds number. Source: [4].

A12. Comparison of four NACA 00XX airfoils lift coefficients

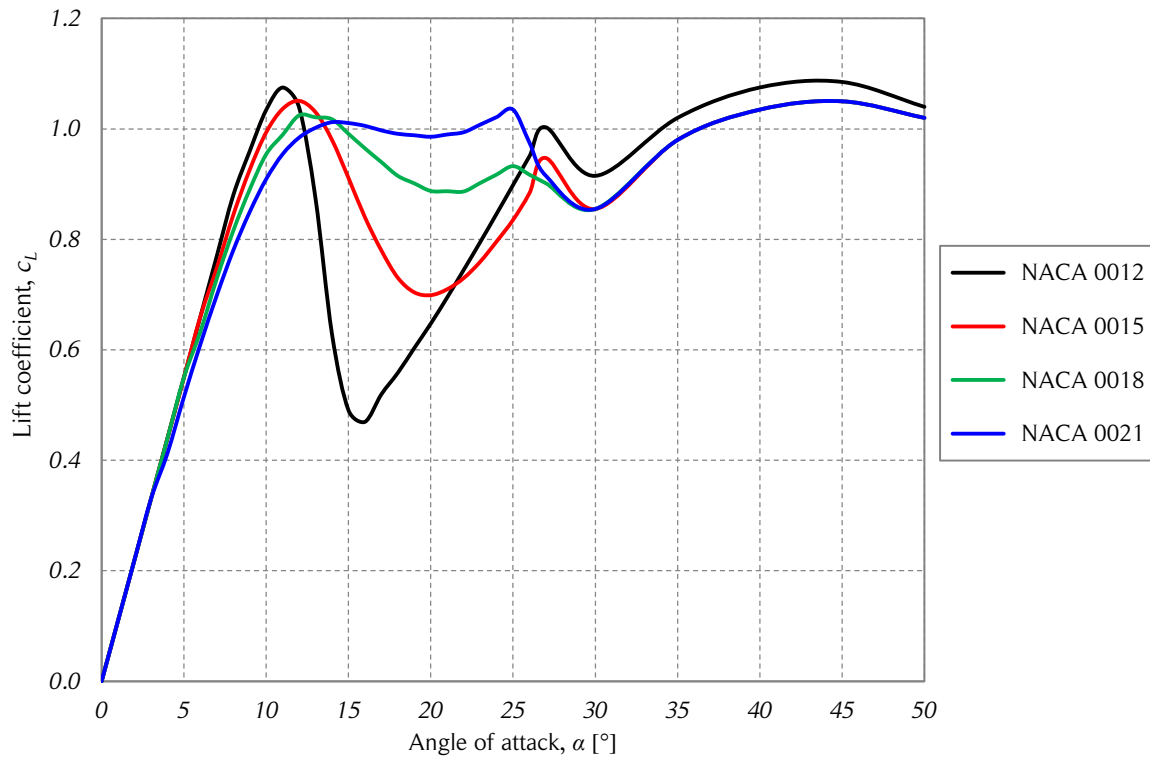


Figure A.3. Lift coefficient comparison of NACA 00XX airfoils.

The figure shows the lift coefficient as a function of the angle of attack of four NACA 00XX airfoils at Reynolds number 700.000. Source: [4].

APPENDIX B. THREE-DIMENSIONAL CORRECTIONS

Computational codes in MATLAB R2008b for the three-dimensional corrections (TDC).

B1. Function that imports aerodynamic coefficients

```
function [ CL, CD ] = f_read_AC( naca )

% function read_data returns the lift and drag coefficient matrix from the respective .txt
% files, where:
% [ CL, CD ] = read_data( naca )
% naca = 12, 15, 18, 21, 25

if naca == 12

    CL = importdata('CL_NACA0012.txt');
    CD = importdata('CD_NACA0012.txt');

elseif naca == 15

    CL = importdata('CL_NACA0015.txt');
    CD = importdata('CD_NACA0015.txt');

elseif naca == 18

    CL = importdata('CL_NACA0018.txt');
    CD = importdata('CD_NACA0018.txt');

elseif naca == 21

    CL = importdata('CL_NACA0021.txt');
    CD = importdata('CD_NACA0021.txt');

elseif naca == 25

    CL = importdata('CL_NACA0025.txt');
    CD = importdata('CD_NACA0025.txt');

else

    disp('ERROR - The aerodynamic coefficients of the chosen airfoil are not available.')

end
```

B2. Flow expansion data from the 2-D CFD simulations

Variable	$TSR = 1$	$TSR = 2$	$TSR = 3$	$TSR = 4$	$TSR = 5$	$TSR = 6$
W_{∞} / D	0.90	0.88	0.86	0.84	0.82	0.80
W_w / D	1.10	1.12	1.14	1.16	1.18	1.20
L_{∞} / D	2.00	2.00	2.00	2.00	2.00	2.00
L_w / D	3.00	3.00	3.00	3.00	3.00	3.00

B3. Function that interpolates the aerodynamic coefficients

```

function [ cl, cd ] = f_AC( naca, alpha, Re , CL, CD )

% function AC (aerodynamic coefficients) returns the interpolated lift and
% drag coefficients for the respective values of alpha and Re, where:
% [ cl, cd ] = AC( naca, alpha, Re , CL, CD )
% naca = 12, 15, 18, 21, 25
% alpha = angle of attack in degrees
% Re = blade Reynolds number
% CL = lift coefficient matrix
% CD = drag coefficient matrix

% Save the sign of alpha
Sa = sign(alpha);
% Absolute value of alpha
a = abs(alpha);
% Set alpha between 0 and 180 deg, save the sign of alpha in case alpha >= 180
a = mod(a,360);
if a >= 180
    a = 360 - a;
    Sa = -Sa;
end

if naca == 12 || naca == 15 || naca == 18

    % find row
    if a <= 27
        I1 = floor(a) + 2;
        I2 = I1 + 1;
    elseif a < 30
        I1 = 29;
        I2 = I1 + 1;
    elseif a > 179.99
        I1 = 60;
        I2 = I1;
    else
        I1 = (floor(a) - mod(floor(a),5))/5 + 24;
        I2 = I1 + 1;
    end

    % find column
    if Re <= 10000
        J1 = 2;
        J2 = 2;
    elseif Re <= 20000
        J1 = 2;
        J2 = J1 + 1;
    elseif Re <= 40000
        J1 = 3;
        J2 = J1 + 1;
    elseif Re <= 80000
        J1 = 4;
        J2 = J1 + 1;
    elseif Re <= 160000
        J1 = 5;
        J2 = J1 + 1;
    elseif Re <= 360000
        J1 = 6;
        J2 = J1 + 1;
    elseif Re <= 700000
        J1 = 7;
        J2 = J1 + 1;
    elseif Re <= 1000000
        J1 = 8;
        J2 = J1 + 1;
    elseif Re <= 2000000
        J1 = 9;
        J2 = J1 + 1;

```

```
elseif Re <= 5000000
    J1 = 10;
    J2 = J1 + 1;
elseif Re < 10000000
    J1 = 11;
    J2 = J1 + 1;
else
    J1 = 12;
    J2 = J1;
end

else % naca 0021 or 0025

    % find row
    if a <= 22
        I1 = floor(a) + 2;
        I2 = I1 + 1;
    elseif a < 25
        I1 = 24;
        I2 = I1 + 1;
    elseif a > 179.99
        I1 = 56;
        I2 = I1;
    else
        I1 = (floor(a) - mod(floor(a),5))/5 + 20;
        I2 = I1 + 1;
    end

    % find column
    if Re <= 10000
        J1 = 2;
        J2 = 2;
    elseif Re <= 20000
        J1 = 2;
        J2 = J1 + 1;
    elseif Re <= 40000
        J1 = 3;
        J2 = J1 + 1;
    elseif Re <= 80000
        J1 = 4;
        J2 = J1 + 1;
    elseif Re <= 160000
        J1 = 5;
        J2 = J1 + 1;
    elseif Re <= 360000
        J1 = 6;
        J2 = J1 + 1;
    elseif Re <= 700000
        J1 = 7;
        J2 = J1 + 1;
    elseif Re <= 1000000
        J1 = 8;
        J2 = J1 + 1;
    elseif Re <= 2000000
        J1 = 9;
        J2 = J1 + 1;
    elseif Re < 5000000
        J1 = 10;
        J2 = J1 + 1;
    else
        J1 = 11;
        J2 = J1;
    end

end

% Reynolds interpolation
if J1 == J2
    c11 = CL(I1, J1);
    c12 = CL(I2, J1);
    cd1 = CD(I1, J1);
```

```

        cd2 = CD(I2,J1);
else
    rRe = ( Re - CL(1,J1) )/( CL(1,J2) - CL(1,J1) );
    cl1 = CL(I1,J1) + rRe*( CL(I1,J2) - CL(I1,J1) );
    cl2 = CL(I2,J1) + rRe*( CL(I2,J2) - CL(I2,J1) );
    cd1 = CD(I1,J1) + rRe*( CD(I1,J2) - CD(I1,J1) );
    cd2 = CD(I2,J1) + rRe*( CD(I2,J2) - CD(I2,J1) );
end

% alpha interpolation
if I1 == I2
    cl = Sa*c11;
    cd = cd1;
else
    ra = ( a - CL(I1,1) )/( CL(I2,1) - CL(I1,1) );
    cl = Sa*(c11 + ra*(c12 - c11));
    cd = cd1 + ra*(cd2 - cd1);
end

% END function AC

```

B4. Three-dimensional correction (TDC) code

```

% Main geometric definitions
N = 3; % Number of blades
R = 3; % Turbine radius [m]
D = 2*R; % Turbine diameter [m]
H = 5; % Turbine height [m]
c = 0.25; % Airfoil chord [m]
naca = 0021; % NACA airfoil geometry
sigma = N*c/R;

% Local air conditions
Uinf = 10; % Local wind speed [m/s]
zr = 6.2; % Reference altitude [m]
PLE = 0.185; % Local power law exponent
rho = 1.225; % Local air density [kg/m^3]
nu = 14.8e-6; % Local air kinematic viscosity [m^2/s]

% Additional geometric definitions
H0 = 3.7; % Ground clearance [m]
DT = 0.2; % Tower diameter [m]
LBT = 1; % Length of blade tapering [m]
BTCF = 0.6; % Blade tapering chord factor
NSPB = 2; % Number of struts per blade
nacaS = 0025; % Struts NACA airfoil geometry
SA = 17.6; % Strut angle [°]
SIC = 0.32; % Strut initial chord [m]
SFC = 0.2; % Strut final chord [m]
NASPB = 2; % Number of auxiliary struts per blade
ASL = 1.3; % Auxiliary strut length [m]
ASA = 30; % Auxiliary strut angle [°]
ASD = 0.08; % Auxiliary strut diameter [m]
ASC = 0.100; % Auxiliary strut chord [m]

% Solution

TLM = 2; % Tip-losses method
% 0: finite aspect, 1: blade spanwise velocity, 2: both

NTSRC = 6; % Number of tsr cases
dtheta = 0.25; % Azimuthal angle discretization [°]
theta = -90 : dtheta : 270 - dtheta; % azimuthal angle vector [°]
LT = 360/dtheta; % Length of vector theta

dz = H/50; % Vertical discretization [m]
z = H0 : dz : H0 + H; % Vertical coordinate vector [m]

```

```

LZ = length(z); % Length of vector z
Fu = zeros(1,LZ); % Upstream tip-losses factor
Fd = zeros(1,LZ); % Downstream tip-losses factor
MF_t = zeros(1,LZ); % Mean tangential force [N]
cp = zeros(1,NTSRC); % Power coefficient

dr = (R - DT/2)/30; % Strut radial discretization [m]
ri = DT/2 : dr : R; % Strut radial coordinate [m]
LR = length(ri); % Length of vector ri
ci = SIC + (SFC-SIC)*(ri - DT/2)/(R - DT/2); % Chord vector [m]

U = zeros(LT,NTSRC); % Local wind velocity [m/s]
W = zeros(LT,NTSRC); % Relative wind velocity [m/s]
alpha = zeros(LT,NTSRC); % Angle of attack [°]
F_t = zeros(LT,LZ,NTSRC); % Tangential force [N]
cL = zeros(LT,LZ,NTSRC); % Lift coefficient matrix
cD = zeros(LT,LZ,NTSRC); % Drag coefficient matrix

dlosses = zeros(NTSRC,LT);
losses = zeros(1,NTSRC);

% Input files
ID = importdata('expansion_data.txt'); % import expansion data
ED = ID*D; % expansion data
IFx = importdata('Fx_data.txt'); % import Fx data from 2-D CFD simulations
IFy = importdata('Fy_data.txt'); % import Fy data from 2-D CFD simulations

[ CL, CD ] = f_read_AC( nacaS ); % Lift and drag data of the strut airfoil section

% TSR cases
for tsr = 1 : NTSRC

omega = Uinf*tsr/R; % angular velocity [rad/s]

% find coefficients
A1 = (D - ED(1,tsr))/(2*( ED(3,tsr) )^2 );
B1 = (D - ED(1,tsr))/( ED(3,tsr) );
C1 = D/2;
A2 = ED(2,tsr)/2;
B2 = 0.5*( ED(2,tsr) - D );
C2 = 2*( D - ED(1,tsr) )/( ED(3,tsr)*( ED(2,tsr) - D ) );

% vertical discretization
for k = 1 : LZ

z(k) = H0 + (k-1)*dz;

% chord as a function of height z
if z(k) < H0 + LBT
cz = c*( BTCF + (1-BTCF)*(z(k)-H0)/LBT );
elseif z(k) >= H0 + LBT && z(k) <= H0 + H - LBT
cz = c;
else
cz = c*( 1 - (1-BTCF)*(z(k)-(H+H0-LBT))/LBT );
end

Ue = Uinf*(z(k)/zr)^0.185*ED(1,tsr)/D; % local velocity at x = 0
su = pi*Ue/(N*omega); % upstream factor
Uw = Uinf*(z(k)/zr)^0.185*ED(1,tsr)/ED(2,tsr); % local velocity at x = R
sd = pi*Uw/(N*omega); % downstream factor
h = H/2 - abs( z(k) - H0 - H/2 ); % change of vertical coordinate

% Tip-losses method
if TLM == 0
Fu(k) = 1;
Fd(k) = 1;
else
Fu(k) = acos( exp(-pi*h/su) )/acos( exp(-pi*H/(2*su)) );
Fd(k) = acos( exp(-pi*h/sd) )/acos( exp(-pi*H/(2*sd)) );
end

```

```

% azimuthal discretization
for t = 1 : LT

    V = omega*R;

    % W and alpha depending on theta and z
    if theta(t) <= 90 % downstream
        WX = 2*( A2 - B2*exp( -C2*R*cosd(theta(t)) ) ); % width at coordinate x
        U(t,tsr) = Uinf*(z(k)/zr)^0.185*ED(1,tsr)/WX;
        W(t,tsr) = ((V+U(t,tsr)*sind(theta(t)))^2+(Fd(k)*U(t,tsr)*cosd(theta(t)))^2)^0.5;
        alpha(t,tsr) = sign( cosd(theta(t)) )*acosd( (V + U(t,tsr)*sind(theta(t)))/W(t,tsr) );
    else % upstream
        WX = 2*( A1*(R*cosd(theta(t)))^2 + B1*R*cosd(theta(t)) + C1 ); % width at coordiante x
        U(t,tsr) = Uinf*(z(k)/zr)^0.185*ED(1,tsr)/WX;
        W(t,tsr) = ((V+U(t,tsr)*sind(theta(t)))^2 + (Fu(k)*U(t,tsr)*cosd(theta(t)))^2)^0.5;
        alpha(t,tsr) = sign( cosd(theta(t)) )*acosd( (V + U(t,tsr)*sind(theta(t)))/W(t,tsr) );
    end

    % W and alpha depending only on theta (original)
    W_o = ( ( V + U(t,tsr)*sind( theta(t) ) )^2 + ( U(t,tsr)*cosd( theta(t) ) )^2 )^0.5;
    alpha_o = sign( cosd(theta(t)) )*acosd( ( V + U(t,tsr)*sind(theta(t)) )/W_o );

    % Force projections
    Ft = IFy(t,tsr)*cosd(theta(t)) - IFx(t,tsr)*sind(theta(t));
    Fr = IFx(t,tsr)*cosd(theta(t)) + IFy(t,tsr)*sind(theta(t));

    FL = Fr*cosd(alpha_o) + Ft*sind(alpha_o);
    FD = Fr*sind(alpha_o) - Ft*cosd(alpha_o);

    % CFD aerodynamic coefficients
    cl_o = FL/(0.5*rho*c*W_o^2);
    cd_o = FD/(0.5*rho*c*W_o^2);

    % Corrected coefficients
    if TLM == 1
        cL(t,k,tsr) = cl_o;
        cD(t,k,tsr) = cd_o;
    else
        cL(t,k,tsr) = cl_o/( 1 + 1.8*( 1 + 0.8*naca/100 ) *c/H);
        cD(t,k,tsr) = cd_o + c/(pi*H)*( cL(t,k,tsr) )^2;
    end

    % Blade tangential force
    c_t = cL(t,k,tsr)*sind( alpha(t,tsr) ) - cD(t,k,tsr)*cosd( alpha(t,tsr) );
    F_t(t,k,tsr) = 0.5*rho*dz*cz*(W(t,tsr))^2*c_t;

    % Strut losses
    if k == 1
        for i = 1 : LR

            xi = ri(i)*cosd(theta(t));
            if theta(t) <= 90 % downstream
                WX = 2*( A2 - B2*exp( -C2*xi ) );
                Ui = Uinf*ED(1,tsr)/WX;
                Wi = ( ( omega*ri(i) + Ui*sind( theta(t) ) )^2 + ( Ui*cosd( theta(t) ) )^2 )^0.5;
                alphai = sign( cosd(theta(t)) )*acosd( ( omega*ri(i) + Ui*sind(theta(t)) )/Wi );
            else % upstream
                WX = 2*( A1*(xi)^2 + B1*xi + C1 );
                Ui = Uinf*ED(1,tsr)/WX;
                Wi = ( ( omega*ri(i) + Ui*sind( theta(t) ) )^2 + ( Ui*cosd( theta(t) ) )^2 )^0.5;
                alphai = sign( cosd(theta(t)) )*acosd( ( omega*ri(i) + Ui*sind(theta(t)) )/Wi );
            end

            Rei = abs(ci(i)*Wi*cosd(alphai)/nu);

            % sign of drag
            if alphai > 90 || alphai < - 90
                alphai2 = 180;
                salphai = -1;
            else
                alphai2 = 0;
            end
        end
    end

```

```
    salphai = 1;
end

[ cLi, cDi ] = f_AC( nacaS, alphai2, Rei , CL, CD );

% auxiliar struts

if ri(i) <= ASL*cosd(ASA)
    las = ASC*(Wi*cosd(alphai))^2*cDi*salphai*ri(i);
end

dlosses(tsr,t) = dlosses(tsr,t) + ci(i)*(Wi*cosd(alphai))^2*cDi*salphai*ri(i) + las;

end
end % strut losses

end % azimuthal discretization

MF_t(k) = N*mean(F_t(:,k,tsr)); % mean tangential force per dz

end % vertical discretization

% power coefficient
cp(tsr) = sum(MF_t)*R*omega/(0.5*rho*D*H*Uinf^3);

% strut losses
losses(tsr) = 0.5*rho*omega*dr/cosd(SA)*N*NSPB*mean(dlosses(tsr,:))/(0.5*rho*D*H*Uinf^3);

end % TSR cases
```